Single crystal ferroelectrics: Macroscopic and microscopic studies

Prashant R. Potnis
Balliol College

Under the supervision of
Dr. John Huber

This thesis has been submitted to the University of Oxford for the degree of Doctor of Philosophy in the Department of Engineering Science.

September 2011

Single crystal ferroelectrics: macroscopic and microscopic studies

Prashant R Potnis, Balliol College, University of Oxford

For the degree of DPhil in Engineering Science, Trinity 2011.

Abstract

The aim of this thesis was to improve the understanding of microstructure in single crystal ferroelectrics. This was achieved through macroscopic testing of Lead Magnesium Niobate – Lead Titanate (PMN-PT) and microscopic observations of Barium Titanate (BT) single crystals.

Multi-axial polarization rotation tests on PMN-PT showed a gradual increase in the change in dielectric displacement due to ferroelectric switching as the electric field is applied at increasing angles to the initial polarization direction. A relatively high remnant polarization for loading angle near to 90° suggested that PMN-PT is more polarizable in certain directions. Strains measured in two directions, parallel to the electric field and perpendicular to the electric field, showed a noticeable variation on two opposite faces of the specimen suggesting an effect of local domain configurations on macroscopic behaviour. A micromechanical model gave an insight into the switching systems operating in the crystal during the polarization rotation test.

Domain structure in BT was mapped using synchrotron X-ray reflection topography. By making use of the angular separation of the diffracted reflections and specimen rocking, different domain types could be unambiguously identified, along with the relative tilts between adjacent domains. Fine needle domains (width ≈ 10μm) were successfully mapped providing a composite topograph directly comparable with optical micrograph.

The domain structure was confirmed using other techniques such as piezoresponse force microscopy and atomic force microscopy/scanning electron microscopy and optical observations on the etched crystal. Results show that combined use of multiple techniques is necessary to gain a consistent interpretation of the microstructure. Finally, domain evolution in BT under compressive mechanical loading was observed in-situ using optical and X-ray diffraction techniques providing a series of images that show ferroelastic transition. The domain configurations influence the switching behaviour and constitutive models that can account for such effects need to be developed. Quantitative and qualitative data presented in this thesis can assist model development and validation.

Acknowledgement

I would like to express my deep sense of gratitude to my PhD supervisor Dr. John Huber for his guidance, support and constant encouragement. I am thankful to him for providing me with many opportunities to develop as a researcher during the course of PhD.

I acknowledge Engineering and Physical Sciences Research Council (EPSRC), UK, for providing financial support for this project. I am indebted to my college advisor, Prof. Paul Buckley, for all the discussions reviewing my progress in each term. I also thank Balliol College, especially to academic administrator (Mrs. Price) and senior tutor (Dr. Trott), for all the support that has been extended during the course of study.

I am very much thankful to Diamond Light Source, UK for allotting beam time to conduct the synchrotron X-ray diffraction experiments. During these experiments, we received great support from Dr. John Sutter, Dr. Kawal Sawhney, Dr. Igor Dolbnya, Dr. Michele Warren, Prof. Alexander Korsunsky, Mr. Brian Abbey and Dr. Felix Hoffman. I believe that these experiments would not have been possible without valuable inputs from all of them. I am grateful to Asylum Research Ltd. for allowing me to conduct the PFM experiments at their facility.

I thank Nien-ti Tsou for the computer program related to synchrotron work and Dan Sui for participating in some of the synchrotron experimentation. I acknowledge Dr. Huber's former students Dr. Jay Shieh and Dr. Qida Liu for the help through email communications.

I was involved in establishing and developing the laboratory for experimental work on ferroelectrics at solid mechanics and materials group. This was a challenging task given a stipulated time period and variety of techniques, instruments. It surely would have been unattainable without huge support from Mr. Richard Duffin and mechanical workshop, Mr. Anthony Cooper and electronics workshop, Dr. Kalin Dragnevski, Ms. Amanda Bradbury and Mr. Jon Gregory. I acknowledge Struers Ltd., Omega Piezo Ltd., Marketech International Inc., Superconix Inc., Omega Engineering Ltd., Techni Measure Ltd., GT vision Ltd. for offering a timely help while purchasing and troubleshooting lab equipments.

It has been a pleasure working at solid mechanics and materials group and I thank all the academic staff and colleagues in the group for an excellent research atmosphere. I would like to acknowledge Prof. David Hills, Mr. Bob Scott and Mr. Paul Bailey for giving me an opportunity to demonstrate in undergraduate engineering labs.

I would also like to take this opportunity to thank all my friends in and out of Oxford who supported and encouraged me from time to time. I am very much thankful to my Indian friends at Oxford for various musical events and endless discussions on bollywood, cricket and politics.

Stay at Oxford was very memorable due to my wife, Suruchi, whose encouragement throughout this work was invaluable. I am grateful to my parents in laws for being very supportive and understanding. Finally, no thanks are sufficient for the encouragement and support given by my parents, sister and her family at all times. I cannot write enough to express my gratitude towards them. I feel blessed to have such a great family support.

Contents

List of figures

1. Introduction

Since the discovery of ferroelectricity, polycrystalline and single crystal piezoelectric and ferroelectric ceramics are widely used in the fields of electronics and optics. Applications, spanning from bulk ceramic capacitors and transducers to thin films used in memory applications, have continuously encouraged technological development and understanding of these materials. It is not surprising that the tremendous potential in these materials has motivated researchers over the globe to explore the new applications of these ceramics.

The research work presented in this thesis focuses on single crystal ferroelectrics. The aim of this work is to develop and apply methods that can enhance the understanding of single crystals at the micro-scale. In this chapter, first, a few basic concepts pertaining to ferroelectrics are introduced. Next, opportunities and challenges relating to single crystal ferroelectrics are discussed along with the motivation and approach of the present research work. Finally, the structure of the chapters of this thesis is given.

1.1. Piezoelectric and ferroelectric materials

Piezoelectricity was conceptualised in 1880 by Jacques and Pierre Curie. Piezoelectricity can be defined as electricity generated by mechanical stress. Based on the geometry of the crystals, there are 32 symmetry point groups. For piezoelectricity to exist the crystal must be non-centrosymmetric, otherwise a uniform stress produces symmetrical charge distribution giving no net moment of charge [1–3]. A homogeneous stress applied to such a non-centrosymmetric crystal causes the net movement of the positive and negative ions

to form electric dipoles thereby making the crystal polar. The electric displacement is a measure of polarity in the crystal and the polarity varies with the applied stress. The piezoelectric effect is thermodynamically reversible in that materials exhibiting the direct piezoelectric effect (polarisation when stress is applied) also exhibit the converse piezoelectric effect (straining when an electric field is applied).

Out of the crystal classes that show piezoelectricity, a few crystal classes are capable of becoming permanently polarised below a certain temperature, and change polarity with temperature, a phenomenon known as pyroelectricity. Of the 21 non-centrosymmetric point groups, 20 are piezoelectric and 10 of these show spontaneous polarisation and hence are pyroelectric (figure 1.1).

A subgroup of such spontaneously polarised pyroelectric materials is ferroelectric materials in which the polarity of the crystals can be reversed by the application of an external electric field. The ability to reorient the spontaneous polarisation in ferroelectrics leads to many useful applications and conscientious efforts are being done to explore and exploit these materials. Factors which affect the polarisation reversibility by an electric field include crystal defects and electric conductivity. Note, terminology in ferroelectricity is analogous to that of ferromagnetism but most ferroelectric materials do not contain the element iron.

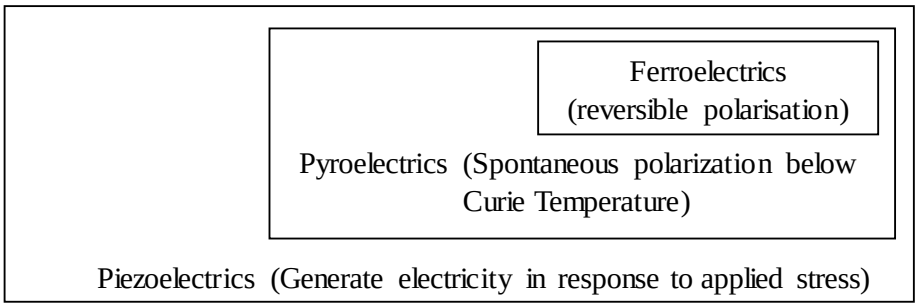

Figure 1.1: Ferroelectric materials are a subset of pyroelectric and piezoelectric materials and possess all the properties of piezo- and pyro- electric materials.

After the discovery of the remarkably high dielectric constant (K > 1100) of Barium Titanate in 1940 [1], higher piezoelectric coefficients and dielectric constants were obtained by alloying various compositions of Lead Zirconate ($PbZrO_3$) and Lead Titanate ($PbTiO_3$), producing Lead Zirconate Titanate (PZT). Between 1960 and 1995, various ferroelectrics were discovered but PZT dominated the market due to the growth of applications in the microelectronics industry. A breakthrough came in 1997 after the discovery of single crystal ferroelectrics showing an order of magnitude strain increase [4]. A systematic and comprehensive overview of progress in ferroelectric ceramics is given by Fousek [5]. A detailed discussion about microstructure and properties of ferroelectric ceramics, single crystals and thin films can be found in the recently published handbook of advanced dielectric, piezoelectric and ferroelectric materials edited by Ye [6] and the book by Tagantsev *et al*. [7].

1.2. Introduction to ferroelectric microstructure

1.2.1. Definitions

The direct and converse effects of piezoelectricity can be observed below a temperature called the *Curie temperature* (T_c). An increase in temperature typically leads to decrease in polarisation effect and the polarisation suddenly falls to zero as the temperature reaches the Curie temperature. Below the Curie temperature, the ceramics are piezoelectric after poling (application of strong electric field). The electric effect induced due to poling is measured in terms of electric displacement (or electric polarisation) and electric field while the mechanical effect is measured in terms of strain and stress. These are tensor quantities and are often denoted using subscript notation.

In the absence of stress or electric field the electric displacement, D_i**,** or polarisation vector, P_i**,** is defined as the sum of dipole moment μ_i per unit volume. In small volume V,

$$P_i = \mu_i / V \tag{1.1}$$

An applied stress σ_{ij} generates elastic strain ε_{ij}, and electric displacement D_i through the piezoelectric effect. Similarly, electric field E_i generates strain through converse piezoelectricity, and electric displacement by the dielectric effect. The relationship is given as below:

$$\varepsilon_{ij} = L_{ijkl}\sigma_{kl} + d_{kij}E_k + \varepsilon_{ij}^{r} \tag{1.2}$$

$$D_i = d_{ikl}\sigma_{kl} + \kappa_{ik}E_k + P_i^{r} \tag{1.3}$$

Here, L_{ijkl} is the tensor of elastic moduli, d_{kij} is the tensor of piezoelectric coefficients and ε_{ij}^{r} is the remnant strain (the strain remaining when electric field and stress are zero). Similarly, κ_{ik} is the tensor of dielectric permittivity and P_i^{r} is the remnant polarisation.

The coupling between electrical, mechanical and thermal parameters of the material can be explained using thermodynamic formulation. The reversible change dU in the internal energy U of the elastic dielectric subjected to a small change in strain dε_{ij}, electric displacement dD_i and entropy dS can be written as [8],

$$\mathrm{d}U = T\,\mathrm{d}S + \sigma_{ij}d\varepsilon_{ij} + E_i dD_i \tag{1.4}$$

where T is the temperature, σ_{ij} is the applied stress and E_i is the applied electric field. The Gibbs free energy, G is given by,

$$G = U - TS - \sigma_{ij}d\varepsilon_{ij} - E_i dD_i \tag{1.5}$$

From equations 1.4 and 1.5, the change in G, dG, can be written as,

$$\mathrm{d}G = -S\mathrm{d}T - \sigma_{ij}d\varepsilon_{ij} - D_i dE_i \tag{1.6}$$

The partial derivative using equation 1.6 is given by equation 1.7 where subscripts indicate the variables held constant.

$$d_{ijk}^{T,\sigma} = \left(\frac{\partial \varepsilon_{ij}}{\partial E_k}\right)_{T,X} = -\left(\frac{\partial^2 G}{\partial E_k \partial \sigma_{ij}}\right) = -\left(\frac{\partial^2 G}{\partial \sigma_{ij} \partial E_k}\right) = \left(\frac{\partial D_k}{\partial \sigma_{ij}}\right)_{T,E} = d_{kij}^{T,E} \quad (1.7)$$

Converse piezoelectric effect Direct piezoelectric effect

Due to the thermodynamic equivalence of direct and converse piezoelectric effect, piezoelectric coefficient that relates change in strain due to the applied electric field is same as the one that relates the change in polarization due to the applied stress.

In commonly used notation [9], the number of indices is reduced by writing σ_1 for σ_{11}, σ_2 for σ_{22} and similarly reducing the other tensors. Equations (1.2) and (1.3) become,

$$\varepsilon_i = L_{ij}\sigma_j + d_{ij}E_j + \varepsilon_i^{\mathrm{r}} \quad (1.8)$$

$$D_i = d_{ij}\sigma_j + \kappa_{ij}E_j + P_i^{\mathrm{r}} \quad (1.9)$$

The electric displacement is directly proportional to the stress applied (holding other quantities fixed) and the constant is called the *piezoelectric coefficient* (*d*). If a uniaxial stress is applied in the 3-direction, coefficient d_{33} relates the electric displacement generated in the 3-direction, D_3, to the applied stress σ_3. Applying stress σ_3 alone generates a change in electric displacement D_3 given by equation 1.10 and similarly, applying electric field E_3 alone gives a change in ε_3 given by equation 1.11.

$$D_3 = d_{33}\sigma_3 \quad (1.10)$$

$$\varepsilon_3 = d_{33}E_3 \quad (1.11)$$

In both the equations, d has units C/N or m/V and high values of d_{33} are typically desirable for the actuator and sensors applications. A coefficient d_{31} relates polarization induced in 3-direction due to the mechanical stress in 1-direction or strain induced in 1-direction due to electric field in 3-direction.

1.2.2. Spontaneous polarization and the concept of domains

Ferroelectricity is an irreversible effect which means that changes in polarity remain after unloading. The *spontaneous polarization (P_s)* is the stable polarisation magnitude in the unit cell of a crystal. There are four main types of ferroelectric solids [1]:

(i) the tungsten-bronze group (e.g. $PbNb_2O_6$)

(ii) the oxygen octahedral group (e.g. Perovskite - ABO_3 type, $BaTiO_3$, $PbZrO_3$)

(iii) the pyrochlore group (e.g. $Cd_2Nb_2O_7$)

(iv) the bismuth-layer structure group (e.g.$Bi_4Ti_3O_{12}$)

Out of these groups, the most important category, for current technology, is the second group, consisting of ABO_3 type perovskite. Typical examples are Barium Titanate (BT), Lead Zirconate Titanate (PZT), Lanthanum-doped Lead Zirconium Titanate (PLZT) and Lead Magnesium Niobate (PMN).

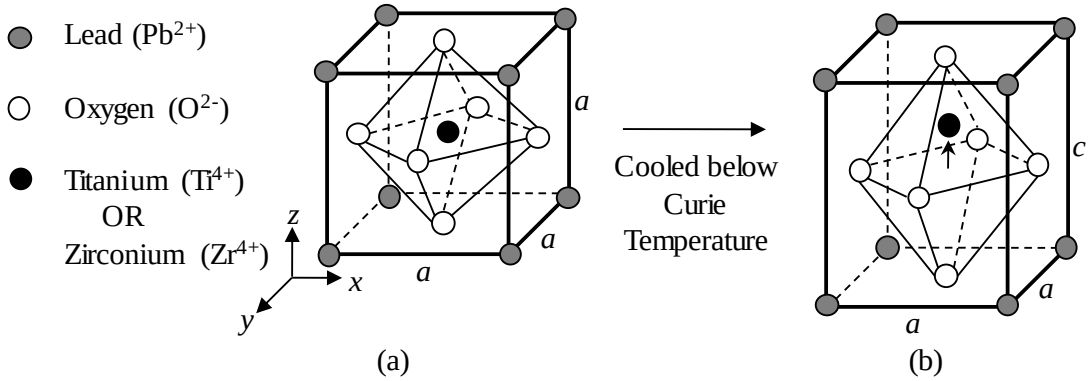

Figure 1.2: PZT unit cell (a) paraelectric cubic structure above Curie temperature (b) ferroelectric tetragonal structure with spontaneous polarization below Curie temperature.

Consider a typical ABO_3 type unit cell of PZT. As shown in figure 1.2(a), above the Curie temperature, a paraelectric cubic structure is observed where oxygen O^{2-} anions occupy the face centres forming oxygen octahedron. The Zr^{4+} or Ti^{4+} cation occupies the central octahedral site and the corner atoms are Pb^{2+}. The polarization in the paraelectric phase is zero, but below the Curie temperature, a tetragonal phase is observed and the

central cation moves into one of the six stable positions along positive and negative directions of the crystallographic axes *x*, *y* and *z*. This gives a spontaneous polarization. (figure 1.2(b)) [3,10].

If an electric field (**E**) is applied to such a crystal, the central cation can move to a new stable position (figure 1.3). Individual movements in every unit cell contribute in giving a net change in polarisation to the crystal in the direction of the applied electric field. This can also result in a shape change or strain in the crystal.

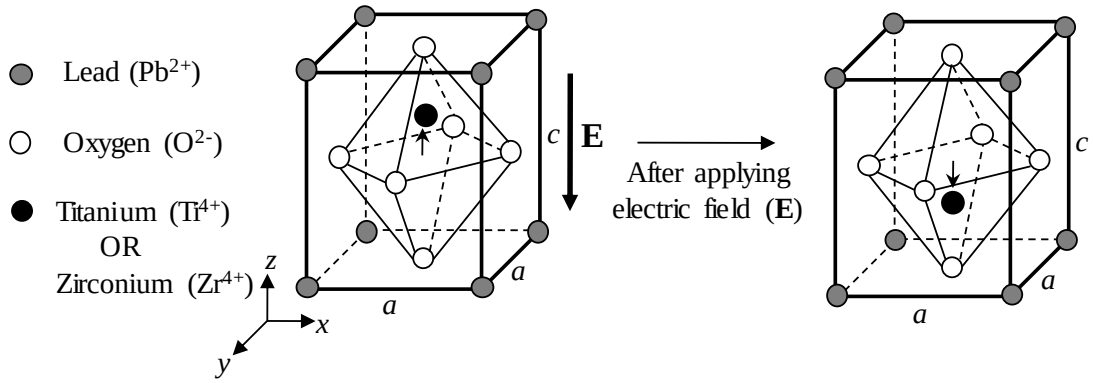

Figure 1.3: 180° switching in tetragonal PZT under the application of electric field.

Figure 1.3 shows the movement of the central cation along the *z*-axis under the application of electric field, termed as 180° *switching*. In the tetragonal system, it is also possible to rotate the polarisation through 90°, referred to as 90° switching. Depending upon the crystal structure, various switching systems are possible, for example, in case of a rhombohedral unit cell, 71°, 109° and 180° switching systems arises and in case of an orthorhombic unit cell, 60°,90°,120° and 180° switching systems are possible. Switching can also be attained under the application of mechanical stress.

A typical ferroelectric crystal may contain a region where all unit cells have the same polarization state, called a *ferroelectric domain* or simply a *domain*. There may be many domains in a crystal, separated by interfaces called *domain* walls. A ferroelectric single crystal, as grown, typically has multiple domains. A very strong electric field could lead

to the reversal of the polarization in the domain, known as *domain switching*. In polycrystalline materials, each grain may contain multiple domains depending on the energy balance between domain wall energy and the stored elastic/dielectric energy [1,10]. Figure 1.4(a) shows domain structure within the grains of a sintered polycrystalline PZT observed under scanning electron microscope (mean grain size is 3μm at 1100° C [11]). The microstructure on the surface of a Barium Titanate single crystal observed using optical microscopy shows many needle-like domains (figure 1.4(b)).

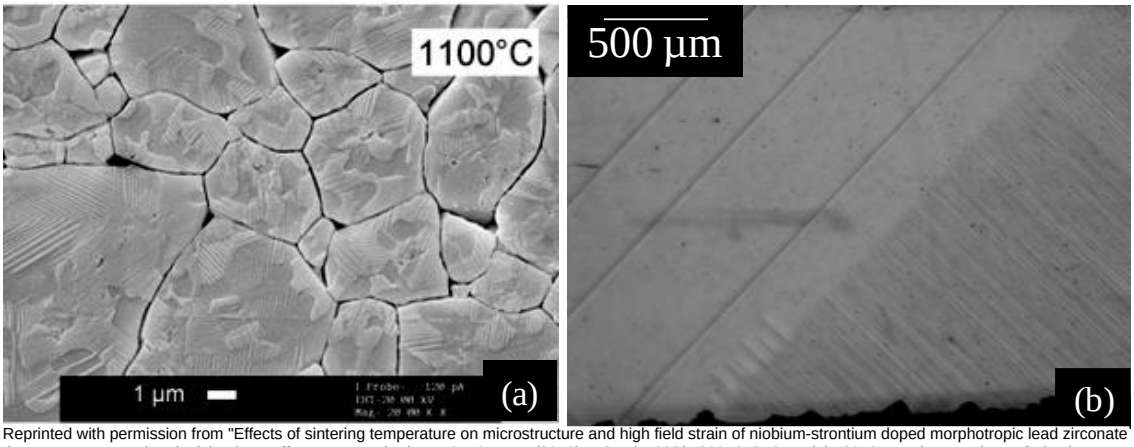

Figure 1.4: (a) Scanning Electron Micrograph of a sintered PZT polycrystal showing domain structure in several grains (after Kungl and Hoffman, 2010 [11]) (b) Optical micrograph of needle type domains in Barium Titanate single crystal.

1.2.3. Poling of ferroelectric ceramics [Microscopic view]

A typical tetragonal polycrystalline ferroelectric may contain many domains, each having different orientation, but has no overall polarity due to cancellation of spontaneous polarization in all the domains on average (figure 1.5(a)). Once a sufficiently high electric field is applied, the non-polar ceramic transforms into polar material by 180° and 90° switching process, the latter of which is accompanied by shape change or strain (figure 1.5(b) and (c)). The process of applying electric field to a ferroelectric ceramics thereby generating a net polarization is called *poling*. During poling, differently oriented domains

are aligned parallel to the direction of the electric field. The ferroelectric ceramic can be depoled by applying an electric field or mechanical stress along an axis perpendicular to the poling direction or by heating above the Curie temperature (thermal depoling).

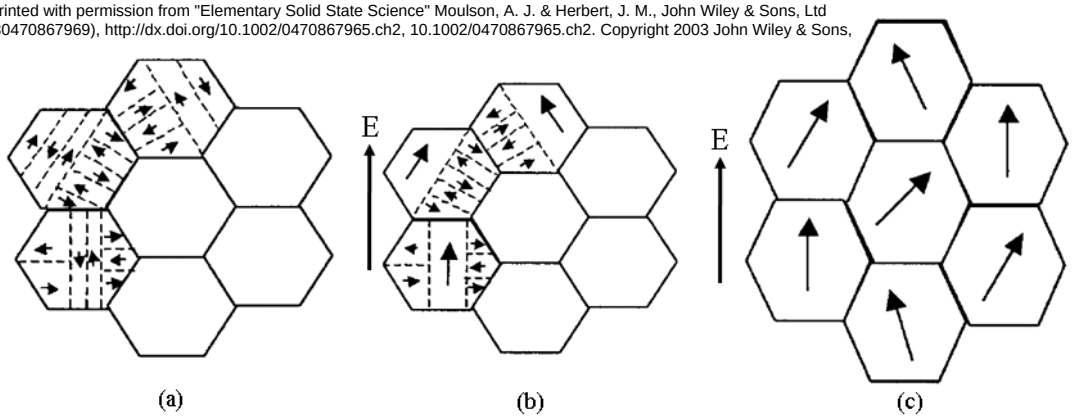

Figure 1.5: Schematic showing changes in the domain structure of a polycrystalline ceramic under the application of external electric field. (a) Initially, the net polarization is zero. (b) Applied electric field causes 180^0 switching, and (c) Further increase in electric field causes 90^0 switching giving net polarization and a strain. (after Moulson and Herbert, 2003 [10]).

1.2.4. Dielectric hysteresis Loop [Macroscopic view]

Macroscopically, polarization reversal can be observed by measuring the dielectric hysteresis which is a plot of electric displacement versus electric field as shown in figure 1.6. This is a representative hysteresis loop measured over one cycle of an alternating electric field at a frequency of 1Hz on a polycrystalline PZT. At low field values, linear dielectric behaviour can be observed (not shown in figure 1.6). Non-linear behaviour is observed at greater field magnitudes and during the positive half cycle of the electric field the polarisation reaches saturation at the maximum field magnitude (Point A). Any further increase in electric field produces very little increase in polarization. The maximum polarization attained is the *saturation polarization* (P_{sat}). As the electric field returns to zero, the polarisation does not become zero even when the field is zero (Point B). The polarisation that remains when the electric field is zero is called *remnant polarisation* (P_r) and is associated with a remnant strain [3]. During the negative half

cycle, the polarisation becomes zero (Point C) at an electric field magnitude which is referred to as the *coercive electric field or coercive field strength* (E_c), which is a characteristic of the material. With further increase in the electric field up to a maximum value, polarization reaches saturation (Point D). Upon removal of the electric field (Point E), the remnant polarisation has the same magnitude as at Point B, but opposite sign. Thus a dielectric hysteresis loop is observed upon application of an alternating electric field. The area enclosed by the loop is a measure of energy dissipated by reversing the polarization twice.

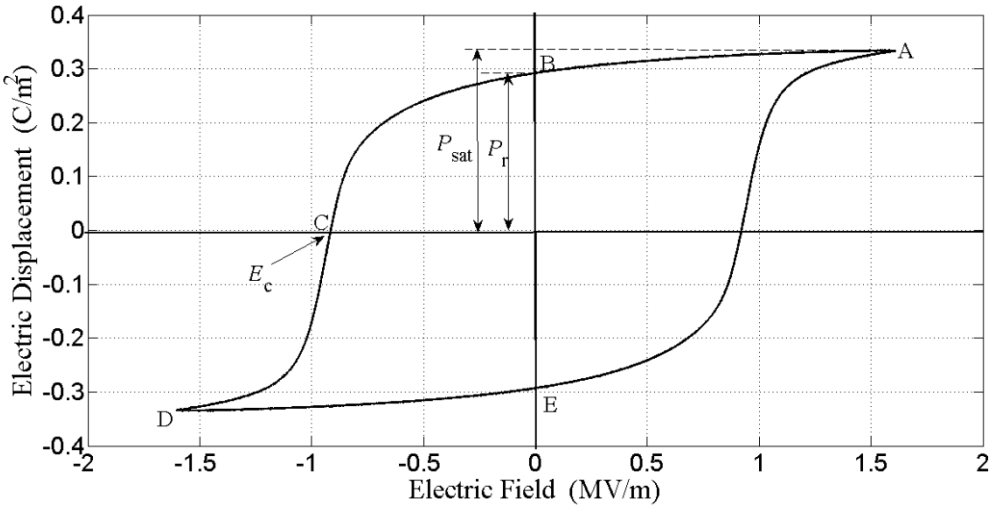

Figure 1.6: Hysteresis loop of a polycrystalline PZT (see Chapter 2 for measurement details).

Another important material constant is *electromechanical coupling factor* which is a measure of the proportion of stored electrical energy that can be converted into mechanical energy (and vice versa) by a piezoelectric material [10]. The effective electromechanical coupling factor can be written as,

$$k_{\text{eff}}{}^2 = \frac{\text{input electrical energy converted into mechanical energy}}{\text{input electrical energy}}$$

$$OR \qquad (1.12)$$

$$k_{\text{eff}}{}^2 = \frac{\text{input mechanical energy converted into electrical energy}}{\text{input mechanical energy}}$$

Higher value of k_{eff} suggests an efficient conversion of energy. Planar electromechanical coupling factor, k_p, is used in case of thin discs of piezoceramic where radial vibrations perpendicular to the direction of applied electric field are measured. Thickness electromechanical coupling factor, k_t, is also used in case of thin discs when surface dimensions are greater compared to thickness of the disc and mechanical vibrations in the same direction as that of electric field are measured. Electromechanical coupling factors k_{33} and k_{31} are used when electric field is applied in 3-direction and longitudinal mechanical vibrations in direction-3 and direction-1 are measured respectively.

1.3. Single crystal ferroelectrics: Background and Breakthrough

Lead based single crystal ferroelectrics: Since 1952, bulk PZT ceramics were used extensively for various applications and were chosen over single crystals for two major reasons: the electromechanical coupling factor for PZT is high (~0.75) and large single crystals having comparable piezoelectric properties were difficult to produce [12]. In 1982, Kuwata *et al*. [13] reported the very high electromechanical coupling factor (>0.9) in a solid solution of Lead Zinc Niobate and Lead Titanate (PZN-PT). Later, in 1997, Park and Shrout [4], reported high strain levels in ferroelectric single crystals, such as PZN-PT and Lead Magnesium Niobate- Lead Titanate (PMN-PT). Excellent piezoelectric properties such as high piezoelectric coefficient (d_{33} > 2500 pC/N) and ultrahigh electromechanical coupling factor (~0.94) were reported. Very high strain levels, up to 1.7%, exhibited by the single crystals are attractive for actuator applications as higher strain gives large displacements and high strain energy density. Electric field induced phase transitions were believed to be the reason for such high strain in these crystals. This breakthrough augmented the study of single crystals in last decade and growth and properties of single crystals have been studied extensively.

Single crystals of PMN-PT and PZN-PT show *relaxor* behaviour. Relaxors show significant change in permittivity with frequency over a temperature range near to Curie temperature [14]. For relaxors, relative permittivity depends on composition, temperature, orientation and frequency. A detailed discussion about relaxor ferroelectrics can be found in a review by Cross [14].

Lead free single crystal ferroelectrics: Since 1949, visualization of the domain structure [15] and observations of domain movements under electric field [16,17] of Barium Titanate (BT) single crystals were actively pursued. In 2000, Burcsu and co-workers reported a maximum strain of 0.9% measured at a constant compressive stress of about 2 MPa and a peak electric field of 10kV/cm on single crystal BT [18–20]. Stress-activated 90° domain switching was found to be responsible for the high strain in BT single crystals. This opened up an opportunity to utilize BT single crystals for actuator applications.

In this thesis, investigations on single crystals of PMN-PT and BT are reported and in the next few sections, opportunities and challenges while working with single crystals are discussed with a focus on these single crystal materials.

1.4. Single crystal ferroelectrics: Opportunities

1.4.1. Engineered domain configuration

The remarkable properties of single crystals present a great opportunity to design devices using these crystals. By carefully selecting the orientation of a single crystal, an enhancement in the piezoelectric properties can be achieved, referred to as *engineered domain configuration* [4]. Figure 1.7(a) gives a schematic representation of a rhombohedral crystal of PZN-PT oriented and poled along <001>. The spontaneous polarization vectors in this crystal system are along the body diagonals <111>.

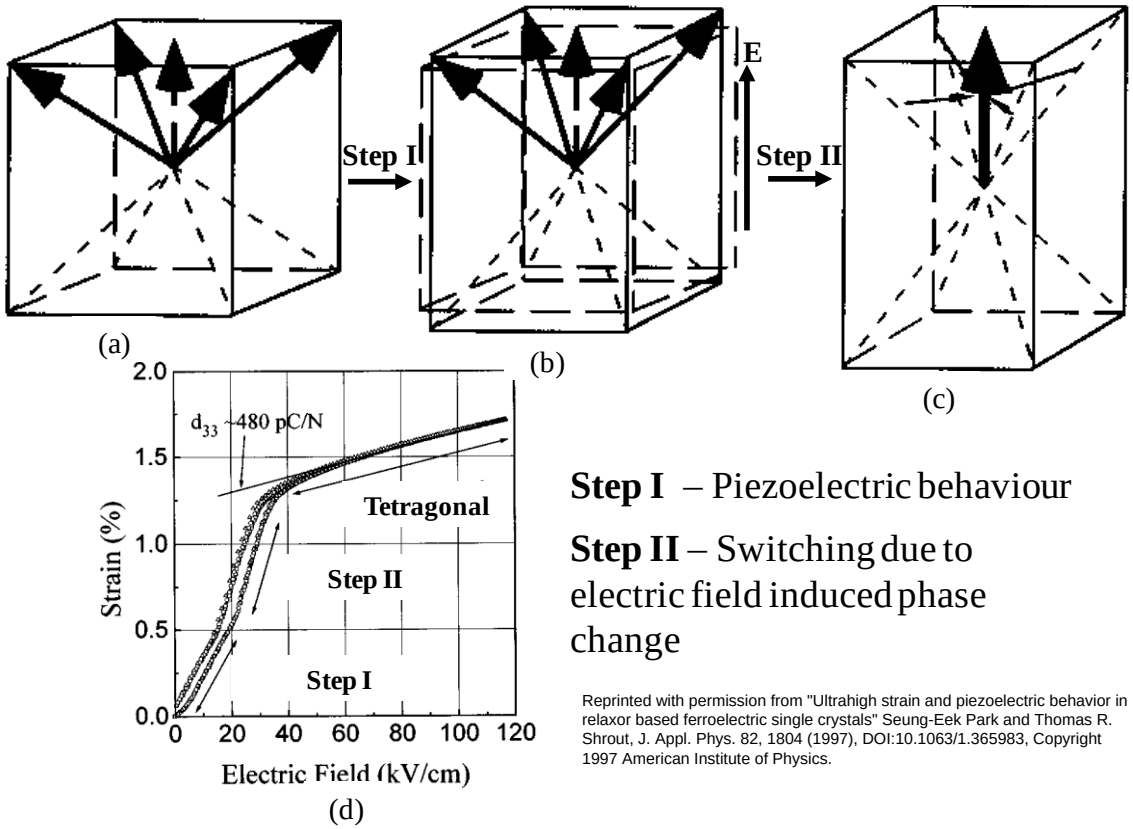

Figure 1.7: Schematic showing engineered domain configuration (a) <001> oriented rhombohedral crystal without electric field (b) Net polarization under applied electric field due to piezoelectric behaviour (Step I) (c) Large strain due to electric field phase change from rhombohedral to tetragonal phase (Step II) (d) Strain vs. electric field, showing a maximum strain of 1.7% at 120 kV/cm. (after Park and Shrout,1997 [4])

When an electric field is applied in the <001> direction, there is piezoelectric distortion of the rhombohedral unit cell (Step I) (figure 1.7(b)). A further increase in strain is believed to be associated with a phase change from rhombohedral to tetragonal due to applied electric field (Step II) (figure 1.7(c)). Thus, under applied electric field, high strains are observed due to phase transition, see figure 1.7(d).

Similarly, Wada *et al*. observed enhanced effects in BT single crystals [21]. Large hysteresis was observed for a [001] oriented BT single crystal with electric field over 20kV/cm. [111] oriented crystal showed a complex behaviour with an electric field induced phase change from tetragonal to monoclinic at around 10 kV/cm and from monoclinic to rhombohedral at around 30 kV/cm. This resulted in a hysteresis-free strain

behaviour giving a d_{33} of 203 pC/N below 6 kV/cm and d_{33} of 295 pC/N over 16 kV/cm. The phases were confirmed using in-situ domain observations and Raman measurements. Raman spectra were measured in the backward scattering geometry and changes in crystal symmetry indicating a phase change were detected. Raman spectroscopy is based on detection of the transitions in the molecular vibrations states of a specimen which is exposed to a monochromatic source of exciting photons.

Another study carried out by Wada and co-workers focused on domain wall engineering [22]. They developed a model to investigate the effect of domain size on the piezoelectric properties of BT single crystal. It is argued that the 90° domain wall density increases due to the fine domain size. The strained region near 90° domain walls is believed to affect the tetragonality of the unit cell changing c/a ratio to 1.0 in the strained region from normal tetragonal with c/a ratio equal to 1.011. This pseudo-cubic structure is believed to be the reason for enhanced piezoelectric properties The model predicted that domain sizes below 1 μm are required to obtain BT single crystals with d_{31} over 1000 pC/N. Poling methods to induce domain sizes smaller than 5 μm were also discussed in detail. Thus, engineered domain configurations can give hysteresis free or low-hysteresis behaviour, can offer high strains and/or piezoelectric properties, and can enable the crystal structure to change due to externally applied electric field [21]. Overall, domain engineering presents an opportunity to exploit and explore differently oriented single crystal configurations for obtaining improved piezoelectric properties.

1.4.2. Applications

Before discussing applications using single crystals, it is necessary to briefly comment about overall applications of ferroelectrics. All ferroelectrics are piezoelectric and pyroelectric materials and have widespread applications with polycrystalline PZT

ceramics dominating the market. Ferroelectric ceramics have been widely used in capacitors due to their high dielectric constant. Ferroelectric thin films are used in non volatile ferroelectric random access memories; a very good review of thin film applications of ferroelectrics is given be Setter *et al*.[23]. Piezoelectricity in ferroelectrics enables their use in accelerometers, transducers (actuators and sensors) [24], in inkjet printers, diesel injectors, sonar, medical ultrasound imaging and in Micro Electro-Mechanical Systems (MEMS) [1,25]. Pyroelectric properties enable their use in infrared sensors. The electro-optical activity of ferroelectrics is utilised in optical switches, colour filter devices etc. [26]. The list is non-exhaustive with new applications being developed continuously.

The remarkable properties of single crystals, in particular PMN-PT and PZN-PT, have inspired a few applications. Ultrasonic and sonar transducers with improved bandwidth and sensitivity could be obtained due to high electromechanical coupling factors (~0.9) and a wide range of dielectric constants (~1000 to 5000) of relaxor single crystals [27]. Ritter *et al*. built ultrasonic transducers using a single crystal PZN-PT composite and an increase in bandwidth (by 141%) and sensitivity were observed [28]. Other applications such as transducers for medical imaging [29], single element ultrasonic probe [30], accelerometer with enhanced single-to-noise ratio [31], stack actuators for vibration damping and sonar highlighted the usefulness of relaxor single crystals [6]. Recently, TRS ceramics have reported development of a PMN-PT single crystal stack actuator for use in deformable mirrors, rotorcraft flap control and cryogenic applications [32,33]. The potential of lead-free single crystals (e.g. BT, Sodium Bismuth Titanate, Sodium Potassium Niobate etc.) has also been realized for sensor and actuators applications [34] but devices built using them remain rare.

1.5. Single crystal ferroelectrics: Challenges

1.5.1. Manufacturing of single crystals

Single crystals are difficult to grow and obtaining large single crystals (~100mm diameter) with good yield and uniformity at low costs is very challenging. Methods for growing single crystals include the flux technique [35], Bridgman or modified Bridgman method [36], top seeded solution growth (TSSG) method [37], Czochralski method [38], solid-state single crystal growth methods (Chapter 6-[6]), templated grain growth method [39] etc. Manufacturing single crystals has been an active area of research for over 50 years. Here, important methods are covered briefly, highlighting the processing issues.

One of the earlier methods was a flux technique used by Remeika and others [40,41] to produce thin plates of Barium Titanate single crystals using potassium fluoride or $BaCl_2$ as a flux. The thin plates obtained by this method were used widely, for example, a complete set of elastic, piezoelectric and dielectric constants on tetragonal BT prepared by Remeika method was given by Berlincourt and Jaffe [42]. The main problems with the technique are that properties were affected due to flux inclusions and it was not possible to obtain thick single crystals (>1 mm).

In a top seeded solution growth (TSSG) method, a Barium Titanate single crystal is used as a seed and crystals of BT are grown by pulling the rotating seed crystal from the melt containing stoichiometric excess of TiO_2 [43–45]. Though high quality single crystal specimens with 1-5 mm thickness and 10 x 10 mm size could be obtained by this method, a precise control over temperature gradients, rate of pulling and speed of rotation of seed crystals is needed.

In case of flux technique for PMN-PT single crystals, PbO is used as a flux [35]. Flux inclusions, small crystal size (<5mm), compositional segregation, appearance of pyrochlore phase due to incorrect flux compositions and effective control on growth parameters are some of the major issues that give poorer piezoelectric properties to flux grown crystals [6]. In the Bridgman method or solution Bridgman method, a crucible containing seed PMN-PT crystal and a mixture of component oxide powders is slowly moved down into a steady temperature gradient [36]. Boules or wafers of single crystals of 50 mm diameter and 80 mm length could be obtained by this method at a reasonable cost with good reproducibility [6]. Evaporation of PbO, Ti content variation across the crystal length, slow growth rate and difficulty of separating crystals from crucible are some of the challenges with this method. Czochralski method is very similar to the TSSG except for the method of heating the furnace [43].

Though there has been good progress in resolving the process related issues, high costs associated with single crystal manufacturing, cracking of crystals during manufacturing, property variation due to compositional segregation and a need for rigorous control over manufacturing parameters remain problematic. Wider usage in practical devices may serve as a catalyst for research related to processing issues.

1.5.2. Morphotropic Phase Boundary (MPB)

In the Lead Zirconate – Lead Titanate system, the greatest piezoelectric response is achieved in compositions of about $PbZr_{0.52}Ti_{0.48}O_3$, close to the boundary between tetragonal and rhombohedral phases. This is commonly called the morphotropic phase boundary (MPB) as there is almost no mixed phase region. Similarly in the PMN-*x*PT system, an MPB region is found near $x = 0.32$. Noheda *et al*. carried out synchrotron X-

ray powder diffraction measurements on PMN-PT ceramic and plotted a modified phase diagram of PMN-*x*PT at low temperatures as shown in figure 1.8(a) [46].

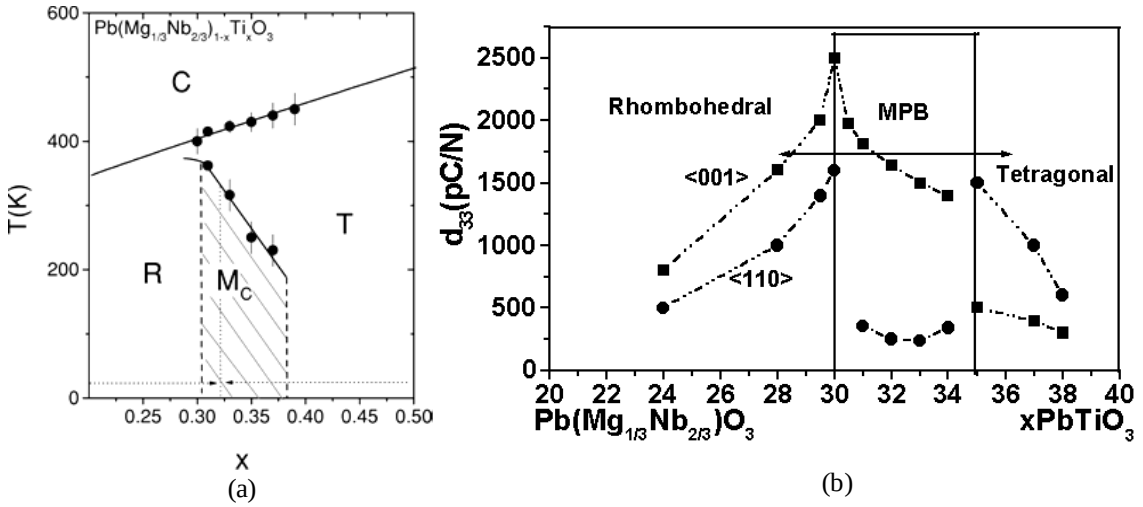

Figure 1.8: (a) Phase diagram of PMN–*x*PT where abbreviations used are T-Tetragonal, C-Cubic, R-Rhombohedral, M_c -Monoclinic phases (after Noheda *et al*., 2002 [46]) (b) Dependence of piezoelectric coefficient on crystal orientation and composition for PMN-PT single crystal (after Guo *et al*., 2003[47].)

The phase diagram shows a transition from rhombohedral to tetragonal phase with increasing PT content. A morphotropic phase boundary (MPB) is a compositional boundary separating different phases, and in PMN-PT, MPB between rhombohedral and tetragonal phases spans a range of 31-37% of PT compositions. A monoclinic phase has also been found to co-exist for PMN-33PT [48]. Piezoelectric properties are sensitive to the compositional variations and orientations, as can be seen from the variation of piezoelectric coefficient in figure 1.8(b). Higher piezoelectric properties such as high d_{33} near MPB compositions are likely to be due to coexistence of phases [47] or phase transitions due to electric field. Notwithstanding the tremendous potential of relaxor single crystals, choosing correct composition and crystal orientation is essential to understand the correlation between microstructure and properties. Thus, an improved understanding of the ferroelectric switching with multiple phases present is desirable for designing with these crystals.

1.5.3. Brittle behaviour and cracking

The brittle nature of PMN-PT single crystals means that their mechanical strength can be compromised by crack growth. Ferroelectrics are often used in multilayered stack actuators (MLA) for example in diesel injectors (figure 1.9 (a)). A typical fuel injector such as that used in Audi's V6 engines comprises 264 piezoceramic layers operated at 140-160 volts producing a displacement of 45 µm within 50-140 µsec [49]. The resulting movement of the stack actuates the metering valve, injecting an accurately measured amount of fuel into the engine cylinder.

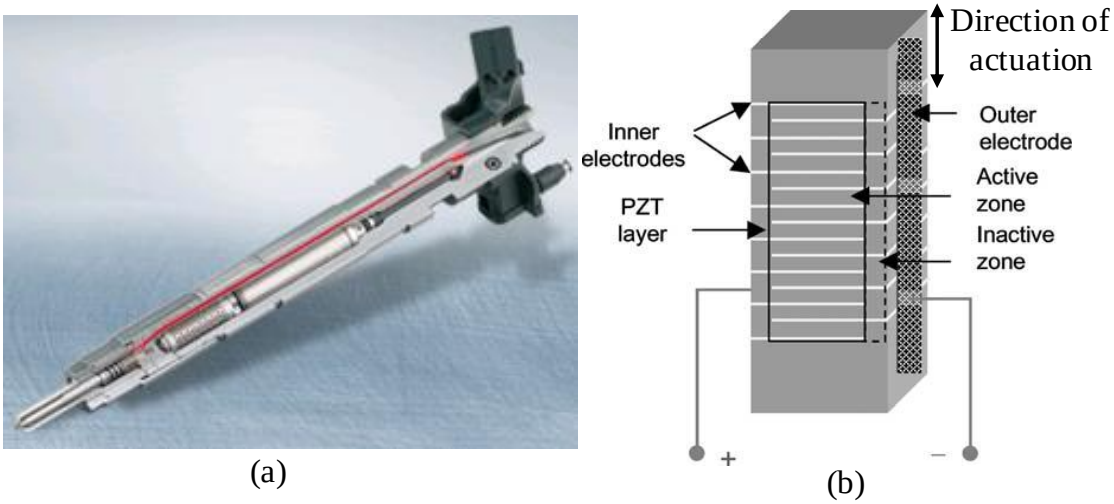

Figure 1.9: (a) Schematic of a stack actuator used in diesel injector (from Bosch website) (b) Sketch of the inner electrode arrangement (interdigital design) (after Müller-Fiedler and Knoblauch, 2003 [50]).

The displacement of the MLA depends upon the strain output of the material (for PZT ~0.1-0.2%) and the depth of the stack. The use of multiple layers reduces the operating voltage and an interdigital design of metallic electrodes is often used as shown in figure 1.9(b). MLAs have significant advantages over the conventional actuator designs such as accurate and reproducible displacements, quick response time and compact design [51]. Fuel injection using MLAs offers other advantages such as fewer moving parts and low weight compared to a conventional common rail system.

However, the interdigital configuration of electrodes is prone to electrode/ceramic interface cracking due to the non-uniform electric fields in the vicinity of the electrode tips (inactive zone in Figure 1.9(b)). The tensile stress around the electrode edge, which can be as high as 0.1 GPa, gives rise to cracks during the service life [51]. Crack propagation around the electrode tips in PZT actuators was studied by Furuta and Uchino [52]. Figure 1.10(a) shows crack propagation after 3000 cycles of operation. Cracks emanating from oppositely charged electrodes lead to failure by electrical breakdown. During poling, other types of cracks can occur as summarized in figure 1.10(b). Fracture behaviour of ceramics used in MLAs has been an active area of research and Schneider presents a good overview of the theoretical and experimental developments [53].

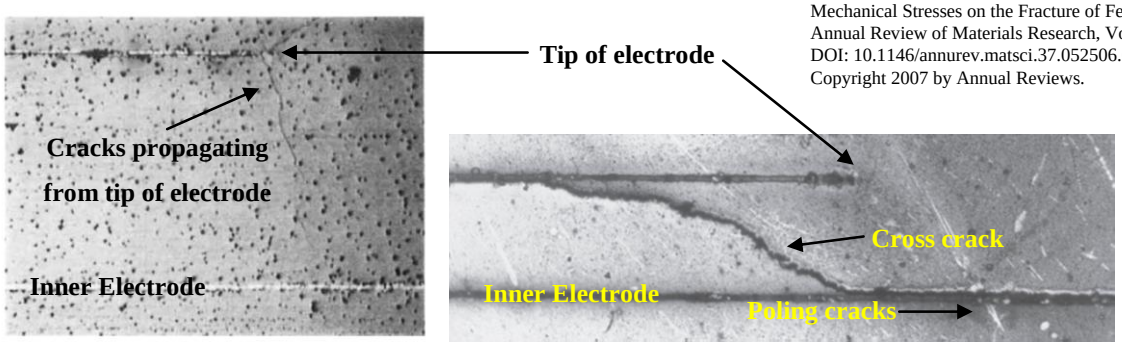

Furuta, A. and Uchino, K. (1993), Dynamic Observation of Crack Propagation in Piezoelectric Multilayer Actuators. Journal of the American Ceramic Society, 76: 1615–1617. doi: 10.1111/j.1151-2916.1993.tb03950.x. (http://onlinelibrary.wiley.com/doi/10.1111/j.1151-2916.1993.tb03950.x/abstract).

Gerold A. Schneider "Influence of Electric Field and Mechanical Stresses on the Fracture of Ferroelectrics" Annual Review of Materials Research, Vol. 37: 491-538, DOI: 10.1146/annurev.matsci.37.052506.084213. Copyright 2007 by Annual Reviews.

Figure 1.10: (a) Crack propagation in PZT ceramic stack actuator after 300 cycles (after Furuta and Uchino, 1993 [52]). (b) Various types of cracks in interdigital electrode configuration in MLAs (after Schneider, 2007 [53]).

Recently, Häusler *et al*. studied interfacial fracture in poled and unpoled PZT MLAs by four point bending under constant electric field. The interfacial toughness in the poled condition is found to be approximately half that of the unpoled condition. Also, the metal-ceramic interface toughness is found to be dependent on the poling direction with respect to the electrode [54]. Busche *et al*. carried out Vickers indentation experiments on single crystals of BT to study the fracture behaviour and domain switching [55].

Single crystals of PMN-PT and PZN-PT show approximately an order of magnitude higher strain than polycrystalline PZTs and are a promising candidate for multilayer actuator applications [4]. However, to design reliable actuators, a better understanding of the internal stresses developed at the inner electrode tips is needed. One approach is to study crack propagation in stack actuators under electrical and mechanical loads. Another approach is to predict non-uniform fields around the electrode tip using finite element simulations. This approach needs constitutive models capable of fully describing the non-linear and multi-axial material behaviour under electro-mechanical loading. The material behaviour can be studied using multi-axial loading experiments which enable formulation of constitutive equations thereby leading to reliable models in complex loading conditions. Thus, the development of accurate and reliable models is important for designing actuators. Multi-axial experimental measurements of single crystal ferroelectrics are needed for validating such models. Also, observation of the underlying switching mechanisms is needed to help formulate models at the micro-scale.

1.5.4. Lead-free ferroelectrics for future applications

Conventional polycrystalline ceramics such as PZT and single crystals of PMN-PT, PZN-PT contain the toxic element lead which has detrimental environmental effects [56,57]. There is a need to develop lead-free ferroelectric materials, both ceramics and single crystals, having comparable piezoelectric properties to that of PZT. Another issue is that the lead based ferroelectrics are not suitable for high temperature applications due to their low Curie temperature (~150-250°C). Also, lead-free ferroelectrics typically have lower density thereby making them more suitable for medical imaging applications due to low acoustic impedance. Highly <001> textured polycrystalline ceramics on alkaline niobate-based compositions are found to exhibit high piezoelectric coefficient (d_{33}) of 416pC/N [58]. Barium Titanate has also been investigated since the 1950s and high strains in single

crystal BT makes it a good candidate for actuator applications; however its brittle behaviour and low Curie temperature are disadvantages. A review of lead-free ferroelectric families of potassium niobate and bismuth titanate is given by Maeder *et al*. which highlights useful electromechanical properties of these compounds for transducer applications [57]. Recently, a high piezoelectric coefficient (d_{33}) of 483pC/N was obtained for relaxor based $Na_{0.5}Bi_{0.5}TiO_3$-$x$$BaTiO_3$ (NBBT) crystals [59]. Part of the work in this thesis will investigate Barium Titanate single crystals with a view of its development as a lead-free actuator material.

1.6. Motivation and approach of the present work

Sections 1.4 and 1.5 highlight opportunities and challenges presented by single crystal ferroelectrics. In summary, it can be said that though single crystals show high strains, few devices have yet been built using these crystals. While growing single crystals of large size at low cost is one of the main obstacles, lack of understanding of microstructure is also another prominent reason. There is a need for improved understanding of the microstructure and the evolution of the microstructure under electromechanical loading in single crystals to fully realise their potential. Recent work has focused on process related issues and macroscopic electromechanical behaviour studies. However, as yet, relatively little has been done towards in-situ observations of domain evolution. The study presented in this thesis focuses on some of the broad questions such as: How does microstructure evolve in the single crystals during electromechanical loading? Can existing constitutive models explain the behaviour of single crystal materials like PMN-PT or BT under electrical and mechanical loading? Can we characterize and interpret the domain structure in single crystals under electro-mechanical loading to understand their non-linear behaviour? Which technique or techniques are best suited for observing domains and their evolution under external loading?

These are the questions that guided the experimental and computational work presented in this thesis. The work follows a systematic approach to explore these questions, through (a) macroscopic measurements and (b) microstructural observations. Both of these approaches are elaborated in the subsequent chapters.

In the quest of improving an understanding of single crystal ferroelectrics, PMN-PT and BT single crystals were studied in this research work. PMN-PT was chosen because it has been extensively studied as a promising candidate for actuator applications. However, PMN-PT contains extremely fine (nanoscale) domain structure, so it was also desirable to explore systems with more easily observable domains. BT single crystals were used for this purpose. BT is also a lead-free system and is widely studied amongst the alternatives to PZT. Macroscopic measurements were carried out mainly on PMN-PT while microscopic observations were made on BT.

1.7. Structure of the thesis

Chapter 2 describes macroscopic electrical and strain measurements on single crystal PMN-PT in a polarization rotation test. Development of a micromechanical model assisting the interpretation of the polarization rotation experiments is presented in Chapter 3. Chapter 4 focuses on mapping the microstructure in single crystal BT using various imaging techniques including synchrotron X-ray diffraction observations. Chapter 5 presents in-situ observation of domain evolution in BT single crystal under compressive mechanical loading using synchrotron X-ray diffraction and optical techniques. Chapter 6 summarizes the key findings of this work along with a discussion on the future work. Relevant background and literature is presented at the beginning of every chapter.

2. Ferroelectric switching in PMN-PT single crystal

In this chapter, we focus on the macroscopic testing of Lead Magnesium Niobate–Lead Titanate (PMN-PT) single crystal. Several macroscopic testing techniques exist such as tensile or compressive loading, electrical loading experiments, combination of electric fields and mechanical loads, indentation experiments, four point/three point bending tests, polarization rotation experiment etc. The loads applied and measurements (typically strain, dielectric displacement) may be multi-axial. Macroscopic measurements provide valuable data for validating the models predicting non-linear behaviour of ferroelectrics.

2.1. Literature review: PMN-PT macroscopic testing

Single crystals of PMN-PT and PZN-PT show high strain levels up to 1.7% and are promising candidates for electromechanical actuator applications [4]. Strains induced due to large electric fields in different orientations of PMN-PT were investigated by Feng *et al* [60]. They found that <001> oriented PMN-PT shows higher strains compared with <110> and <111> oriented crystals. In their work, an electric field of 7 MV/m was found to induce ultrahigh strain of 1.8% in PMN-33PT with a low hysteresis.

Existing literature reports a number of studies on the behaviour of PMN-PT single crystals under electrical loading that are mainly aimed at understanding field induced phase transformation. Viehland *et al*. [61] measured the polarization and strain response of PMN-30PT single crystals under uniaxial stress and electric field. The results showed enhanced piezoelectric coefficients and electroacoustic power with increasing stress;

however significant increases in hysteretic losses accompanied this. Under moderate compressive stress (~$1*10^7$ N/m^2) an electromechanical coefficient of 0.92 with low hysteresis losses can be obtained. The properties of single crystals were also compared with PMN-PT ceramics and PZT ceramics under similar loading conditions by the same research group [62]. Single crystals were found to offer enhanced bandwidth and higher acoustic power compared to ceramics which makes them an ideal candidate for transducer applications. A combined study of electric field, mechanical stress and thermal loading on <011> and <001> PMN-32PT was carried out by McLaughlin *et al*. [63,64]. Electric field and stress induced polarization and strain behaviour was studied using a stress dependent electromechanical characterisation system. The effect of simultaneously applied stress, electric field and temperature was presented using three-dimensional plots of material behaviour. The phase transformation was observed at various electric field and stress values which were used to formulate the phase change criterion. Similar studies, without temperature, were carried out on varying composition of PMN-PT (28 to 32 % of PT) to study rhombohedral to orthorhombic phase transition [65], where axial compressive stress was found to have a smaller effect on phase transition. Domain switching in a single edge notched beam PMN-PT single crystal specimen was studied in-situ using polarised light microscopy under electromechanical loading by Li *et al*. [66]. Both 90^0 and 180^0 domain switching zones were observed near the crack tip and a larger switching zone was observed for more acute crack tips. Recently, a good overview of the dielectric, piezoelectric, pyroelectric and electro-optic properties of PMN-PT single crystals is given by Li and Luo [59].

2.2. Polarization rotation test

Huber and Fleck studied non-linear behaviour of polycrystalline PZT using a test that is commonly referred as polarization rotation test [67]. In this test, in the first step, a

ferroelectric specimen is poled by applying an electric field i.e. the specimen has some magnitude of remnant polarization in the direction of applied electric field at the end of first step. In the second step, the poled specimen is subjected to an electric field at an angle with respect to the initial direction of polarization. Huber and Fleck measured the change in dielectric displacement by applying electric field at angles between 0° and 180° in steps of 15°. It was observed that as the angle between electric field loading direction and initial polarization is increased, change in dielectric displacement increases. The experimental data was further used to compare three modelling approaches describing multi-axial behaviour of ferroelectric ceramics. The test has also been performed on hard PZT and Barium Titanate ceramic by Shieh *et al*. reporting similar observations [68]. Zhou *et al*. performed electrical as well as strain measurements in a polarization rotation test on soft PZT [69]. The experimental data in a polarization rotation has also been used for validating models describing non-linear behaviour of ferroelectrics [70–72].

In this chapter, electrical and strain measurements in a polarization rotation test on PMN-PT single crystal are presented. Single crystal PMN-PT is, however, an expensive material and it is necessary to establish the technique for multi-axial testing before carrying out tests on PMN-PT. Hence, for a preliminary study, polarization rotation test was carried out on relatively cheaper polycrystalline PZT ceramic. Another objective behind performing tests on PZT was to check the consistency of results by altering the specimen dimensions and hence understand the boundary conditions in this experiment. This is important from the point of view of deciding the specimen geometry as obtaining large single crystals of PMN-PT may not be possible due to processing issues.

First, the polarization rotation test was done on PZT where only electrical measurements were made and the results were compared with the literature. In these mainly

confirmatory tests, cubic specimens were used. Then the tests were carried out by altering the geometry of the PZT, which are referred to as shape dependency tests, and results were compared with the standard (cubic) specimen. This helped to finalize the dimensions of PMN-PT single crystals. Finally, a polarization rotation test was carried out on single crystal PMN-PT where electrical and strain measurements were performed. In the subsequent section, the experimental procedure for the polarization rotation test is discussed in detail followed by the results of PZT and single crystal PMN-PT tests.

2.3. Experimental arrangement: Polarization and strain measurement

Figure 2.1 shows a schematic of the experimental set up used for the electrical and strain measurements of ferroelectric ceramics by application of electric field at room temperature. The main components of the set up include (a) Electrometer for charge measurement, (b) Specimen immersed in oil bath (c) High voltage amplifier (d) Data logger for acquiring analogue voltage signals (e) computer with a data acquisition card and (f) strain measurement system – not shown in the schematic.

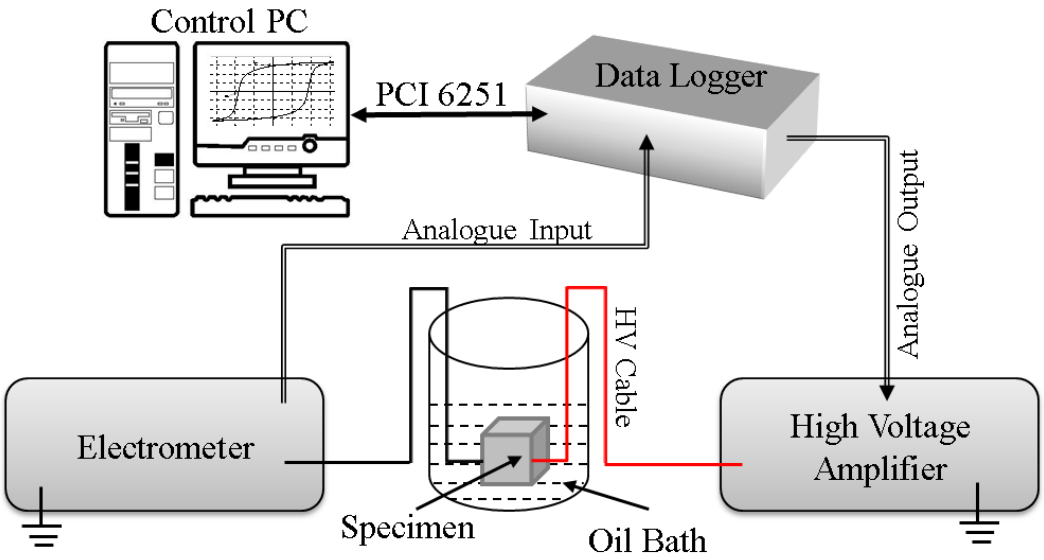

Figure 2.1: Experimental arrangement for high voltage electrical experiments.

Typically cubic specimens of suitable sizes were used in the polarization rotation test (specimen preparation is described in the next section). Two opposite faces of a cubic specimen were electroded using silver conductive epoxy. The specimen was immersed in a transformer-oil bath to prevent arcing. Suitable voltages, depending on specimen geometry and the required electric field, were applied by making connections between an electrode on one of the specimen faces and a high voltage amplifier (Trek 10/10B; maximum applied voltage = 10 kV). The other electrode is connected to an electrometer for measuring dielectric displacement/polarization. The electrometer measures the accumulated surface charge as a result of an applied electric field using a standard Sawyer-Tower method [73]. In this method, a metering capacitor having a capacitance C, is used in series with the specimen (figure 2.2) and it is assumed that no current is drawn at V_c i.e. charge is equal across the capacitor and specimen ($Q_{sp}=Q_c$). The electric displacement is then calculated by dividing the charge accumulated across the capacitor ($Q_c=CV_c$) by the surface area of electrode (A) (equation 2.1). As the data logger is capable of measuring a maximum voltage of 10 V, a capacitance (C) of the metering capacitor is chosen such that V_c remains below 10 V. The capacitance also depends on the area of electrodes and maximum dielectric displacement value. Range of capacitance used varied from 1-30 μF.

$$D=\frac{CV_c}{A} \tag{2.1}$$

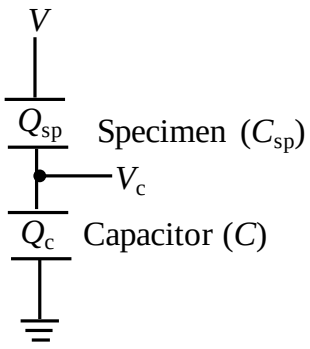

Figure 2.2: Charge measurement using a metering capacitor.

The electric field applied is assumed to be uniform i.e. same electric field at every point on the specimen. The mean electric field is given by equation 2.2.

$$|\mathbf{E}| = \frac{V - V_c}{d} \tag{2.2}$$

where V is the voltage applied across specimen thickness (d) and V_c is the voltage across the capacitor. Usually, the voltage applied is very high compared to the voltage across the capacitor ($V \gg V_c$).

The applied voltage and the voltage across the metering capacitor were recorded using a National Instruments SC-234 data logger and PCI-6251 card using a suitable sampling frequency. A Lab-VIEW software generated Virtual Instrument (VI) program was used to generate the driving signal for the high voltage amplifier and to collect the data.

Strain gauges (obtained from Techni Measures Ltd. Gauge factor = 2.1, Gauge resistance = 120 Ω) were used for the strain measurement. A foil type strain gauge consisting of a 90° rosette pattern of resistive foil mounted on a backing material was used. For each measurement, strain gauges were attached on the opposite faces of the specimen surfaces using Cyanoacrylate adhesive. Measuring the strain on two faces was essential to know if there was a variation in strain across the specimen and to check the accuracy of the measurements. Strain gauges were connected to a strain meter which is a quarter bridge Wheatstone bridge circuit. Strain meter and electrometer were checked for drift and found to be stable to ±0.01 $Cm^{-2}$and 100 με for more than 30 minutes of continuous high voltage experimentation. Figure 2.3(a) shows a typical specimen with strain gauges on one face. Another pair of strain gauges attached on the opposite face of the specimen is not shown. Length and width of the strain gauge are 1 and 0.7 mm, respectively (figure 2.3(b)). The strain gauges were positioned on the surface of the specimen away from the

high voltage electrode so that the backing or wires leading to strain meter were not near the high voltage cable.

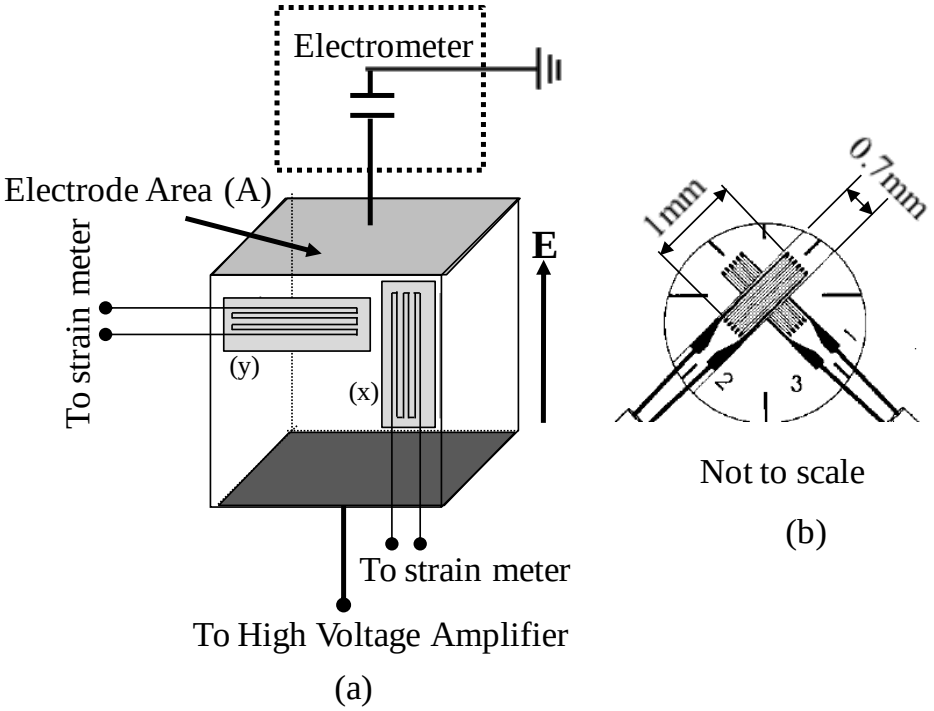

Figure 2.3: (a) Schematic of a typical specimen with strain gauges (x) and (y) measuring strain in two directions viz. parallel (ε_{33}) and perpendicular (ε_{11}) to direction of the applied electric field (**E**). (b) Strain gauge zoomed-in view showing rosette pattern and gauge dimensions.

2.4. Polarization rotation test on PZT

2.4.1. Specimen preparation

Unpoled polycrystalline PZT (Grade 855, Supplier - APC International Ltd., USA) was available in the form of 50 mm square plates of 5 mm thickness. Before the polarization rotation test, preliminary measurements were done to evaluate coercive field (E_c) and remnant polarization (P_r) by applying an electric field to a 5 mm cubic specimen. For the polarization rotation test, rectangular bars of PZT were machined to the suitable dimensions using a precision cutting saw. The thickness (t) of the rectangular bars was varied such that angled cubic specimens of 5 mm could later be cut from the bars for all the angles (θ) between 0° and 180° in steps of 15°. Bars of unpoled polycrystalline PZT of dimensions 50 x 5 x t mm (length x width x thickness) were polished using 1000/1200

grit Silicon Carbide (SiC) paper and electroded using conductive silver epoxy. These bars were then poled by applying an electric field of magnitude $1.3E_c$ across the thickness (t mm) and the dielectric response of the material was recorded. Surface electrodes were then removed by polishing. Cubes of size 5 mm were cut from the poled rectangular bars at various angles (θ) between 0° and 180° in steps of 15° using suitable machining jigs and were subsequently polished. These cubes were electroded such that the electric field was applied at an angle to the original polarization direction and then poled to the same magnitude of electric field (figure 2.4(a)). In this way, electric field is applied at angles between 0° and 180° in steps of 15° to the direction of initial polarization (figure 2.4(b)).

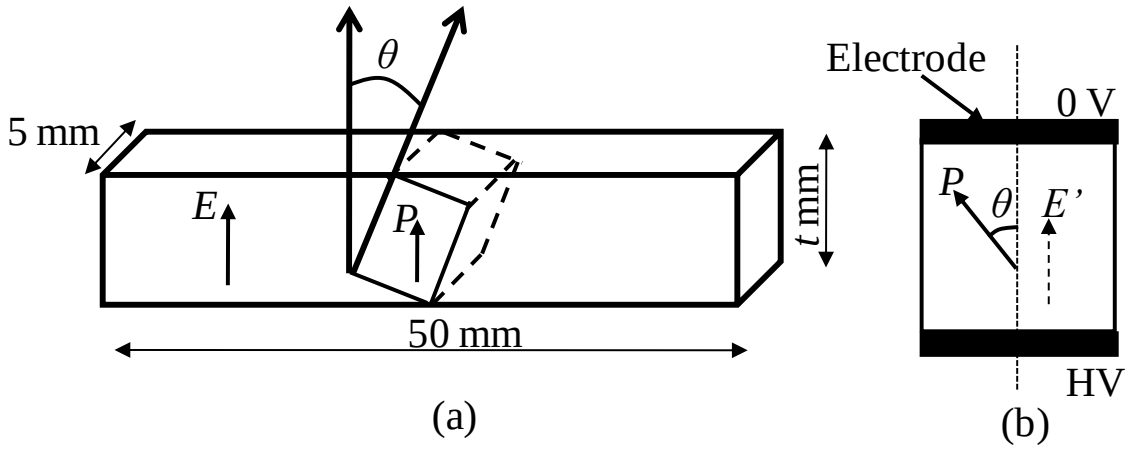

Figure 2.4: (a) Cutting out cubic specimen orientated at an angle θ to the direction of polarization. (b) Electric field (E') is applied at an angle θ to the direction of initial polarization (P).

2.4.2. Preliminary measurements

The coercive electric field and remnant polarization were measured by applying a cyclic electric field of amplitude 1.6 MVm^{-1} triangular waveform and frequency 0.025 Hz to a 5mm cubic specimen at room temperature. Figure 2.5 shows hysteresis loops at various magnitudes of electric field. The coercive electric field (E_c) and remnant polarization (P^r) were measured to be 0.85 MVm^{-1} and 0.28 Cm^{-2} respectively. The values are found to be in good agreement with earlier measurements by Shieh *et al*. [68] on PZT.

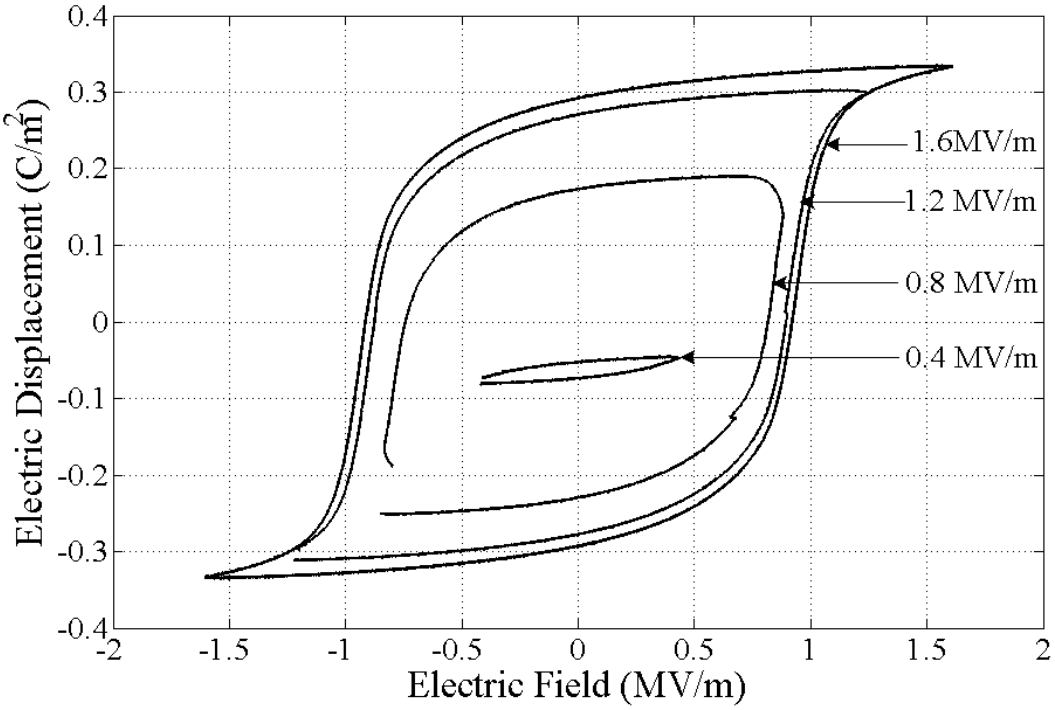

Figure 2.5: Dielectric hysteresis loops in PZT at various electric field amplitudes. Note: As the cyclic electric field amplitude was gradually increased, some of the loops don't close.

2.4.3. Results: Polarization rotation test - PZT

As mentioned in section 2.2, in the first step in the polarization rotation test, rectangular bars of PZT were poled by applying a cyclic electric field of amplitude $1.3E_c$ (1.105 MVm^{-1}) triangular waveform at a frequency of 0.025 Hz. A stable hysteresis loop was obtained by applying electric field for 10 full cycles and a positive half cycle so that at the end of the first step, rectangular bar specimens had a remnant polarization of 0.28 Cm^{-2}. Next, a loading cycle, as shown in figure 2.6, was applied to the 5 mm cubic specimens that are cut at various angles to the direction of initial polarization. This completed the second step in the polarization rotation test. The change in dielectric displacement was compared with the results of Huber and Fleck [67] as shown in figure 2.7. Here, only the loading cycle results in the second step are shown for clarity.

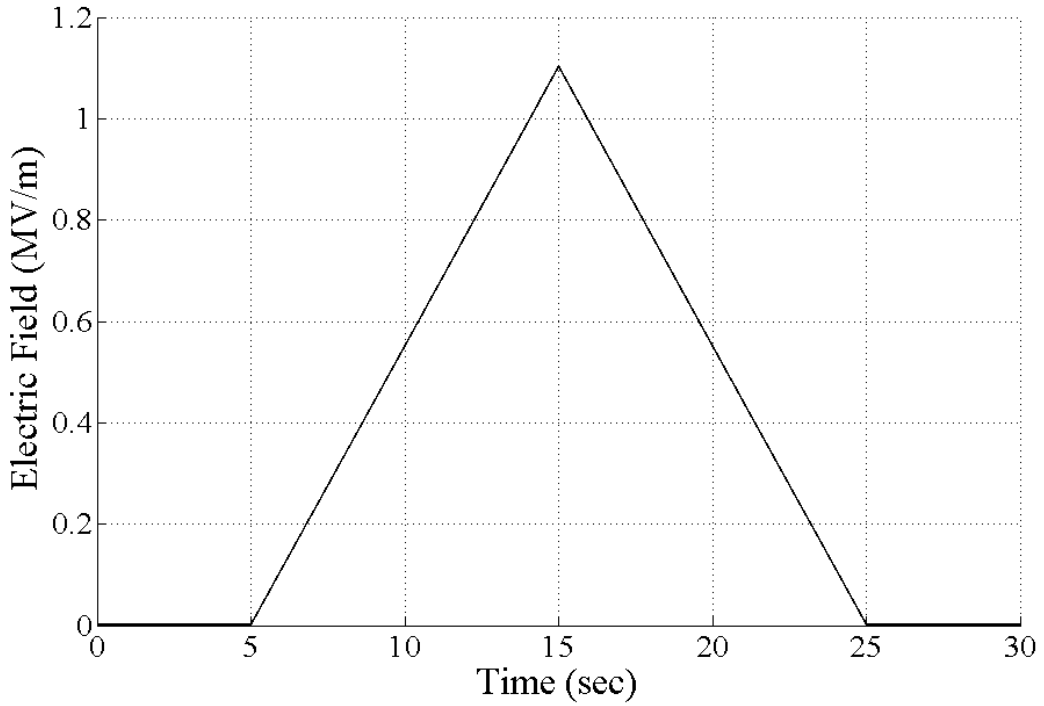

Figure 2.6: Loading cycle used for poling after cutting the specimen at various angles θ.

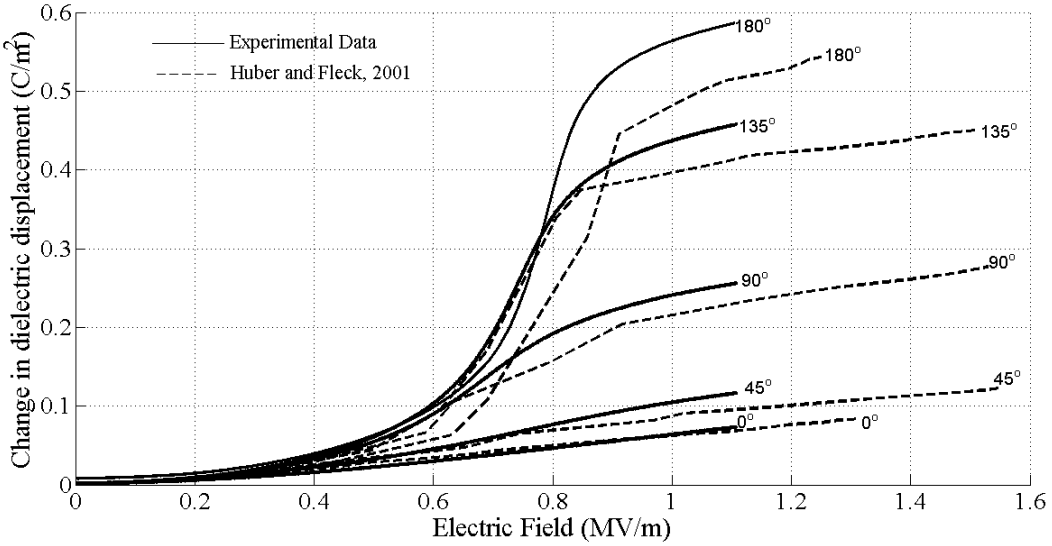

Figure 2.7: Comparison of dielectric response of the PZT with the published data by Huber and Fleck, 2001 [67].

The experimental results show a good qualitative agreement with the published data. The experiments in the reference [67] were performed on a similar grade of the material sourced from a different supplier. The difference between the published results and experimental data may be due to (a) compositional variation in the materials or (b)

different amplitudes of electric loading. In our experiments, consistent 5 mm cubic specimens were used along with the same peak amplitude of the electric field was used. In case of the results in reference [67], specimens varied in size from 5 × 5 ×4 mm (cut at θ = 0°) to 3.5 × 3.5 × 4 mm (cut at θ = 45°) were used. Also, the 0° and 180° specimens were subjected to peak electric field amplitude of approximately 1.3 MVm^{-1} as against other specimens that were subjected to 1.5 MVm^{-1} due to limitations imposed by test apparatus. Furthermore, in our experiments rectangular bar specimens were subjected to smaller peak amplitude of electric field (1.105 MVm^{-1}) compared to 1.5 MVm^{-1} that is used in the published results during the first step in polarization rotation test. These factors may account for the differences in the values of dielectric displacement attained in our experiments and published data.

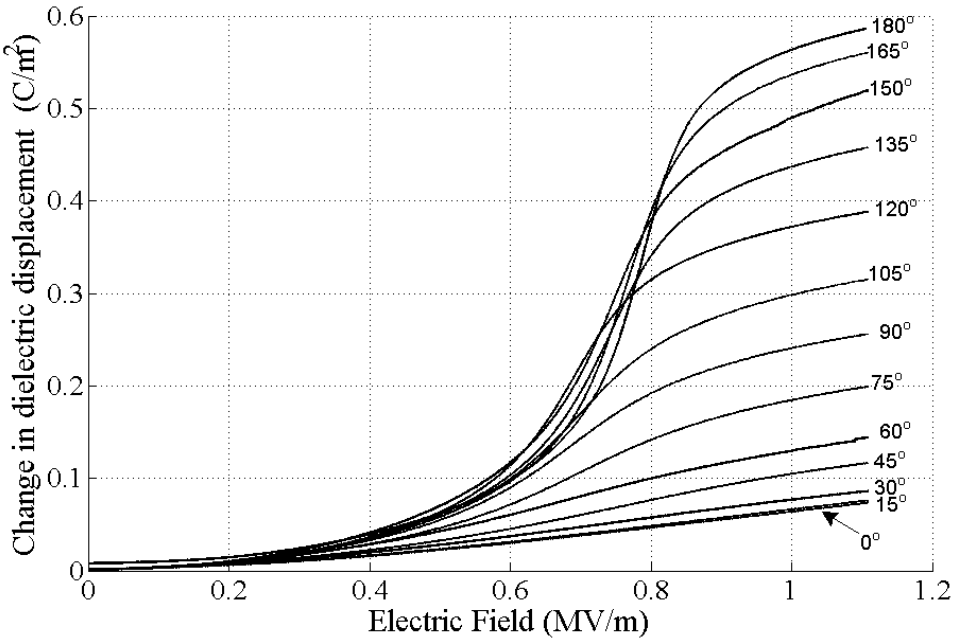

Figure 2.8: Dielectric response of the PZT for electric fields at various angles to initial polarization direction (0°-180°).

Applying an electric field at an angle to the previously poled specimen produces a non-linear behaviour. Figure 2.8 shows the full set of results in 15° angle increments. In case of the 0° specimen, electric field is parallel to the direction of remnant polarization and a

very small change in dielectric displacement is observed (~0.074 Cm^{-2}); whereas when the electric field is in the exact opposite direction to the initial polarization direction (θ = 180° case), a large change in dielectric displacement (~0.586 Cm^{-2}) can be seen. For the intermediate angles, a gradual increase in the change in dielectric displacement suggests ferroelectric switching due to domain reorientation in the direction of electric field.

2.4.4. Experimental saturation curve and isotropic saturation curve comparison

The maximum change in dielectric displacement at each angle is the sum of change in remnant polarization and a dielectric contribution, as given by equation 2.3.

$$\Delta D = \Delta P^{r} + \kappa E \tag{2.3}$$

where, ΔP^{r} is the change in remnant polarization, κ is the dielectric permittivity and E is the peak magnitude of the applied electric field. The dielectric permittivity, κ, is given as KK_0 where K is the dielectric constant and K_0 is the permittivity of the free space (K_0 = 8.85*10^{-12} Fm^{-1}).

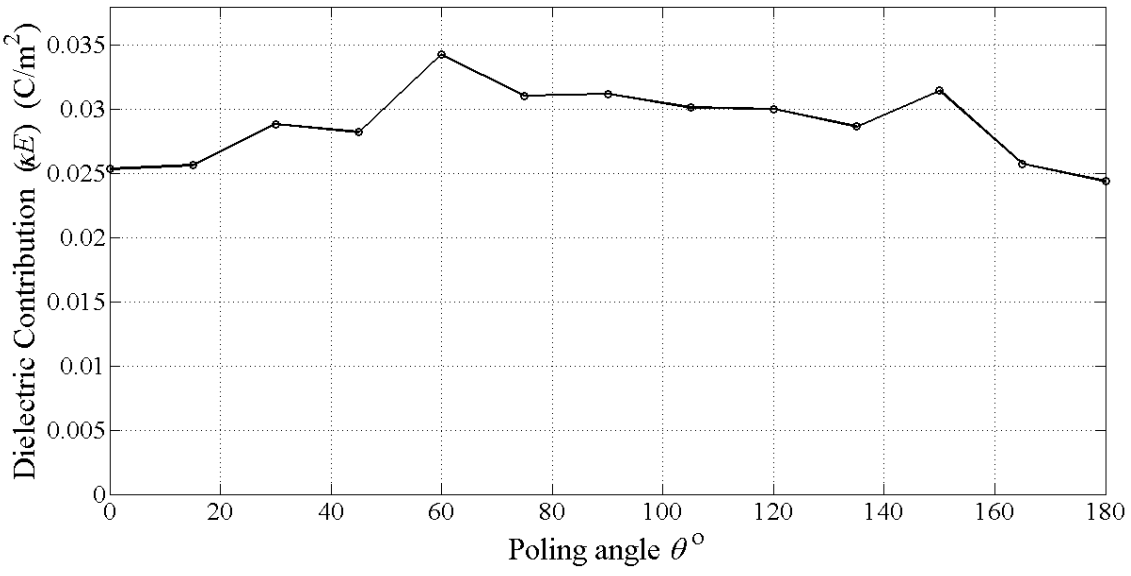

Figure 2.9: Dielectric contribution variation with respect to the poling direction.

Thus, the dielectric contribution (κE) in equation 2.3 can be computed using dielectric constant of PZT and peak amplitude of the electric field (1.105 MVm^{-1}). Here, the dielectric permittivity (κ) can be evaluated from the slope of initial portion of loading

curve (E < 0.25 MVm^{-1}) in figure 2.8. Figure 2.9 shows the plot of the dielectric contribution for each poling angle (θ) and it can be seen that the poling direction has a very slight effect on the dielectric contribution. The average value of the dielectric contribution is 0.029 Cm^{-2}. The change in remnant polarization is calculated by subtracting the average dielectric contribution from the total change in dielectric displacement for each angle.

Figure 2.10 shows the ferroelectric switching in the polarization rotation test. Let the saturation level of the remnant polarization (P_{sat}) be parallel to OA, at the end of the first step. Here, it is assumed that specimen is fully saturated and the initial state is isotropic. In the second step, electric field is applied at an angle θ, parallel to OB. If the electric field along OB fully saturates the material and there is no reverse transformation of polarization during unloading, P_{sat} will be reoriented parallel to OB.

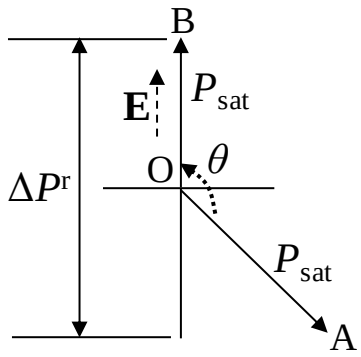

Figure 2.10: Reorientation of remnant polarization during the polarization rotation test.

In such a case, the change in remnant polarization (ΔP^r) follows a simple expression given by equation 2.4, based on geometry of switching shown in figure 2.10.

$$\Delta P^r = P_{sat}(1 - \cos\theta) \tag{2.4}$$

The value of P_{sat} was calibrated using the 180° specimen, giving P_{sat} = 0.28 Cm^{-2}.

Figure 2.11 shows a comparison between isotropic saturation curve and experimental saturation curve. The isotropic saturation curve is obtained by plotting the equation 2.4.

The experimental saturation curve is obtained by subtracting the linear dielectric effect contribution (using an average value of 0.029 Cm^{-2}) from the maximum value of change in dielectric displacement for each angle θ.

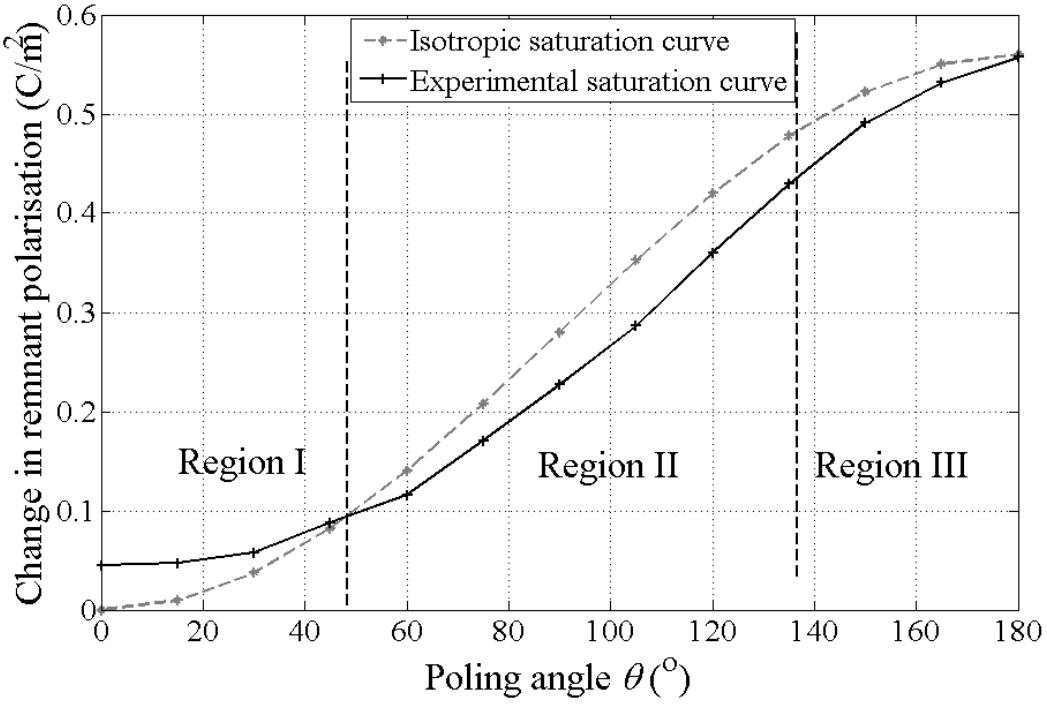

Figure 2.11: Comparison between isotropic saturation curve and experimental saturation curve for maximum value of change in remnant polarization (ΔP^r).

It can be seen from figure 2.11 that for $\theta < 45°$, the experimental curve is above that of the isotropic saturation curve, indicating higher values for remnant polarization attained during experiments (Region I). This may be because in the initial poling operation a small amount of reversal of polarization might be taking place during unloading from 1.3Ec to 0 MVm^{-1}. Then during reloading, some forward switching can happen which is not accounted for in the isotropic curve. An alternative interpretation is that, if the switching process is time-dependent, and as the electric field amplitude is only $1.3E_{c,}$ the full saturation of switching may not be achieved in the initial poling process. Then, further forward switching could take place during reloading of the specimen.

In region III ($\theta > 135°$), the difference between the two curves is less which suggests that for large angle rotations the isotropic curve is realistic. This is expected as the value of P_{sat} used in isotropic curve is based on the 180° measurement.

For region II (angles close to 90°), generally the experimental curve lies below the isotropic curve which raises questions about the boundary conditions assumed in the isotropic saturation curve. To exemplify the boundary condition assumed, consider the side faces of the cube in the 90° case. Before the polarization rotation is carried out, the side faces are expected to have surface charges as shown in figure 2.12(a).

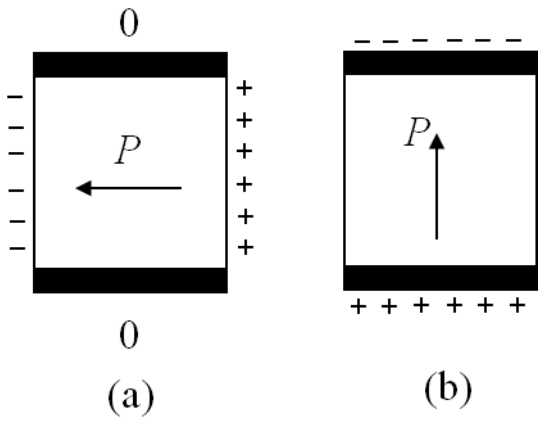

Figure 2.12: Schematic of the charges present on the side faces of a cube during polarization rotation experiment: (a) Before polarization rotation i.e. after initial poling (b) after polarization rotation i.e. after loading at angle θ ($\theta = 90°$ in this case).

The presence of these charges follows from Gauss's law applied at the surface. Taking the simplifying assumption that the electric displacement inside the specimen is much greater than that of the surrounding oil, the surface charge density is $q = -\mathbf{P}.\hat{\mathbf{n}}$, where $\mathbf{P}$ is the local polarization of the specimen and $\hat{\mathbf{n}}$ is the outward surface normal. After the polarization rotation, the isotropic saturation curve assumes a polarization state as shown in figure 2.12(b): the charges on the side faces have vanished. However, since the test is conducted in an insulating medium (transformer oil), charge transfer from these surfaces is strongly resisted. The charged side faces impose a constraint on the switching process

which would be expected to reduce the observed polarization relative to equation 2.6. This could be verified by changing the specimen geometry, thereby altering the extent to which boundary conditions influence the experiments. Tests devised for this purpose are referred to, in the following sections, as *shape dependency tests*.

2.5. Shape dependency tests for PZT

2.5.1. Specimen geometry

A shape dependency test was designed to verify or challenge the assumption of free charge transfer at the side faces of the cube in the polarization rotation experiment. This was done by repeating the polarization rotation test with different specimen geometry and comparing the response with the cubic specimen tests. The original specimen was a 5 mm cube. Two new specimen geometries were chosen such that the thickness to width ratio (aspect ratio) is varied by 2 orders of magnitude. Figure 2.13 shows the schematic of the original specimen, a "Thin Tall" specimen ($w = 0.1h$) and "Thick Short" specimen ($w = 10h$); where w and h denotes the width and height of the specimen respectively. In case of a Thin Tall specimens, the side charges are expected to have a strong effect on the polarization reversal for angles close to 90° whereas for Thick Short specimens, a very negligible effect of the side charges is expected, which may increase the remnant polarization for angle close to 90°.

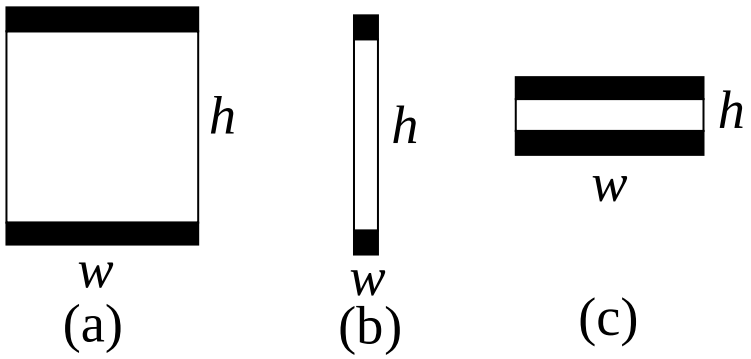

Figure 2.13: Shape dependency test: (a) Cubic specimen ($w = h$), (b) Thin Tall specimen ($w = 0.1h$) and (c) Thick Short specimen ($w = 10h$)

Thin Tall and Thick Short specimens were machined and repoled by applying electric field at angles between 0° and 180° in steps of 45° to the direction of initial polarization. The loading rate, peak electric field and other parameters were same as that in the polarization rotation test for cubic specimens so that the results are comparable. In case of Thick Short specimens, it was challenging to maintain a clean surface due to a smaller thickness. For the Thin Tall specimens, electroding the top surface was tricky due to the reduced surface area. Due to these reasons, tests were repeated to gain confidence over the measurements. Electrometers with appropriate metering capacitors were used, based on the electrode area in each case.

2.5.2. Results

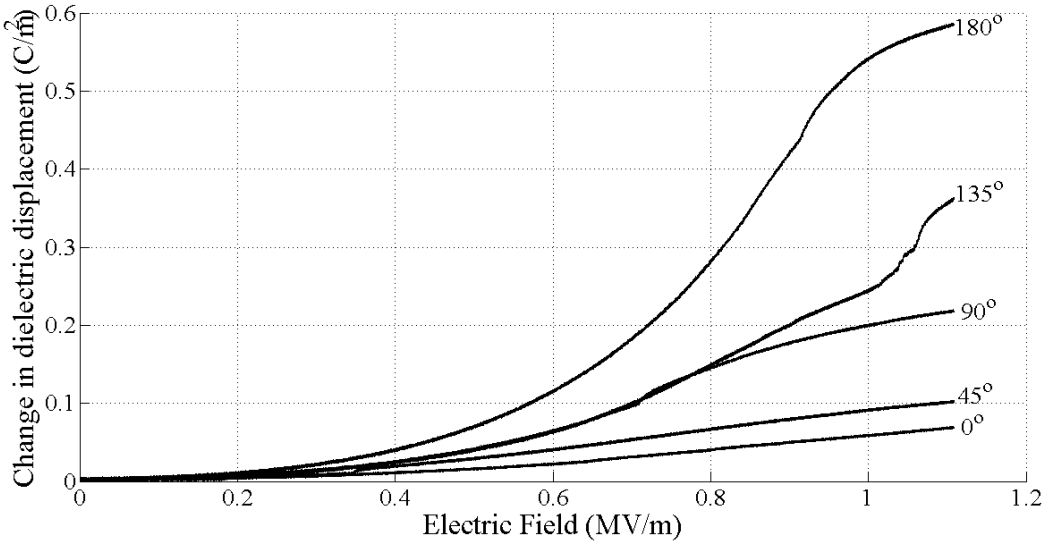

Figure 2.14: Dielectric response of the Thin Tall specimen ($w = 0.1h$).

Figure 2.14 and 2.15 show the change in dielectric displacement in Thin Tall and Thick Short specimens, respectively. In each case, the curves are qualitatively similar to those of the cubic specimen suggesting that some amount of polarization reorientation occurred in both specimen geometries. Thin Tall specimens show some abrupt kinks in the 90° and 135° specimen, suggesting that some sudden discharges may have taken place. This is consistent with the idea that charge has to be removed from the insulated side surfaces in

order to rotate the polarization, and that this charge removal may take place in abrupt steps.

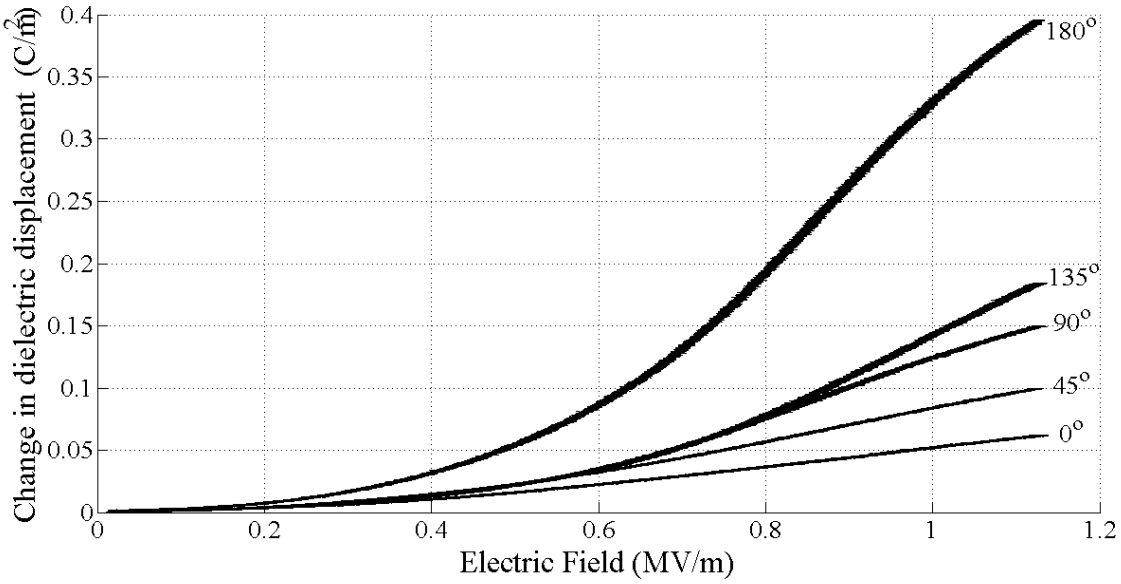

Figure 2.15: Dielectric response of the Thick Short specimen (w = 10h).

The results from specimens with $w = 10h$ do not show such kinks. However, full saturation does not appear to be reached in any of the Thick Short specimens. Note that, in figure 2.15, the 180° specimen reaches a peak ΔD value of about 0.4 Cm^{-2} which is only 70% of the peak ΔD reached in the cubic specimen (see figure 2.8).

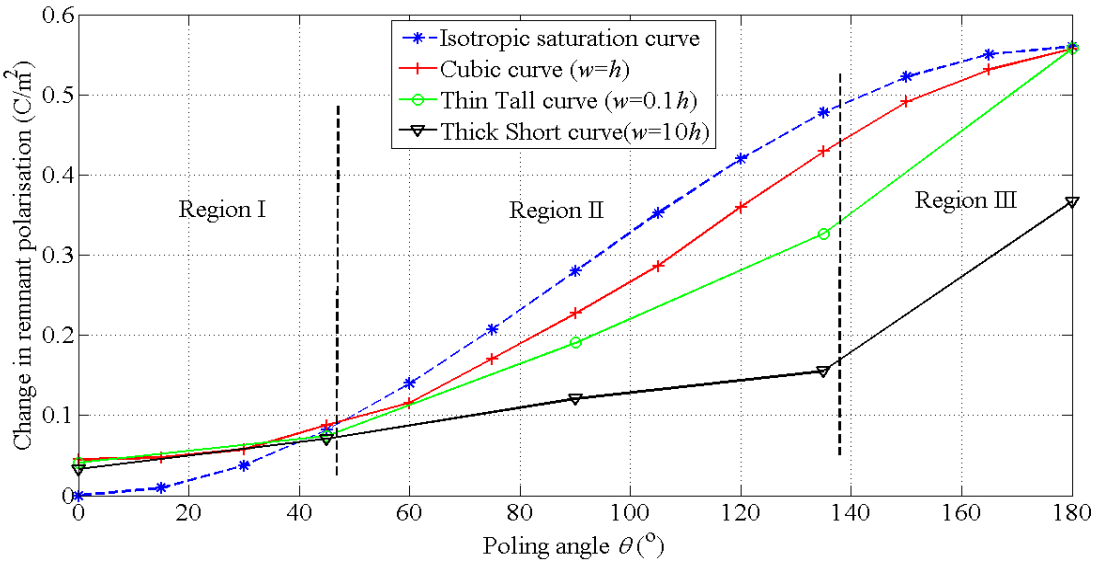

Figure 2.16: Comparison between saturation curve and experimental data for Thin Tall, Thick Short and cubic specimens.

Further interpretation can be done by comparing the maximum value of change in remnant polarization for Thick Short and Thin Tall specimen (Thin Tall curve and Thick Tall curve) with isotropic and cubic specimen saturation curve (figure 2.16). All the experimental data was corrected for linear dielectric effect. The cubic curve is the same as the experimental saturation curve used in figure 2.11.

Thin Tall curve: As shown in figure 2.14, for the thin tall ($w = 0.1h$) specimen, for lower angles (region I), there are almost no side charges and hence, side charge effects are not expected. The Thin Tall and the cubic specimen show similar behaviour in this region. Strong side charge effect is expected in region II, which is supported by lower values of ΔP^r than that of the cubic specimen in this region. In region III, similar to region I, strong effects were not expected and as θ approaches 180°, cubic and Thin Tall specimen show similar behaviour. Hence, lesser values of remnant polarization for 45°, 90° and 135° Thin Tall specimens than corresponding cubic specimens and a good agreement for 0° and 180° specimen suggests that the side charges may have an effect on the polarization reversal.

Thick Short curve: For thick short (w=10h) specimen (figure 2.15), the side surfaces are small and so the side charge effect is expected to be an end-effect in a small volume of material (~10%) at each end. Surprisingly though, the results give a significantly lower ΔD throughout. This is consistent with the observation that a fully saturated state was not reached, suggesting that the effective coercive field in these specimens is greater than that observed in cubic specimens. Hysteresis loop measurements made using Thick Short specimen confirm the variation in the apparent coercive field strength in this specimen geometry. Coercive field is known to be thickness dependent in ferroelectric thin films, where nucleation effects or blocking layers have been used to account for the effect. In

these bulk samples, the effect is more likely to result from surface damage during machining, giving rise to a layer of reduced permittivity material. For the present purpose, it is clear that varying the specimen geometry gives different values of polarization. Thus in subsequent work with single crystal PMN-PT a specimen geometry close to cubic is used.

2.6. Polarization rotation test on PMN-PT single crystal

2.6.1. Specimen preparation

Single crystals of PMN-32PT were obtained from Omega Piezo Technologies Inc., USA. Thinner (1 mm) and Thicker (5 mm) plates of 25 mm square cross section of <001> oriented PMN-PT specimens were poled in the <001> direction by the supplier. The magnitudes of electric field applied and procedure of poling was not revealed due to proprietary information issues. These crystals were grown by Czochralski method at Omega Piezo Tech. and had gold electrodes sputtered on the two opposite 25 x 25 mm sides. The crystals were dark-brown or yellow coloured and opaque with no apparent cracks or visible domain structure.

First, preliminary measurements were done to evaluate coercive field (E_c) and remnant polarization (P_r) and to understand the polarization state of the crystal. For the polarization rotation test, 5 mm thick rectangular bars of dimensions 25 mm x 5 mm (length x width) were machined from 25 mm square plates using a precision cutting saw. The bars were electroded and strain gauges were attached as illustrated in figure 2.3. Next, the bars were poled by applying an electric field of magnitude $5E_c$. Strain gauges and electrodes were removed after poling and the bars were cut at a range of angles defined by 0° to 180° in steps of 15° to obtain the cubic specimens. Cubes of varying size (d) were obtained; smallest being 3.5 mm for 45° and 135°angles and largest being 5 mm

for 0°, 90° and 180°. Again, strain gauges were attached on two faces measuring the strain in the parallel and perpendicular direction of applied electric field. Strain measurement was done only for angles between 0° and 180° in steps of 45°.

2.6.2. Preliminary measurements

Electrical and strain measurements were made using a 5 mm cubic specimen of PMN-PT at room temperature by applying a cyclic electric field of amplitude 1.2 MVm^{-1} triangular waveform at a frequency of 0.1 Hz. Figure 2.17 shows a hysteresis loop giving the values of coercive field E_c = 0.24 MVm^{-1} and remnant polarization P^r = 0.25 Cm^{-2} respectively, in good agreement with those reported for the same composition (PMN-32PT) by Wan *et al*. [74].

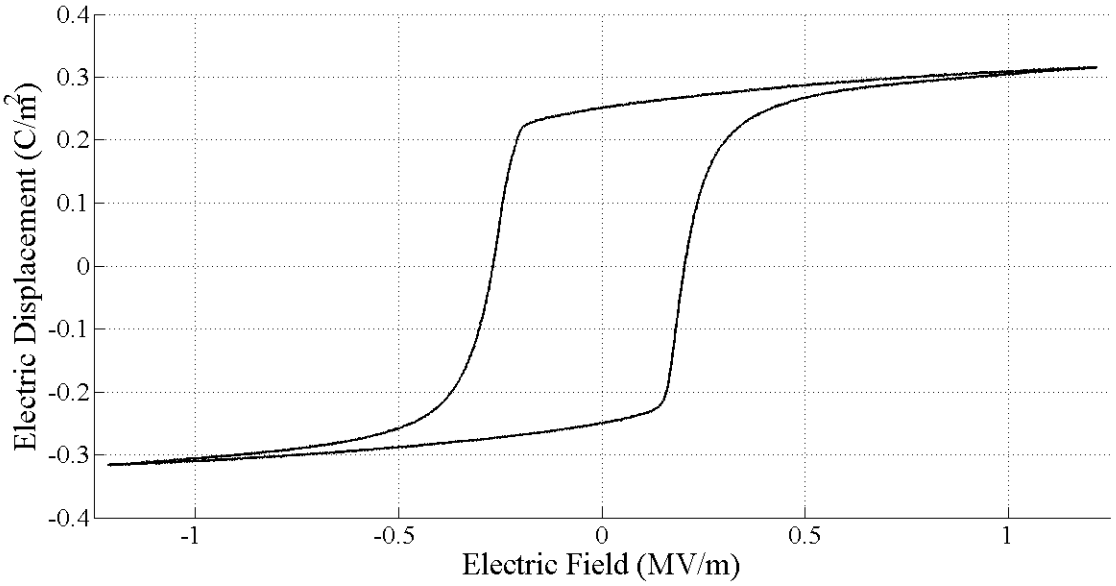

Figure 2.17: Dielectric hysteresis loop for PMN-PT at peak electric field of 1.2MVm^{-1}.

As received, the crystals were already poled, giving an anisotropic dielectric response and an unknown initial state of remnant polarization. A zero polarization state was found approximately, using the dielectric hysteresis loop and figure 2.17 shows the hysteresis loop shifted to a symmetric position on the electric displacement axis. However, it is important to note that the crystal retains an asymmetric coercive field. This commonly

occurs in poled ferroelectrics due to stabilization of the poled state through a space charge distribution. However, this does not alter any of the experimental procedure described earlier.

Butterfly loops showing strain in the parallel (ε_{33}) and perpendicular (ε_{11}) direction of applied electric field were measured on two opposite faces of the cubic specimen. Figure 2.18 and 2.19 show the strain response on each face and an average strain response.

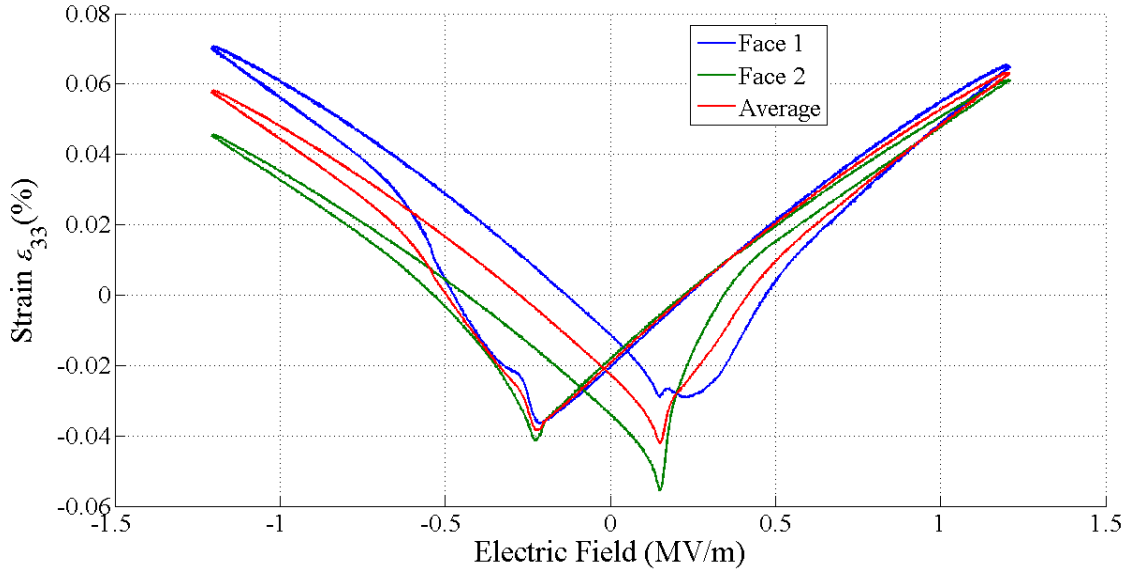

Figure 2.18: Strain parallel to the direction of electric field.

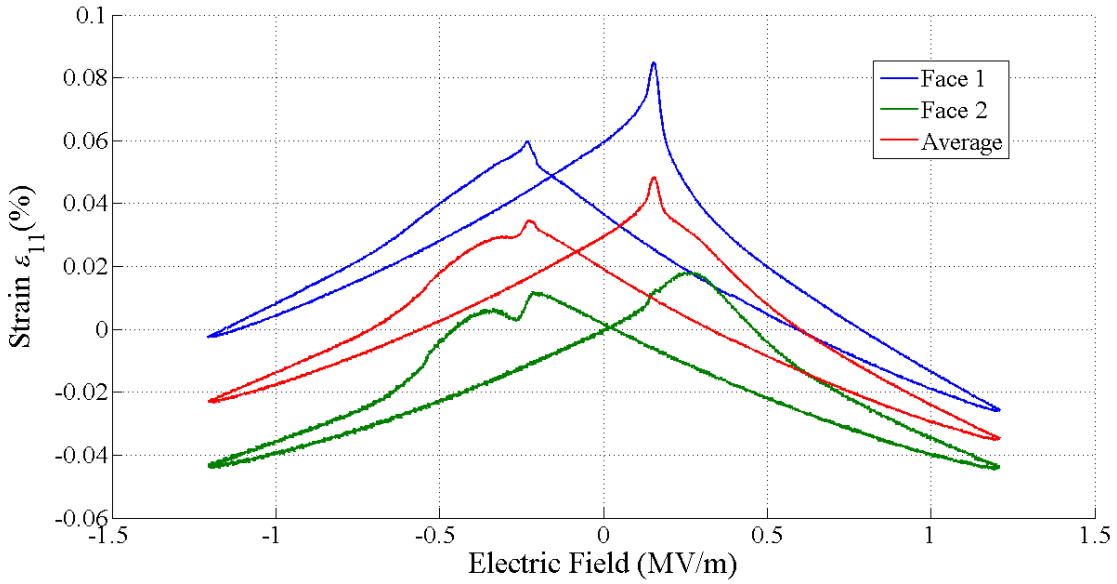

Figure 2.19: Strain perpendicular to the direction of electric field.

It can be observed that the magnitudes of both ε_{33} and ε_{11} differ between opposite two faces of the specimen. This may be partly due to the fact that strain gauge area is only 0.7 mm^2 which implies that the strain response only on a small portion on the specimen surface is measured. This means local variations in the composition and local microstructural patterns may have an effect on the strain measurements. Moreover, Ti content variation across the crystal length is a well known issue with single crystals (figure 2 in reference [75]). The compositional segregation across the single crystal specimen due to processing issues such as incongruent melting, incorrect flux composition has been discussed in Chapters 1-3 in the reference [6]. Due to these variations, average strain (the arithmetic mean of the strains on both the faces) is used here to represent the specimen behaviour as a whole. Strain magnitudes of 0.09-0.11% and 0.05-0.07% were attained for ε_{33} and ε_{11} respectively.

2.6.3. Polarization rotation test – PMN-PT

As the specimen geometry may affect the results of polarization rotation test, cubic specimens ($w = h$) of PMN-PT were chosen for polarization rotation test. The specimen preparation is identical to that of PZT specimen as described in section 2.4.1 except for different magnitudes of electric field and strain measurement in addition to electrical measurements. Rectangular bars of PMN-PT were poled by applying electric field of magnitude $5E_c$ (1.2 MVm^{-1}) at 0.1Hz for 10 full cycles and a positive half cycle so that at the end of the first step, rectangular bar specimens had a remnant polarization of 0.24 Cm^{-2}. After cutting the cubic specimens at various angles, a loading cycle similar to the one shown in figure 2.6 was used; except that a peak electric field of $5E_c$ at 0.1 Hz was used. Figure 2.20 shows the change in dielectric displacement versus the applied electric field.

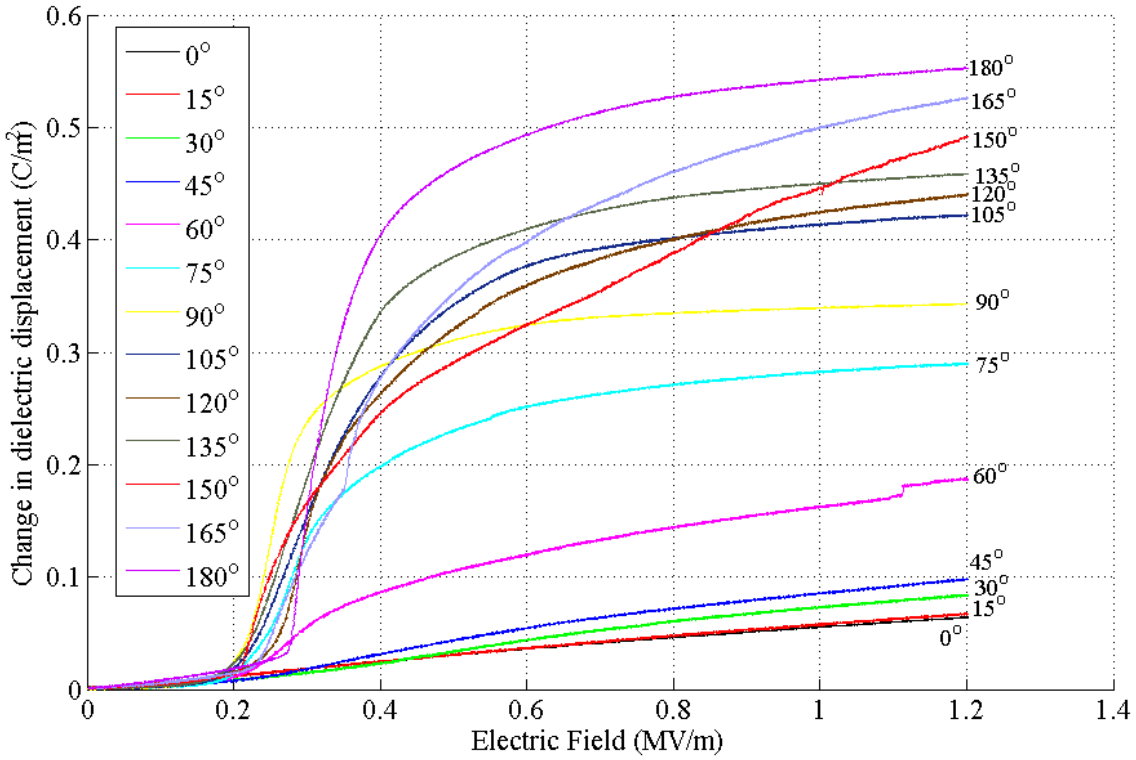

Figure 2.20: Dielectric response of PMN-PT to an electric field applied at various angles to the direction of initial polarization.

The polarization reorientation can be observed from the increase in dielectric displacement as the applied electric field becomes more misaligned with the initial polarization direction. A change of 0.552 Cm^{-2} can be observed when the electric field is in the opposite direction of the initial polarization (180° case). Some of the curves, for example 150° and 165°, show kinks or inflections suggesting a sudden switching of polarization. The 60° curve shows a small step which indicates that an electric discharge occurred during the test.

Using equation 2.3 the change in remnant polarization can be calculated from the change in dielectric displacement by subtracting the dielectric effect contribution. Here, the dielectric permittivity (κ) is calculated from the slope of unloading curve as shown in figure 2.21. A linear fit was used to obtain the slope of the unloading curve in a range of electric field from 1.2 to 0.9 MVm^{-1} (see inset of figure 2.21).

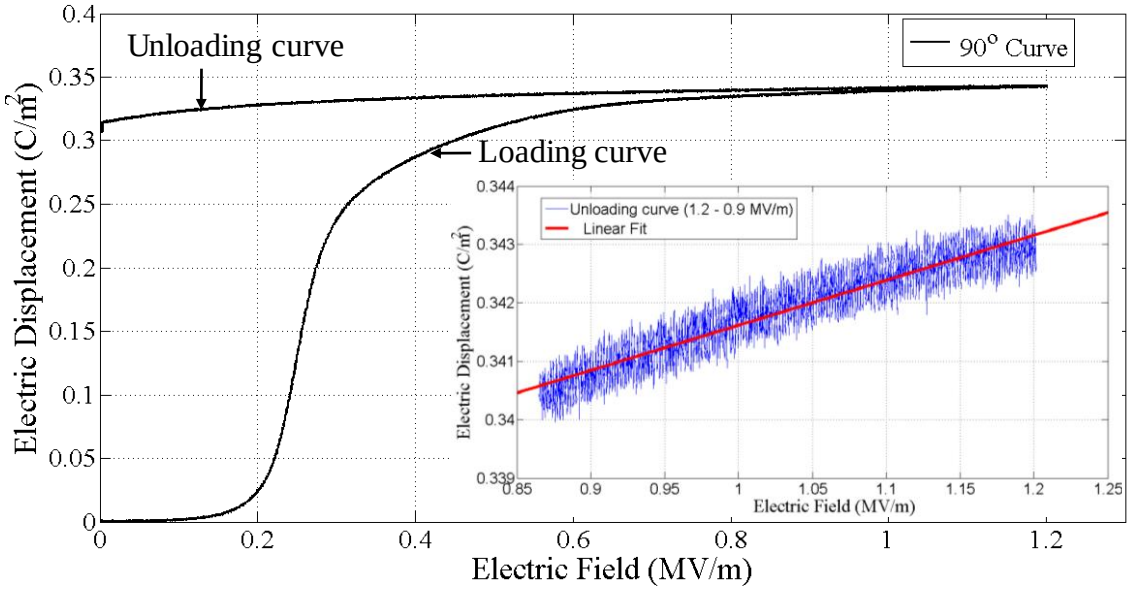

Figure 2.21: Slope of the unloading curve used to compute dielectric contribution. Inset shows a linear fit at the end of the unloading curve.

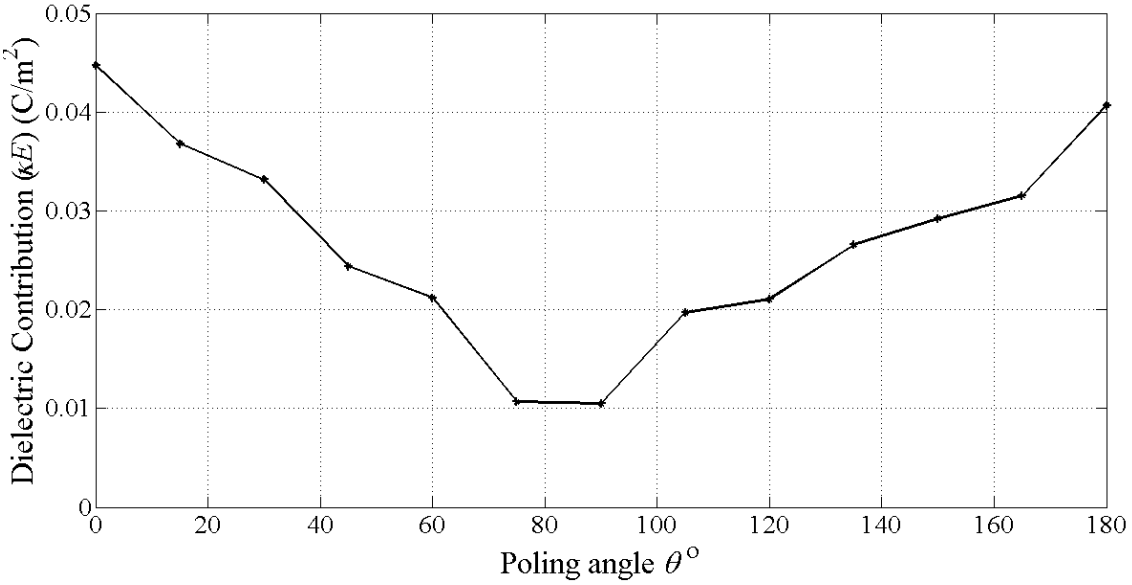

Figure 2.22: Dielectric contribution variation with respect to the poling direction.

Figure 2.22 shows linear dielectric effect contribution to the change in dielectric displacement computed. In contrast with the PZT (figure 2.9), here the poling strongly affects the dielectric behaviour. The dielectric contribution is found to be decreasing as the electric field becomes more misaligned to the direction of initial polarization.

2.6.4. Saturation curve comparison

The total change in remnant polarization can be calculated for each angle after correcting for the dielectric effect, allowing a comparison with the isotropic saturation curve following the method in section 2.4.4. The isotropic saturation curve was obtained using equation 2.4 and the value of P_{sat} was calibrated using the 180° specimen, giving P_{sat} = 0.255 Cm^{-2}. Figure 2.23 shows the comparison between the isotropic and the experimental saturation curve.

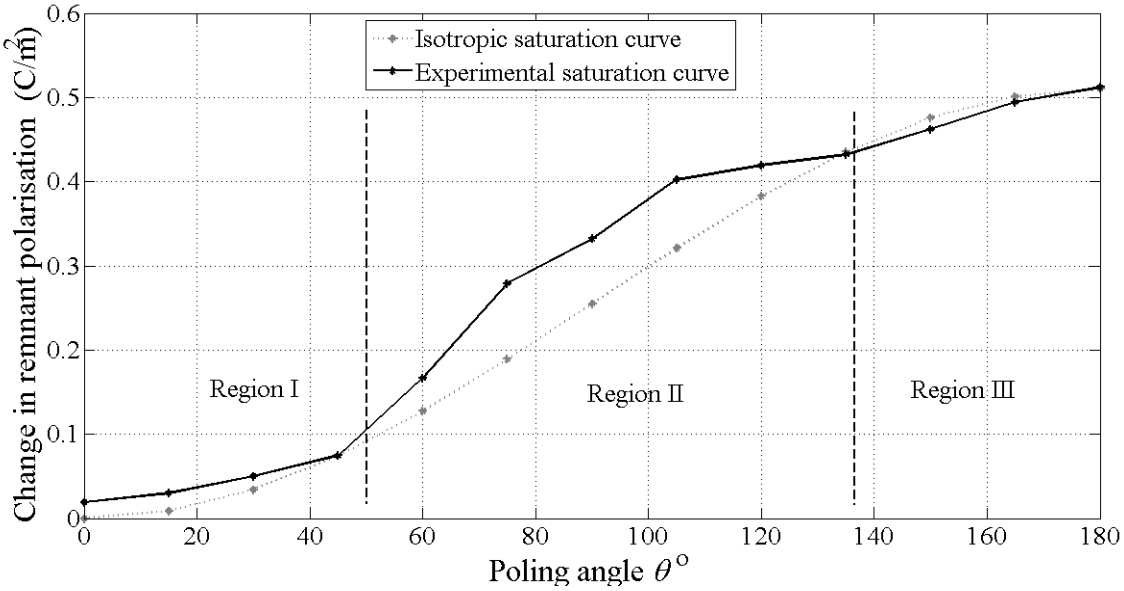

Figure 2.23: Comparison between the isotropic and experimental saturation curve for PMN-PT polarization rotation test.

For regions I (θ < 45°) and III (θ > 135°), the experimental data matches fairly closely to the isotropic curve, as was found for the polycrystalline material. However, it is interesting to note that, contrary to the case of polycrystalline PZT, the experimental data lies above the isotropic curve for region II (45< θ < 135°). This is not in accordance with the hypothesis that surface charges impose a barrier for polarization reorientation. Though a lesser linear dielectric contribution is observed for this region (figure 2.22), the data seems to suggest that PMN-PT is strongly polarizable in certain directions (close to

90°). This is an interesting case to explore as poling in certain directions seems to activate more switching systems giving higher values of remnant polarization.

2.6.5. Effect of polarization rotation on strain

Figure 2.24 and 2.25 show the change in ε_{33} and ε_{11} for angles between 0 and 180° in steps of 45°. An average strain is plotted against electric field.

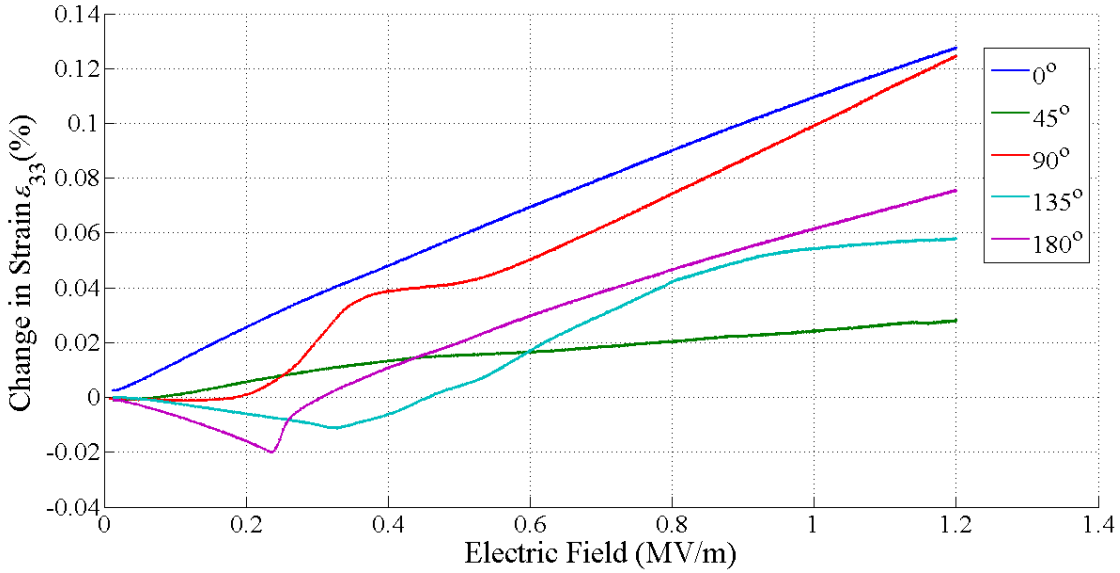

Figure 2.24: Change in strain ε_{33} during polarization rotation.

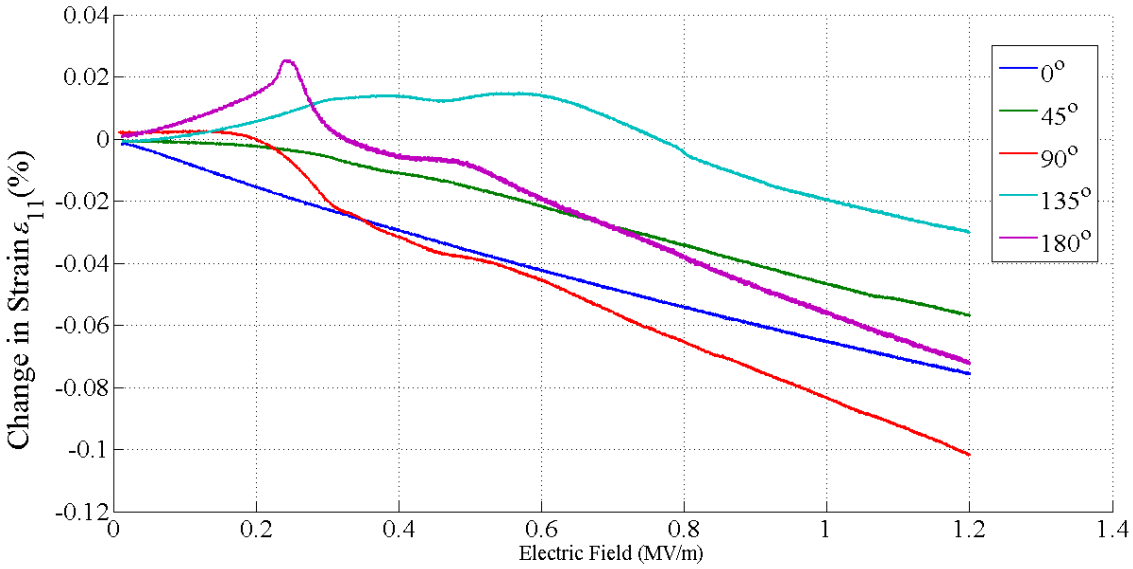

Figure 2.25: Change in strain ε_{11} during polarization rotation.

In the 0° specimen, the total change in strain ε_{33} and ε_{11} is 0.12% and 0.07%. Some polarization reorientation may take place if the material is not fully saturated in the previous poling process. The linear piezoelectric effect should contribute to the strain. The maximum values of strain are in good agreement with those observed in the butterfly loop measurements. The 0° curves show expected linear behaviour due to no or very small polarization reversal.

For the 180° case, the strain initially changes in the opposite way to that observed for the 0° specimen while $E_{applied} < E_c$. As the applied electric field increases beyond E_c, sudden change in the direction of strain with respect to electric field is observed i.e. for $E_{applied} > E_c$, ε_{33} increases with increasing electric field. This is as expected because of the sign reversal of the piezoelectric coefficients during ferroelectric switching. A sharp trough for ε_{33} and sharp peak for ε_{11} near the coercive electric field (E_c ~ 0.22-0.25 MVm^{-1}) are observed due to the sudden switching of the polarization in the direction of the electric field.

For the 45° specimen, the strain response is fairly similar to that of the 0° specimen, as electric field is slightly misaligned with the initial polarization. Similarly, the 135° specimen shows similar features as that of the 180° specimen with a trough for ε_{33} and a peak for ε_{11}. However, the remnant strain levels attained are lower due to partial reorientation of the polarization and features are not as sharp as in the 180° curve. Perhaps the most interesting case is that of the 90° specimen which shows large change in strains. PMN-PT single crystal may have tetragonal or rhombohedral or a co-existence of both phases for the composition PMN-32PT used in the experiment. 90° switching in the tetragonal system is accompanied with strain change whereas 180° switching is strain free. In the rhombohedral system, the 71° and 109° switching is accompanied with a

strain change. The complex mixture of phases and strong polarizability of PMN-PT in certain directions needs to be further explored to fully understand the higher strain response observed for 90° curve. Again, it is worth mentioning that the strain response was measured over a small region of the specimen surface and hence is highly sensitive to local changes in microstructure and composition. This may well be the reason for kinks observed in the 90° curve.

In the next chapter, the experimental results are further analyzed with the help of a micromechanical model based on a switching criterion utilizing various switching systems.

2.7. Conclusions

A polarization rotation test on polycrystalline PZT showed good agreement with the literature. The isotropic saturation curve comparison shows lower remnant polarization around 90° suggesting the effect of boundary conditions at the free surfaces. The polarization test was extended to test for the influence of specimen shape, and it was found that the sample aspect ratio affects the results – this may call into question some results of Shieh *et al*. [68], where various specimen aspect ratios were used. For a thick short specimen, low values of polarization suggest variation in the apparent coercive field strength in this specimen geometry. The geometry has an effect on the polarization switching in these tests and careful selection of the specimen geometry is required for reliable test results.

A polarization rotation test was done on PMN-PT single crystal and results were compared with the isotropic saturation curve. In case of single crystals, the dielectric effect was found to show noticeable variation as the electric loading direction is altered. For loading angles near to 90°, high values of remnant polarization were observed. This

suggests that the PMN-PT is more polarizable in certain directions. Strain changes were also measured during the polarization rotation test and electrical and strain data provides a set of multi-axial measurements that are potentially useful for validation of constitutive models. Due to the small area sampled by the strain gauges, measurements were susceptible to local variations in behaviour. In PMN-PT, this could be due to compositional variations or due to local arrangement of domain structure. Further investigation of local structure is needed to confirm this.

3. Micromechanical modelling of ferroelectric switching

Ferroelectric ceramics exhibit complex non-linear macroscopic behaviour under the application of external loads such as mechanical stress and/or electric field. Models based on constitutive laws governing the ferroelectric switching mechanism are widely used to study the response of the material. Broadly, the various modelling approaches can be divided into two categories viz. phenomenological and micromechanical.

The motivation for modelling in this thesis is to gain insight into the experimental results presented in chapter 2. The measured electrical and strain response of PMN-PT single crystal in the polarization rotation test can be further analyzed with the help of a switching model including dielectric and piezoelectric effects and domain switching. In this chapter, an assessment of various models already available in the literature is used to select a suitable model that has the potential to capture the switching phenomena observed in the experiments. Then the experimental results are simulated using appropriate loading conditions and material parameters, aiming for maximum consistency between the experiments and simulations. The development of a micromechanical model to simulate the polarization rotation test on PMN-PT single crystal is discussed in detail. Note that the focus of the modelling effort here is towards developing a tool to assist in the interpretation of experimental results rather than a new constitutive law.

A brief introduction to phenomenological and micromechanical modelling approaches is presented next, followed by a detailed description of the model and comparison between experimental and modelling results.

3.1 Background

Most of the constitutive models for ferroelectrics developed so far focus on polycrystalline ferroelectrics containing large number of grains with multiple domains within each grain. Phenomenological and micromechanical modelling utilize internal state variables that describe the state of the material. The main distinction between these two types of models is that in micromechanical models the internal variables describe a microstructural feature, such as the volume fraction of a domain type. By contrast, phenomenological theory aims to match external measurable quantities, such as strain or polarization, but the internal variables need not represent a physical feature of the material. In both cases, the non-linear dependence of polarization and strain on applied loads is then evaluated by assuming a switching surface (analogous to a yield surface) in electric field-stress space for electrical or electromechanical loading. The complex history dependence of material is brought in through a hardening law that allows the switching surface to move and change shape depending on material state. Typically, kinematic hardening is used. By formulating a switching criterion based on balancing external work done with energy dissipated during switching, thermodynamic constraints on the material model are satisfied. The models are calibrated against experimental data which is typically a ferroelectric hysteresis loop and butterfly loop. Various uniaxial and/or multi-axial electromechanical test results are then simulated to examine model's accuracy in predicting the non-linear material behaviour. Papers by Hall [76], Kamlah [70] and Bhattacharya and Ravichandran [77] review various modelling approaches.

3.1.1. Phenomenological modelling

Phenomenological models [67,72,78–82] are based on a thermodynamic framework utilizing free energy formulations involving a number of internal state variables to model the non-linear behaviour of ferroelectrics. One of the early theories was proposed by

Rayleigh for ferromagnetic materials. The Rayleigh law states that a linear relationship exists between magnetic susceptibility and magnetic field at low field value (less than coercive field). Further, a weak field hysteresis loop could be obtained by approximating the relationship between magnetisation and magnetic field using a reversible linear and irreversible quadratic expression derived using Rayleigh law. The physical interpretation of the law is based on the interactions of the domain walls with the pinning defects that are randomly distributed in a ferromagnetic material [76,83]. In the Landau-Ginzberg-Devonshire thermodynamic theory, free energy is expressed in a power law using an appropriate order parameter such as polarization in the case of ferroelectrics [3]. The theory can provide a description of ferroelectric switching and hysteresis loop [84].

Perhaps the most complete phenomenological model for isothermal behaviour is that of McMeeking and Landis [85] which is based on remnant polarization vector and remnant strain tensor as internal variables. In this model, the physics of deformation and the switching mechanism in the material defines the dependence of free energy on the invariants of the internal state variables. The model also introduces full electromechanical coupling to account for changes in remnant strain due to electric field and remnant polarization due to mechanical stress. Landis' model showed a satisfactory agreement with the experimental data such as combined electromechanical loading of polycrystalline Lead Lanthanum Zirconate Titanate (PLZT) [86] and multi-axial polarization rotation test on polycrystalline soft Lead Zirconate Titanate (PZT) [67]. A simplified version of the same model [72] has only remnant polarization as the internal state variable. More detailed discussion about various phenomenological models can be found in a review by Landis [87].

For present purposes, a difficulty in using phenomenological approaches, such as that of Landis is that the model is developed around a description of polycrystal behaviour. It is not straightforward to adapt the approach to single crystal materials. The strongly anisotropic behaviour expected from the single crystals can be contrasted with the isotropic initial state in the Landis model. Similarly, Landis uses carefully calibrated fitting functions to describe the saturation of switching and its dependence on the remnant strain state. These functions are based on polycrystal behaviour, and are unsuited to single crystal behaviour. Finally, in the present context, insight into the switching behaviour is sought. For example, it would be of value to know which domain types were involved in switching. Landis's model cannot provide this level of underlying detail.

3.1.2. Micromechanical modelling

In the case of a typical micromechanical model, such as the one proposed by Hwang *et al*. [88], domains are represented by a set of crystal variants, where a single variant corresponds to a distinctive polarization vector direction. Each crystal variant can be assigned a volume fraction, and these act as internal state variables. Most of the micromechanical models are based on a central concept that switching or polarization reorientation occurs when the work done by external electromechanical loads exceeds a certain critical threshold. The switching of domains is modelled by transfer of volume fraction from one crystal variant to another, which is normally more aligned to the direction of applied load. The choice of variants is dependent on the crystal structure of the material being modelled, for example, in the tetragonal system, we have 6 crystal variants whereas for the rhombohedral system, there are 8 variants. Macroscopic polarization and strain is computed by averaging over a number of grains for a polycrystalline material; each grain can be thought of as containing a single domain or multiple domains. The switching captured through a transfer of volume fraction is rate

independent in Hwang's model [88] but rate dependence can be introduced [67], which is more realistic when compared with the experimental observations. The saturation of switching can be realized by controlling the transfer of volume fraction as the transferring crystal variant approaches zero volume fraction. Other complexities like the constraints imposed by neighbouring grains on switching (grain to grain interactions), inhomogeneities in electric field and stress etc. can be incorporated to tailor the model to more sophisticated scenarios. A detailed discussion of micromechanical models is given in a review paper by Huber [89].

3.1.3. Experimental investigations

An important aspect of model development is the availability of the experimental data which can be used, first, to calibrate the model and then to compare and evaluate the model against measured experimental data. All the experimental investigations reported below are for polycrystalline materials unless otherwise specified. Lynch [86] carried out electromechanical tests on PLZT and showed that stress driven depolarization can begin at a low stress level (5 MPa). Cao and Evans [90] compared the depolarization effects in hard and soft PZT and concluded that hard PZTs can perform better at higher stress levels. Huber and Fleck designed a polarization rotation test giving a multi-axial loading data on soft PZT which was subsequently used for comparison in many models [67]. Shieh *et al*. [68] extended the polarization rotation test to hard PZT and Barium Titanate along with providing measurements of uniaxial compressive stress and parallel electric field applied simultaneously. Zhou *et al*. [69] performed electrical as well as strain measurements on soft PZT in a polarization rotation test and found significant difference in the size of switching surfaces obtained from polarization and strain measurements. Similarly, coaxial electromechanical loading experiments on soft PZT by Zhou *et al*. [91] provide a systematic experimental data for model evaluation.

All of these investigations measured macroscopic variables such as average stress, strain, electric field and electric displacement. However, in depth analysis of the underlying structural configuration has also been carried out, for example, X-ray and neutron diffraction techniques have been used to study strain and texture development. Hall *et al*. [92–94] used synchrotron X-day diffraction to study the linear dependence of elastic strain on the grain orientation relative to the poling direction and the crystallographic texture development in the poled condition. Studies were conducted on tetragonal and rhombohedral soft PZT and the observed relationship was analyzed with the help of a micromechanical model. Lattice strain and texture evolution in PZT under uniaxial compressive stress was studied in-situ using neutron diffraction by Rogan *et al*. [95]. Domain texture changes due to electric poling in tetragonal PZT were studied using neutron diffraction by Jones *et al*. [96].

One recent technique that may have potential to provide useful information about the domain fractions within a single grain is Piezo-response Force Microscopy (PFM) [97]. In single crystal Barium Titanate, a combination of lateral and vertical PFM (known as vector PFM) is used to quantify the distribution of domains. However, the method is very sensitive to the surface topography and needs improvement for mapping domain configurations in polycrystalline ceramics. Further discussion about these techniques is given in Chapter 4.

3.2. Micromechanical model

3.2.1. Modelling approach

In the polarization rotation test, as the electric field becomes increasingly misaligned to the direction of initial polarization, the multi-axial response (change in remnant polarization direction) becomes more prominent and this results in increased switching.

This suggests that the active switching system changes with the direction of the applied electric field. Therefore, it seems important to understand which switching systems become active with increased misalignment of applied field and what role they play in switching. The micromechanical approach readily provides information about the volume fractions corresponding to each crystal variant. It is also possible to model multiple switching systems and any number of crystal variants. Compared with phenomenological approach, it is perhaps more easy to understand the microstructural developments occurring in the crystal under multi-axial electromechanical loading using a micromechanical approach. Furthermore, application to single crystal is straightforward, even though the models have mainly been calibrated against polycrystal data. Hence, a micromechanical model based on switching criterion given by Hwang *et al*. [88] is used to simulate and interpret the polarization rotation test results.

3.2.2. Crystal variants and switching systems

The composition of PMN-32PT single crystal used for the experiments discussed in Chapter 2 lies near a morphotropic phase boundary. This suggests that the domain structure is complicated with the presence of possibly multiple phases viz. tetragonal, rhombohedral and/or monoclinic. Monoclinic phase is believed to always coexist with either tetragonal or rhombohedral phases. Presence of a monoclinic phase gives a complex mixture of phases with complicated domain arrangements [46,98,99]. In the present modelling work, the simplifying assumption is made that only the tetragonal and rhombohedral phases coexist and these dominate the macroscopic response. This is a reasonable assumption considering that it is difficult to have a precise control on the compositional variation in single crystals due to segregation of solid and liquid phases during processing. A combination of tetragonal and rhombohedral phases can provide at

least a qualitative description of the switching without a need of the complex and only partially understood monoclinic phase and associated switching systems.

In the case of the tetragonal unit cell (figure 3.1 (a)), there are 6 possible directions of the local polarization vector given by the possible positions that the central cation can occupy in a unit cell. This gives 6 distinct crystal variants with polarization, $\mathbf{P}_i$, for i=1...6, and spontaneous strain, $\boldsymbol{\varepsilon}_i$, for i=1...6 associated with each variant, given by equation 3.1 and 3.2 respectively.

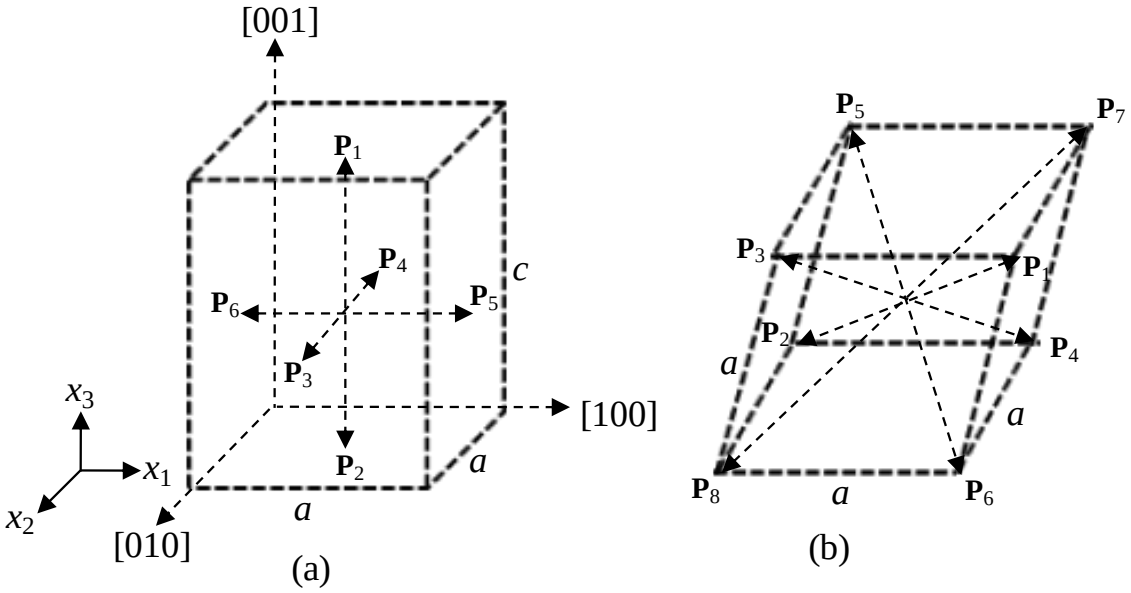

Figure 3.1: Polarization states/crystal variants in (a) tetragonal and (b) rhombohedral crystal system.

$$\mathbf{P}_1 = [0 \quad 0 \quad P^0] \qquad \mathbf{P}_2 = [0 \quad 0 \quad -P^0]$$

$$\mathbf{P}_3 = [0 \quad P^0 \quad 0] \qquad \mathbf{P}_4 = [0 \quad -P^0 \quad 0]$$

$$\mathbf{P}_5 = [P^0 \quad 0 \quad 0] \qquad \mathbf{P}_6 = [-P^0 \quad 0 \quad 0] \tag{3.1}$$

$$\boldsymbol{\varepsilon}_1 = \boldsymbol{\varepsilon}_2 = \begin{bmatrix} -0.5 & 0 & 0 \\ 0 & -0.5 & 0 \\ 0 & 0 & 1 \end{bmatrix} \varepsilon^0$$

$$\boldsymbol{\varepsilon}_3 = \boldsymbol{\varepsilon}_4 = \begin{bmatrix} -0.5 & 0 & 0 \\ 0 & 1 & 0 \\ 0 & 0 & -0.5 \end{bmatrix} \varepsilon^0$$

$$\boldsymbol{\varepsilon}_5 = \boldsymbol{\varepsilon}_6 = \begin{bmatrix} 1 & 0 & 0 \\ 0 & -0.5 & 0 \\ 0 & 0 & -0.5 \end{bmatrix} \varepsilon^0 \tag{3.2}$$

Here P^0 and ε^0 are the spontaneous polarization and spontaneous strain (transformation strain from the high temperature cubic phase) respectively. For the polarization of any crystal variant, say $\mathbf{P}_1$, four equivalent 90° switching systems can switch the polarization to new states ($\mathbf{P}_3$, $\mathbf{P}_4$, $\mathbf{P}_5$ and $\mathbf{P}_6$). One 180° switching system also exists, which produces polarization $\mathbf{P}_2$. The crystal variants corresponding to polarization $\mathbf{P}_1$ to $\mathbf{P}_6$ are each assumed to have volume fraction v_i which acts as an internal state variable. The remnant polarization, $\mathbf{P}^r$, and remnant strain, $\boldsymbol{\varepsilon}^r$, of the entire crystal is given by volume averages as

$$\boldsymbol{\varepsilon}^r = \sum \boldsymbol{\varepsilon}_i v_i, \tag{3.3}$$

$$\mathbf{P}^r = \sum \mathbf{P}_i v_i. \tag{3.4}$$

Equations 3.3 and 3.4 are valid in the absence of internal residual stress and electric field. Although residual fields might be expected, there is some evidence that compatible domain arrangements form to minimise the internal energy, and thus reduce residual stresses and electric fields.

Turning to the rhombohedral unit cell, the polarization vector directions are along the body diagonals of the unit cell, giving 8 distinct crystal variants (figure 3.1(b)). Polarization ($\mathbf{P}_i$ for i=1...8) and strain ($\boldsymbol{\varepsilon}_i$ for i=1...8) associated with each variant, are given by equation 3.5 and 3.6 respectively.

$$\mathbf{P}_1 = [1 \quad 1 \quad 1]P^0 \qquad \mathbf{P}_2 = [-1 \quad -1 \quad -1]P^0$$

$$\mathbf{P}_3 = [-1 \quad 1 \quad 1]P^0 \qquad \mathbf{P}_4 = [1 \quad -1 \quad -1]P^0$$

$$\mathbf{P}_5 = [-1 \quad -1 \quad 1]P^0 \qquad \mathbf{P}_6 = [1 \quad 1 \quad -1]P^0$$

$$\mathbf{P}_7 = [1 \quad -1 \quad 1]P^0 \qquad \mathbf{P}_8 = [-1 \quad 1 \quad -1]P^0. \tag{3.5}$$

$$\boldsymbol{\varepsilon}_1 = \boldsymbol{\varepsilon}_2 = \begin{bmatrix} \alpha & \beta & \beta \\ \beta & \alpha & \beta \\ \beta & \beta & \alpha \end{bmatrix} \qquad \boldsymbol{\varepsilon}_3 = \boldsymbol{\varepsilon}_4 = \begin{bmatrix} \alpha & -\beta & -\beta \\ -\beta & \alpha & \beta \\ -\beta & \beta & \alpha \end{bmatrix}$$

$$\boldsymbol{\varepsilon}_5 = \boldsymbol{\varepsilon}_6 = \begin{bmatrix} \alpha & \beta & -\beta \\ \beta & \alpha & -\beta \\ -\beta & -\beta & \alpha \end{bmatrix} \qquad \boldsymbol{\varepsilon}_7 = \boldsymbol{\varepsilon}_8 = \begin{bmatrix} \alpha & -\beta & \beta \\ -\beta & \alpha & -\beta \\ \beta & -\beta & \alpha \end{bmatrix}. \tag{3.6}$$

Here P^0 is the spontaneous polarization and α and β are material parameters. Assuming a pseudo-cubic structure as a reference configuration, α=0. In the rhombohedral unit cell, the angle between the crystallographic axes was measured by synchrotron X-ray diffraction equal to 89.89° [46]. The shear strain, $\beta = \tan(x)$ (figure 3.2).

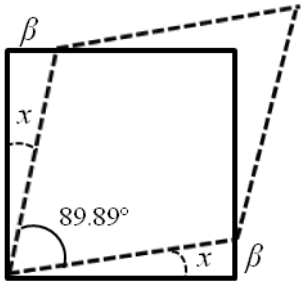

Figure 3.2: Distorted rhombohedral unit cell.

For a polarization vector oriented along a crystal variant, say $\mathbf{P}_1$, three equivalent 71° switching systems can switch the polarization to $\mathbf{P}_3$, $\mathbf{P}_6$ and $\mathbf{P}_7$. Similarly, three equivalent 109° switching systems also exist that can switch the polarization to $\mathbf{P}_4$, $\mathbf{P}_5$ and $\mathbf{P}_8$ and finally one 180° switching system can switch the polarization to $\mathbf{P}_2$.

3.2.3. Switching Criterion and rate dependency

Under the application of external electric field or mechanical stress or a combination of both, the direction of the remnant polarization vector ($\mathbf{P}^r$) of the crystal can change. If the external load is high enough, the spontaneous polarization fully aligns itself in the direction of external field/stress (full switching). Full switching involves losing a

polarization P^0 in one direction and gaining the same amount P^0 in one of the other possible directions, depending upon the switching systems available. Domain walls dissipate energy to overcome lattice defects or pinning by other domain walls; that makes domain switching a dissipative process. The external work done, W_E, per unit volume in switching the polarization by an electric field, $\mathbf{E}_i$ is given by,

$$W_E = \int \mathbf{E}_i dD_i, \tag{3.7}$$

where dD_i is the increment in electric displacement.

Let us suppose that for 180° switching, the external electric field switches the spontaneous polarization from $+P^0$ to $-P^0$ at a critical field value of electric field, $-E_{crit}$. Then, the change in electric displacement for 180° switching is given by $-2P^0$ and energy required for switching, G_c, can be written as

$$G_c = 2P^0 E_{crit}. \tag{3.8}$$

Note that the dielectric effect was neglected here, as the stored dielectric energy is assumed to be unchanged during switching due to symmetry. Under the application of external electric field, the work done per unit volume in switching the spontaneous polarization from one direction to another can be written as:

$$G = E_i \Delta P_i, \tag{3.9}$$

where ΔP_i is the change in polarization i.e. the local polarization vector.

Hwang *et al*. [88] proposed that when the external work done exceeds the energy required for switching, the spontaneous polarization switches in the direction of applied electric field. Thus, for polarization switching the criterion that needs to be satisfied is:

$$G \geq G_c,$$
$$\text{i.e. } E_i \Delta P_i \geq 2P^0 E_{crit}. \tag{3.10}$$

The criterion can be extended to incorporate the work done under the application of mechanical stress. However in the experiments of chapter 2 only electric field was applied, so the criterion given by 3.10 is sufficient. For every increment in external electric field, the model computes the change in polarization ΔP for each possible switching system. For example, the change in polarization for m^{th} variant switching to n^{th} variant ($m \rightarrow n$) is given by

$$\Delta P_{m \rightarrow n} = P_n - P_m. \tag{3.11}$$

Using equation 3.11, the left hand side of the equation 3.10 can be computed at each electric field value. Once the switching criterion given by equation 3.10 is satisfied, switching is implemented by transfer of volume fraction. Hence, for m^{th} variant switching to n^{th} variant, the volume fraction of the m^{th} variant (v_m) is added to the volume fraction of n^{th} variant (v_n). So after switching we have

$$m \rightarrow n: \qquad v_n = v_n + v_m \; ; \qquad v_m = 0. \tag{3.12}$$

The volume fractions are updated at each increment of electric field. Remnant polarization and strain are evaluated using equation 3.3 and 3.4. This model is rate independent i.e. the entire volume fraction of the m^{th} variant (v_m) transfers completely to the n^{th} variant (v_n) once the switching criterion is satisfied. The polarization response from such volume fraction transfers consists of sharp transitions or steps. However, in real conditions, the polarization changes are spread more gradually over the time, even if the electric field is held constant [100]. This suggests that switching is a rate dependent phenomenon. One of the ways to explain such behaviour is that the switching happens through the motion of domain walls in an incremental fashion [101]. The kinetics of this process would then determine the associated rate. To incorporate such behaviour, an

approach similar to viscoplastic behaviour in a crystal plasticity models can be used. This has the additional benefit that it stabilizes simulations of mass/volume transfer [67]. For viscoplastic behaviour, we can use equation 3.13.

$$\dot{v}_{mn} = c \left| \frac{G}{G_c} \right|^q \left(\frac{v_m}{v_o} \right)^r \text{ if } v_m > 0, \tag{3.13}$$

As the switching criterion is satisfied for the m^{th} variant to switch to the n^{th} variant, v_m starts decreasing and v_n starts increasing at a rate $\dot{v}_{mn}$ which depends on rate exponent q and a rate constant c. As the system approaches saturation, i.e. $v_m \rightarrow 0$, the rate of transformation is controlled by a saturation index r and v_o is the initial volume fraction of variant m in the unpoled condition. Volume fraction increments during time step δt can be written by summing over all switching systems

$$\delta v_n = \sum_{m=1}^{N} \dot{v}_{mn} \delta t - \dot{v}_{nm} \delta t \tag{3.14}$$

where N is the number of crystal variants.

Appropriate parameter values for q, r and c enable rate controlled transformation of volume fractions, capable of simulating the non-linear ferroelectric switching. The condition $v_m > 0$ ensures positive volume fractions.

The model based on this criterion has certain assumptions. The electric field experienced by each domain is assumed to be identical (effectively Reuss approximation). Domain to domain interactions are also neglected, such as stresses due to incompatibility. In fact, these assumptions may not be unreasonable in single crystals, due to the formation of compatible domain arrangements as discussed in section 3.2.2. The model neglects changes in dielectric effects due to switching.

3.2.4. Dielectric and piezoelectric effect

The electric displacement (D_i) and strain (ε_{ij}) under an applied electric field (without mechanical stress) are given by

$$D_i = \kappa_{ik} E_k + P_i^r \tag{3.15}$$

$$\varepsilon_{ij} = d_{kij} E_k + \varepsilon_{ij}^r. \tag{3.16}$$

Here, κ_{ik} is the tensor of dielectric permittivity and d_{kij} is the tensor of piezoelectric coefficients. P_i^r is the remnant polarisation, and ε_{ij}^r is the remnant strain which can be calculated from equations 3.3 and 3.4. As the main purpose of modelling here is to track the polarization changes, simplifying assumptions will be made regarding the dielectric and piezoelectric response. The dielectric permittivity is assumed to be isotropic and hence κ calculated as below

$$\kappa_{ij} = K \mathrm{K}_0 \delta_{ij} \tag{3.17}$$

where K is the dielectric constant for PMN-PT which can be computed from slope of the P-E curve and K_0 is the permittivity of the free space ($K_0 = 8.85*10^{-12}$ Fm^{-1}).

Strain from the linear piezoelectric contribution can be calculated from equation 3.18.

$$\varepsilon_{kl}^{\text{piezo}} = \sum_{i=1}^{n} d_{jkl}^{i} E_j \tag{3.18}$$

where n is the number of crystal variants and d_{jkl}^{i} is the piezoelectric coefficient of the i^{th} variant. Piezoelectric coefficients for individual domains or crystal variants within PMN-PT are not readily available in the literature and are difficult to obtain experimentally. Hence, for simplicity, effective piezoelectric coefficients, d_{333}^{eff} and d_{311}^{eff}, are used. In the polarization rotation experiment described in chapter 2, an electric field was applied in the [001] direction i.e. parallel to the x_3 direction in figure 3.1. In these experiments, strain is measured parallel to the direction of electric field (ε_{33}) and perpendicular to the

direction of electric field (ε_{11}). The corresponding piezoelectric strain, ε_{33}^{piezo} and ε_{11}^{piezo} is computed using equation 3.19 utilising effective piezoelectric coefficients, d_{333}^{eff} , and d_{311}^{eff}. Further, the effective piezoelectric coefficients are computed using a rule of mixtures assuming a linear relationship between polarization (P) and piezoelectric coefficient (d) (equation 3.20).

$$\varepsilon_{33}^{piezo} = d_{333}^{eff} E_3 \; ; \; \varepsilon_{11}^{piezo} = d_{311}^{eff} E_3 \tag{3.19}$$

$$d_{333}^{eff} = \frac{P_3}{P_{sat}} d_{333} \; ; d_{311}^{eff} = \frac{P_3}{P_{sat}} d_{311} \tag{3.20}$$

where, P_3 is the polarization component in the direction of electric field, P_{sat} is the saturation polarization and d_{333} and d_{311} are the measured piezoelectric coefficients which can be found from the slope of the corresponding ε- E curves. It is important to note that here only quasi-static or low frequency behaviour is under consideration.

3.2.5. Calibration of the model using experimental data

The aim is to simulate the polarization rotation test results for comparison with experimental data. It is first necessary to calibrate the model against a measured hysteresis and butterfly loop to fix appropriate modelling parameters and material constants. The model explained above was set up for the tetragonal and rhombohedral systems independently; for each system, it was calibrated against the experimental data of figure 2.17 (for dielectric hysteresis loop), figure 2.18 and 2.19 (for butterfly loop: using average curve).

To simulate the dielectric hysteresis and butterfly hysteresis, a cyclic electric field, **E**, of peak amplitude, e =1.2 MVm^{-1}, triangular waveform, and frequency of 0.1 Hz was applied in [001] direction, similar to the experimental conditions. Polarization (P_E) in the direction of electric field is calculated as

$$P_E = \mathbf{P^r} . \hat{\mathbf{E}}, \tag{3.21}$$

where $\hat{\mathbf{E}}$ = [0 0 1] and $\mathbf{P}^r$ is evaluated from equation 3.4. The total electric displacement (D) was obtained using equation 3.15.The remnant strain in the direction of the electric field is given by

$$\varepsilon_{33} = \hat{\mathbf{E}} . (\boldsymbol{\varepsilon}^{\mathbf{r}} . \hat{\mathbf{E}}) , \tag{3.22}$$

Strain perpendicular to the direction of the electric field can be written as

$$\varepsilon_{11} = [-1 \quad 0 \quad 0] . (\boldsymbol{\varepsilon}^{\mathbf{r}} . [-1 \quad 0 \quad 0]) . \tag{3.23}$$

The piezoelectric contribution to the strain, ε_{33}^{piezo} and ε_{11}^{piezo}, was added to obtain the total strain in the parallel and perpendicular direction of electric field, as given by equation 3.16. Table 3.1 summarizes the parameters used in tetragonal and rhombohedral models. Each crystal variant was assigned equal volume fraction in the beginning. The remnant strain (ε_0) for tetragonal case is calculated by assuming a pseudo cubic reference structure with lattice parameter (a_0). The tetragonal structure with lattice parameters (a_t and c_t) has the same volume as that of the reference cubic structure. Hence, we have $a_t^2 c_t = a_0^3$ where a_t = 4.000 Å and c_t = 4.044 Å giving a_0 = 4.014 Å [46]. The strain (ε_0) is given by $\varepsilon_0 = (c_t - a_0)/a_0$. In the rhombohedral system, using measurements from Noheda *et al*., [46], shear strain β = 0.0955%. Thus, remnant and shear strain values used in model are derived from measured lattice parameters.

Table 3.1: Parameters used for fitting experimental hysteresis and butterfly loop.

Parameter	Tetragonal case	Rhombohedral case
Initial volume fraction (v_o)	1/6	1/8
Remnant strain (ε_0) (for tetragonal) (%)	0.747	--
Shear strain (β) (for rhombohedral) (%)	--	0.0955
Piezoelectric coefficient (d_{333}) (pmV^{-1})	850	850
Piezoelectric coefficient (d_{311}) (pmV^{-1})	-450	-450
Dielectric constant (K)	6500	6500

Spontaneous polarization (P^0) (Cm^{-2})	0.25	0.25
Critical electric field (E_{crit}) (MVm^{-1})	0.125	0.108
Saturation polarization (P_{sat}) (Cm^{-2})	0.31	0.31
Rate constant (c)	0.001	0.001
Saturation index (r)	2.8	2.5
Rate exponent (q)	8	7

The procedure for fitting the model parameters is as follows: Initial guess for spontaneous polarization (P^0) and critical electric field (E_{crit}) was based on the remnant polarization (P_r) and coercive electric field (E_c) of the experimental hysteresis loop respectively. The values of parameters q, c and r were chosen to approximately fit the shape of the dielectric hysteresis. First estimates for the dielectric constant (K) and piezoelectric coefficients (d_{333} and d_{311}) were taken from the slope of experimental hysteresis loop and butterfly loop (K ~ 5000, d_{333} ~ 700 pmV^{-1} and d_{311} ~ -450 pmV^{-1}). Next, the butterfly hysteresis loop was fitted using strain values obtained using lattice parameters, first estimates of piezoelectric coefficients and saturation polarization P_s, using experimental data. The dielectric and piezoelectric constants were adjusted slightly to obtain a good fit to the experimental data. Finally, small adjustments were made to the values of q, c and r to improve the accuracy of the fit. Figure 3.3 shows a comparison of dielectric hysteresis loop fitted using the parameters given in Table 3.1 with the experimental data. In the experimental data, an asymmetric hysteresis loop is seen due to a small field bias offset. This may be because of initial poling operation of the crystals at supplier's end. This offset has not been accounted for in the model. Comparison of the simulated butterfly hysteresis loop with the experimental data is shown in figures 3.4 and 3.5.

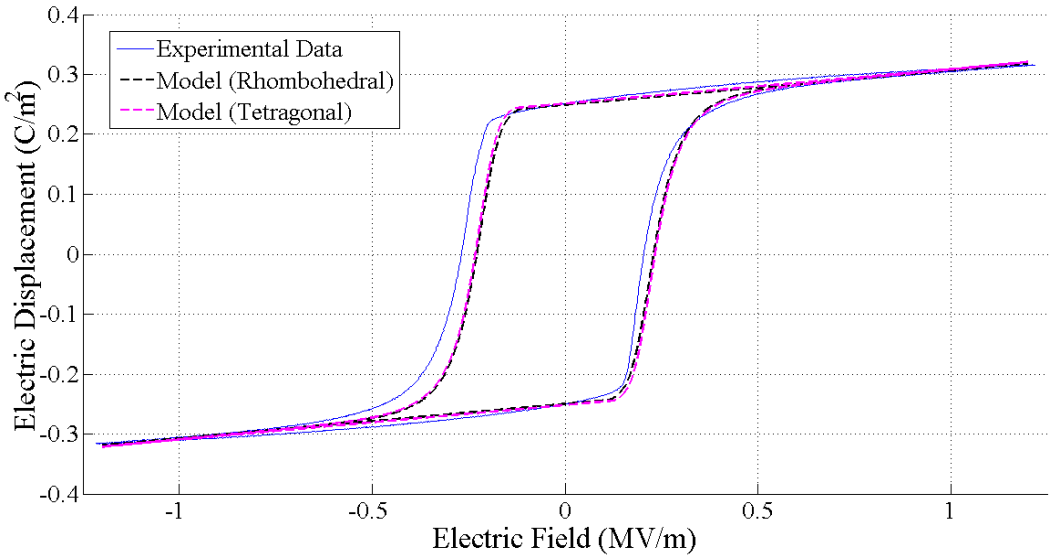

Figure 3.3: Comparison of dielectric hysteresis loop with experimental data.

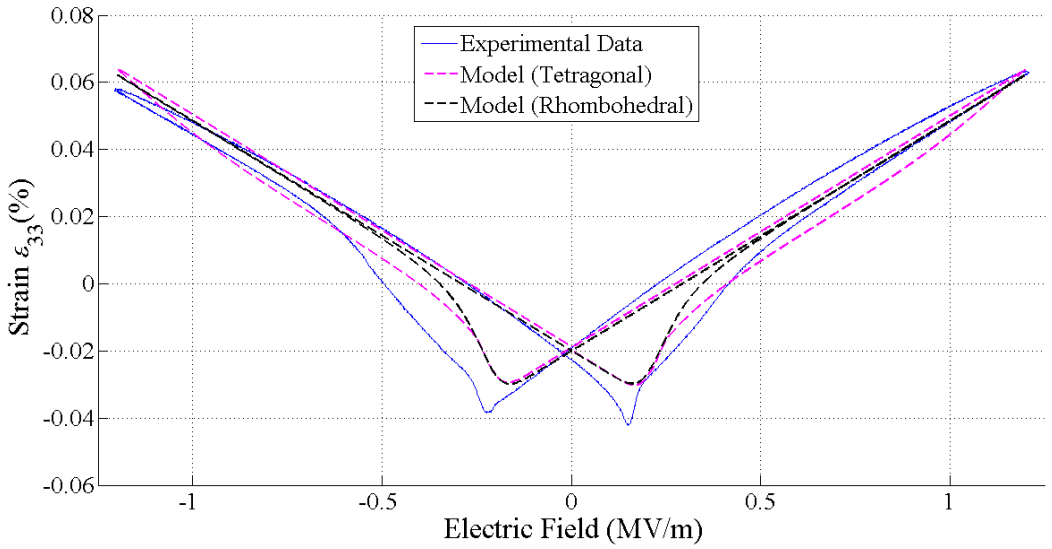

Figure 3.4: Model vs. experiment: Strain (ε_{33}) parallel to the direction of electric field.

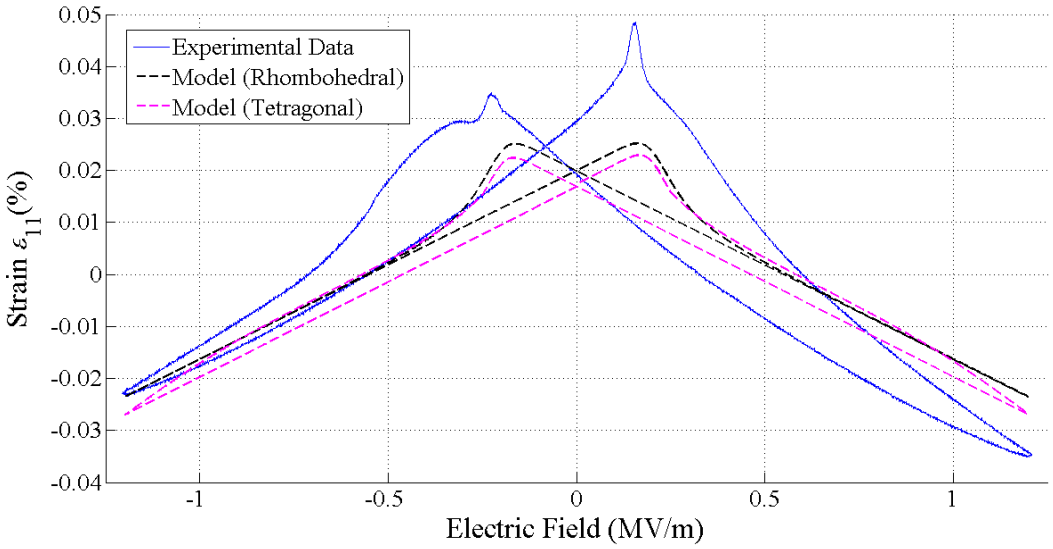

Figure 3.5: Model vs. experiment: Strain (ε_{11}) perpendicular to the electric field direction.

3.3. Effect of modelling parameters

The rate exponent (q) and rate constant (c) in equation 3.13 control the rate of transformation of volume fraction once the switching criterion is satisfied and allow fitting the characteristic shape and slope of the dielectric hysteresis loop into the model. The effect of variation of q, c and r can be seen from figures 3.6, 3.7 and 3.8. All other parameters are held at the values in table 3.1.

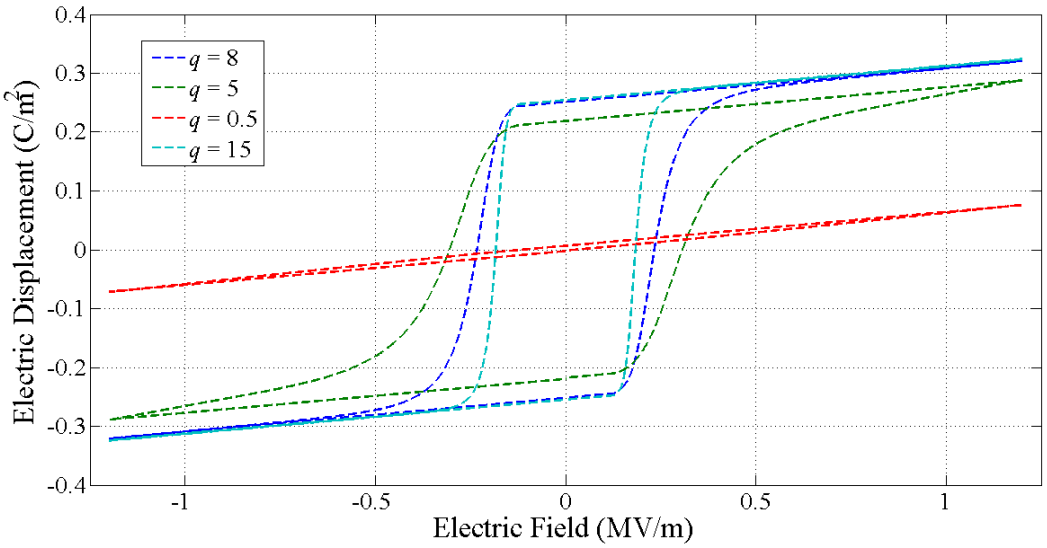

Figure 3.6: Effect of rate exponent (q) on the shape of the dielectric hysteresis loop.

As can be seen from figure 3.6, with a high value of q the hysteresis is similar to the time independent case where the entire switching event happens at a single value of electric field, giving approximately a box-shaped hysteresis loop (cyan curve). As $q \rightarrow 0$, the transformation rate becomes low and behaviour close to linear dielectric response is recovered (green and red curve). For intermediate values, the rate of transformation and hence, the slope of the straight lines in a dielectric hysteresis, is controlled by q.

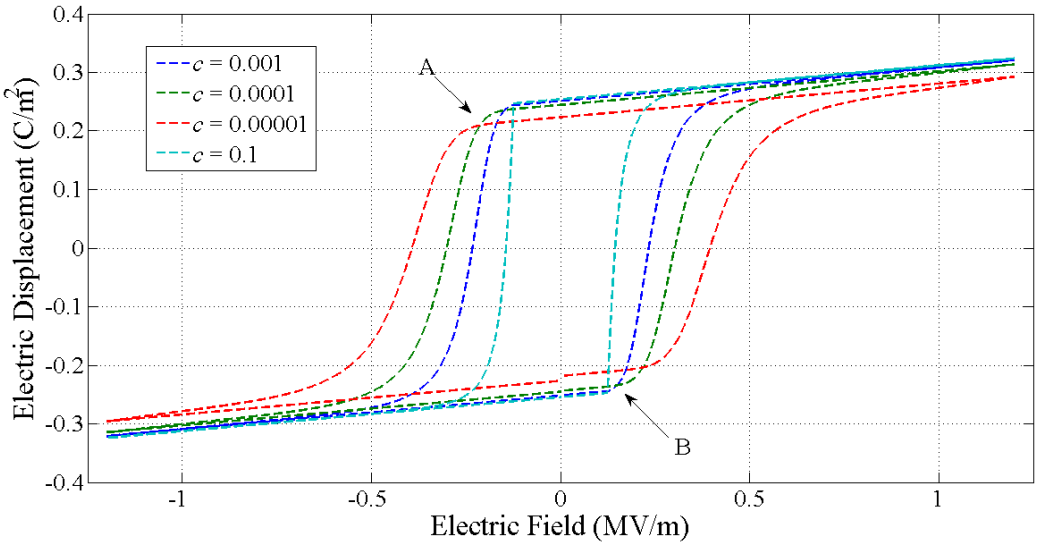

Figure 3.7: Effect of rate constant (c) on the shape of the dielectric hysteresis loop.

For low values of the rate constant (c), shoulders of the hysteresis curve (points A and B) show lesser curvature suggesting that switching is spread over a wider range of electric field (red and green curve in figure 3.7). For high c values, a box shaped dielectric hysteresis is observed suggesting a quick switching process (cyan curve). The characteristic shape of the dielectric hysteresis is controlled by rate constant c.

Saturation characteristics are controlled by the saturation index (r), which decreases the volume fraction transfer rate as the transferring volume fraction of the depleted variant approaches zero. The effect of variation of r can be seen from the onset of saturation. For high values of r, the hysteresis loop closes at lower electric field values and vice versa (figure 3.8).

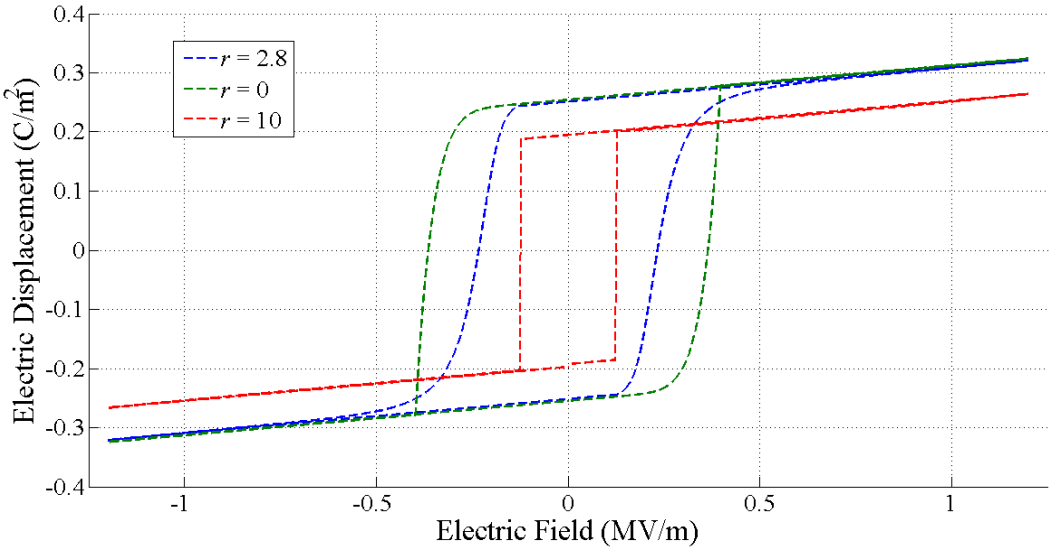

Figure 3.8: Effect of saturation index (r) on the shape of the dielectric hysteresis loop.

A combination of all these parameters gave good control over the dielectric hysteresis, and an adequate, though imprecise butterfly hysteresis. The difficulty of obtaining an accurate strain hysteresis loop after fitting the dielectric hysteresis loop highlights the complexity of ferroelectric behaviour, and the more general problem of obtaining an accurate constitutive description using a micromechanical approach. This is not merely an issue concerning the number of fitting parameters, as the way that switching of polarization and strain occur is intrinsically coupled by the switching systems in the micromechanical model. The problem of how to obtain data for accurate fitting of micromechanical models is an area of current research of interest to those applying the method to device modelling [97]. However, for qualitative interpretation of the experimental data of chapter 2, the quality of fit obtained here is sufficient.

As domain wall motion is thermally activated, the coercive electric field is also temperature dependent. The rate parameters, q and c, could be modelled as functions of temperature. Belov and Kreher [102] argue that thermal activation which could be described by Arrhenius equation is equivalent to power-law type relationship. Liu and

Huber [100] measured time dependence of remnant polarization on electric field and proposed such power-law relationship with a high power law index.

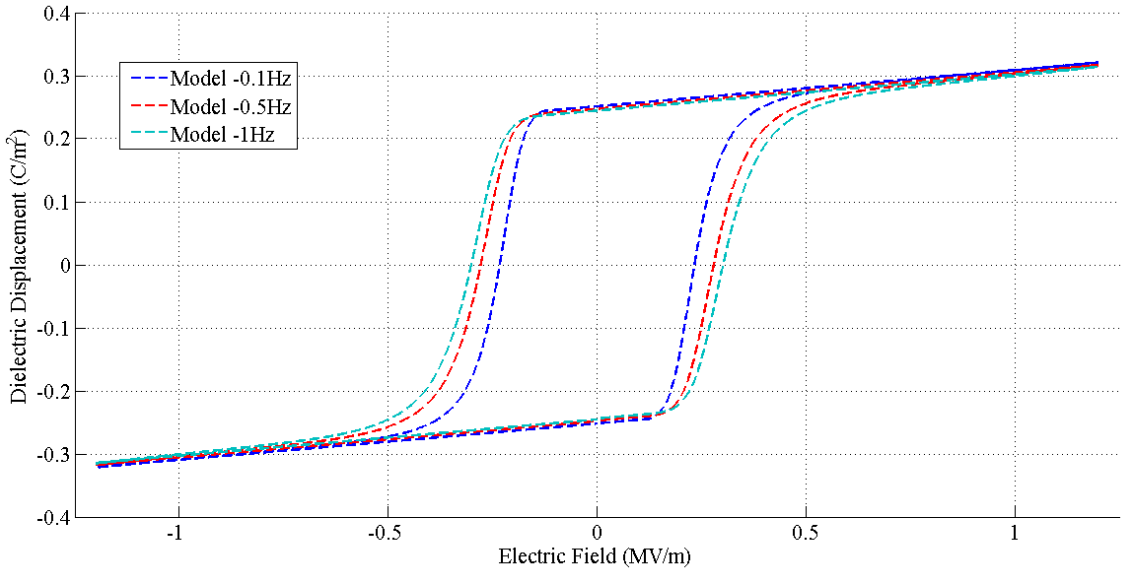

Figure 3.9: Effect of frequency on hysteresis loop (model).

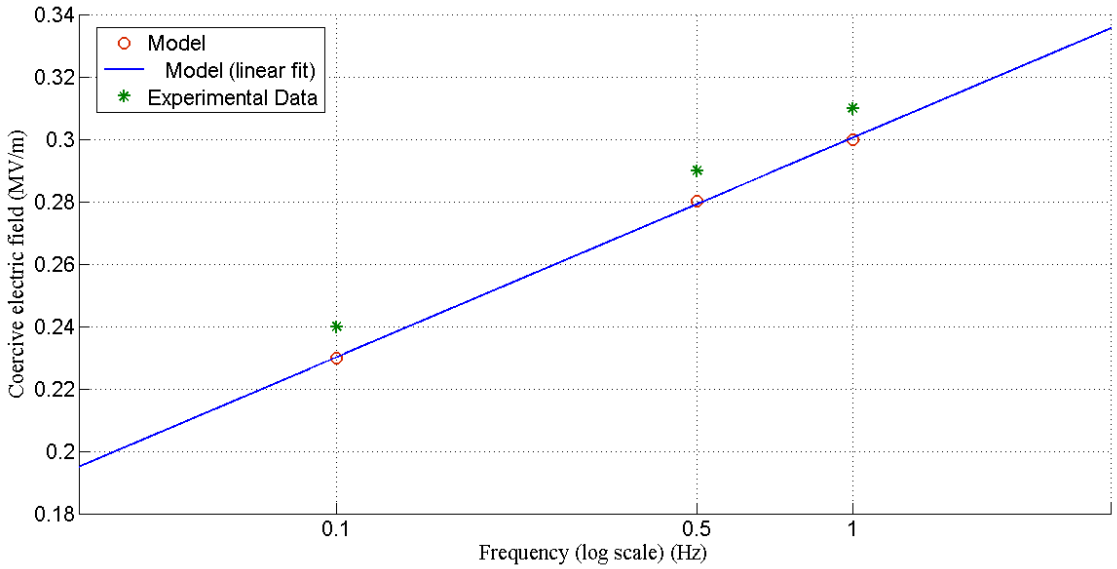

Figure 3.10: Comparison between model and experimental data.

Frequency of the applied electric field also has an effect on the hysteresis loop simulations as this is rate dependent model. This frequency dependence is explored as shown in figure 3.9. The coercive electric field increases slightly with the frequency of applied electric field and comparison of the model response with experimental data

(figure 3.10) shows a satisfactory agreement. In the next section, simulations of polarization rotation test are explained. Frequency of the applied electric field used in these simulations is 0.1 Hz which is same as the frequency during experimental measurements (section 2.6.3).

3.4. Simulation of the polarization rotation test

For simulating the polarization rotation test, a monotonically increasing electric field of peak amplitude e (e = 1.2MVm^{-1}) is applied in the direction $\hat{\mathbf{E}}$ = [sinθ, 0, cosθ]. For the first step, θ = 0°, which gives electric field, $\mathbf{E}_a$, parallel to the [0 0 1] direction. In the second step, an electric field, $\mathbf{E}_b$, is applied at angle θ to the initial poling direction, with θ varying between 0° and 180° in steps of 15°. Figure 3.11 shows the electrical loading in both the steps with respect to the crystallographic axes in tetragonal and rhombohedral unit cells.

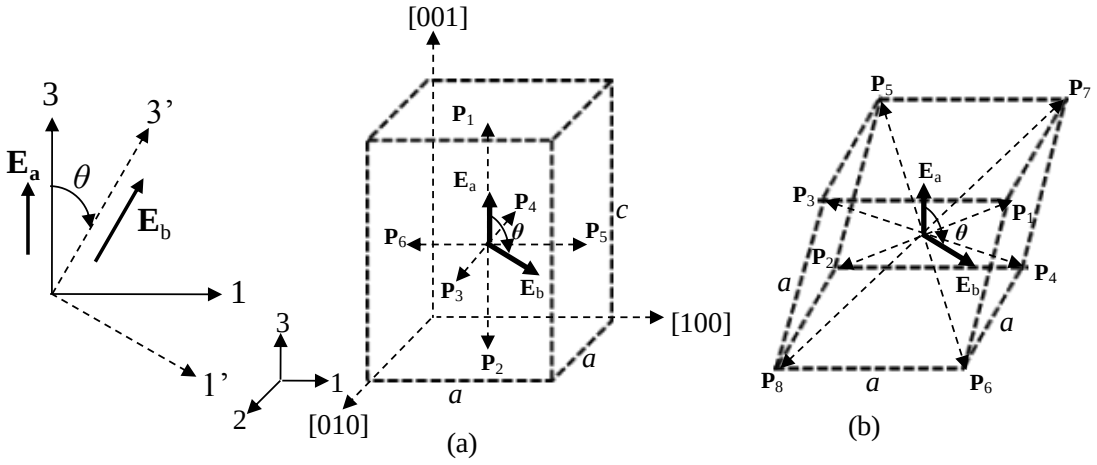

Figure 3.11: Loading path for electric field in step 1 ($\mathbf{E}_a$) and after rotation by angle θ with respect to initial polarization direction ($\mathbf{E}_b$).

The electric displacement is calculated following equation 3.15 and 3.21. The change in remnant strain in the direction of electric field (ε_{33}) is given by equation 3.22. Change in the remnant strain perpendicular to the direction of electric field (ε_{11}) can be written as,

$$\varepsilon_{11} = [-\cos\theta \quad 0 \quad \sin\theta] \cdot (\boldsymbol{\varepsilon}^{\mathbf{r}} \cdot [-\cos\theta \quad 0 \quad \sin\theta]) . \tag{3.24}$$

3.5. Results and discussion

3.5.1. Change in dielectric displacement: Model vs. Experiment

Figure 3.12 and 3.13 show the comparison between the experimental data and model predictions of tetragonal and rhombohedral system respectively. The change in dielectric displacement is plotted against the applied electric field. For clarity, only the dielectric response in steps of 45° is shown first.

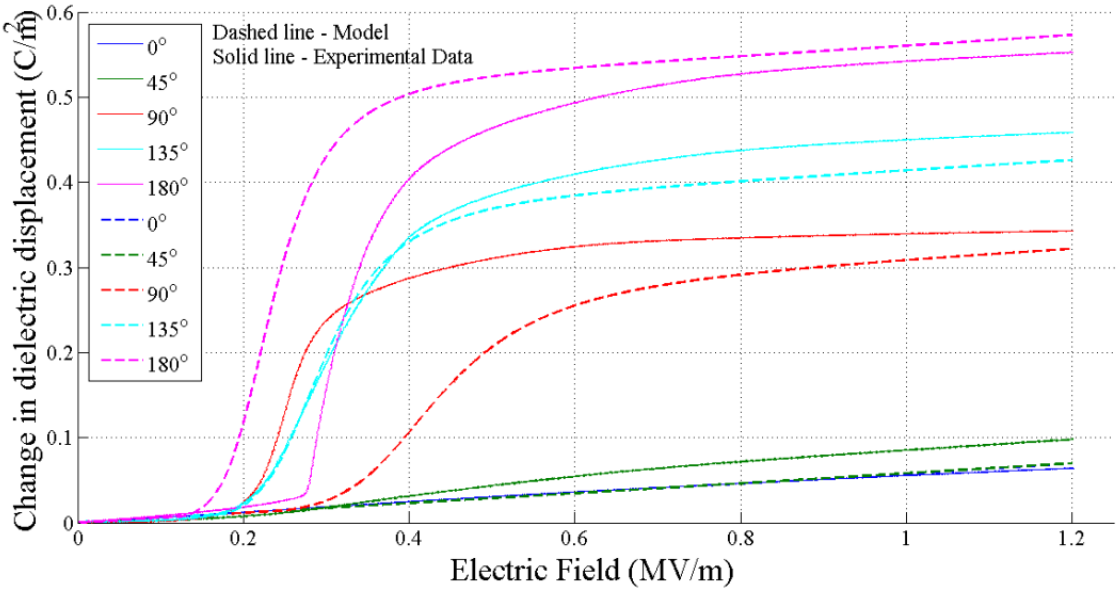

Figure 3.12: Model vs. Experiment: Dielectric response - tetragonal system.

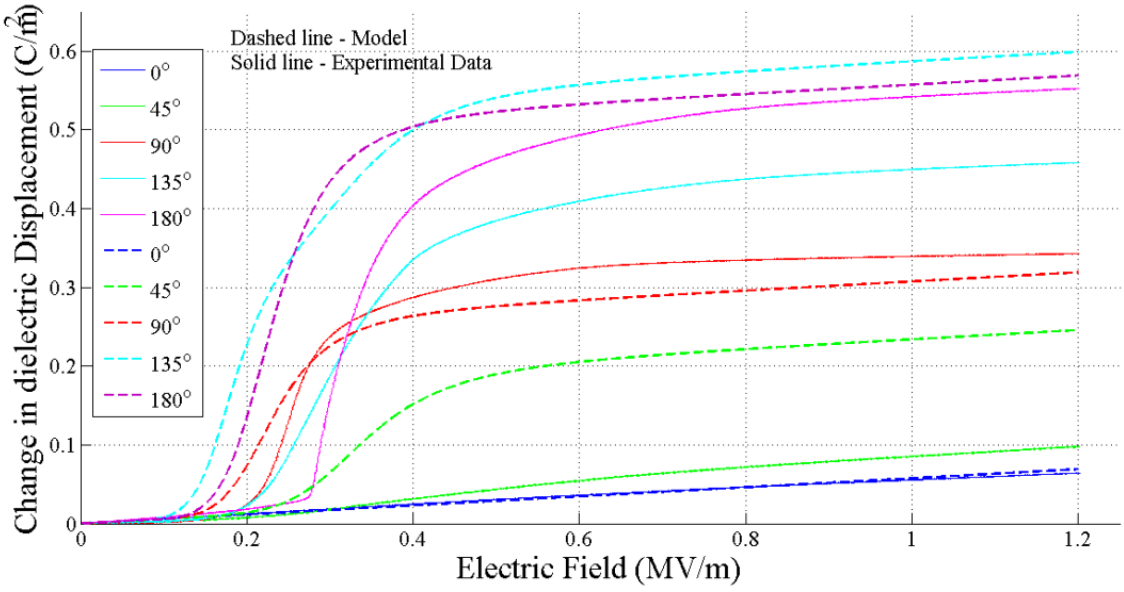

Figure 3.13: Model vs. Experiment: Dielectric response - rhombohedral system.

For both the crystal systems, the simulated results show qualitatively similar trends as seen in the experimental data. An increase in extent of polarization reorientation with increasing misalignment of the electric field (i.e. increasing θ value) can be observed in the model responses, similar to the measured data. The onset of switching and the rate of switching are in reasonable agreement for most of the curves. Note that the dielectric contribution in the model is calculated using the same dielectric constant (K) for all angles (i.e. neglecting anisotropy), whereas noticeable variation in the dielectric effect with the poling angle (θ) is found in the experimental data (figure 2.22 in section 2.6.3).

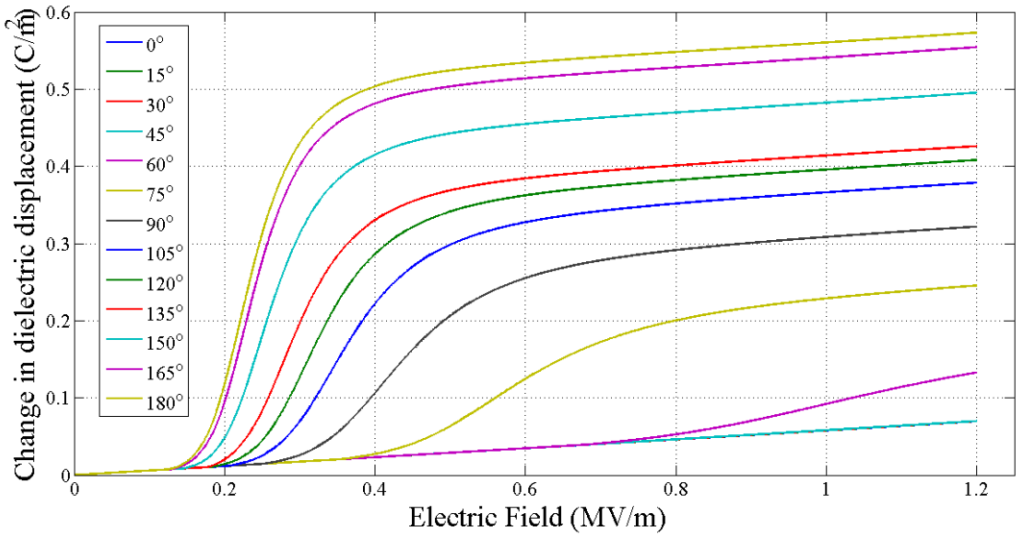

Figure 3.14: Dielectric response in the polarization rotation test (tetragonal model).

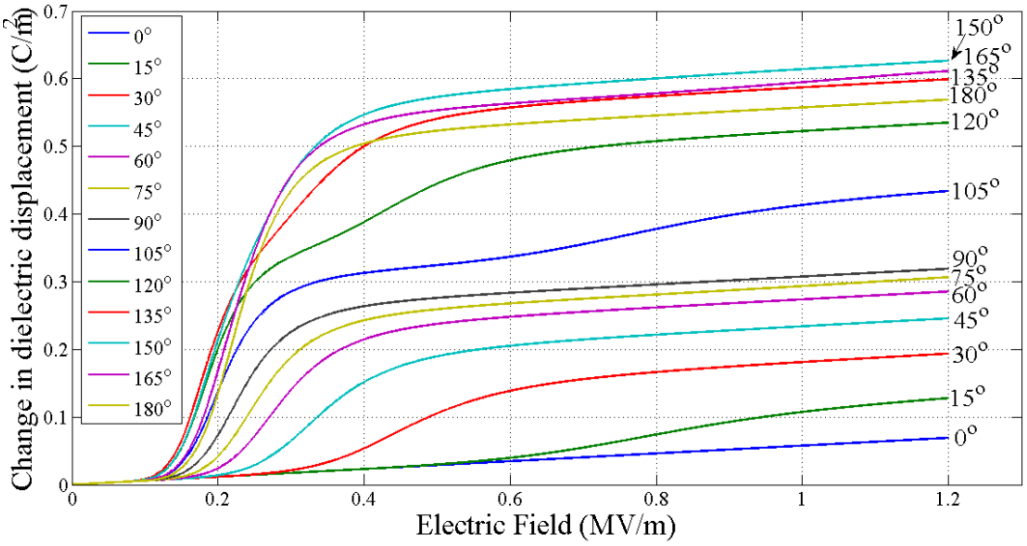

Figure 3.15: Dielectric response in the polarization rotation test (rhombohedral model).

A full set of simulated results are shown in figure 3.14 and 3.15 for tetragonal and rhombohedral system respectively. In the tetragonal system, the maximum dielectric displacement (180° curve) is 0.5731 Cm^{-2} which is in reasonable agreement with the experimental value of 0.5522 Cm^{-2}, while for other angles the change in dielectric displacement increases as expected. It is interesting to note that in the rhombohedral system, the maximum dielectric displacement (= 0.6264 Cm^{-2}) is predicted for θ = 150°. In fact, the maximum dielectric displacement for 135°, 165° and 150° cases are greater than 180° case. The maximum dielectric displacement of 0.5689 Cm^{-2} predicted for a 180° curve is very close to the values obtained in both the experimental data and the tetragonal model. The rhombohedral model thus predicts a greater change in dielectric displacement for angles between 135° and 180°. It can also be noted that the rhombohedral curve for 120° shows slight inflection between 0.2 to 0.5 MVm^{-1} suggesting a sudden switching event. Some of the experimental curves (for example, 165° curve in figure 2.20) show similar inflections. Further discussion of the model predictions against experimental observations follows, a saturation curve comparison aided by analysis of volume fraction changes.

3.5.2. Saturation curve comparison

Figure 3.16 shows the modelling curves (tetragonal and rhombohedral), experimental curve, isotropic saturation curve and an "average" curve obtained by assuming equal contribution of tetragonal and rhombohedral phases. The experimental and isotropic saturation curves are the same as in figure 2.23, obtained as explained in section 2.6.4 in Chapter 2. All the data has been corrected for the dielectric effect and the maximum change in remnant polarization is plotted against the poling angle θ. Maximum change in the remnant polarization refers to the end of the second step of electric loading ($\mathbf{E}_b$).

Let us first consider the tetragonal model response. Figure 3.17 shows the changes in volume fraction in the tetragonal model with increasing electric field magnitude E_b at various angles θ with respect to the initial polarization.

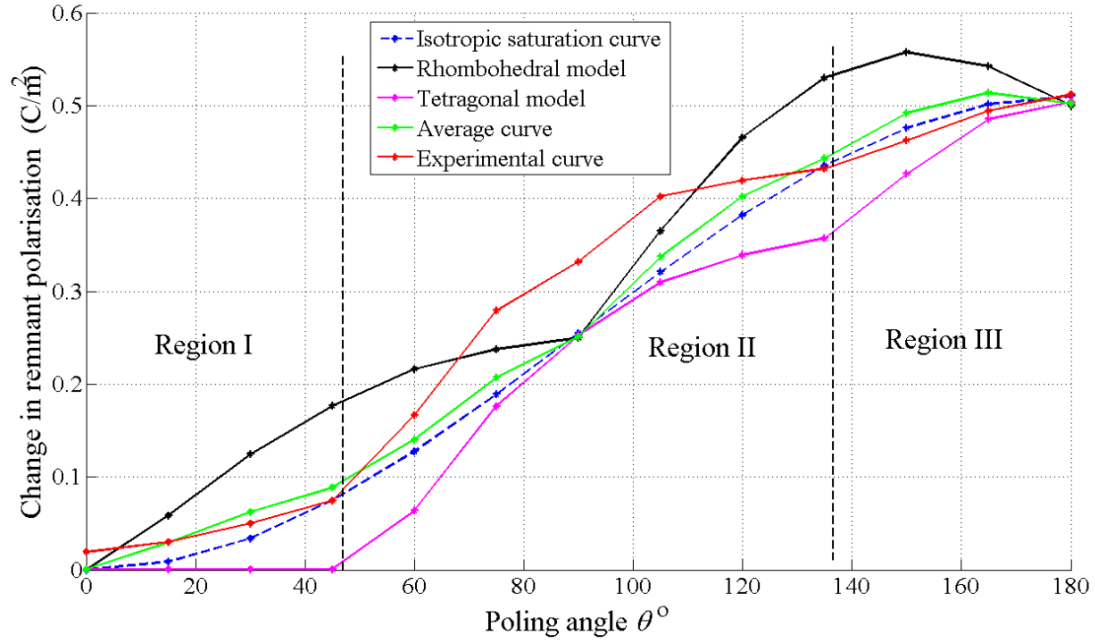

Figure 3.16: Comparison between the isotropic saturation curve, simulations for tetragonal model and rhombohedral model, an "average curve" obtained by assuming equal contribution of tetragonal and rhombohedral phases and experimental data.

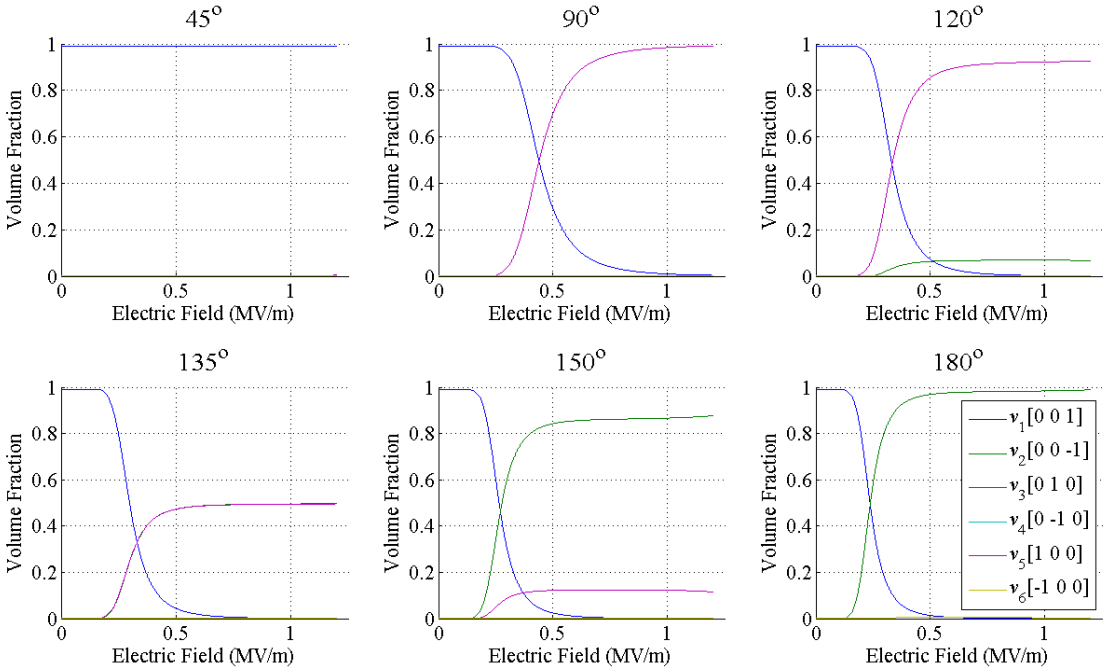

Figure 3.17: Changes in volume fraction (v_1 to v_6) for selected angles (tetragonal system).

At the end of the first step of electric loading, $\mathbf{E}_a$, the polarization is almost completely switched in the direction of electric field, $\mathbf{P}_r \parallel \mathbf{P}_1$ and the corresponding volume fraction $v_1 = 0.98$ and $v_i \approx 0$ for $i \neq 1$. The magnitude of the remnant polarization is 0.25 Cm^{-2} which close to that measured in the experiments.

Region I (0°- 45°): As can be seen from figure 3.16, there is very little increase in the remnant polarization. For example, the change in the remnant polarization is 0.0007 Cm^{-2} for the 30° case. This is also evident from the volume fraction change curve for 45° which shows that volume fractions remain unchanged during the second step of the polarization rotation test. The slight increase in polarization is due to the switching of variants 2 to 6 to the variant 1 such that $v_1 \approx 0.99$. In the experiments, comparatively greater values of remnant polarization are obtained in this region. This may be because in the initial poling operation a small amount of reversal of polarization might be taking place during unloading. Then in the second step, during reloading, some forward switching can happen. Also, in the model, almost a full saturation of switching is assumed at the end of first step ($v_1 = 0.98$) which seems not to be the case in the experiments.

Region II (45° - 135°): For $45° < \theta < 90°$, the 90° switching system ($v_1 \rightarrow v_5$) is operative and an increase in remnant polarization due to switching can be observed. For $\theta = 90°$, the electric field, $\mathbf{E}_b$, is parallel to the polarization vector of the crystal variant 5 ($\mathbf{P}_5$) and 90° switching causes volume fraction v_1 to completely transfer to v_5 ($v_5 = 0.99$) (see 90° case in figure 3.17). The maximum change in remnant polarization is 0.25 Cm^{-2} for the 90° case which is the same as the isotropic saturation case. For $\theta > 90°$, the 180° switching system ($v_1 \rightarrow v_2$) also becomes active and volume fraction starts transferring to v_2 along with v_5; however the 90° switching system ($v_1 \rightarrow v_5$) dominates the response till 135°. The volume fraction change for $\theta = 135°$ shows an equal volume fraction for v_2 and

v_5 ($v_2 \approx v_5 \approx 0.5$, see 135° case in figure 3.17). This is expected as the electric field is misaligned with respect to both $\mathbf{P}_2$ and $\mathbf{P}_5$ by the same amount. Thus, the 90° and 180° switching systems become active giving a change in remnant polarization that shows similar trends as that of the experimental data. Quantitatively, greater values of the maximum change in remnant polarization are attained in the experiments. This suggests that PMN-PT is strongly polarisable in certain directions. Another reason is that the noticeable variations in the dielectric effect due to anisotropy in single crystals are not accounted for in the model.

Region III (135° - 180°): As θ increases above 135°, the 180° switching system ($v_1 \rightarrow v_2$), dominates the switching process giving greater values of remnant polarization. This is evident from the volume fraction change for θ = 150° in figure 3.17. A full 180° switching takes place for θ = 180° as polarization $\mathbf{P}_r \parallel \mathbf{P}_2$ and the corresponding volume fraction v_2 = 0.98 and $v_i \approx 0$ for $i \neq 2$. For θ = 180°, the maximum change in remnant polarization = 0.5 Cm^{-2} which is in good agreement with the experimental data.

Overall, the tetragonal model predicts lesser remnant polarization for all the angles in comparison with the experimental data. One of the possible reasons is that there are relatively few switching systems to facilitate the polarization reorientation. Qualitatively, the model response and the experimental behaviour show similar trends.

Next, we will focus on the rhombohedral model response. Figure 3.18 shows the changes in volume fraction in the rhombohedral model with increasing electric field magnitude E_b at various angles θ with respect to the initial polarization. Contrary to the tetragonal model, at the end of first step, the remnant polarization is approximately evenly distributed along $\mathbf{P}_1$, $\mathbf{P}_3$, $\mathbf{P}_5$ and $\mathbf{P}_7$ with the corresponding volume fractions $v_1 \approx v_3 \approx v_5 \approx v_7 \approx 0.25$. The magnitude of the remnant polarization is 0.25 Cm^{-2} which matches the experimental data and tetragonal model. Now, the electric field applied at various angles

to $\mathbf{P}_r$ is an engineered domain configuration set up similar to the one explained in section 1.4.1 in chapter 1.

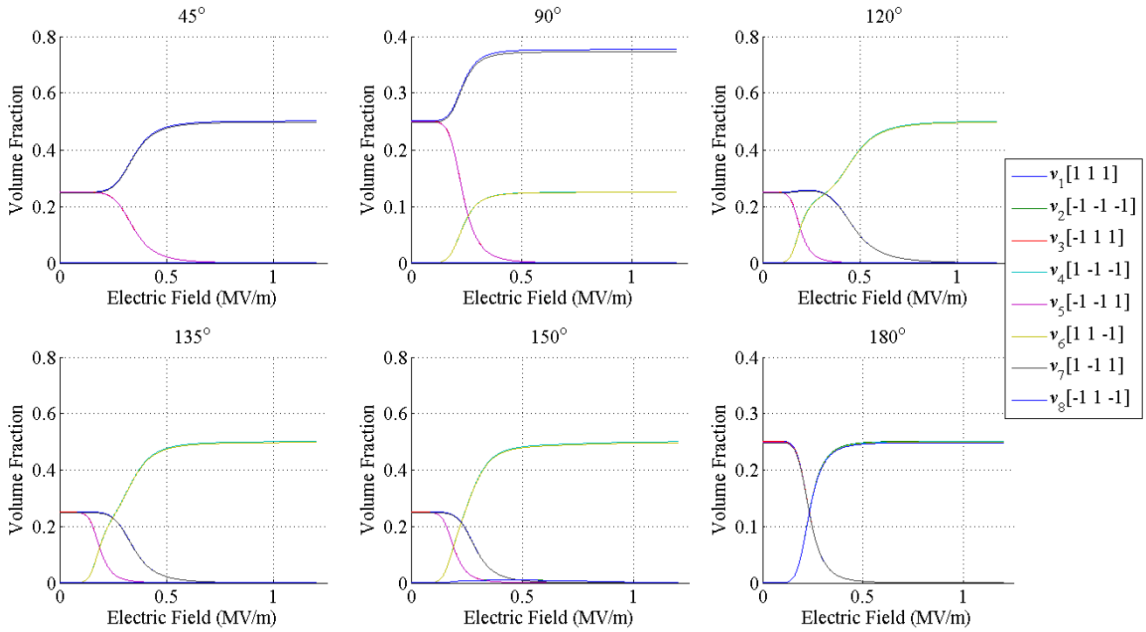

Figure 3.18: Changes in volume fraction for selected angles (rhombohedral system).

Region I (0°- 45°): As can be seen from figure 3.16, a change in remnant polarization due to switching is observed in this region. Four switching systems comprising of two distinct 71° ($\mathbf{P}_3 \rightarrow \mathbf{P}_1$ and $\mathbf{P}_5 \rightarrow \mathbf{P}_7$) and 109° ($\mathbf{P}_3 \rightarrow \mathbf{P}_7$ and $\mathbf{P}_5 \rightarrow \mathbf{P}_1$) switching systems become active as θ increases from 0° to 45°. For θ = 45°, volume fractions for $\mathbf{P}_1$ and $\mathbf{P}_7$ are almost equal ($v_1 \approx v_7 \approx 0.5$) as can be seen from the volume fraction changes in figure 3.18. The magnitudes of maximum change in remnant polarization predicted are considerably greater than those measured in the experiments, for example in the 45° case, 0.1766 Cm^{-2} is predicted by the model as against 0.0989 Cm^{-2} measured in the experiments. So, while the tetragonal model does not show any polarization reorientation in this region, the rhombohedral model gives an overestimated response when compared with the experimental measurements.

Region II (45° - 135°): As θ increases above 45°, in addition to the existing four switching systems that were active in region I, another four switching systems are

activated. Additional switching systems comprising of two distinct 180° ($\mathbf{P}_3 \rightarrow \mathbf{P}_4$ and $\mathbf{P}_5 \rightarrow \mathbf{P}_6$) and two more 109° ($\mathbf{P}_3 \rightarrow \mathbf{P}_6$ and $\mathbf{P}_5 \rightarrow \mathbf{P}_4$) switching systems become active. For $\theta = 90°$, volume fractions are $v_1 \approx v_7 \approx 0.37$ and $v_2 \approx v_4 \approx 0.12$ as can be seen from figure 3.18. A maximum change in remnant polarization = 0.25 Cm^{-2} is predicted. Though $\mathbf{P}_1$, $\mathbf{P}_4$, $\mathbf{P}_6$ and $\mathbf{P}_7$ are oriented symmetrically with respect to the direction of electric field for $\theta = 90°$, volume fractions v_1, v_2, v_4 and v_7 are not equal as at the end of the first step, $v_1 \approx v_7 \approx 0.25$ while $v_2 \approx v_4 \approx 0$.

As $\theta > 90°$, eight distinct switching systems are active as follows: two 71° ($\mathbf{P}_1 \rightarrow \mathbf{P}_6$ and $\mathbf{P}_7 \rightarrow \mathbf{P}_4$), four 109° ($\mathbf{P}_1 \rightarrow \mathbf{P}_4$, $\mathbf{P}_3 \rightarrow \mathbf{P}_6$, $\mathbf{P}_5 \rightarrow \mathbf{P}_4$ and $\mathbf{P}_7 \rightarrow \mathbf{P}_6$) and two 180° ($\mathbf{P}_3 \rightarrow \mathbf{P}_4$ and $\mathbf{P}_5 \rightarrow \mathbf{P}_6$). These switching systems facilitate volume fraction transfers from v_1, v_3, v_5 and v_7 to v_4 and v_6 such that $v_4 \approx v_6 \approx 0.5$ as can be seen from figure 3.18 for 120° and 135° case. The maximum change in remnant polarization attained increases due to the existence of multiple switching systems. Except for values of θ close to 90°, the magnitudes of maximum change in remnant polarization predicted by the rhombohedral model are greater than the experiments and tetragonal model.

Region III (135° - 180°): As θ increases above 135°, in addition to the existing eight switching systems that were active for $\theta > 90°$, another eight switching systems are activated. The additional eight switching systems are two 71° ($\mathbf{P}_3 \rightarrow \mathbf{P}_8$ and $\mathbf{P}_5 \rightarrow \mathbf{P}_2$), four 109° ($\mathbf{P}_1 \rightarrow \mathbf{P}_8$, $\mathbf{P}_3 \rightarrow \mathbf{P}_2$, $\mathbf{P}_5 \rightarrow \mathbf{P}_8$ and $\mathbf{P}_7 \rightarrow \mathbf{P}_2$) and two 180° ($\mathbf{P}_1 \rightarrow \mathbf{P}_2$ and $\mathbf{P}_7 \rightarrow \mathbf{P}_8$). The availability of sixteen switching systems facilitates polarization reorientation and a maximum change in remnant polarization = 0.5573 Cm^{-2} is attained for the 150° case. For $\theta = 180°$, a complete reorientation of the polarization takes place with as volume fractions $v_2 \approx v_4 \approx v_6 \approx v_8 \approx 0.25$ and the polarization is distributed almost evenly in $\mathbf{P}_2$, $\mathbf{P}_4$, $\mathbf{P}_6$ and $\mathbf{P}_8$. This is evident from the volume fraction change curve for 180° in figure 3.18.

The Rhombohedral model predicts greater magnitudes of maximum change in the remnant polarization than experimental data for most of the angles. One of the reasons could be the availability of a large number of switching systems as the electric field becomes more skewed with respect to the initial polarization directions ($\mathbf{P}_1$, $\mathbf{P}_3$, $\mathbf{P}_5$ and $\mathbf{P}_7$). Also, for the 120° case, rhombohedral model shows inflection (figure 3.15) which can also be seen in the volume fraction change curve (figure 3.18). The reason for this is that for certain electric field values, several switching systems become active resulting in a sudden surge in the volume fraction transfer.

Thus, it can be inferred that the tetragonal and rhombohedral systems alone may not represent the switching behaviour of PMN-32PT in a polarization rotation test accurately. It can be noted that the choice of crystal system has a visible effect on the maximum change in remnant polarization due to difference in number of switching systems that become active. The experimental data gathered in this work cannot provide an estimate for the proportions of rhombohedral and tetragonal phases present at this particular composition. X-ray diffraction measurements may prove helpful for this purpose; however a simplistic approximation can be to assume an equal distribution of both the phases. This assumption gives the average curve in figure 3.16. Quantitatively, the average curve predicts the magnitudes of maximum change in remnant polarization that are comparable with the experimental data in regions I and III. In Region II, higher values of remnant polarization measured in the experiments could be due to the better polarizability of PMN-PT in certain directions and anisotropic behaviour of single crystals. The average curve also shows a good agreement with the isotropic saturation curve. The co-existence of multiple phases with distinct switching systems makes the simulation and interpretation of the experimental data challenging. Next, we turn to the strain response predicted by the models.

3.5.3. Strain

Figures 3.19 and 3.20 show the comparison between the strain response predicted by the models and the measured experimental data. As can be seen from figure 3.19 and 3.20, for the 0° and 180° cases, the simulated response of both the models qualitatively agree with the experimental data. This can be expected as very modest polarization reorientation takes place in the 0° case while 180° switching systems dominate for the 180° case. The 180° switching gives no change in the switching induced strain due to symmetry, however, the sign of piezoelectric effect changes during 180° domain switching. For the 45° and 135° case, the tetragonal model predicts a response which is in agreement with the experimental data. Some of the features of experimental data for ε_{33} - 135° curve such as trough around 0.3 MVm^{-1} also appear in the model response. On the other hand, the rhombohedral model predicts high strains for the 45° and 135° cases. As explained in section 3.5.2, a number of 71° and 109° switching systems are active in the case of 45° and 135° angles which can produce a greater polarization induced strain. For the 90° case, the rhombohedral model shows a reasonable agreement with the experimental data. This may be because additional 180° switching systems become active as $\theta > 45°$ in the rhombohedral system. On the other hand, the tetragonal model predicts a massively greater remnant strain which may be due to the 90° switching system that dominates the behaviour at this angle.

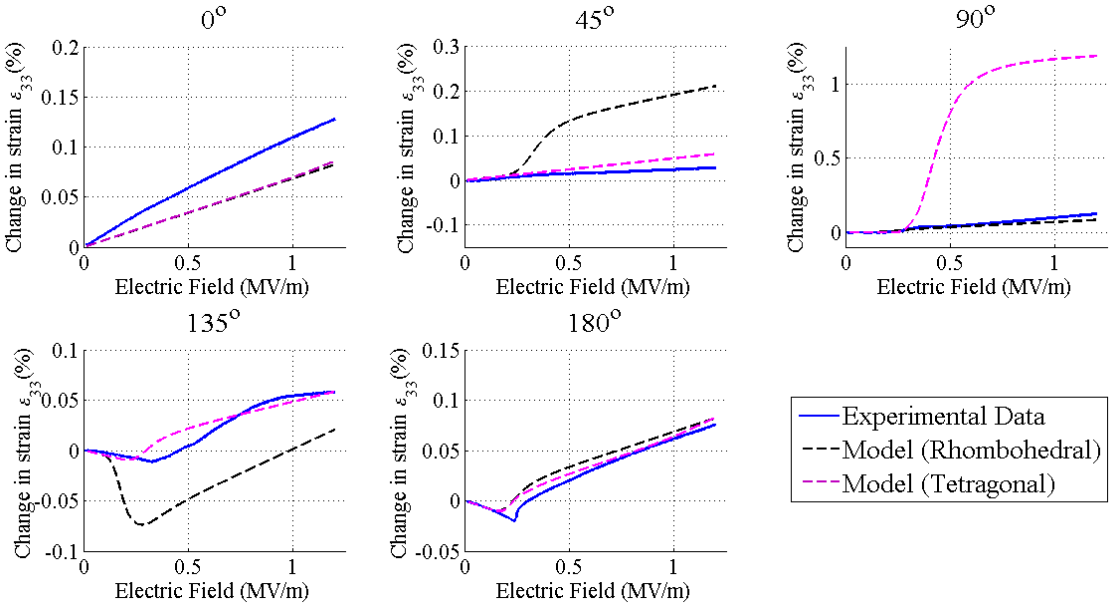

Figure 3.19: Change in strain ε_{33} for various angles.

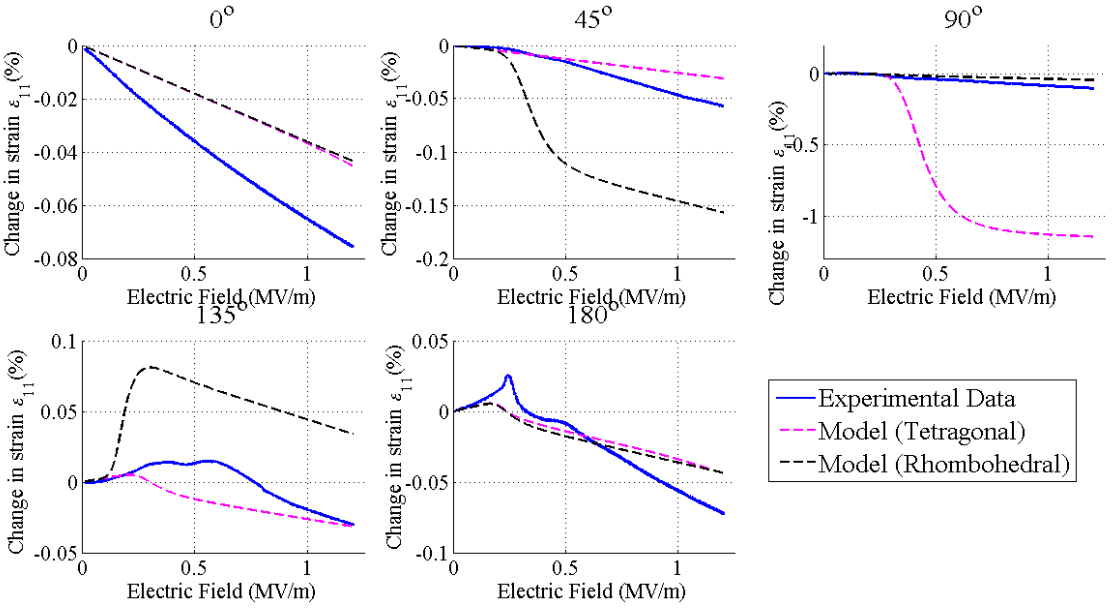

Figure 3.20: Change in strain ε_{11} for various angles.

From the model responses for θ = 90° in the tetragonal case and θ = 45° and 135° in rhombohedral case, it appears that greater strains are predicted when non-180° switching systems are active. Hence, it is of interest to further investigate the strain response of the model by allowing only 180° switching.

3.5.4. Model – Only 180° switching allowed

Maintaining the same the parameters as listed in Table 3.1, simulations were performed for both the crystal systems by allowing only 180° switching. Figure 3.21 and 3.22 shows the strain response predicted by the models when there is no change in remnant strain due to switching and the strain response is purely due to the piezoelectric effect.

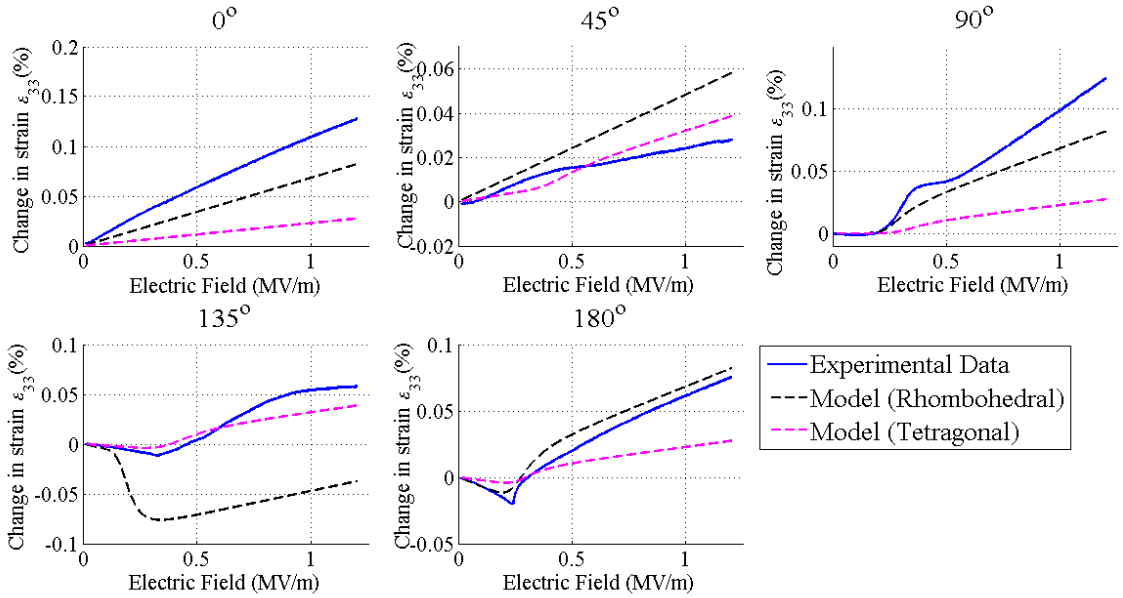

Figure 3.21: Change in strain ε_{33} for various angles (only 180° switching is allowed).

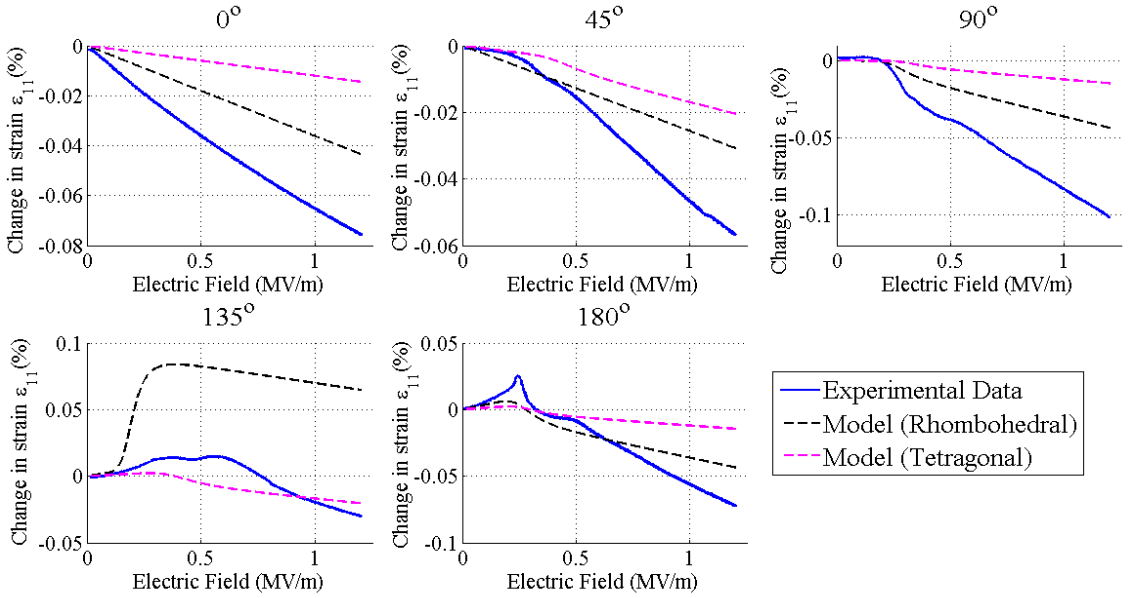

Figure 3.22: Change in strain ε_{11} for various angles (only 180° switching is allowed).

As only 180° switching is allowed, the change in remnant polarization (and hence in the dielectric displacement) due to switching is reduced compared to the previous results shown in figures 3.14, 3.15. However, here the main focus is to assess the effect of polarization switching induced strain. For convenience, the strain response obtained when all the switching systems are active (figure 3.19 and 3.20) is referred to as Case 1 whereas the present results (figure 3.21 and 3.22) with only 180° switching allowed is referred to as Case 2.

Before comparing the responses of case 1 and 2, it is important to note the effect of allowing only 180° switching on the distribution of volume fractions in the two crystal systems. For the tetragonal model in case 1, at the end of the first step of the polarization rotation test, crystal variant 1 almost reaches saturation ($v_1 \approx 0.98$) with the remnant polarization $P^r = 0.25$ Cm^{-2}. In the case 2, volume fractions do not reach the saturation level for any crystal variant due to the unavailability of non-180° switching systems (volume fraction distribution is $v_1 \approx 0.33$, $v_2 \approx 0$ and $v_i \approx 0.16$ for $i \neq 1, 2$). Hence, the remnant polarization attained is much lesser (0.08 Cm^{-2}) for case 2 compared to case 1. Further, in the second step of polarization rotation test, reorientation of the polarization is limited due to the lesser number of switching systems: maximum change in remnant polarization (ΔP^r) attained for the 180° case is 0.16 Cm^{-2} as against 0.5 Cm^{-2} for case 1. The effective piezoelectric coefficient computed using equation 3.20 is therefore reduced giving a lesser piezoelectric strain compared to case 1. However, for the rhombohedral model, the same level of remnant polarization is attained in case 1 and 2 at the end of the first step of the polarization rotation test. The polarization reorientation is limited but the change in remnant polarization (ΔP^r) for the 180° case is 0.5 Cm^{-2}, the same as that obtained in case 1. However, greater changes in remnant polarization for the 135°, 150° and 165° cases were not observed due to the low number of switching systems.

It is expected that for the 0° and 180° cases, the strain response in case 2 would be similar to case 1, as very little switching takes place for 0° whereas strain free 180° switching systems dominate the behaviour for 180°. This can be confirmed from the strain response in case 2 for θ = 0° and 180° which is in reasonable agreement with the experimental data. The Rhombohedral model response is unchanged for these angles in case 2. However, in the tetragonal model in case 2, it can be seen that lesser magnitudes of the change in strain are attained compared to case 1 due to the reasons explained above. When θ = 45° and 135° for the rhombohedral model the strain response is markedly lower compared to Case 1, for example the maximum change in strain ε_{33} attained for the 45° case is 0.05% compared to 0.21% in Case 1. A reasonable agreement between rhombohedral model and experiments suggests that during the experiments, strain response is mainly due to the piezoelectric effect rather than remnant straining. The strain response of the tetragonal model for these angles is qualitatively similar to the experimental data, with lesser magnitudes of the change in the strain compared to case 1.

In the tetragonal model, for θ =90°, the strain response in case 2 is significantly less than that observed in case 1 and is more consistent with experimental values. As very high strain vanishes with the constraint on switching systems, this further supports the idea that strain measured during the experiment is mainly due to the piezoelectric effect. For θ =90°, the strain response in the rhombohedral case remains unchanged from the Case 1.

Thus, when only 180° switching is allowed, a lesser strain response is observed for θ = 90° in the tetragonal system and for θ = 45° and 135° in the rhombohedral system. This suggests that the remnant strain due to switching through angles other than 180° exceeds that observed in the experiments and the strain measured in the experiments was mainly due to the piezoelectric effect. In summary, it can be said that though the tetragonal and

rhombohedral models predict a polarization response comparable with experimental data, strain responses for certain angles may be misleading. However, it is possible to use this model as a point model at each gauss point in a Finite Element (F.E.) simulation. Such F.E. simulation would enable modelling of components with distribution of stress as well as examining the effect of particular arrangements of domains or grains which may influence macroscopic response. Haug *et al*. [103] used a similar approach to validate self consistent approximations of ferroelectric polycrystal behaviour, and also showed that particular grain arrangements give rise to highly stressed grain boundaries in polycrystals.

3.6. Effect of domain configurations on switching

It is difficult to simultaneously predict an accurate polarization and strain response using the micromechanical approach because of the intrinsic coupling between the switching of polarization and strain by the switching systems. The strains were measured over a small area of the specimen in the experiments and the measurements are susceptible to the effects of local domain configurations. To illustrate this, consider a stack of two alternating types of 90° domains where each domain in the stack has a spontaneous polarization P_0, see figure 3.23(a).

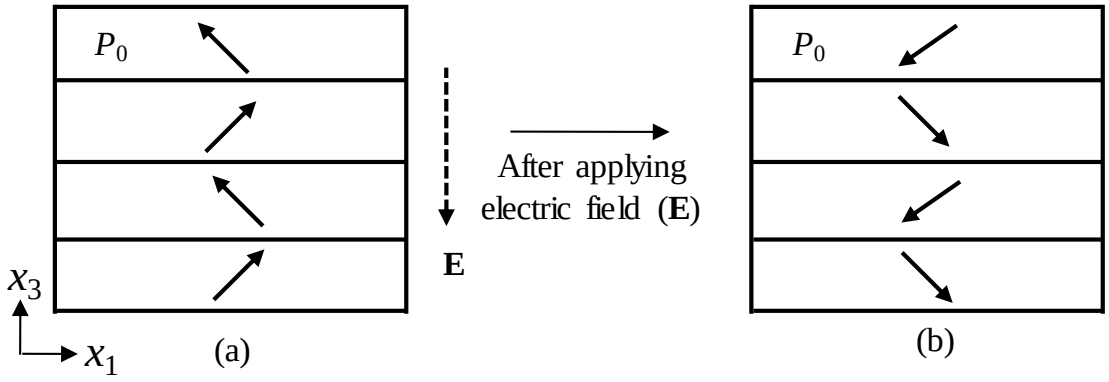

Figure 3.23: In the domain configuration as shown in (a), 90° switching within each domain results in 180° polarization reversal for the entire stack under the application of electric field (**E**) giving a domain configuration as shown in (b).

The average polarization, **P**, of the stack is parallel to the positive x_3 direction. Now, if an electric field (**E**) is applied in the negative x_3 direction, 90° polarization rotation can occur within each domain. This is possible by a mechanism such as nucleation of a transient 90° domain wall that is driven through the stack by the electric field [104,105]. The average polarization of the stack at the end of the switching (figure 3.23(b)) is parallel to the negative x_3 direction i.e. a polarization inversion can be observed due to a cooperative 90° switching in each domain. Thus, due to the specific domain arrangement, 90° switching in each domain produces 180° rotation of the average polarization. This switching process is accompanied with very small reversible and almost no irreversible deformations [104]. Thus, the detail of domain patterns can strongly influence switching. This brings into attention the limitations of using a micromechanical approach based only on volume fractions and also highlights the importance of imaging the local microstructural configurations for a better understanding of the switching process and allied macroscopic properties.

3.7. Conclusions

To assist the interpretation of a multi-axial polarization rotation test on PMN-PT single crystals, a rate dependent polarization switching model was developed based on the switching criterion given by Hwang *et al*. [88]. As there may be a co-existence of tetragonal and rhombohedral phases, both crystal systems were implemented independently in the model and calibrated against experimental dielectric hysteresis and butterfly hysteresis loops. Polarization rotation test simulations were carried out to model the polarization and strain response.

Qualitatively, the model response for both crystal systems shows some agreement with the experimental measurements. Further comparison was done with experimental and

isotropic saturation curves to assess each model's accuracy in predicting the total change in remnant polarization in the polarization rotation test. The tetragonal model showed generally lesser values of remnant polarization than measured experimentally. This may be due to the relatively small number of switching systems available in the tetragonal system. The rhombohedral model, by contrast, gives higher values of remnant polarization for almost all angles except for θ near to 90°. The behaviour of each model was explained by considering the volume fraction transfers and activated switching systems. An average response, obtained by assuming equal fractions of tetragonal and rhombohedral phases, matches closely with the experimental data for almost all angles except for θ near to 90°.

The change in strain predicted by the model was compared with the experimental data. It was found that the model massively overestimates the strain response when θ = 90° in the tetragonal system and θ = 45° or 135° in the rhombohedral system. This is due to the operation of 90°, 71° and 109° switching systems in the model, that are not activated in the experiment. The model was further adjusted to allow only 180° switching which does not produce any strain changes. A better agreement was then found between the predicted strain response and experimental measurements. Finally, the importance of understanding the local microstructural arrangements in giving the macroscopic response is highlighted. This motivates closer observation of domains to identify the mechanism of switching. In the next chapter, domain observations in single crystal Barium Titanate are discussed.

4. Domain observations in Barium Titanate single crystal

For understanding how domains of various types respond to externally applied loads, first it is necessary to develop suitable techniques to visualize the domains. In this chapter, the aim is to study and use various techniques for domain observations and compare them with respect to their usefulness for observing the domain evolution under electromechanical loading, preferably in-situ. Although several techniques are available, identifying a reliable, fast, convenient and non-destructive technique that can unambiguously distinguish between different domain types is a challenge. We focus on imaging the domain structure in single crystal Barium Titanate (BT).

The choice of Barium Titanate for microstructural observations was determined by the availability of suitable sizes of single crystals, ease of domain visualisation, measurements and interpretation. Also as single crystals are expensive, cost was a factor in deciding specimen sizes. Advantages of BT include transparent crystals with domains that can be readily seen using techniques such as optical microscopy and low coercive field, to allow use of moderate fields for studying domain evolution.

Section 4.1 describes the domain structure in BT. An overview of commonly used domain imaging techniques is presented in section 4.2. In the subsequent sections, domain observations in BT using optical microscopy, etching followed by optical microscopy, Scanning Electron Microscopy (SEM) and Atomic Force Microscopy

(SEM), synchrotron X-ray topography, and Piezoresponse Force Microscopy (PFM) are presented.

4.1. Microstructure in single crystal barium titanate

Barium Titanate has perovskite (ABO_3) type crystal structure as shown in figure 4.1. The central Ti^{4+} cation can occupy any of the six possible positions along the positive and negative direction of the crystallographic axes 1, 2, and 3 giving spontaneous polarization to the crystal [3].

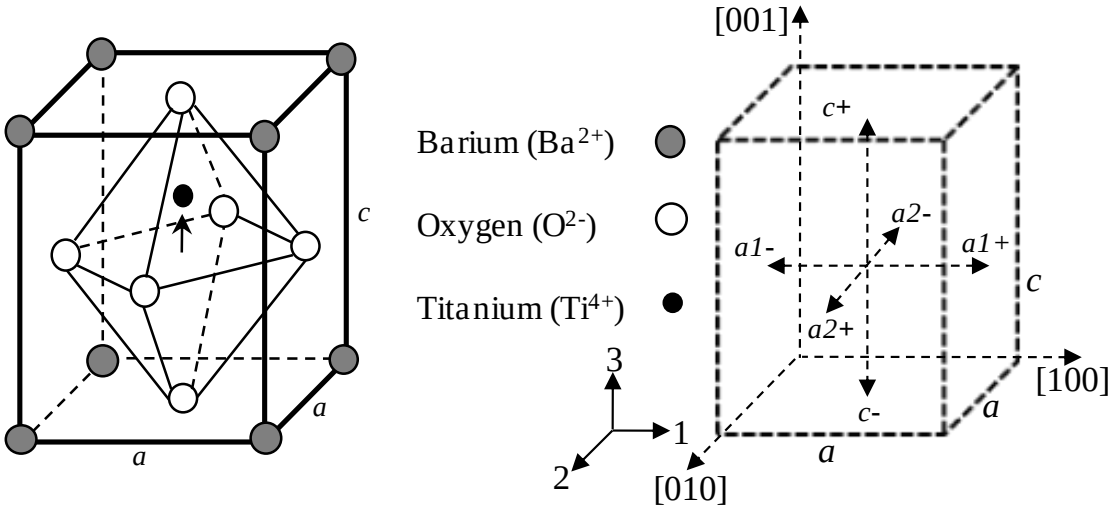

Figure 4.1: Crystal structure and different domain types based on position of central cation in BT single crystal at room temperature.

Each of these positions is associated with a spontaneous strain. In an [001] oriented sheet of BT single crystal, typically *a* domains and *c* domains are observed: In *a* domains, the polarization is parallel to the crystal surface while *c* domains have polarization perpendicular to the crystal surface [106] (figure 4.2(a)). Based on the six possible directions of polarization (positive and negative directions along the 1, 2 and 3 axes as shown in figure 4.1), there can be *c*+, *c*-, *a1*+, *a1*-, *a2*+, *a2*- domains (figure 4.2(b)). The arrangement of domains depends on electrical continuity and local compatibility of

strains, such that domain arrangements that minimize energy are more favourable. The low energy domain arrangement is referred to as a compatible arrangement of domains.

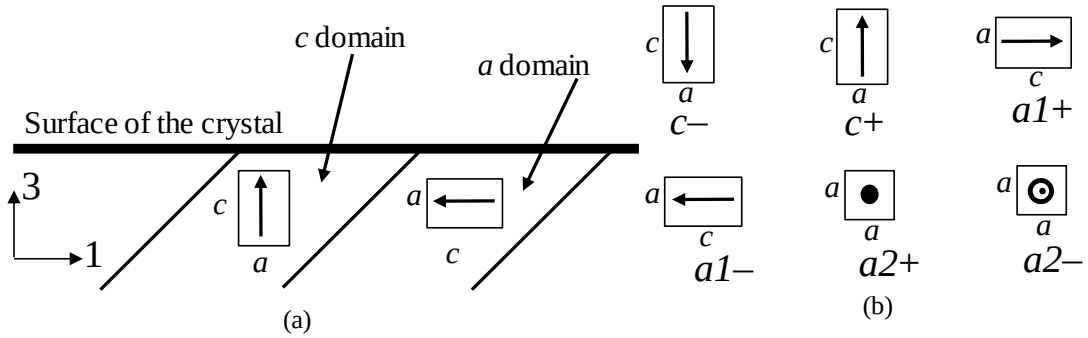

Figure 4.2: (a) *a* and *c* domains in single crystal Barium Titanate depending on the direction of polarization relative to the surface of the crystal (b) Types of domains based on six possible polarization directions.

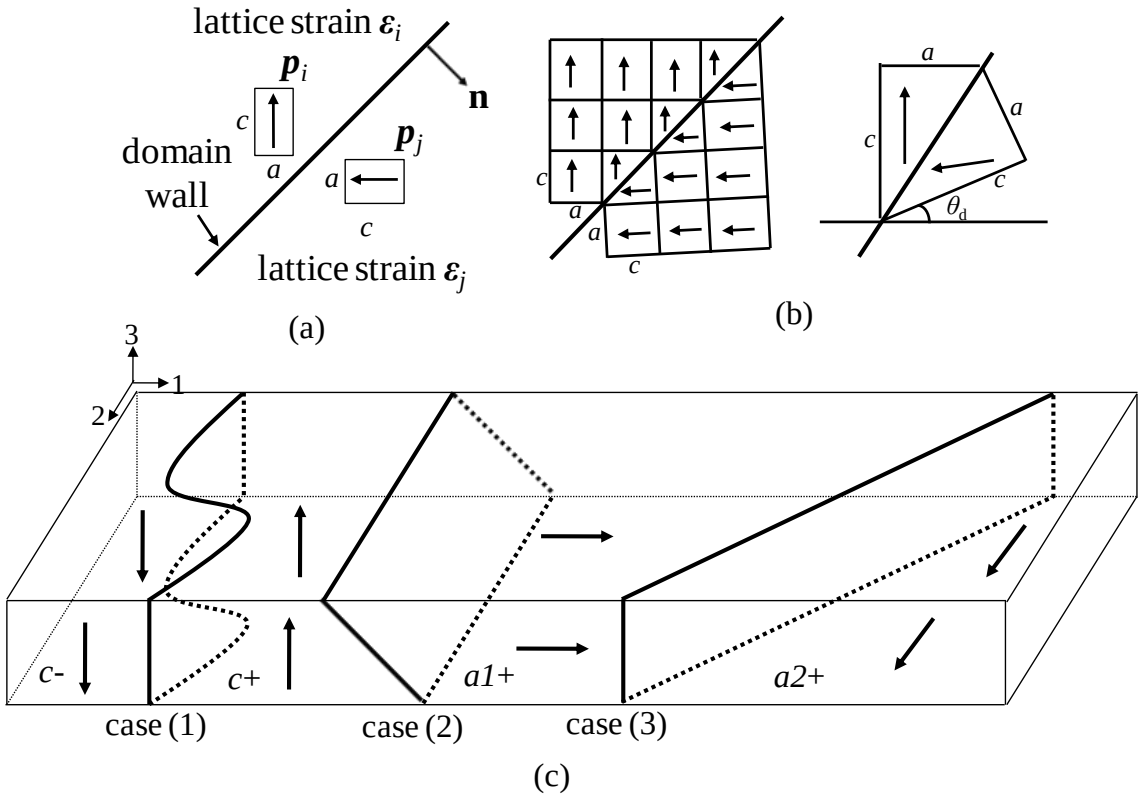

Figure 4.3: (a) Domain wall separating adjacent domains *i* and *j* need to satisfy compatibility equations for a low energy microstructure (b) low angle *a*-*c* tilt boundary (c) typical domain walls in tetragonal BT – case (1) 180° *c*-*c* domain wall, case (2) 90° *c*-*a* domain wall and case (3) 90° *a*-*a* domain wall.

Consider two adjacent domains *i* and *j* with strain states $\boldsymbol{\varepsilon}_i$, $\boldsymbol{\varepsilon}_j$ and polarization states $\mathbf{p}_i$, $\mathbf{p}_j$. The interface normal vector **n** of a compatible domain wall separating *i* and *j* (figure 4.3 (a)) must satisfy the compatibility equations 4.1 and 4.2 for some vector **a** [107]:

$$\boldsymbol{\varepsilon}_i - \boldsymbol{\varepsilon}_j = \frac{1}{2}\left(\mathbf{a} \otimes \mathbf{n} + \mathbf{n} \otimes \mathbf{a}\right) \tag{4.1}$$

$$\left(\mathbf{p}_i - \mathbf{p}_j\right).\mathbf{n} = 0 \tag{4.2}$$

For a stress free interface between two adjacent domains a simple compatibility criterion given by Liang *et al*. [108] can be stated as,

$$\det(\boldsymbol{\varepsilon}_i - \boldsymbol{\varepsilon}_j) = 0 \tag{4.3}$$

A domain wall has a particular orientation depending on the compatibility of the adjacent domain types. In the case of tetragonal BT, two domain wall types are observed, named 90° walls and 180° walls. The 90° wall refers to an arrangement in which the angle between the polarization directions in the adjacent domains is nearly 90° and for 180° wall, polarization directions in the adjacent domains are antiparallel. Figure 4.3(b) shows a 90° domain wall separating *a* and *c* domains. Due to the difference in lattice parameters, this domain wall is a low angle tilt boundary with a small tilt angle (θ_d) [16] which is given by equation 4.4. This tilt angle is useful for distinguishing between *a* and *c* domains by X-ray diffraction techniques.

$$\theta_d = \frac{\pi}{2} - 2\arctan\left(\frac{a}{c}\right) \tag{4.4}$$

Figure 4.3(c) shows typical domain wall orientations in single crystal BT. 180° domain walls do not have a particular habit plane and they commonly curve as shown in figure 4.3(c)-case(1) which is also referred to as “watermark” pattern [109]. A 90° domain wall is oriented along one of the {110} planes and appears as shown in case(2) for *c*-*a* type of arrangement and case(3) for *a*-*a* type of arrangement. The domain walls are very narrow, typically of the order of few nm or 4–10 unit cells [110].

4.2. Overview of domain imaging techniques

The various techniques used for domain observation can be classified based on their operating principle as: (1) Surface treatment techniques (surface decoration, etching) (2) Optical techniques (optical microscopy, polarized light microscopy, photorefractive methods) (3) Diffraction techniques (reflection and transmission measurements, anomalous dispersion, X-ray or neutron methods) (4) Electron microscopy techniques (scanning electron microscopy, transmission electron microscopy and related methods) (5) Scanning probe microscopy techniques (piezo-response force microscopy, electrostatic force microscopy). Each technique has distinct capability of resolving domain structure along with special specimen preparation or instrumentation requirements. A detailed discussion of several of these techniques can be found in the reviews of Soergel [111] , Potnis *et al*. [112] and Chapter 4 of the book by Tagantsev *et al*. [7]. Imaging of domains in a variety of single crystals has been an active area of research for more than 50 years. However, here the techniques are reviewed with a focus on imaging domains in BT single crystal and usefulness of the technique for in-situ domain observations where the domain types are unambiguously identified.

4.2.1. Surface Treatment Techniques

Early attempts to reveal ferroelectric domain structure exploited surface decoration methods that use colloidal solutions, liquid crystals, or other polar particles to produce contrast or colour suitably oriented domains or domain walls [113]. Evolution of microstructure could be observed, but this technique works best only for slow processes and requires a cleaved and polished crystal surface. Lateral resolution is limited by the choice of decorating medium, but resolution better than 1 μm is readily achieved.

A second type of surface treatment is etching the crystal surface using acids such as HF, HCl or HNO_3. In the case of BT, the etching rate is fastest at the positive end of a dipole which enables unambiguous identification of *c*+ and *c*- domains; whereas *a* domains get etched intermediate between *c*+ and *c*- domains [106]. The surface topography produced by etching can be observed using various methods such as optical microscopy [106], scanning electron microscopy [114] or atomic force microscopy [115]. DeVris and Burke [109] identified the domain types in etched polycrystalline and single crystal BT using optical and electron microscopy (figure 4.4). They argued that the microstructure in polycrystals is complex compared to single crystals due to constraints imposed by randomly oriented grains. Though etching enables rapid identification of domains with sub-micron resolution [111], it is a destructive technique, restricted to surfaces and does not allow in-situ observation of domain evolution. The technique also relies on identifying appropriate specimen preparation, etchant composition, and etching time.

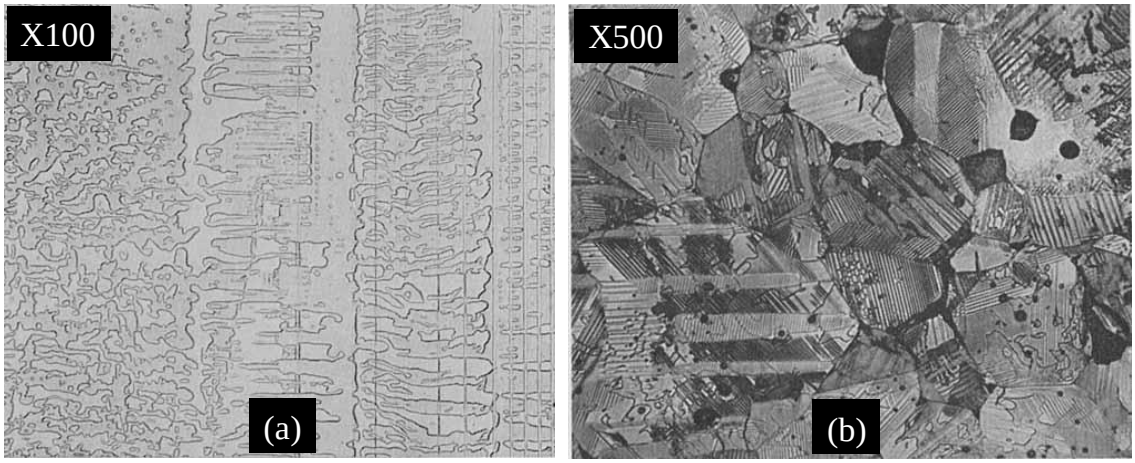

Figure 4.4: Etched domain pattern in (a) single crystal BT and (b) polycrystalline BT showing 90° and 180° domain walls (after DeVries and Burke, 1957 [109]).

4.2.2. Optical Techniques

Optical methods provide simple, non-contact, imaging and allow in-situ observation of domain evolution under thermal and electro-mechanical loads. Under the polarizing

microscope, *c* domains appear dark as the optical axis for the tetragonal phase is the *c*-axis whereas *a* domains appear bright [15,116]. Use of transmission polarized microscopy becomes complicated if the crystal has multiple domains through thickness. Forsbergh [17] conducted a systematic study of the domain patterns that are formed due to twinning in single crystal BT. Wedge shaped laminar domains and a "square-net" pattern of domains were observed under crossed polarizers (figure 4.5(a)) and underlying twinning mechanisms were discussed in detail. The growth and nucleation of the domains as a function of electric field and temperature was studied by Merz [15,117]. 90° and 180° domain walls were distinguished using polarized light and the domain wall width and wall energy was estimated. Polarized light microscopy has also been used for in-situ observation of domain evolution during phase transformation as a function of temperature [118]. Polarized light microscopy is fast and convenient, but can only differentiate between *a* and *c* domains and is not capable to distinguish between *c*+ and *c*-.

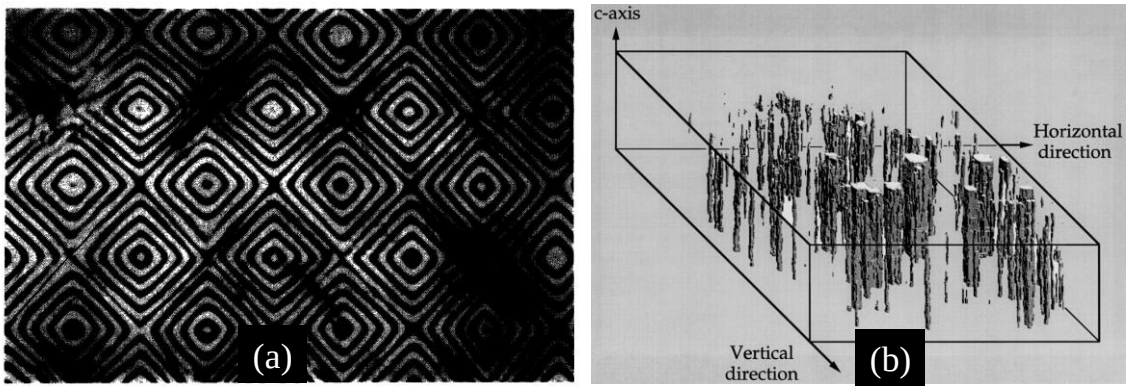

Figure 4.5: (a) Intersection of two groups of laminar domains forming a square-net pattern of domains in single crystal BT (after Forsbergh, 1949 [17]) (b) A 3-dimensional map of 180° domains in BT single crystals (Grubsky *et al.*, 1996 [119]).

A sophisticated birefringence imaging technique using rotating polarizers was developed by Glazer *et al.* [120] to automate the separation of birefringence magnitude and orientation data. Typical ferroelectrics have anisotropic dielectric permittivity, making

them suitable for this technique. The method was used to show twin structure in barium titanate during the cubic-tetragonal phase transition. The technique allows full field, rapid imaging of domains and has sensitivity to strains of the order of 10^{-7}, but is limited to transparent crystals. It also presents difficulty distinguishing surface from sub-surface structure, and resolution is typically limited to a few μm.

A 3-dimensional mapping of domain structure is possible by using a photorefractive beam-coupling method [119,121]. Here, the experimental set up consists of two beams of argon laser light: a probe beam propagating along the *c*-axis of the crystal, and a pump beam intersecting the probe beam in the crystal. As the probe beam travels through *c* domains, it either loses or gains energy depending on the domain orientation; providing contrast in the detected image. By scanning the position of the crystal across the pump beam, a 3-dimensional image is built up in slices as shown in figure 4.5(b). The spatial resolution was limited to about 7μm, by the pixel size of the CCD camera used. The technique looks promising for 3-D mapping but is limited only to 180° domain walls.

Second harmonic generation microscopy (SHGM) exploits the interference of second harmonic waves, produced by the difference in non-linear optical coefficients of antiparallel domains, to identify the domains present. SHGM has been used to image 90° domain walls and domains in BT [122].

4.2.3. X-ray Techniques

X-ray diffraction techniques can identify crystal structure and domain types in ferroelectrics. The underlying principle is the detection of the distinct lattice parameters: this can readily distinguish, for example, between *a* and *c* domains. However, where there is no change of lattice parameter, such as across a 180° domain wall, refinement of the technique is needed. Anomalous dispersion of X-rays causes a difference in the intensity

of reflections between antiparallel domains. This method was used by Niizeki and Hasegawa [123] to observe antiparallel 180° domains in BT single crystals. Park *et al*. [124] carried out white beam X-ray topography to observe the domains and strain fields. Ferroelectric domains in BT single crystals were observed by Fogarty *et al*. [125] in Laue geometry (transmission topography) and Bragg geometry (reflection topography) using a high resolution X-ray diffraction imaging with monochromatic light (figure 4.6). High flux due to the use of synchrotron X-ray source in these experiments enabled visualising the domains in transmission. Also, the large-area beam allowed imaging large specimen areas without multiple scans. This technique revealed domains in the interior of a 1 mm thick specimen with a spatial resolution of about 1 μm. X-ray transmission topography was also used by Caslavsky and Polcarova [126] for observing 90° domain walls in BT single crystal. The resolution achieved is limited by the detectors and the quality of the light source.

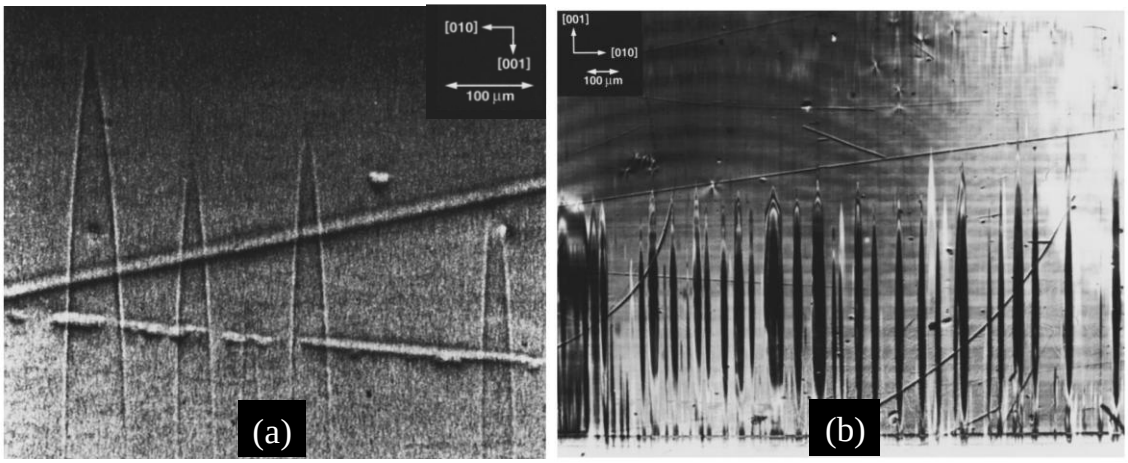

Fogarty G., Steiner B., Cronin-Golomb M., Laor U., Garrett M. H., Martin J., and Uhrin R., 1996, "Antiparallel ferroelectric domains in photorefractive barium titanate and strontium barium niobate observed by high-resolution x-ray diffraction imaging," Journal of the Optical Society of America B, 13(11), p. 2636.

Figure 4.6: Domains in BT observed in (a) Bragg geometry (402) and (b) Laue geometry (002) using 12 keV X-ray light.(after Fogarty *et al*., 1996 [125]).

Application of electric field produces deformations of opposite sign in the antiparallel domains due to the converse piezoelectric effect, increasing the contrast in Bragg reflections. The method has the potential to map *in-situ* domain evolution under

electromechanical loading and domain structure in Lithium Tantalate and Lithium Niobate has been studied in this way [127].

Neutron diffraction techniques have the advantage of penetrating the full specimen thickness and thus give statistical information about lattice spacing and orientation over the specimen volume. This has been used with in-situ loading to examine polarization reversal in lead zinc niobate—lead titanate (PZN-PT) [128] and phase transformations in PZT ceramics [129]. Collection times are typically greater than those for X-ray diffraction, and lower lateral resolution is achieved. A comprehensive review on application of X-ray and neutron diffraction in ferroelectric materials is given by Jones [130].

4.2.4. Electron Microscopy Techniques

Imaging of domains using scanning electron microscopy (SEM) is challenging as ferroelectrics are semiconductors with high enough resistivity that charge build-up occurs on non-metallized surfaces. However, ferroelectric surfaces can be directly imaged in secondary electron mode due to topographic contrast arising from the slightly longer c-axis of the unit cell. An early attempt to view BT single crystals using SEM was done by Robinson and White [114], where the crystals were coated with an evaporative aluminium film to avoid surface charging. Also, by using intense beam currents, local domain switching was observed in an uncoated sample. However, in this work, most of the observations were done on etched crystals to improve the contrast. Another way of observing the domain structure under SEM is to use low acceleration voltages. Aristov *et al*. [131] viewed a BT single crystal in secondary electron mode using 2-4 kV accelerating voltage (figure 4.7(a)) and contrast was believed to be due to electric potential effects arising from variations in dielectric permittivity and conductivity in

different regions of sample surface. It is argued that, due to the low voltages used the topographic contrast would not be sufficient to image the different domains. Bihan [132] presents a good review of SEM observations on a number of ferroelectric crystals where contrast between domains through electrostatic interactions between the specimen and electron beam has been discussed in detail. SEM can be used for real time domain evolution studies, but suitable accelerating voltage, beam intensity and scanning speed need to be identified.

The topographic contrast is not normally visible in back-scattered electron (BSE) mode, and is highly sensitive to use of the correct accelerating voltage. However, BSE mode can be used to image the domain structure in ferroelectrics by exploiting the contrast due to electron channelling that depends on the tilting of the domains. This method has been exploited by Gruner and Shen [133] for imaging domains in BT ceramic. The use of environmental-SEM (ESEM) alleviates charge build-up, enabling greater acceleration voltages. Scanning electron microscopy is a rapid technique with sub-micron resolution, but surface charging and surface damage can interfere with measurements. Also, the need for vacuum makes in-situ domain evolution experiments somewhat difficult.

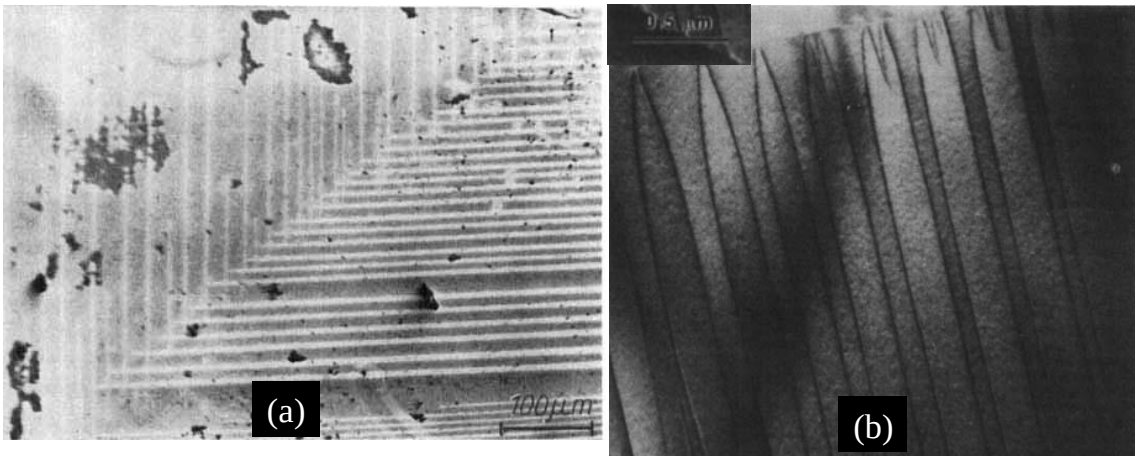

Figure 4.7: (a) *a-c* domain boundary and lamellar *a* domains in single crystal BT observed using SEM at an accelerating voltage of 2 kV (after Aristov *et al*., 1983 [131]). (b) Bright field TEM micrograph showing 90° *a-a* domain wall in Ca doped BT single crystal (after Hu *et al*., 1986 [134]).

Early investigations using transmission electron microscopy (TEM) have been mainly focused on imaging of the domain walls and estimation of wall thickness, for example, Blank and Amelinckx [135] estimated domain wall thickness to be less than 100Å in single crystal foils. 180° domain walls in BT ceramic were observed by Malis and Gleiter [136]. In these studies, the contrast was believed to be due to diffraction from the differently oriented *c*-axis of the domains. TEM has also been used to image microdomains in BT over a paraelectric-ferroelectric phase transition [137]. Hu *et al*. [134] used bright field imaging, dark field imaging and selected area diffraction to image domains in doped BT and diffraction contrast is believed to distinguish different domain types (figure 4.7(b)). High resolution transmission electron microscopy (HRTEM) has been used for the measurement of domain wall thickness [110,138]. The domain walls were reported to be of thickness ~5 nm or 4–10 unit cells. Contrast at domain walls in the HRTEM images is attributed to lattice distortions or ionic displacements. Excellent lateral resolution, of the order of 1nm, can be obtained, but the preparation of thin samples, typically 10 μm or less, is vital. Thin specimens make in-situ testing very difficult. Also, the various steps in specimen preparation such as machining, thinning, polishing may give rise to mechanical stresses that can reorganise the domain structure [139].

Scanning electron acoustic microscopy has also been used to map the domain structure. Here an acoustic wave generated by the converse piezoelectric effect is sensed using a piezeoelectric transducer. The signal is read through a lock-in amplifier and the phase of the signal indicates the orientation of the domains (electron acoustic image). This method, together with surface topography using secondary electrons (secondary electron image), can identify specific domains. The technique was used by Zhang *et al*. [140] to image domains in single crystal BT with sufficient lateral resolution to show 5 μm domain

bands clearly. Though promising, the method suffers with the drawbacks of electron microscopy as listed above.

Electron Back Scatter Diffraction (EBSD) is a SEM based technique that uses the diffraction patterns (called Kikuchi patterns) generated by Bragg reflection of the electrons by the lattice planes to gives the local crystallographic orientation at points within an SEM image. This technique has been used for mapping herringbone domain structure in tetragonal ferroelectrics such as PZT and bismuth ferrite-lead titanate single crystals [141,142]. Domain switching along indentation cracks in BT ceramic subjected to Vickers indentation was studied using X-ray diffraction in conjunction with EBSD by Cheng *et al*. [143]. Indexing of domain patterns needs careful selection of machine parameters and due to the tilting of the specimen, domains with their lengths parallel to the tilt directions are helpful for high lateral resolution (~ 25 nm) [144].

4.2.5. Scanning Probe Microscopy

Characterizing domain structure with a spatial resolution of a few nanometers is made possible by scanning probe microscopy techniques, which has been one of the most significant advancements in domain visualization. The Atomic Force Microscope (AFM) is the key instrument underlying scanning probe techniques. Reviews by Bonnell [145] discussing the origins of AFM, and Kalinin [146,147], Gruverman and Kholkin [148] on applications to ferroelectrics provide a broad coverage of this extensive field of study. In AFM, a sharp tip mounted on one end of the cantilever is scanned on the specimen surface. The deflection of the cantilever due to the interaction with the surface is measured using a laser beam reflected from the cantilever onto a photodetector. The AFM is typically operated either with the tip in contact (repulsive force regime) or in non-contact (attractive force regime). Lift or interleave mode can also be used, in which a

surface is first scanned in contact and then rescanned with the tip lifted to a predetermined height. In addition to direct topographic measurement, specific modes of AFM used for detecting domain structure include electrostatic force microscopy (EFM), Kelvin probe force microscopy (KPFM) and piezoresponse force microscopy (PFM).

Domain imaging can be achieved by conventional AFM methods, without exploiting the electrical nature of ferroelectric crystals. Imaging of 90° domains can be achieved by purely topographic methods due to the shear distortion of ferroelectric crystals across 90° domain walls. This causes a surface distortion that is readily observed in AFM topographic images. For example, non-contact AFM was used by Eng *et al*. [149,150], to image the reorientation of the *a* domains during the tetragonal-cubic phase transition in a BT single crystal. Other sources of topographic contrast include steps at domain boundaries [151] and surface corrugation [152,153].

In EFM, the electrostatic field of surface charges due to polarized domains is detected in non-contact mode. The interaction between the surface charge and tip charge produces a force that varies across domain walls [152]. Though this method is effective in distinguishing topographic features from electrostatic effects, achieving good contrast is a challenge. A good contrast can be obtained by applying a.c. voltage to the probe tip which is also referred to as dynamic contact EFM (dynamic contact means the cantilever is oscillating but does not make full contact with the surface). This method has been used to map the domain structure in periodically poled lithium niobate, where surface deformation due to the piezoelectric effect is believed to be the reason for contrast [154]. Resolution is limited by the long range nature of electrostatic interactions and is typically around 100nm. Surface contamination and cross-talk can cause difficulty. KPFM, also called scanning surface potential microscopy, is based on detecting the surface potential

associated with a spontaneous polarization state by applying a combination of a.c. and d.c. voltages to the probe tip in non-contact mode. More detailed discussion of EFM and KPFM is given by Kalinin and Bonnell [155].

Perhaps the most successful of the scanning probe techniques for ferroelectric crystals is piezoresponse force microscopy (PFM) (figure 4.8). This is a contact mode technique in which piezoelectric surface deformations are generated by applying a voltage to the probe tip. Mechanical vibrations are produced due to the converse piezoelectric effect which can then be interpreted to map the local orientation of the polarization vector as piezoelectric coefficient typically depends on the local polarization state. In tetragonal ferroelectrics, it is possible to identify out-of-plane $c+$ and $c-$ domains by vertical PFM. This relies on the d_{33} piezoelectric coefficient producing normal surface displacements that deflect the cantilever probe. Similarly, in-plane *a*-domains can be distinguished using lateral PFM, which exploits the d_{15} piezoelectric coefficient to generate shear displacements of the specimen surface that twist the cantilever probe. In vector PFM both sets of measurements are combined to construct a map of the three dimensional polarization vector [146]. PFM is commonly used on thin films, where moderate tip voltages are effective; however, it can also be used on bulk crystals.

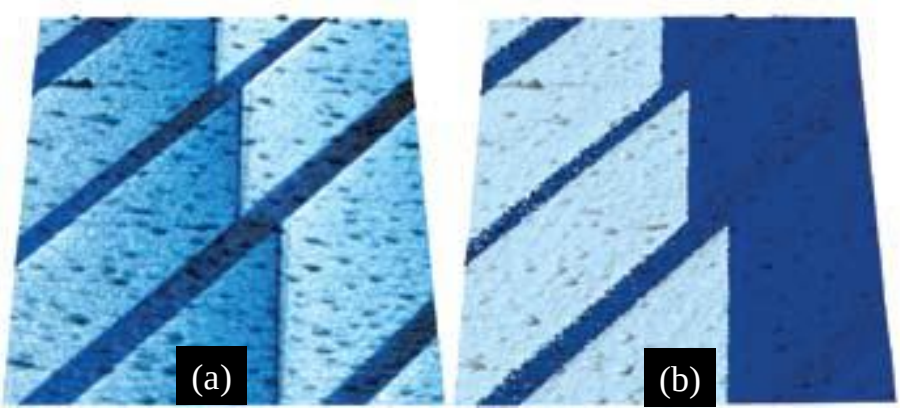

Figure 4.8: (a) PFM amplitude and (b) PFM phase overlaid on a AFM topograph showing 90° and 180° domain walls in single crystal $BaTiO_3$ (10 μm scan) (after Proksh and Kalinin, 2009 [156])

In summary, scanning probe methods can offer extremely high (sub nanometre) resolution, and very good contrast for mapping fine domain structure. The resulting images need careful interpretation due to the possibility of cross-talk between the various effects that can give contrast. The spatial resolution is limited by tip radius, humidity and dielectric properties of materials [156]. The main drawbacks of the technique are the limitation to surfaces and the limited scan area. An opportunity offered by scanning probe methods is the manipulation of domain structure using the probe. Also, domain evolution could be studied, though scan times are typically of the order of seconds to minutes with current technology. Experimental arrangements for applying mechanical and/or electrical loads under AFM can be challenging due to space constraints.

4.2.6. Use of combined Methods

As each observation method has different capabilities, more than one technique may be needed to map the microstructure and have an unambiguous interpretation of the domains present. For example, scanning and transmission electron microscopy, optical microscopy and X-ray diffraction were used in combination to image herringbone and lamellar domain structure in BT single crystals by Park and Chung [139]. Use of multiple techniques enables viewing smaller features as such δ fringes (TEM image) and large features such as zigzagged boundaries of the same domain structure (optical image) (figure 4.9). Similarly, 90° *a–c* domain boundaries were imaged using polarized light microscopy, SEM and contact mode AFM in single crystal BT [157]. By applying various techniques to the same region of microstructure, domain information which is not available from any single technique, can be revealed. Table 4.1 summarizes capabilities of various techniques to reveal particular domain types in tetragonal BT.

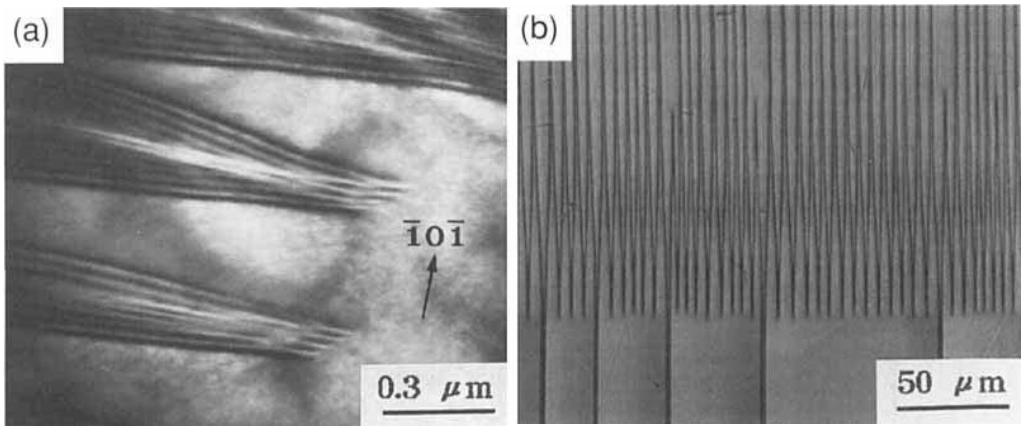

Figure 4.9: Wedge shaped lamellar domains are observed using (a) transmission electron micrograph and (b) an optical micrograph (after Park and Chung, 1994 [139]).

Table 4.1: Various techniques and their capabilities for domain observation.

Technique	Capability to reveal domain structure
Optical microscopy	Domain walls but not domain types.
Polarized light microscopy	*a1*, *a2* and *c* domains, but not *c*+/*c*-
Etching + Optical microscopy/SEM/AFM	*c*+ , *c*- *a* domains, but not *a1*/*a2* boundaries or *a*+/*a*- boundaries.
Piezoresponse Force Microscopy	*c*+, *c*-, *a*+ and *a*- domains could be distinguished
Synchrotron X-ray topography	*a1*, *a2* and *c* domains; *c*+/*c*- and *a*+/*a*- boundaries by anomalous dispersion.

Most of the literature discussed above is focused on revealing domains, but there is relatively little work that aims to map domain patterns with definitive information about the domain type present at each point on the specimen. This proves to be difficult, as using only one technique listed in table 4.1 does not provide all the necessary information. Mapping of domain patterns and developing the necessary techniques is important as this knowledge could then be used to understand how domains evolve under external electrical or mechanical loading. Also, the domain patterns in ferroelectrics can be modelled using various approaches, for example, compatibility conditions [158] or phase field simulations [159]. Experimental techniques that can map the domain patterns, preferably in 3D, are needed for validating such models.

Next, we discuss mapping domain structure in BT single crystal by using various techniques such as synchrotron X-ray diffraction, PFM and etching followed by AFM, SEM and optical microscopy.

4.3. Domain wall observations

Unpoled substrate grade single crystal specimens of <001> oriented BT of 10 x 10 x 0.5mm size were obtained from Marketech International Inc., USA. BT single crystals were grown by TSSG method, were transparent with both sides polished and were without any electrodes. 90° domain walls were apparent in a few crystals which were seen oriented at 45° with respect to specimen edges. Optical observations of these 90° walls in as-received crystals suggested that the other two sides were oriented in <100> and <010> direction. Thin crystals were difficult to handle and needed storing above 10° C to avoid any phase transformation. No cracks or surface damage was apparent in the crystals. For the domain observations reported in this chapter, the crystals were not poled or subjected to any mechanical stress prior to imaging. Suitable sized specimens were machined by Struers Acutom 50 precision cutting saw with slow feed rate.

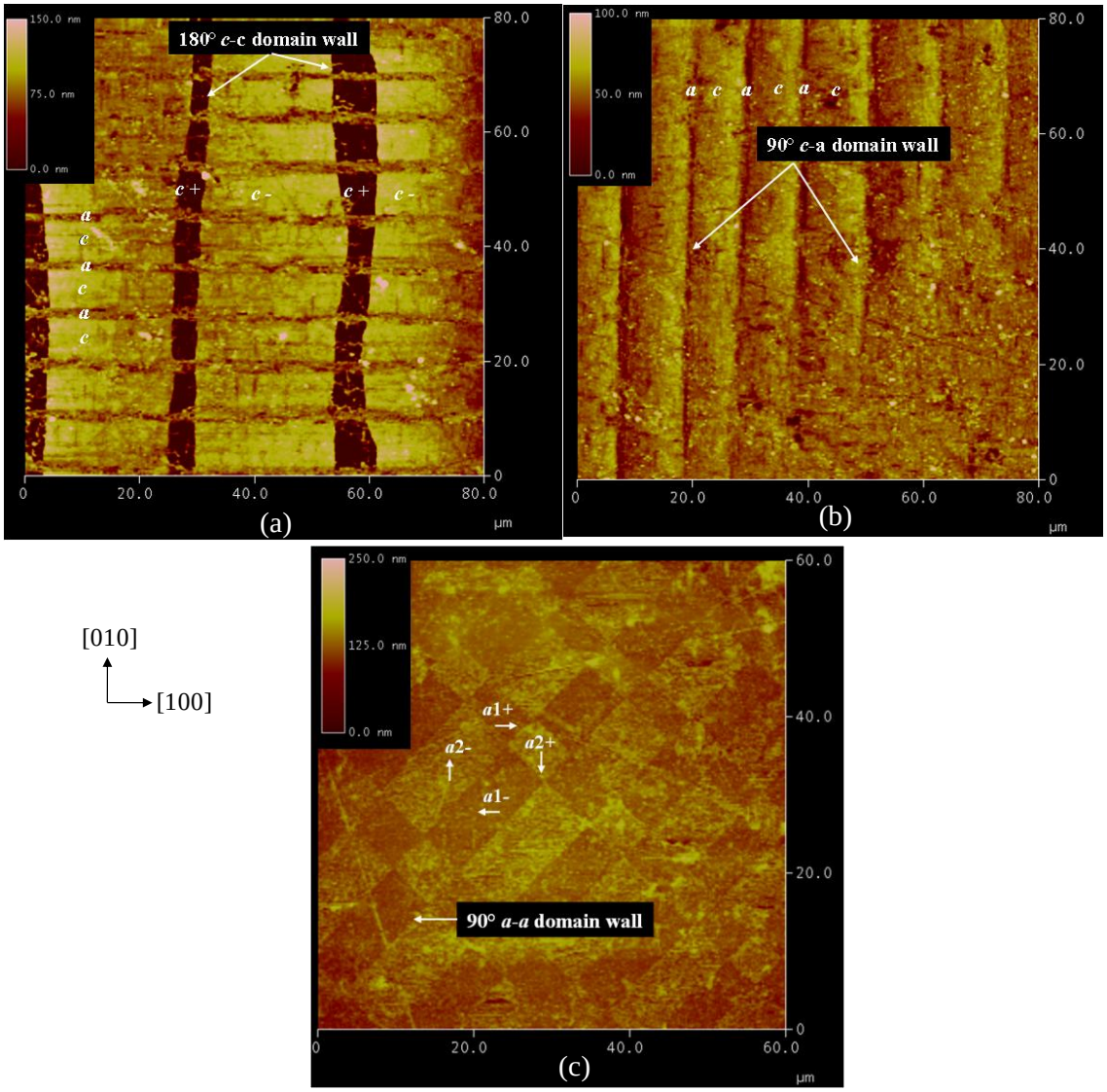

Figure 4.10: Atomic force micrographs of etched BT single crystal showing (a) 180° *c*-*c*, (b) 90° *c*-*a* and (c) 90° *a*-*a* domain walls.

To observe various domain walls and their orientations, BT single crystals were etched using 10% HF solution in water for about 1 minute. Subsequent atomic force micrographs using Veeco's Dimension 3100 AFM with Nanoscope IIID Controller are shown in figure 4.10. The SCM-PIC tips were used in contact mode at a scan rate of 1Hz revealing a topographic unevenness of about 100nm; note that etching rate is rapid for *c*+ domains slow for *c*-.

Figure 4.10(a) shows a domain pattern containing alternate bands of *a* and *c* domains with 180° domain walls, separating *c*+ and *c*- domains. It is interesting to note that the 180° domain wall alternates between fixed orientation and flexible orientation as it crosses the pattern, resulting in curved domain walls between the crystal variants polarized in the out-of-plane direction. Figure 4.10(b), shows needle type *a* domains interspersed within bands of *c* domains revealing 90° *c*-*a* domain walls. As the etching rate for *a* domains is intermediate between *c*+ and *c*- domains, relatively weak contrast was achieved. Figure 4.10(c) shows a domain arrangement of in-plane *a* domains in a pattern exhibiting an array of polarization vortices. This "vortex" structure has not been widely observed, perhaps due to the strong disclinations present, which make this a relatively high energy state [158]. This arrangement containing 90° domain walls in a checkerboard pattern oriented at 45° to the crystallographic axes shows 90° *a*-*a* domain walls. Next, large area observations of the specimen were conducted using scanning electron microscopy and optical microscopy.

Figure 4.11 (a) and (b) are scanning electron micrographs of the etched specimen surface captured using Zeiss's EVO LS 15 ESEM in the secondary electron mode. The operating voltage and working distance used are 10 kV and 7 mm respectively. Figure 4.11 (a) shows a watermark domain pattern with antiparallel out-of-plane polarization directions. Curved 180° *c*-*c* domain walls could be seen in this figure. Figure 4.11(b) is in the same region as that of figure 4.10(b). Here, a better contrast could be seen for long pointed needle type *a* domains that intersect the *c* domain bands forming 90° *c*-*a* domain walls. If suitably oriented, in-plane *a* domains can be readily observed on unetched surface of the specimen using optical microscopy. Figure 4.11(c) captured using Alicona's InfiniteFocus microscope, shows an arrangement of closely separated needles of *a*

domains interspersed in a differently oriented single large domain along with 90° *a-a* domain walls parallel to {110}.

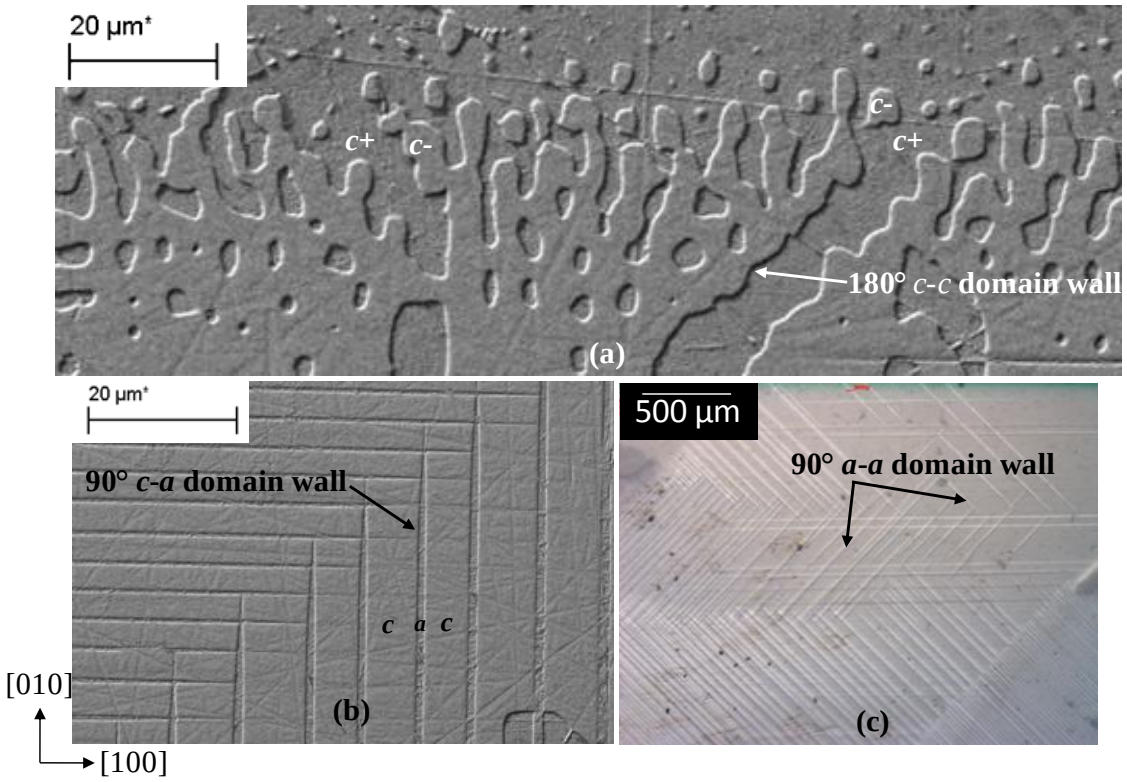

Figure 4.11: (a) Scanning electron micrograph of etched BT single crystal showing 180° *c-c* and (b) 90° *c-a* domain walls. (c) Optical micrograph of unetched single crystal showing 90° *a-a* domain walls.

4.4. Optical observations of domains in unetched specimen

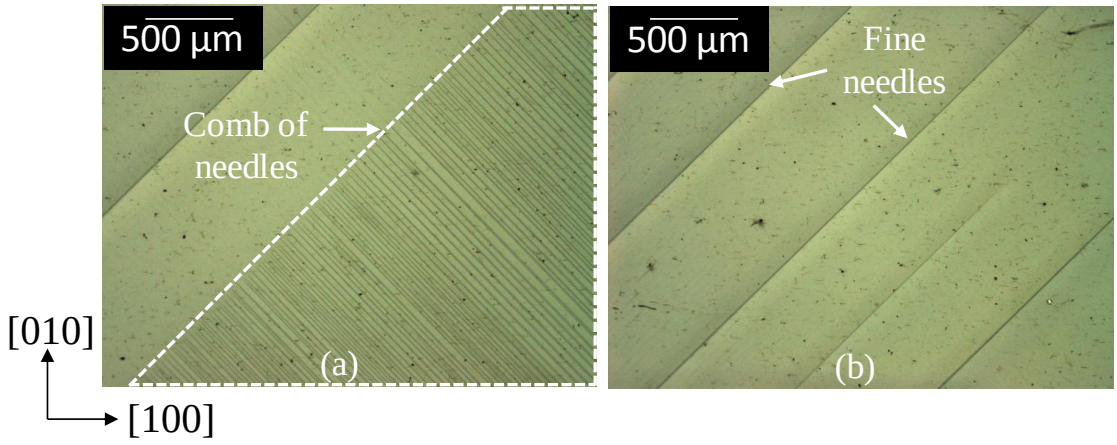

Figure 4.12: Optical micrographs showing (a) comb of needle type domains (b) fine needle type domains.

BT crystals were observed under Alicona's InfiniteFocus microscope without etching (figure 4.12(a) and (b). Two types of arrangements of needle types domains with wedge shaped ends were seen at different sample locations: Figure 4.12(a) shows a microstructure containing a comb of needles. This comb of needles comprises of many fine needles that are spaced very close to each other. Figure 4.12(b) shows widely separated fine needles interspersed in a differently oriented large domain. Though such optical observations are easy to make, it is not possible to identify the domain types and the local orientation of the polarization vector could only be understood by the simultaneous use of other techniques. Further observations using optical microscopy were done on etched crystals and will be presented in section 4.6.

4.5. Synchrotron X-ray reflection topography: Experiment 1

4.5.1. Experimental details

BT Single crystal specimens of size 10 x 10 x 0.5 mm were observed by reflection topography using unfocussed monochromatic synchrotron X-ray light at beamline B16, Diamond Light Source, UK. Specimens were mounted onto the diffractometer (5-circle Huber diffractometer with χ circle/cradle) using an aluminium specimen holder that exposed a 10 x 10 mm face of the crystal to incident light. Figure 4.13(a) shows a typical arrangement whereby the specimen is illuminated by the X-ray beam and surface reflections were detected by an Photonic science X-ray eye mini FDI camera (1392 x 1040 pixels, pixel size = 6.5 µm), at a detector distance (*dd*) of 550 mm. Monochromatic X-rays of energy 12.4 keV (1Å wavelength) were used in this experiment. Here, [200] and [002] reflections were detected, corresponding to *a* and *c* domains respectively. Reflection topograph images of the specimen surface were collected with 150 ms integration times, at a range of tilts in the ω-axis defined by 13.3° to 14.5° in steps of

0.005° (figure 4.13(b)). This gave angular resolution better than 0.1 mrad and provided a set of images representing the rocking curve data for each illuminated point on the specimen surface.

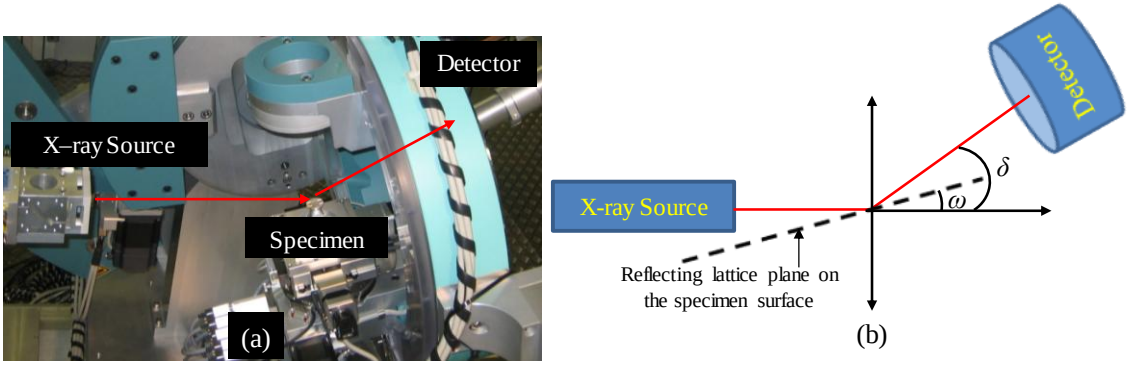

Figure 4.13: (a) General arrangement of the experiment showing X-ray source, specimen and detector. (b) A series of reflection topographs were collected over a range of tilts about the ω axis.

Figure 4.14 shows important angles, such as ω, χ, δ and ϕ that were useful for understanding tilt between adjacent domains while interpreting the resulting topographs. The X-ray beam was slitted to 8 x 1 mm (width x height); accounting for foreshortening, this allowed the entire specimen to be imaged in ten overlapping scans as shown in figure 4.15. Each scan consisted of 241 images: one at each step of the tilt in the ω axis defined by 13.3° to 14.5° in steps of 0.005°. The sample position was incremented using the *x*-*y* stage of the diffractometer and in total 10 such scans were collected so that the entire surface area of the specimen was covered. Overlapping regions in the scans enabled the construction of a collage map of the entire specimen surface.

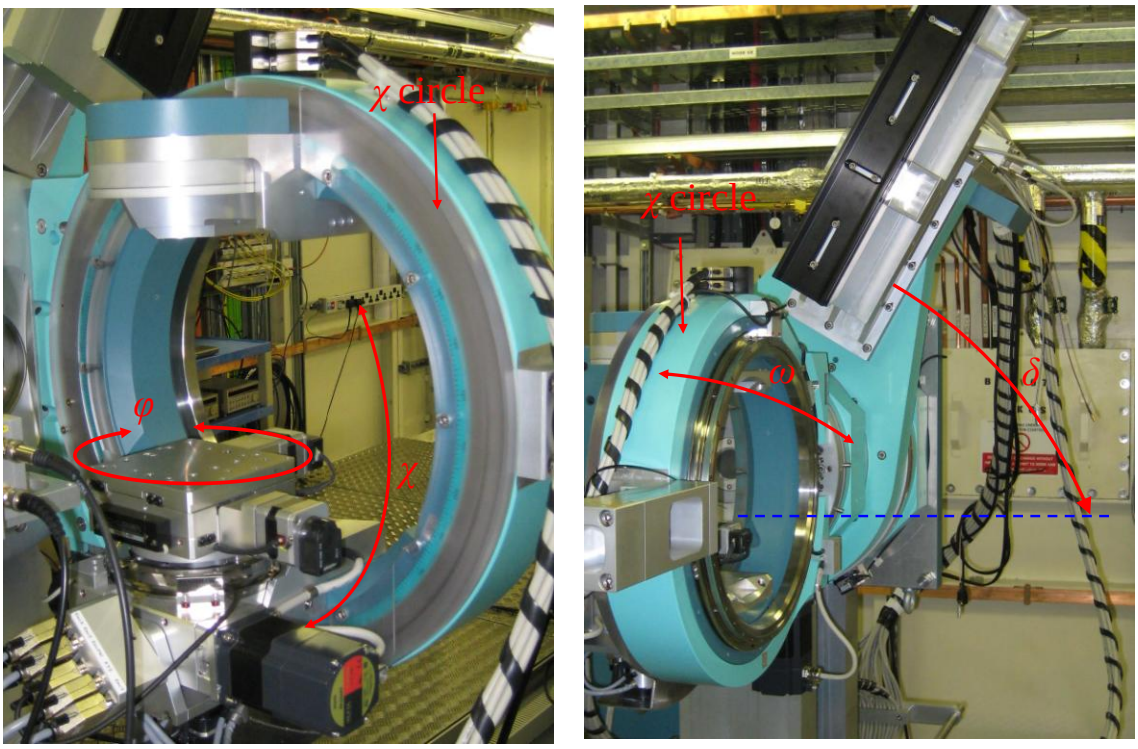

Figure 4.14: Important angles in the synchrotron set up.

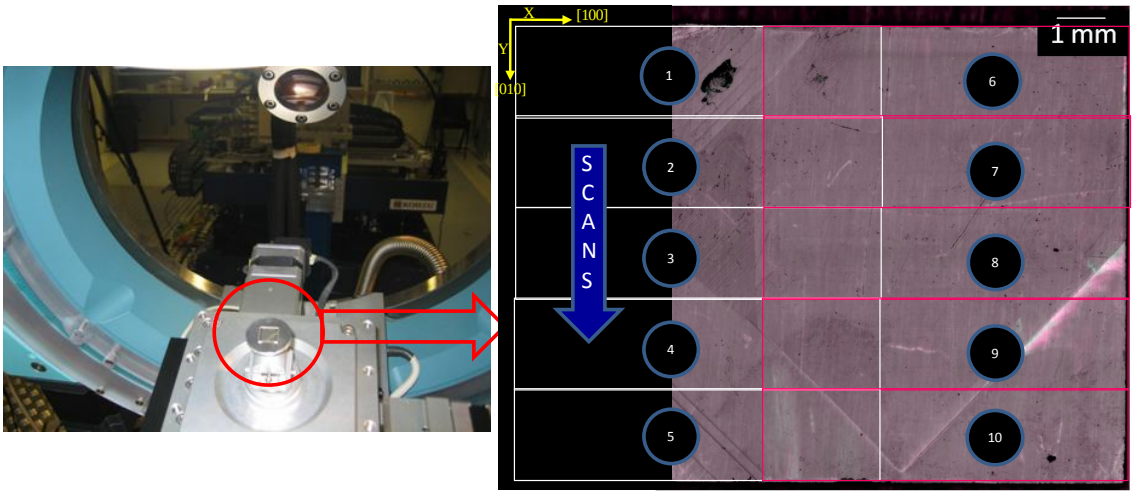

Figure 4.15: Optical micrograph of the entire specimen showing the positions of the X-ray scans.

4.5.2. Data processing

According to the Bragg's law, the intensity of the reflected light is maximum when the condition $n\lambda = 2d\sin\theta$ is satisfied, where n is an integer representing order of reflection, λ is the wavelength of X-ray light, d is the interplanar spacing of the reflecting planes and θ is the angle of incidence of the X-ray light relative to reflecting planes. Due to slight

curvature of the crystal and tilt between domains, only a portion of the specimen surface entered the Bragg condition at any given value of angle ω when the specimen was rocked over a range of tilts about the ω axis. Table 4.2 lists the angles at which a maximum intensity was observed for *c* and *a* domains. The angle δ (=2θ) is very sensitive to a particular reflection type and was used to identify the domain types.

Table 4.2: Symmetric reflections and corresponding angles.

	c reflection [002]	*a* reflection [200]
χ (°)	90.6	90.6
δ (°)	28.74	29.06
ω (°)	13.84	13.37

In the present experiment, using the values in table 4.2, lattice parameters were measured to be *a* = 3.985Å and *c* = 4.029Å. Using equation 4.4 and the δ measurements from table 4.2, the relative tilt θ_d in lattice planes between *c* and *a* domains is calculated as 0.63° which is in good agreement with the literature [160]. Now, considering the ω measurements in table 4.2, the measured tilt between the lattice planes in the *c* and *a* domains is given by:

$$\theta_d = \left(\omega_c - \frac{\delta_c}{2}\right) - \left(\omega_a - \frac{\delta_a}{2}\right) \tag{4.5}$$

Note that equation 4.5 corrects for the small ω misalignment due to specimen mounting, Equation 4.5 gives θ_d = 0.63° in exact agreement with equation 4.4.

A typical topograph showed regions containing both *a* and *c* domain reflections. Due to the higher δ value, the *a* domain reflections would lie vertically above the *c* domain reflection as can be seen in figure 4.16(a) which was obtained by summing intensity over all ω values in scan 7. Also, *a* domains shifted horizontally with respect to *c* domains could be seen in some of the topographs as illustrated in figure 4.16(b). This horizontal shift is due to tilt about the χ axis and would be discussed in more details later.

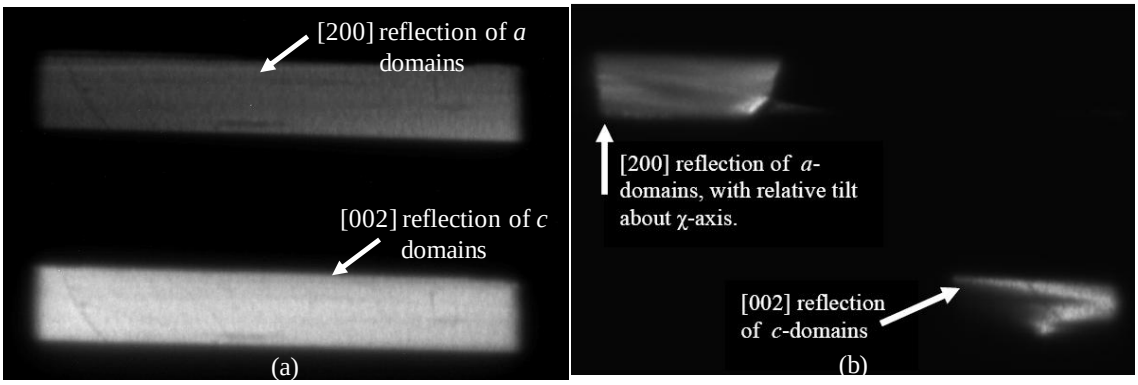

Figure 4.16: (a) *a* and *c* domains with relative tilt about ω axis could be seen by summing intensity over all ω values. (b) topograph showing *a* and *c* domain reflections at a particular ω value (ω =13.865º) in scan 1.

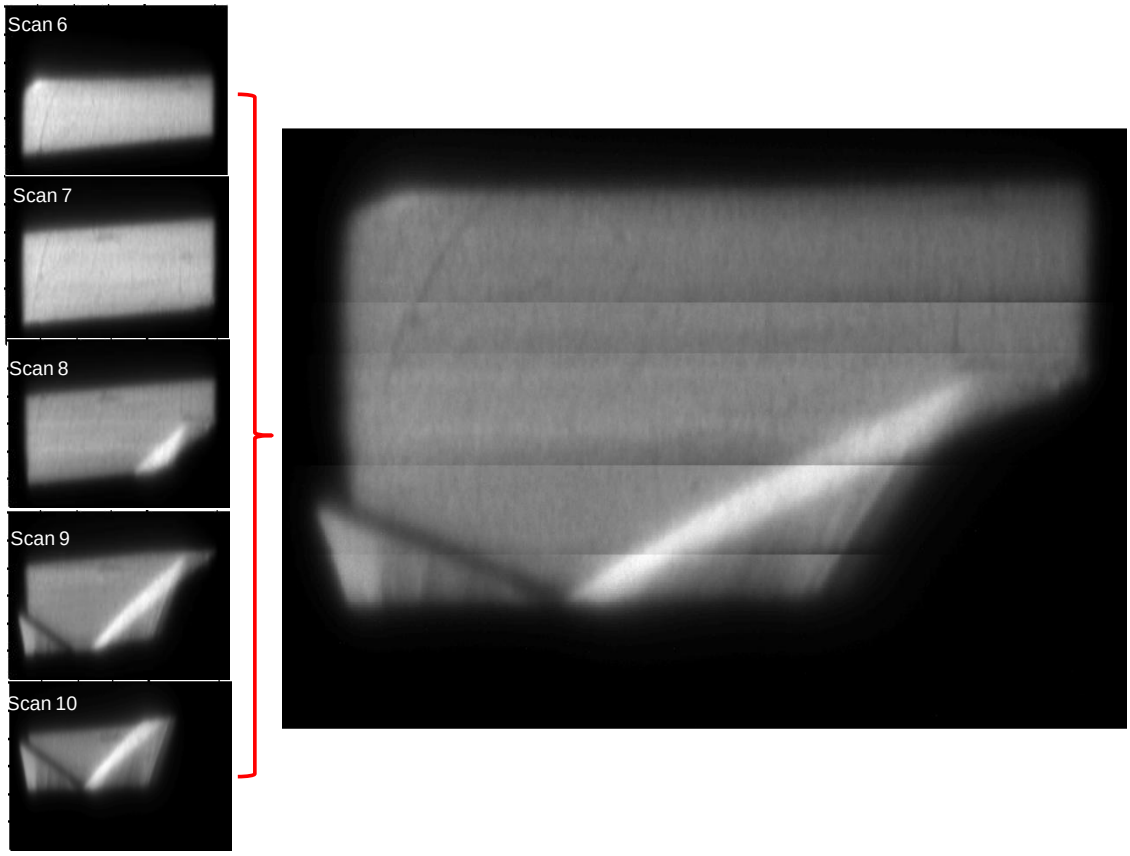

Figure 4.17: Integrated *c* domain topographs (scans 6-10) joined to form a composite image.

As each scan comprised a set of topographs obtained for a range of ω values, the relative tilt in the domains about the ω axis was known. Reflections from *a* and *c* domains were separated from the raw-data set by selecting the subset of data corresponding to [200] and [002] reflections respectively. This was possible as the reflections within a single scan were vertically separated from each other with no overlap. These images were then

integrated over ω to provide intensity data that could be used for assembling the composite image of the specimen by aligning the overlapping regions of reflections from distinct scans. Surface features such as scratches were used to align the scans to form a composite image, for example, as shown in figure 4.17, integrated *c* domain topographs from scans 6-10 are joined together to form a composite image.

The data was further processed pixel-wise to extract the mean ω tilt and intensity value for each pixel using the first moment of area as given by equations 4.5. Other methods such as Gaussian fitting or full width at half maximum (FWHM) could also be used. However, these methods may not work if peaks overlap.

$$\bar{\omega} = \frac{\int I(\omega).\omega \, d\omega}{\int I(\omega) \, d\omega} \qquad \bar{I} = \int I(\omega).d\omega \tag{4.6}$$

Foreshortening of the reflected images was removed from the data in an approximate way by stretching the processed data by a factor of cosec(ω) in the *y*-direction, using an average ω value for the dataset. This process generated an ω-orientation map and an intensity map for *a* and *c* domains which could be compared with the optical micrographs.

4.5.3. Analysis and interpretation of composite images

Inspection of the raw images showed that certain matching reflections within the same image often had a relative shift in the horizontal (*x*) direction. This shift could be interpreted as a consequence of small relative rotations of the reflecting lattice planes about the χ-axis of the diffractometer. The magnitude of these rotations was estimated based on the sample to detector distance (*dd*), the horizontal displacement (*x*) and average ω tilt value for the *a* domains as follows:

$$\delta\chi = \frac{x}{2dd \sin(\omega)} \tag{4.7}$$

The direction of the relative tilt is positive if the horizontal shift is in $+x$ direction and vice versa. Composite images showing an ω-orientation map and intensity map for *a* and *c* domains are shown in figure 4.18.

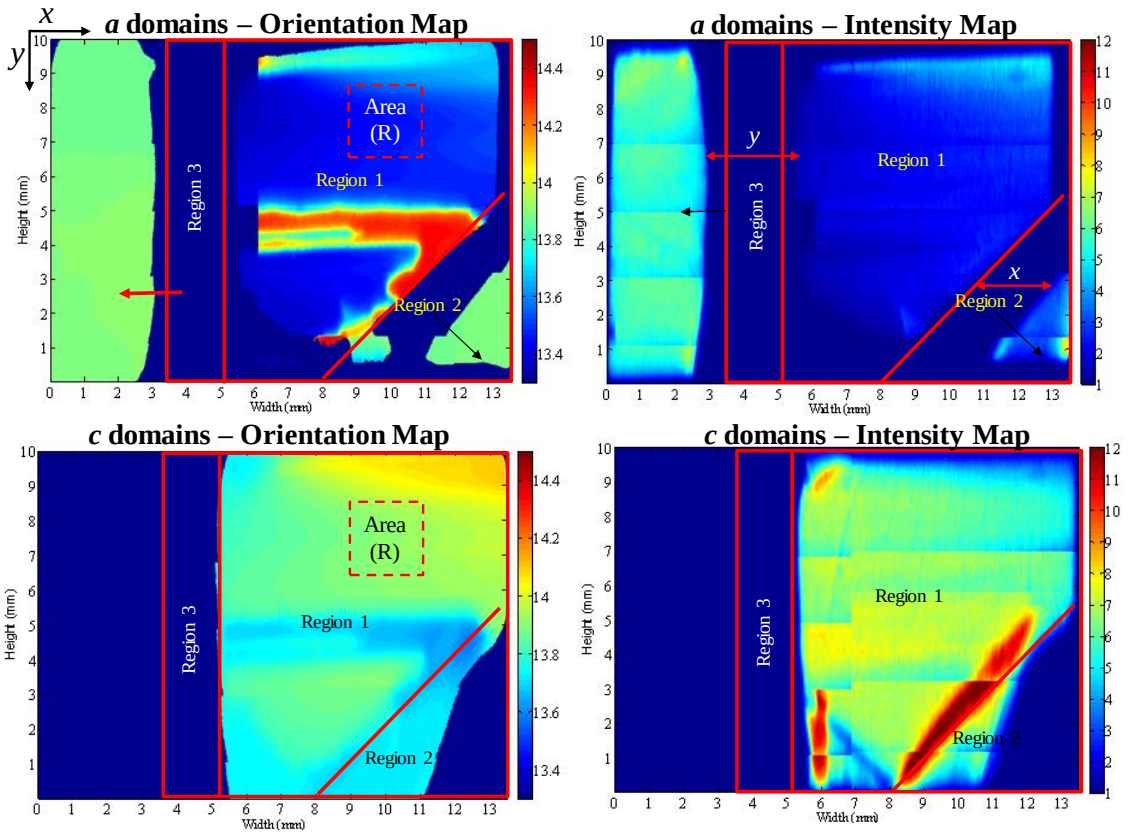

Figure 4.18: Orientation maps and intensity maps for *a* and *c* domains for the entire surface of the crystal showing tilts in the ω and χ axes.

Orientation map: A typical region of the crystal surface produced both *c* and *a* domain reflections, indicating that both types of domain were present over most of the crystal surface. However, the domain patterns were not visible which suggests that the *a* and *c* domain regions may be too finely interspersed to resolve the individual domains. However, it was observed that fairly large regions of crystal, of order mm in size, contained both *a* and *c* domain reflections with a constant relative tilt between the finely interspersed *a* and *c* domains. This can be seen in figure 4.18, where, for example, a 2 x 2 mm area (R) within region 1 contains *a* domains of a fairly uniform ω tilt of 13.46°, and *c*

domains at a different but uniform tilt of 13.91°. The relative tilt in this case, computed using equation 4.5, is 0.61° which suggests that elastic strain of order of 0.07% may be present in the crystal. In figure 4.18, a sketch of the footprint of the specimen (red coloured rectangle) has been superimposed onto the synchrotron data that allowed the crystal surface to be separated into different regions, as follows:

(i) **Region 1**: This covers the majority of the surface area of the specimen and contains both *a* and *c* domains. As there is no relative horizontal shift in the reflections, *a* and *c* domains present in this region do not have any relative tilt about the χ axis. The average ω value for *a* domains is 13.5° and that for *c* domains is 13.9°.

(ii) **Region 2**: A triangular region at the lower right hand corner contains *a* domains tilted relative to region 1 about both the ω and χ axes. The average ω value for the *a* domains is 13.9° and that for the *c* domains is 13.7°. The shifted *a* domains are shown with an arrow and the displacement *x* is shown in the intensity map. The relative tilt about the χ axis ($\delta\chi$) is 0.43°, found using equation 4.7, where x = 2 mm, dd = 550 mm and ω = 13.9°. The direction of tilt is positive due to the displacement in $+x$ direction.

(iii) **Region 3**: On the left hand side of the crystal, a large strip spanning the entire height of the crystal (1.5 x 10 mm) shows only *a* domains with the average ω tilt value of 13.9°. The reflections are displaced horizontally in the negative *x*-direction, appearing outside the original footprint of the specimen. The shifted *a* domains are shown with an arrow and the corresponding displacement *y* is shown in the intensity map. The relative tilt about the χ axis is estimated as -0.54° using equation 4.7, y = 2.5 mm, dd = 550 mm and ω = 13.9°. An arrow indicates the shift of the reflection from this region. The orientation map for *c* domains suggests complete absence of *c* domains in region 3. More scans were made outside the observation window shown here to check for *c* reflections, but no such reflections were found.

Intensity map: The intensity maps for *a* and *c* domains in figure 4.18 indicate the fraction of each type of domain present at the crystal surface. As the structure factor for *a* and *c* domains does not differ much, the intensity of the reflected light from these domains represents the corresponding domain fractions and could be compared within different regions of the specimen. In region 1, the intensity of *c* domain reflections is greater than that of *a* domain reflections, indicating a greater proportion of *c* domains. For a 2 x 2 mm area (R) shown in figure 4.18, the ratio is 2.44. For the region 1, the ratio varies between 2.2 to 3. Similarly, for the region 2, the proportion of *c* domains is greater than the proportion of *a* domains and in this case, the ratio is about 2 to 2.5.

Microstructural Interpretation: The orientation and intensity maps provide evidence that can be interpreted in terms of microstructural arrangement. The maximum penetration depth is estimated to be 22 μm, which implies that the topographs reveal microstructure very close to the surface. The composite images suggest a finely interspersed mixture of *a* and *c* domains such as those illustrated in figure 4.19.

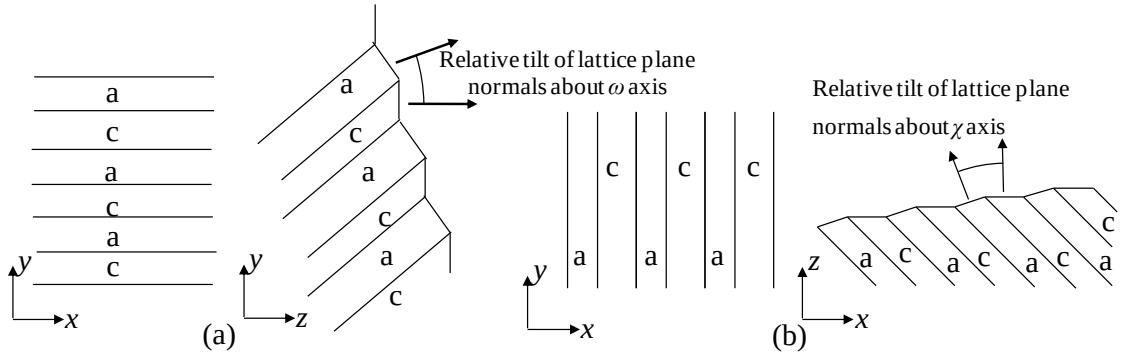

Figure 4.19: (a) Schematic of fine periodic structure giving rise to *c* and *a* domain reflections from the same regions of crystal, and a relative tilt at the *c*-*a* domain wall in the ω axis and (b) relative tilt at the *c*-*a* domain wall resulting in displaced reflections at the camera, giving tilt about the χ axis.

Figure 4.19(a) shows one possible periodic arrangement of *a* and *c* domains with a relative tilt about ω-axis (the axis perpendicular to the *y*-*z* plane) similar to that observed in region 1. The alternative arrangement shown in figure 4.19(b) gives a relative tilt about

the χ-axis, which is perpendicular to the *x-z* plane and it demonstrates a possible domain arrangement in region 2. Next, the specimen used in the synchrotron studies was etched and AFM/SEM observations were made for comparison with the synchrotron results.

4.5.4. Optical/AFM/SEM observations of the etched specimen

Optical and AFM observations: The specimen used for the synchrotron study was etched using 10% HF solution in water for about 1 minute. The etchant preferentially attacks *c*+ domains; *c*- domains are less deeply etched, while *a* domains are etched intermediately. This revealed surface domain patterns, which were observed using an Alicona InfiniteFocus microscope (figure 4.20(a)). Various regions of interest were also observed by Atomic Force Microscopy using a Veeco Dimension 3100 AFM system with Nanoscope IIID Controller. SCM-PIC tips were used in contact mode at a scan rate of 1Hz, revealing a topographic contrast of about 100 nm between *c*+ and *c*- domains.

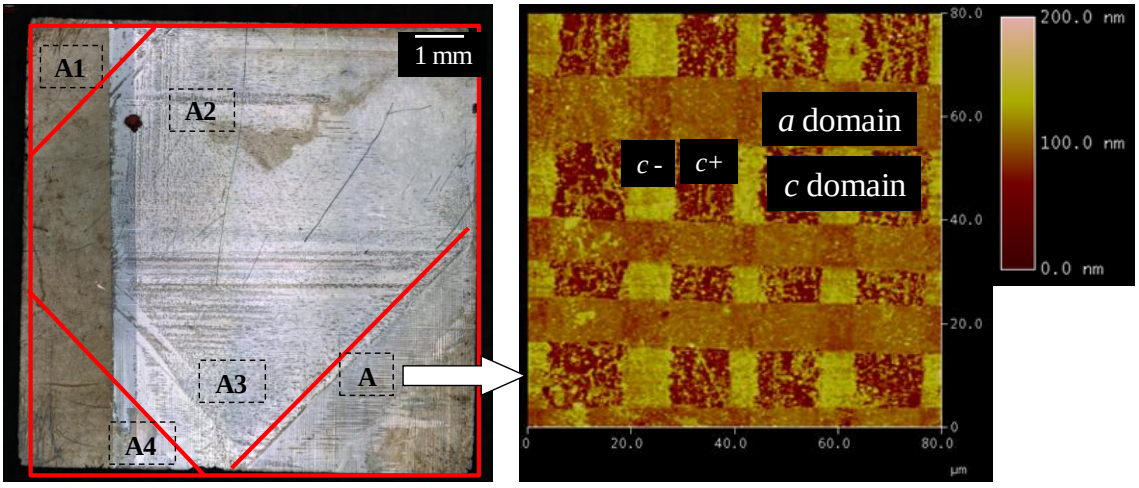

(a) (b)

Figure 4.20: (a) Etched specimen showing differentially etched domains (b) AFM micrograph in the area A confirming the presence of *c* and *a* domains and further distinguishing between *c*+ and *c*- domains.

Figure 4.20(b) shows an AFM micrograph in the area A. The synchrotron data from this region indicated the presence of both *a* and *c* domains, with a relative tilt about the *ω*

axis. The AFM observation unambiguously identifies the distinct domain types such as *c*+, *c*- and *a* domains, but does not distinguish ±*a*1 or ±*a*2 domains.

Atomic force microscopy of 80 x 80 µm areas was thus able to identify the domain pattern present in each region of the crystal. Such observations were made over a number of areas to get a local confirmation of the structure and these observations confirmed the presence of the domains detected by synchrotron diffraction. Here some representative optical and AFM micrographs in the regions marked as A1, A2, A3 and A4 in figure 4.20 are shown in figure 4.21. Note that, though the micrograph in region A1 does not show fine domain patterns, it is because region A1 contains only *a* domains and etching cannot distinguish between differently oriented in-plane *a* domains.

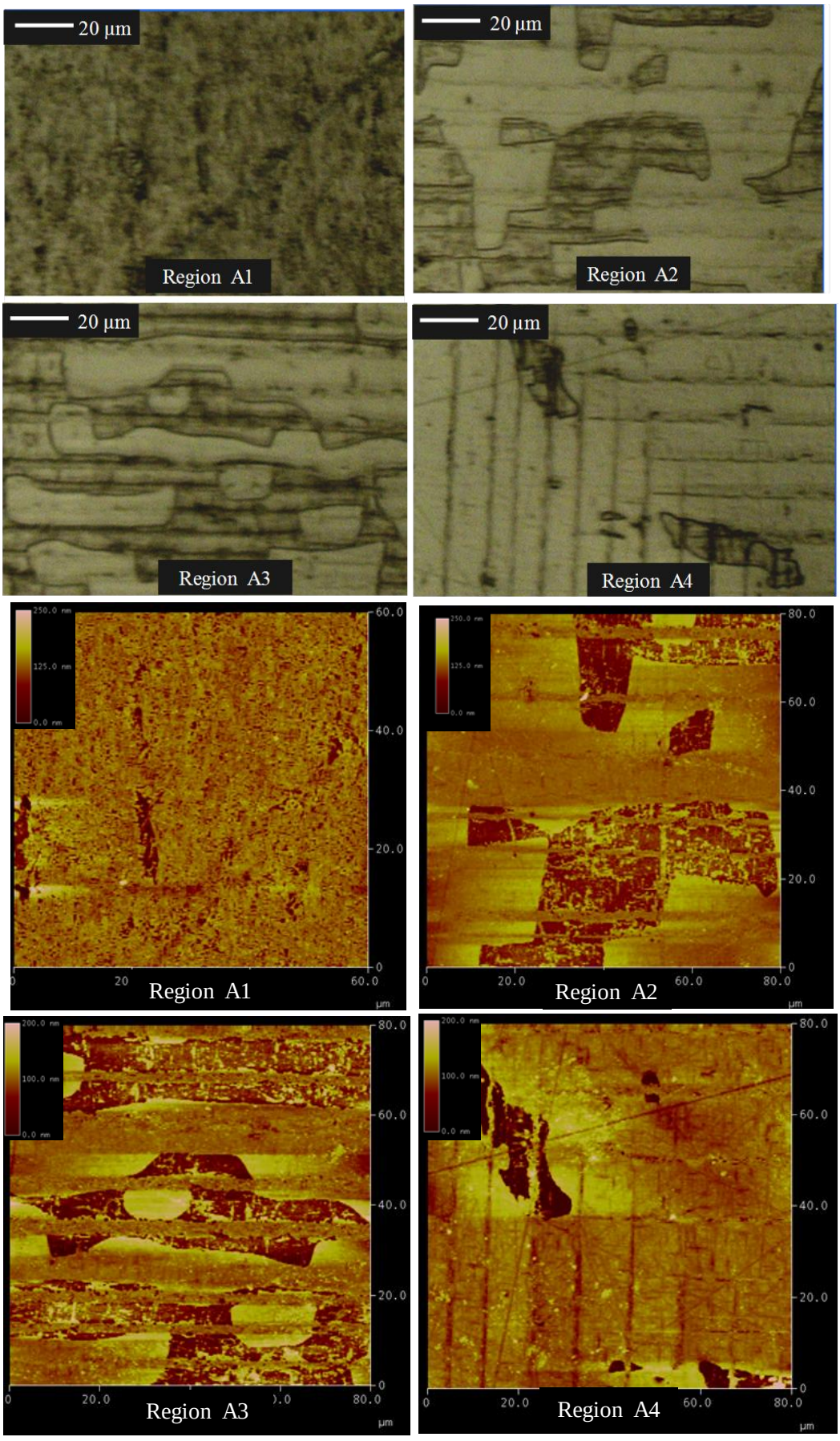

Figure 4.21: Optical and AFM micrographs in regions 1-4.

SEM observations: In order to confirm the proportions of domains observed in the synchrotron intensity maps, scanning electron microscopy was used to observe larger areas of microstructure. A Zeiss EVO LS15 ESEM was used in secondary electron mode, with a 10 keV beam and 7 mm working distance. Figure 4.22(a) shows a scanning electron micrograph (approximately 300 x 180 µm) in area A of the specimen (area A is marked in figure 4.20).

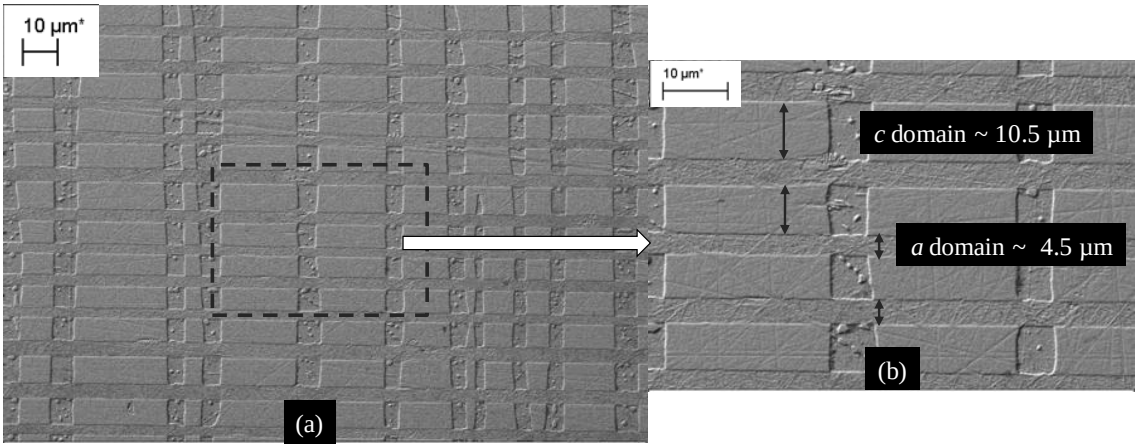

Figure 4.22: (a) Scanning electron micrograph in area A of Figure 4.20(a). (b) Zoomed in micrograph of the same area giving typical domain widths.

The typical domain width for *c* and *a* domains was found to be 10.5 µm and 4.5 µm respectively (figure 4.22(b)). This gives the ratio of *c* domains to *a* domains as 2.3, which is in good agreement with the synchrotron intensity data which suggests the ratio to be about 2 to 2.5. Here, the particular domain types were known from the AFM scans, while the larger area observed using SEM allowed an estimate of the typical domain widths over a representative area.

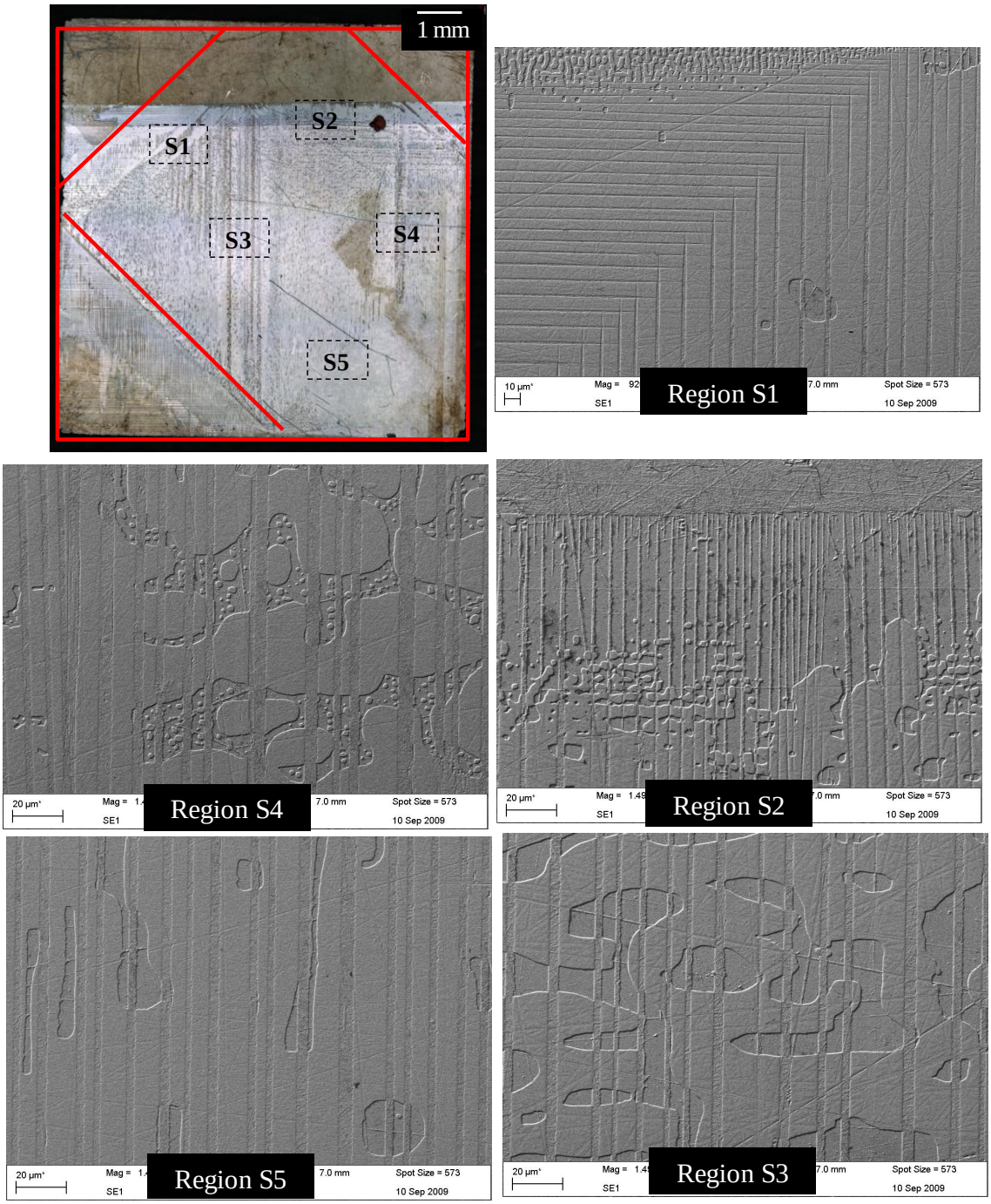

Figure 4.23: Scanning electron micrograph in various regions S1-S5 marked in the optical micrograph. Typically, a fine domain spacing (< 10 μm) can be seen in all the micrographs.

Further, different regions of the specimen were observed using SEM are shown in figure 4.23 where the micrographs correspond to regions S1, S2, S3, S4 and S5 as marked in the optical micrograph. These observations confirm that the domain spacing is typically less than 10 μm, so that the domain patterns were too fine to be resolved by the synchrotron

measurements using a camera having a pixel size of 6.5 μm. Also, even for the few areas with domain spacing slightly greater than 10 μm, the domain patterns could not be seen in the X-ray topographs due to the blurring of the images because of small local tilts.

4.5.5. Summary and issues in experiment 1

Multiple techniques (X-ray topography, etching followed by AFM, SEM) used simultaneously help in the interpretation by giving the local confirmation of the microstructure along with additional information about domain widths. However the following limitations/issues arose while using this method for domain mapping:

(1) In the reflection topographs, the physical space on the specimen surface and reciprocal space of the reflections interact producing distortions and overlaps. Though the method was successful in indicating the presence of interspersed *c* and *a* domains, a further refinement is needed to identify the spatial arrangements of domains. An alternative could be to illuminate smaller regions of the specimen and raster the scan area over the entire surface. But this is time consuming if large specimen areas were to be mapped.

(2) Domain patterns were not revealed in this experiment due to the fineness of the microstructure. However, using a high resolution camera with finer pixel size may be helpful. Another way to tackle this issue is to map a specimen with more widely spaced domains.

(3) As only symmetric reflections were used, it was not possible to distinguish between in-plane *a* domains. However, by using asymmetric reflections it is possible to discriminate between *a*1 and *a*2 domains.

4.6. Synchrotron X-ray reflection topography – Experiment 2

In experiment 2, X-ray topography was used in an attempt to resolve a fine domain structure using the Optique Peter X-ray microscope with PCO CCD camera (4008 x 2672 pixels, optical objectives from 1.25X to 40X). The camera gives a capability to zoom-in on regions of interest by selecting an appropriate objective lens. The experiment uses the same technique of rocking the specimen through a range of tilts in the ω-axis and recording topographs. In the selected region of interest, asymmetric reflections were collected to differentiate between two in-plane orientations of *a* domains, *a*1 and *a*2, and *c* domains.

4.6.1. Experimental details

The experimental arrangement was similar to that of experiment 1 (figure 4.13) except for the use of PCO camera at a detector distance (*dd*) of 445 mm. A specimen BT crystal (10 x 5.6 x 0.55 mm) was positioned in an aluminium specimen holder with 10 x 5.6 mm face exposed to X-ray light. Unfocussed monochromatic X-ray light of 18.6 keV energy was used to map the domains in the selected region of interest. At 18.6 keV, *a*1, *a*2 and *c* domains were identified using 3rd order reflections of type {306}.Table 4.3 lists the reflections and corresponding angles. For the asymmetric reflections, the specimen was tilted about the χ-axis such that the reflecting planes satisfy the Bragg condition.

Table 4.3: Asymmetric reflections and corresponding angles (experiment 2)

	c-reflection [306]	*a*1-reflection [603]	*a*2-reflection [360]
χ (°)	63.22	63.759	63.493
δ (°)	67.586	68.08	68.26
ω (°)	34.124	33.559	33.915

The reflections were first identified by rocking the specimen about the ω-axis and using the X-ray eye miniFDI camera. The large field of view of the miniFDI camera enabled quick and unambiguous identification of different domains types and the corresponding ω

positions for the peak intensity of each reflection. The intensity of reflections was strongest for *a*2 domains, intermediate for *a*1 domains and very weak for c domains, which suggested that the region of interest predominantly has in-plane domains present. Then, around each bright peak, three 10X magnification topographs were gathered using the PCO camera with 5 min integration time, corresponding to left, centre, and right of the peak position in ω angle. Thus, the topographs were obtained at each of three tilt positions (ω-angle) in the region of interest. This method proved useful, as collecting reflections using PCO camera was time consuming.

4.6.2. Data processing

The aim is to patch together the *a*1 and *a*2 reflections to examine if the domain pattern could be seen in the topographs captured using PCO camera. A typical raw topograph obtained from the PCO camera is shown in figure 4.24 (a). The image was despeckled and corrected for background (figure 4.24(b)). As the specimen was tilted about ω and χ axes to obtain the reflections, the resulting camera image is a distorted view of the sample surface and it is necessary to map back the topographs onto the specimen surface to be able to patch together *a*1 and *a*2 reflections. A MATLAB code, developed by Tsou and Huber was used to map the topographs back into the sample surface co-ordinates. The code first identifies the position of each pixel of the topograph onto the specimen surface using a rotation matrix. Then the intensity of a projected pixel is computed using a weighted average of the intensities of the nearby pixels in the topograph. The method is non-conservative as the intensity of the projected pixels may be overestimated and is also time consuming. To reduce the processing time, only bright regions in the topographs, as outlined by the dashed yellow coloured rectangle (see figure 4.24(b)), were processed.

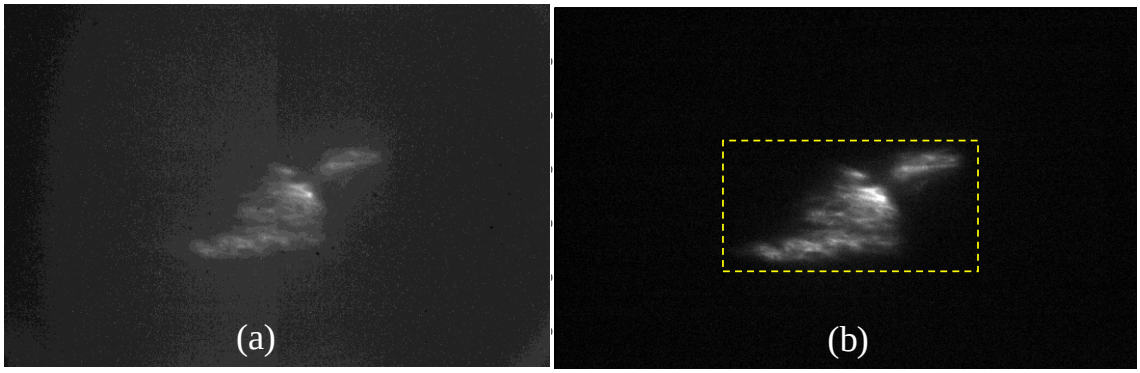

Figure 4.24: (a) Raw image of *a2* reflection at ω = 33.915° (b) Same image despeckled and corrected for background. A dashed rectangle indicates the region mapped back onto the specimen surface.

Individual topographs corresponding to each tilt angle were processed to obtain maps in the specimen co-ordinates. The three resulting images taken across each peak in ω were then summed to give a total intensity map. Figure 4.25 shows total intensity maps for *a*1 and *a*2 domain, as mapped onto the specimen surface. The PCO camera with 10X objective has an effective pixel size of 0.36 µm and this allows length scales to be placed on the total intensity maps.

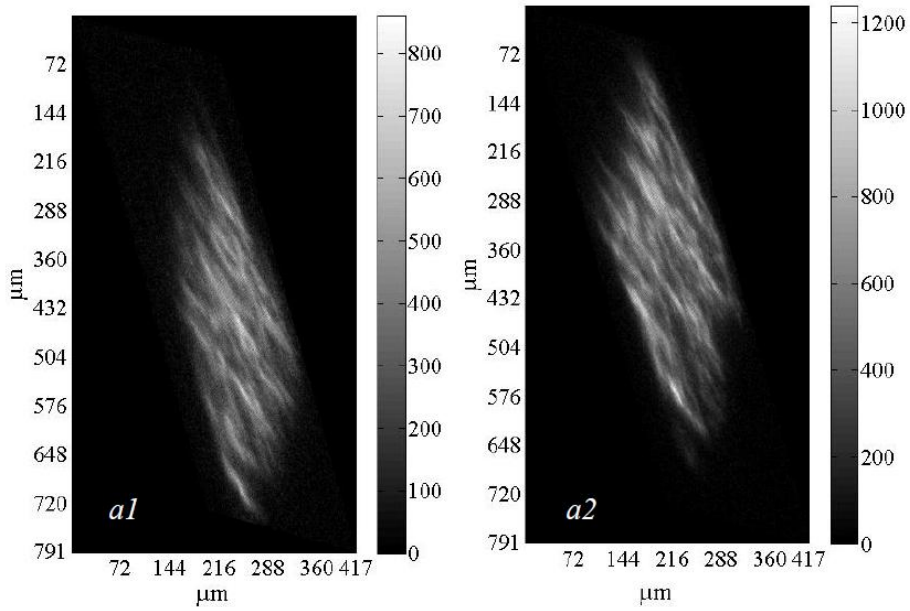

Figure 4.25: Total intensity maps for *a1* and *a2* domain types on the specimen surface.

As can be seen from figure 4.25, the total intensity for *a1* domains is less than that of *a2* domains (see scale bars on the right hand side of each map). However, while there is

some banding suggestive of patterned domains, the images look fuzzy rather than showing a clear domain structure comprising of *a1* and *a2* domains.

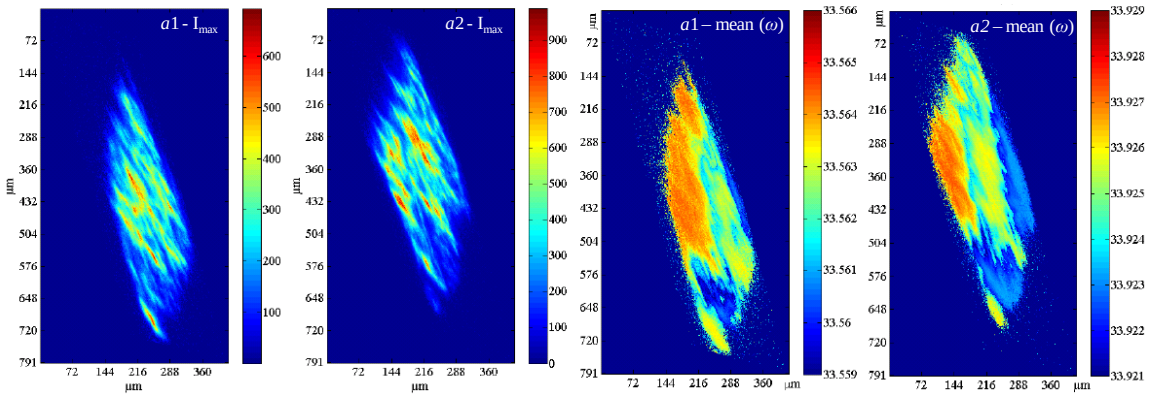

Figure 4.26: I_{max} and mean ω-tilt ($\overline{\omega}$) map for *a1* and *a2* domain types on the surface of the specimen

One reason for this fuzziness could be that the simple summation used to find the total intensity is sensitive to weak reflections present over a wide range of ω values. An alternative approach is to find the maximum intensity (I_{max}) and mean ω–tilt ($\overline{\omega}$) for each pixel using a Gaussian fit. The data was processed pixel-wise to fit a Gaussian curve and I_{max} and $\overline{\omega}$ maps were obtained as shown in figure 4.26. Fitting a Gaussian curve appears to improve the intensity images, but does not completely remove the fuzziness in the domain maps. There are number of factors that could have contributed towards such fuzziness in these images. One of the main reasons is the sample to detector distance which was 445 mm in this case. This allows spreading of the wavefront by Fresnel diffraction thereby reducing the clarity of the images. There may also be a contribution from sub-surface diffraction that blurs the images (penetration depth ≈ 36 μm). Local straining or tilting of the domains can also be an important factor as that would shift the camera position of the reflections slightly. To reduce fuzziness, the PCO camera could be moved closer to the specimen, but this was not possible in the present experimental arrangement because of the space constraints.

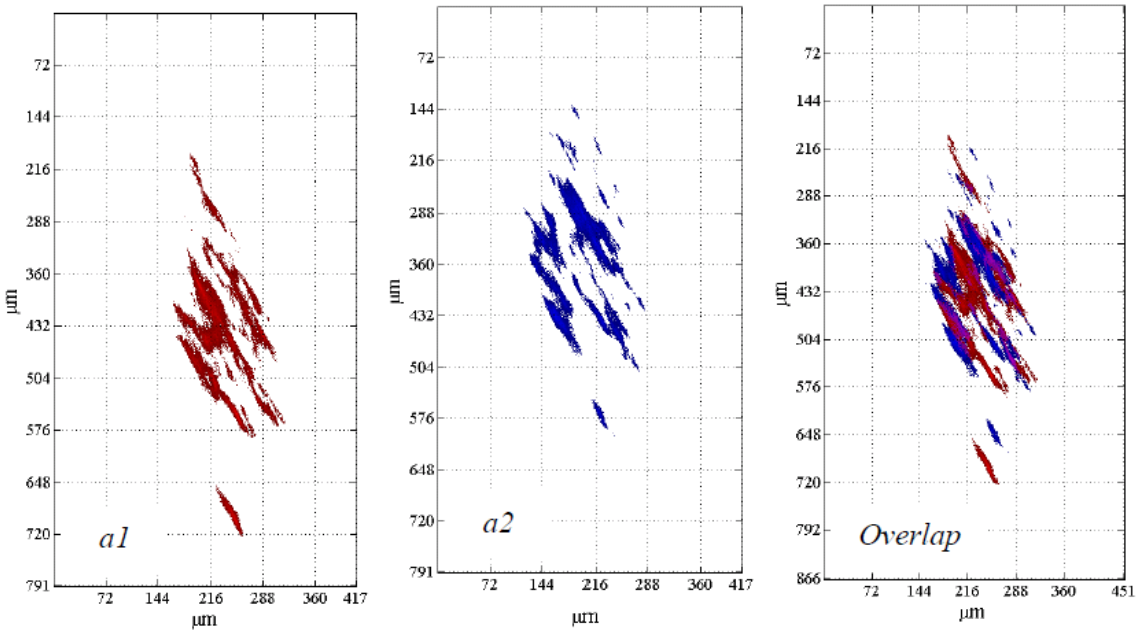

Figure 4.27: I_{max} maps for *a1* and *a2* domain types overlapped on each other.

It is of interest to overlap the reflection topographs corresponding to *a1* and *a2* domains such that *a2* reflections fill gaps in the *a1* topographs and vice-versa. Figure 4.27 shows an attempt at overlapping the maximum intensity images in this way. The images were first passed through a threshold filter to remove low intensity parts of the reflection. It appears that some features in these images fit together in complementary fashion, but the images are not sufficiently clear to be conclusive.

4.6.3. Summary: Experiment 2

Asymmetric reflections used in this experiment to map the in-plane domains produced poor quality (fuzzy) topographs and the fine microstructure was not revealed clearly. Improvement in the quality of images could be obtained by reducing the specimen to camera distance, which would be challenging while using the PCO 4000 camera.

4.7. Mapping needle domains by X-ray topography: Experiment 3

In experiment 3, a specimen containing needle domains was mapped using the asymmetric reflections. In a few of the regions on the specimen surface, coarsely spaced

needles with spacing of about 0.2 mm and width of about 10 μm were observed. One of the aims was to test if this fine structure could be resolved using the MiniFDI camera (pixel size of 6.5μm). Also, a smaller detector distance was used in a quest to improve the clarity of topographs.

4.7.1. Experimental details

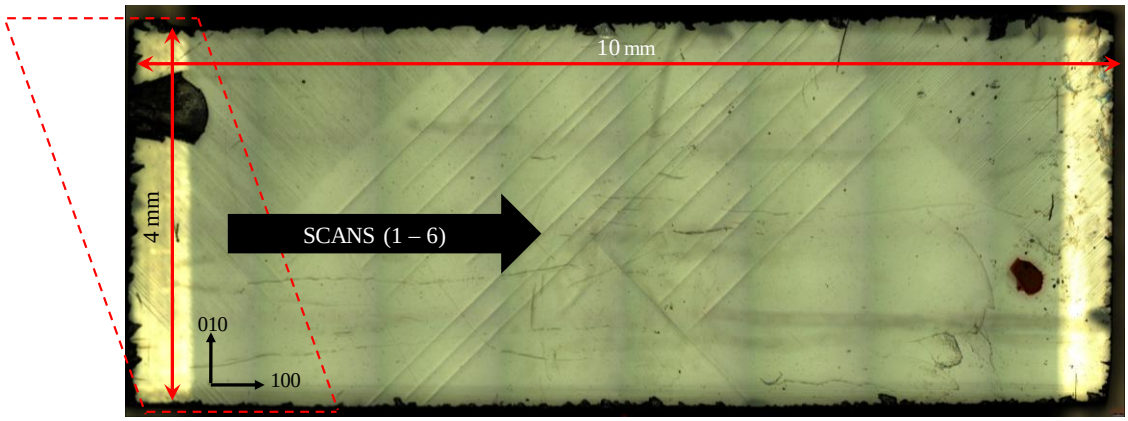

Figure 4.28: Optical micrograph of the needle specimen mapped by using synchrotron X-ray light.

A BT single crystal specimen (10 x 4 x 0.55 mm) containing needle type of domains (figure 4.28) was mapped using 18.6 keV X-ray light. The experimental arrangement is similar to figure 4.13. Here, first, the MiniFDI X-ray eye camera was used at a detector distance of 375 mm to discriminate between various domain types based on their position on the camera image. The camera was then moved to a "close" detector distance (115mm) to produce reflection topographs. To achieve the close detector distance, the 2nd order reflections of type {402} were used at 18.6 keV: this reduced the diffractometer angles ω and δ sufficiently to avoid collision between the camera and eulerian cradle (for the $a2$ reflection: $\delta_{[306]}$ = 68.26° and $\omega_{[306]}$ = 33.915° while $\delta_{[402]}$ = 42.04° and $\omega_{[402]}$ = 22.02°). The close detector distance had the advantage that the effects of beam divergence after reflection from the sample were minimised. This greatly improved the clarity of the topographs, however, a disadvantage of the close detector distance was a low intensity haze evident in some of the topographs, possibly due to parasitic scattering,

or sub-surface diffraction. Figure 4.29 shows the planes of asymmetric reflections, where the angle $\chi' = 90° - \chi$.

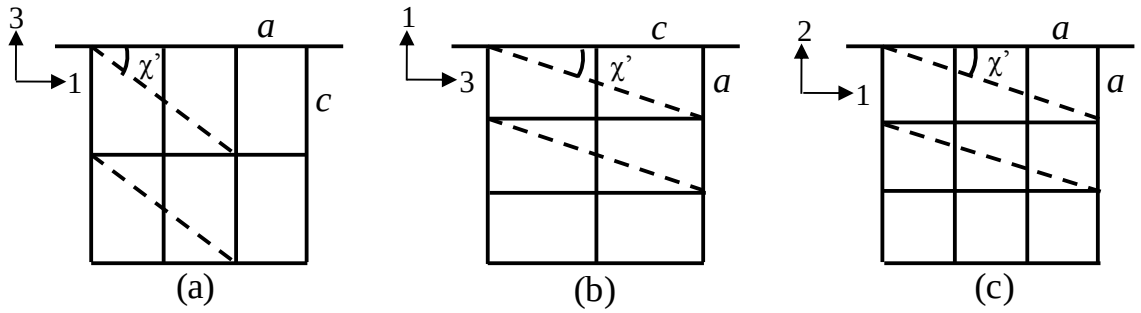

Figure 4.29: Asymmetric reflections (a) *c*-reflection [204] (b) *a*1-reflection [402] and (c) *a*2-reflection [240].

Table 4.4 lists the angles for the lattice planes computed using the lattice parameters a = 3.985Å and c = 4.029Å.

Table 4.4: Asymmetric reflections and corresponding angles computed using Bragg's equation (λ = 0.67 Å, 2nd order reflections of {402} type).

	c-reflection [204]	*a*1-reflection [402]	*a*2-reflection [240]
d-spacing (Å)	1.7978	1.786	1.7821
χ' (°)	26.817	26.314	26.565
δ (°) (= 2θ)	43.761	44.065	44.166

The beam was slitted to 2 mm width x 3 mm height and specimen area was mapped by tilting the specimen, at a range of tilts in the ω axis defined by 21.02º to 23.02º in steps of 0.005º, with 1s integration time for each image. The sample position was incremented using the *x*-*y* stage of the diffractometer and in total 6 such scans were collected to map the entire surface area of the specimen. Dashed red coloured lines in figure 4.28 show the illuminated region of the specimen at a typical sample position.

4.7.2. Results

Use of "close" and "far" detector distance: As can be seen from the rocking curve (figure 4.30), *a*1, *a*2 and *c* domains on the specimen surface could be identified. The domain

structure on the specimen surface comprises of a comb of *a*1 and *a*2 domains (*a*1(comb) and *a*2(comb)), a few fine *a*1 needles (*a*1(needles)), *c* domains (*c*(bottom) and *c*(top)) and a large *a*2 domain (*a*2(matrix)).

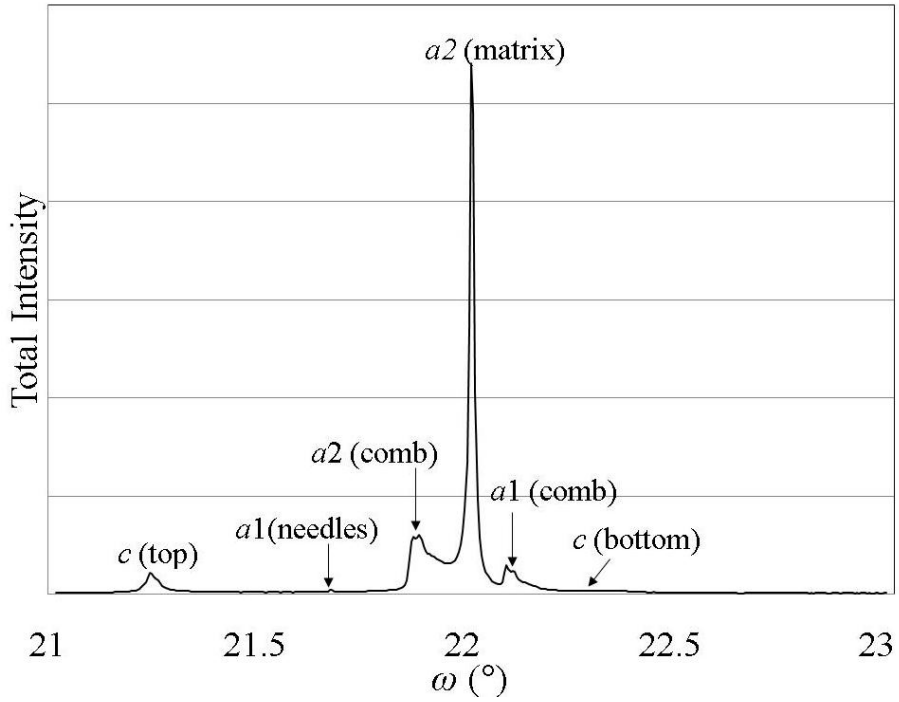

Figure 4.30: Rocking curve at x = -1 mm and y = 0.41 mm (Scan 1) on the specimen surface showing different domain types.

Now, topographs were captured for two detector distances – "far" detector distance (*dd* = 375 mm) and a "close" detector distance (*dd* =115mm). A range of ω values was defined for each domain type such that the peak entirely lies within that range, for example, in the case of the *a*2(comb), the ω range used was 21.79°-21.955°. Next, integrated images were obtained by summing intensity over the corresponding range of ω values for each domain type. This gave two sets of integrated images, one for each detector distance as shown in figure 4.31.

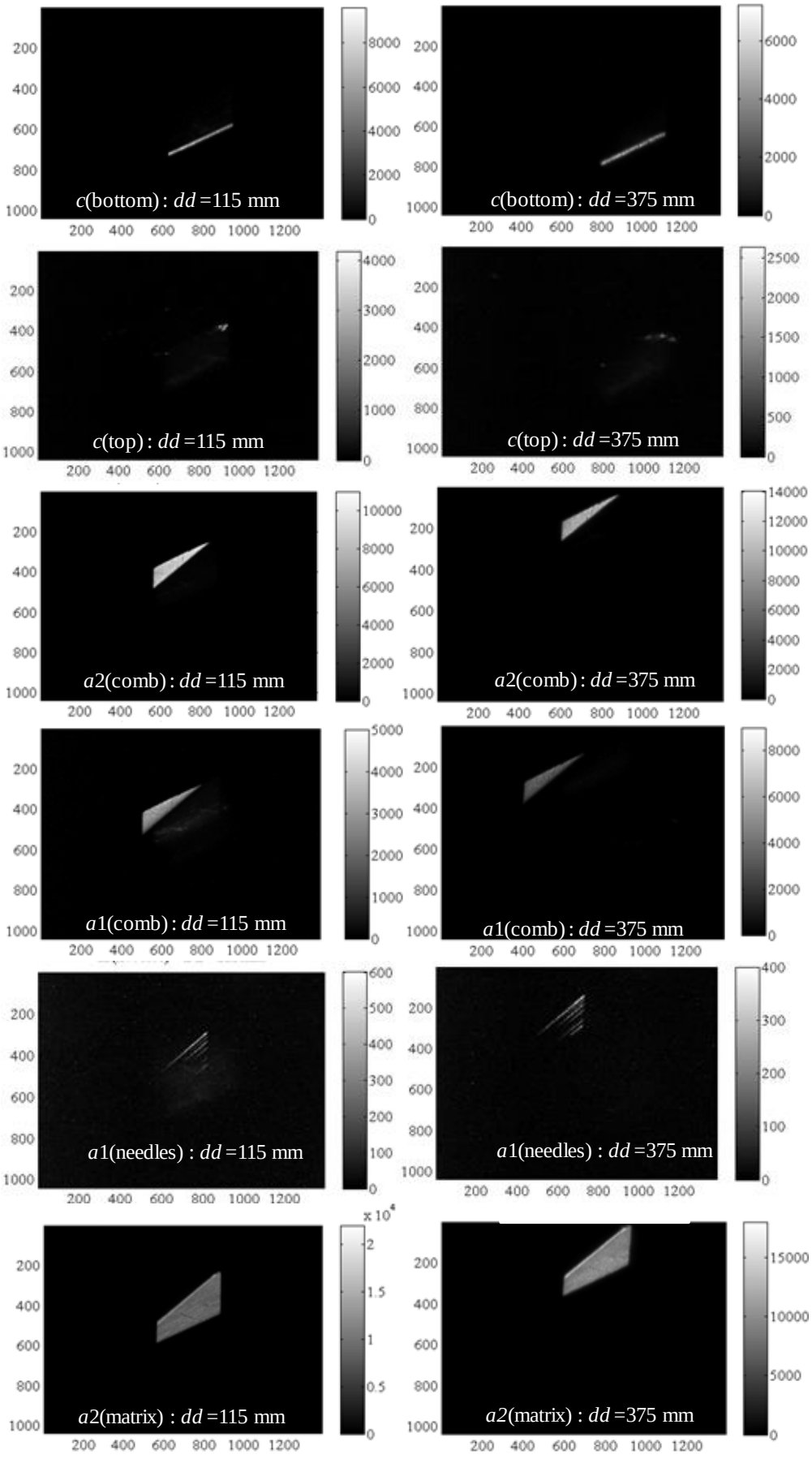

Figure 4.31: Comparison between Integrated images at a two detector distances.

At the far detector distance, the reflections are spatially separated due to the difference in δ values (given in table 4.4). Reflections having higher δ value appear vertically above those with lower δ value. Hence, *c* domain reflections would appear vertically below *a*1 and *a*2 reflections. Further, due to the difference in χ values, an *a*1 reflection would appear horizontally displaced to the left side of an *a*2 reflection. These separations are prominent at the "far" working distance allowing identification of the different domain types. However, the intensity and quality of the reflections is compromised at the "far" working distance. For the "close" detector distance, the reflections are not spatially separated, but higher intensity is obtained for each reflection, which improves the clarity. Note the scale on the left of each image for maximum intensity values.

Composite image: A set of topographs was generated by mapping the entire specimen surface using the "close" detector distance. These topographs were further processed to produce a composite image for comparison with optical micrographs. Various reflections were colour coded according to their spectral range for easy identification. The resulting composite image was generated as follows: (1) integrating over a range of ω values, within which a particular reflection was observed for each scan (images as shown in figure 4.31), (2) Within each scan, the integrated images of different domain types were overlapped on each other. Each domain type was then attributed a colour depending on its position in the spectrum of ω values and (3) joining together overlapping images of all the scans with the help of surface features. The resulting composite image is shown in figure 4.33 and the colour scheme is given by the colour bar.

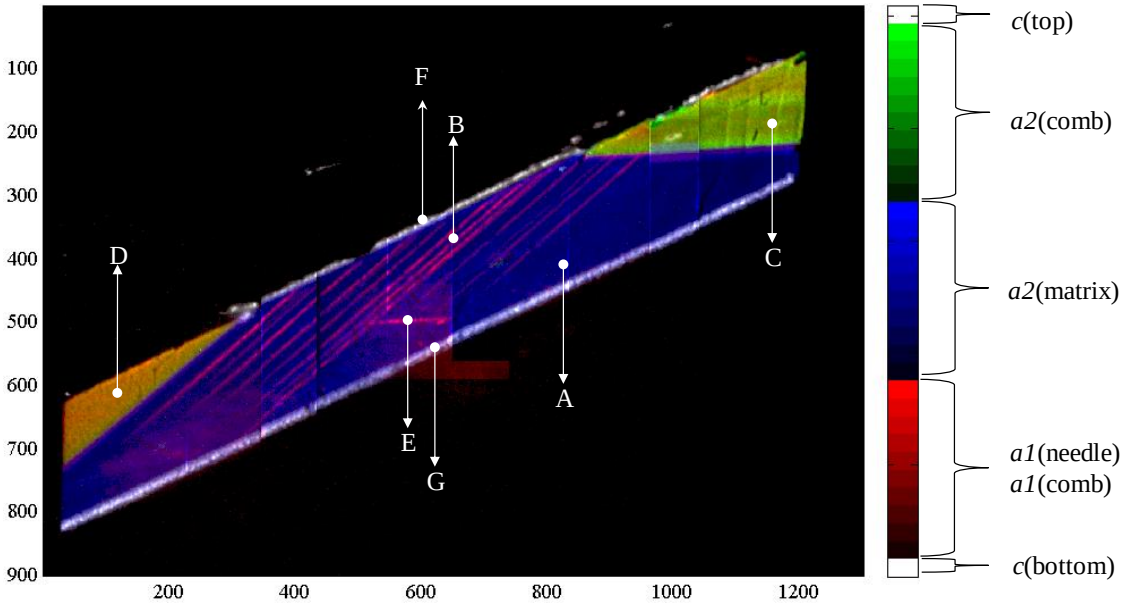

Figure 4.32: Composite image with colour coded domains.

The composite image shows a good agreement with the optical micrograph and demonstrates the capability of synchrotron topography to resolve fine needles having width about 10 μm. It also reveals information, such as presence of *c* domains as closure domains near the specimen edges which were not visible in the optical micrographs. The closure *c* domain is shown in the figure 4.33(a). Use of asymmetric reflections has successfully discriminated between in-plane *a*1 and *a*2 domains. The composite image shown in figure 4.32 is skewed due to rotation about ω and χ axes; in figure 4.33(b) the composite image of figure 4.32 is transformed to remove foreshortening. This corrected image shows a good correlation with the optical image in figure 4.33(c).

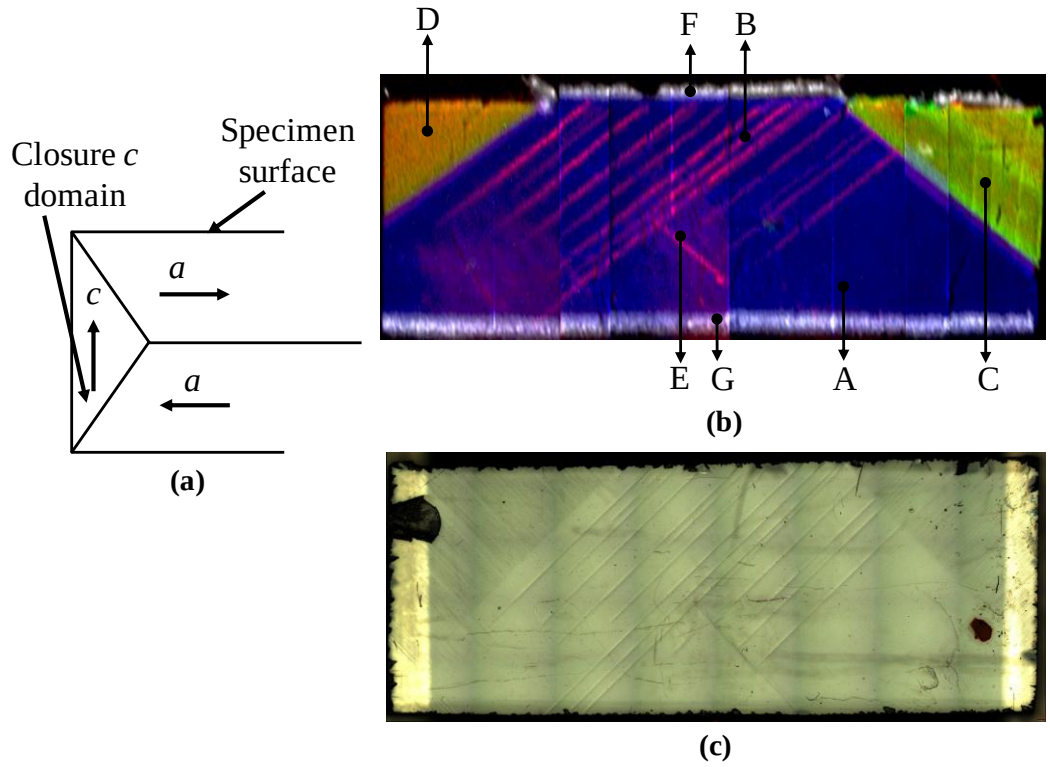

Figure 4.33: (a) closure domains (b) composite image corrected for foreshortening compared with optical micrograph.

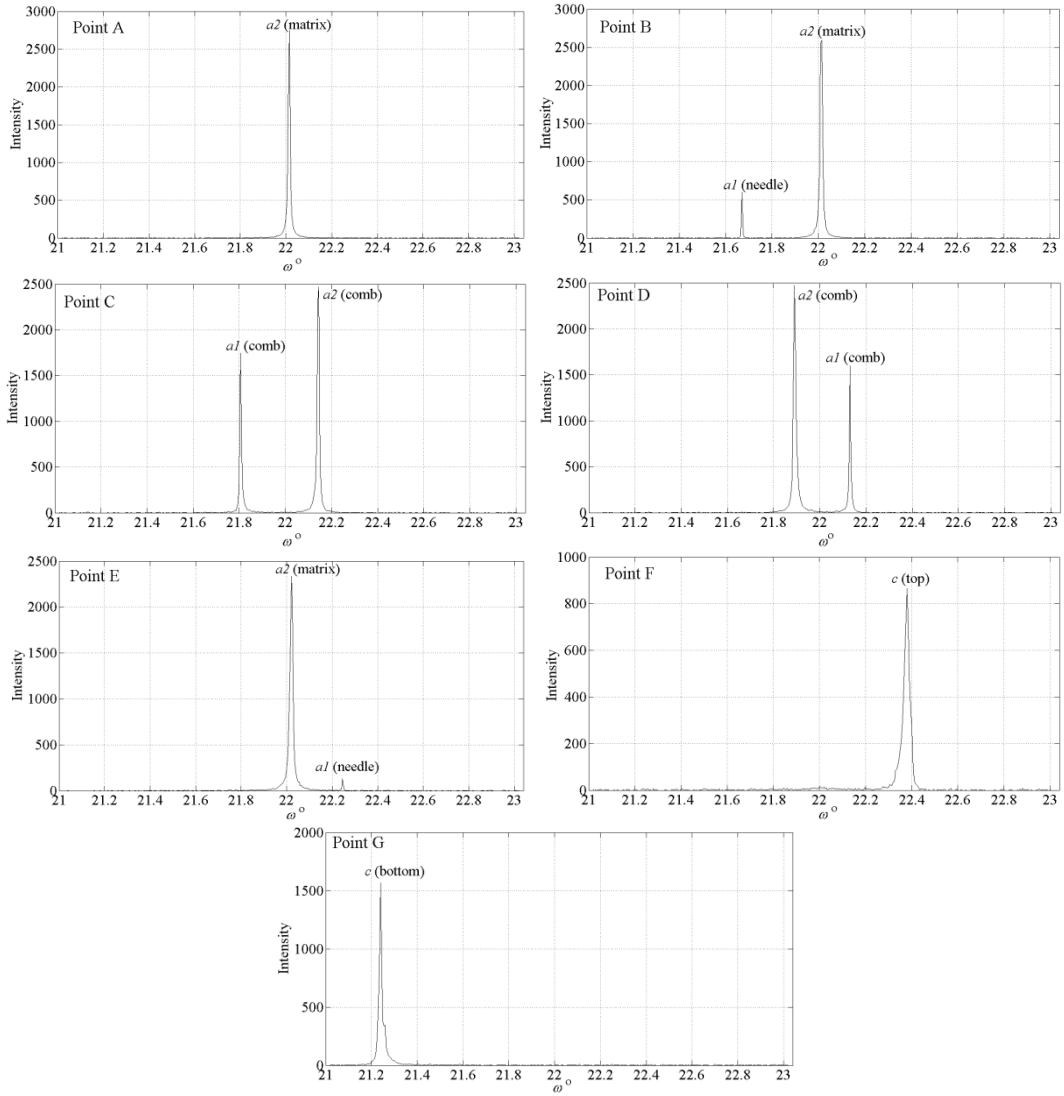

Figure 4.34: Rocking curves corresponding to points A to G at various locations on the surface of the specimen.

Further, it is possible to obtain point-wise rocking-curve data from the underlying data set. Points A to G in figure 4.32 and 4.33 lie at different locations on the specimen surface and are chosen such that each domain type is covered. Figure 4.34 shows rocking curves for points A to G. Thus, the technique is capable of revealing small relative tilts between the domains at each point on the specimen surface and regions where fine mixtures of domains are present, such as points C and D.

4.8. Piezoresponse Force Microscopy (PFM)

In synchrotron diffraction experiment 2 (section 4.6), asymmetric reflections showed that in-plane *a*1 and *a*2 domains are present in the region of interest on the specimen surface. However, due to fuzziness of the topographs, the domain configuration could not be clearly identified. Etching the crystal would not be able to reveal the pattern as etching affects *a*1 and *a*2 domains equally. Another technique, piezoresponse force microscopy (PFM) was used to reveal the domain pattern in this crystal. This technique is explained in detail in reference [156]. In this section, first the two modes of PFM are explained with an illustration of the technique.

4.8.1. Vertical PFM

Two modes of PFM, vertical and lateral PFM were used to image the out-of-plane (*c*+ and *c*-) and in-plane (*a*1+/-, *a*2+/-) domains respectively. Antiparallel domains in single crystal BT were mapped using vertical PFM. Asylum Research's MFP-3D AFM system with an Olympus AC240TM cantilever was used in piezoresponse mode. The other parameters were: scan rate = 1 Hz, driving voltage = 4.4 V and frequency = 267 kHz with a contact resonance. Surface displacements of the out-of-plane domains give a phase difference of 180° across domain walls. A 90 x 90 μm region was mapped at two nearby locations on the specimen surface such that there was an overlap of about 30μm. Figure 4.35 shows the PFM phase response where *c*+ and *c*− domains are identified based on phase difference. In the case of *c*+ domains, the application of the positive bias results in compression of the local region and the response is out of phase with the applied bias i.e. phase difference is 180°. An opposite electromechanical response is sensed for *c*- domains which give 0° phase difference. Thus vertical PFM is able to distinguish out-of-plane domains, such as the watermark pattern seen in figure 4.35.

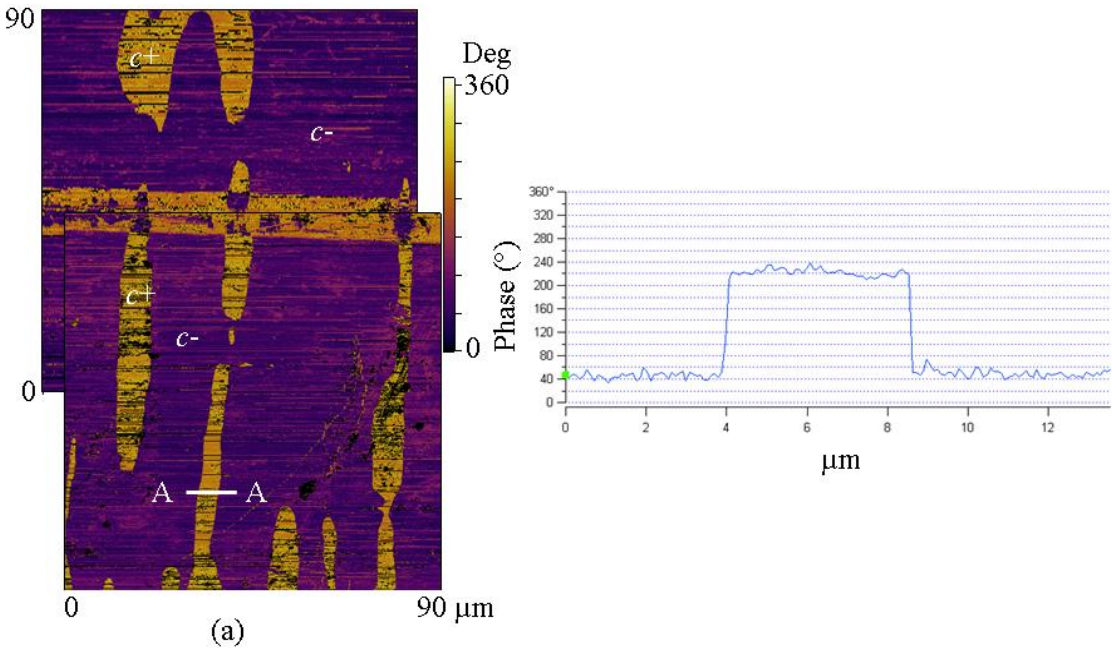

Figure 4.35: Vertical piezoresponse force microscopy on BT single crystal showing $c+$ and $c-$ domains with 180° domain boundaries.

4.8.2. Lateral PFM

A small region of the specimen used in synchrotron experiment 2 was mapped by lateral PFM. The experimental settings used were similar to those used for vertical PFM, except that a higher frequency of 885 kHz was used for lateral contact resonance. Here again the phase response of the surface displacement is used to distinguish between the different polarities of the in-plane *a* domains. The upper part of figure 4.36(a), marked "Top" shows strongly contrasting bands of domains with a 180° phase change within the band indicating 180° domain walls (cyan and red colours). These domains are oriented such that their d_{15} coefficient gives rise to surface displacements in the x_1 direction. Also visible in the "Top" image are intermediate bands of 90° domains which do not show strong contrast as their piezoelectric response produces displacements in the x_2 direction. By turning the specimen through 90°, the other half of figure 4.36(a), marked "Bottom", was recorded. Superimposing the phase responses reveals a particular arrangement with alternate bands of 90° domains, each band containing 180° domain walls. This is a well

known herringbone structure schematically represented in figure 4.36(b). Thus, the herringbone pattern of in-plane *a* domains which could not be seen in the synchrotron X-ray topographs, was successfully imaged by lateral PFM.

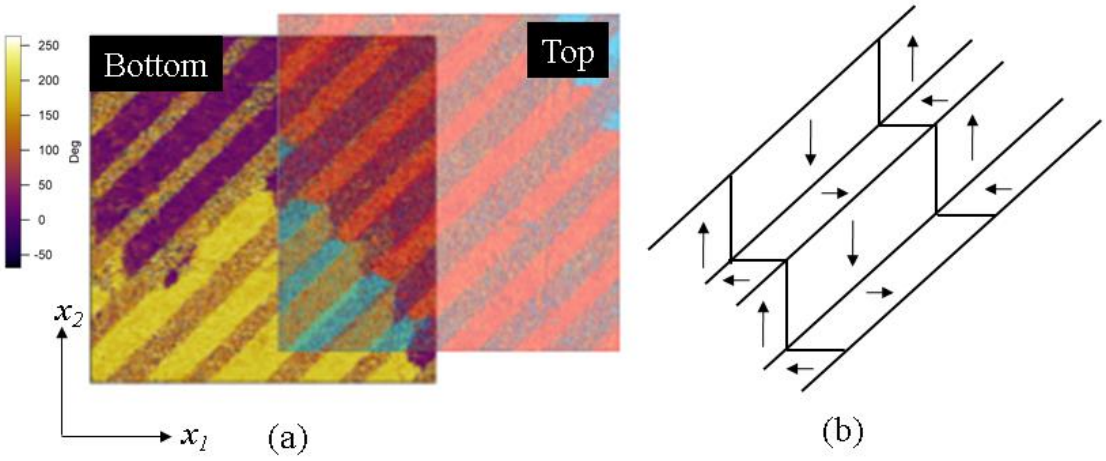

Figure 4.36: (a) Lateral piezoresponse force microscopy on a BT single crystal showing herringbone structure (two 40μm regions), schematically represented in (b).

4.9. Theoretical predictions vs. observed microstructure

Typically, low-energy compatible microstructures form multirank laminate patterns which can be theoretically predicted. A laminate structure is compatible if it has one-to-one perfectly aligned domain pattern with the resulting domain walls satisfying the compatibility equations given in section 4.2. Tsou *et al*. [161] developed a method to systematically classify all the laminate domain patterns that are exactly compatible using a limited set of crystal variants. A pair of variants combines to form a rank-1 laminate structure while a rank-2 laminate is obtained by combining a pair of rank-1 laminates. Subsequently higher rank laminations could be obtained which results in a fine microstructure. Tsou *et al*. found all the possible rank-2 arrangements of domains in the polar tetragonal crystal system [158]. It is interesting to note that only eight distinct rank-2 laminate patterns that satisfy compatibility conditions at all domain walls were found. More details about the theoretical model could be found in [158].

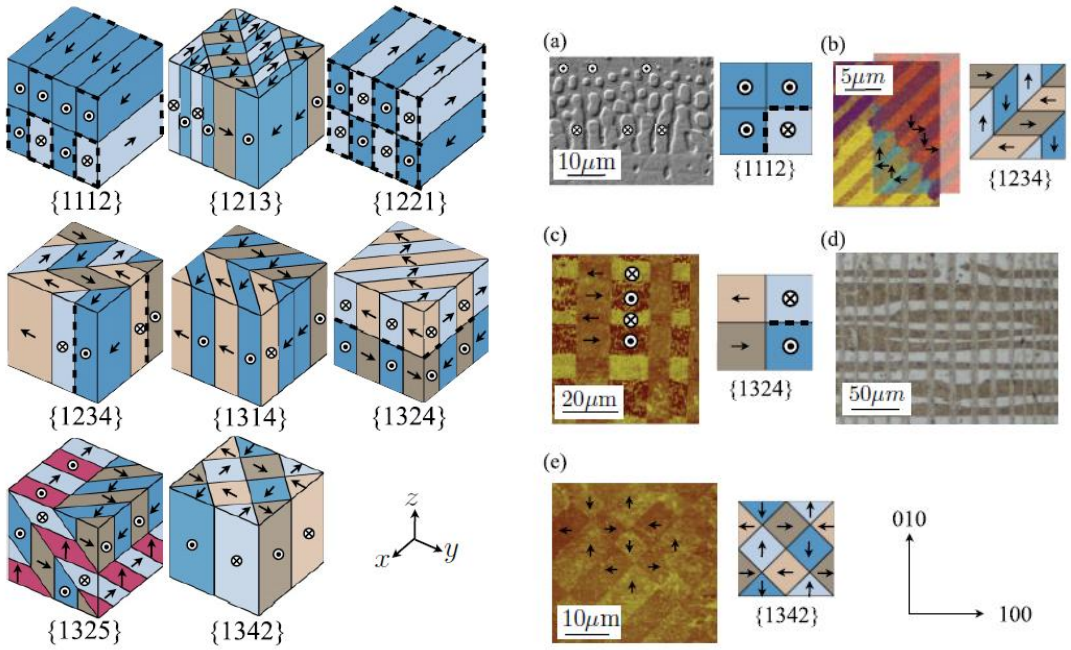

Figure 4.37: Eight distinct rank-2 laminated exactly compatible domain patterns were compared with the micrographs using techniques such as PFM, etching followed by SEM, AFM, and optical microscopy (after Tsou *et al.*, 2011, [158]) .

These theoretically predicted patterns were compared with the observed domain structures in single crystal BT. Figure 4.37 shows the correlation between the patterns and the observed structures; the structures shown in (a), (b), (c) and (e) are discussed in this chapter (figure 4.11, 4.36, 4.20(b) and 4.10 respectively). The optical micrograph (d) shows the same microstructure as (c) over a larger region of the specimen.

4.10. Conclusions

In this chapter, domains in a single crystal of BT were studied using optical microscopy, synchrotron X-ray topography, etching followed by scanning electron microscopy, optical microscopy and atomic force microscopy and piezoforce response microscopy.

Successive experiments were carried out by reflection topography using unfocussed monochromatic synchrotron X-ray light. In all the experiments, domains were mapped by rocking the specimen through a range of tilts and recording topographs at each tilt

position. In experiment 1, symmetric reflections differentiating between the *a* and *c* domains were captured on a 10 x 10 mm specimen surface. The reflection topographs were then processed to obtain orientation maps for the entire surface of the specimen showing the relative tilts between adjacent domains about two orthogonal axes. The orientation maps also showed well defined boundaries between regions of distinct microstructure containing finely interspersed *a* and *c* domains and intensity maps gave an indication of their relative proportions.

The surface of the crystal used in synchrotron experiment 1 was etched and observed using optical microscopy, scanning electron microscopy (SEM) and atomic force microscopy (AFM) to obtain a local confirmation of the structures inferred from the synchrotron measurements. Optical and scanning electron microscopy also gave an estimate of the typical domain spacing which was in good agreement with the domain fraction estimated using the intensity maps in the synchrotron experiment. Typical domain spacing was found to be less than 10 μm and could not be resolved in synchrotron experiment 1 due to the limitations of the detector pixel size.

Synchrotron experiments were further developed using a high resolution camera along with asymmetric reflections to differentiate between in-plane *a* domains and *c* domains (experiment 2). Though the experiment was successful in identifying *a*1, *a*2 and c domains, a clear domain pattern could not be seen due to the fuzziness in the topographs. The fuzziness could be minimised using a smaller specimen to detector distance, which was difficult in experiment 2.

In the synchrotron experiment 3, a specimen containing coarsely spaced in-plane domains was mapped using the same technique as experiment 1 and asymmetric reflections. Unlike experiment 2, the detector used in this experiment allowed use of a smaller

specimen to detector distance: this greatly improved the clarity of the topographs allowing mapping of fine needles having width of about 10 μm. A composite image was produced using multiple scans over the entire specimen surface (10 x 4 mm). The composite image showed a good agreement with optical micrographs and also revealed the presence of closure domains. The method was also successful in revealing small relative tilts between the domains at each point on the specimen surface.

Next, the vertical and lateral Piezoresponse force microscopy (PFM) was used to resolve the out-of-plane (*c*+ and *c*-) and in-plane (*a*1+, *a*1-, *a*2+ and *a*2-) domains respectively. Finally, the observed domain configurations were correlated with the theoretically predicted rank-2 laminated domain patterns. The distinct capabilities of the various techniques used complemented each other and assisted the interpretation of the microstructure.

5. In-situ observations of ferroelastic switching in Barium Titanate

Domain walls move under externally applied electrical or mechanical loads enabling complete or partial reorientation of the domain structure. In this chapter, we focus on domain evolution in single crystal Barium Titanate (BT). The specimens used for mechanical testing are characterized by optical microscopy, etching and synchrotron X-ray diffraction to identify distinct domain types and domain configurations. An in-situ testing method is developed using a micromechanical test rig and domain evolution observations were made in selected regions of interest using optical and X-ray diffraction techniques. Tests and observations pertaining to different domain configurations under compressive mechanical loading are presented in this chapter.

5.1. Overview of domain evolution studies in BT single crystal

Early experiments to observe domain evolution in single crystal BT used polarized light for observing the domain structure and made electrical measurements mainly focusing on domain wall movements. Domain wall motion in single crystal BT was studied by Merz [15] as a function of external electric field and temperature. While the nucleation of domains under applied electric field is observed, the study also reports domain wall energy and wall thickness. Little [16] studied the nucleation and growth of 90° and 180° domains under externally applied electric field in a BT crystal which was a single domain initially. Nucleation of long thin wedge shaped domains was observed under optical microscope and the nucleation rate for 90° domains was estimated as a function of amplitude and frequency of electric field. Fousek and Brezina [162,163] characterised the

movement of a single 90° domain wall and 90° wedge shaped domains under cyclic electric field. Many key occurrences such as bending of a 90° wall, changes in the wall movement with time, interactions of 90° and 180° domain walls were discussed in detail. Miller and Savage [164] made similar observations and measured the velocity of 180° domain walls as a function of applied electric field, sample thickness and impurity in the crystal melt. Kim *et al*. [165] observed the changes in domain structure in sintered BT ceramic by applying a uniaxial compressive stress while cooling from 200°C to room temperature. Applied stress was found to align 90° domains and a simple lamellar structure was seen instead of a banded structure. Though there was an enhancement in the theoretical understanding of the domain evolution, very few micrographs/pictures showing domain structure at various loads were reported in these earlier studies.

Evolution of domain structure under the application of constant compressive stress and variable electric field was studied in-situ using polarized light microscopy by Burcsu *et al*. [20]. A maximum strain of 0.9% was measured at a compressive stress of about 2MPa and a peak electric field of 10 kV/cm. It is believed that stress-activated 90° domain motion and switching are responsible for such a high strain and in-situ domain observations provided evidence for the same. Shieh *et al*. [166] performed similar measurements and suggested the existence of multiple 90° switching systems to account for disproportional changes in polarization and strain during electric field unloading. The piezoelectric properties of [001] and [111] oriented BT single crystals were measured by Wada *et al.* [21]. An electric field induced phase transformation was observed in a [111] oriented crystal resulting in a d_{33} of 295 pC/N for the new engineered domain configuration. In-situ domain observations and Raman measurements assisted the interpretation, showing the domain configuration at various electric fields and identifying the phase changes. Polarization microscopy provided a useful technique to observe the

domain changes, but the method could only be used to distinguish between in-plane and out-of-the-plane domains.

Other than polarization microscopy techniques, in-situ domain observation studies in BT single crystal also utilized techniques such as X-ray and neutron diffraction, transmission electron microscopy and scanning force microscopy. Mulvmill *et al*. [118] used transmission optical microscopy coupled with a CCD camera to observe the distinct domain configurations during phase transformation on heating and cooling between 200°C and -185°C. Similarly, Synchrotron X-ray transmission topography was used to capture the domain changes during the paraelectric-ferroelectric phase change [167]. It was possible to collect several topographs simultaneously with an exposure time between 15 to 30 seconds due to synchrotron radiation and smaller collection times helped to minimize the effect of temperature variation on the topographs. The work was more focused towards development of a technique, rather than the study of domain dynamics.

Optical microscopy and scanning force microscopy were used to examine lateral domain wall motion and 90° domain switching in single crystal BT under compressive stress [153]. Figure 5.1 shows the nucleation of a new domain almost normal to the direction of applied stress and its sidewise growth with increasing applied stress. Further, PFM observations characterize the domain structure fully.

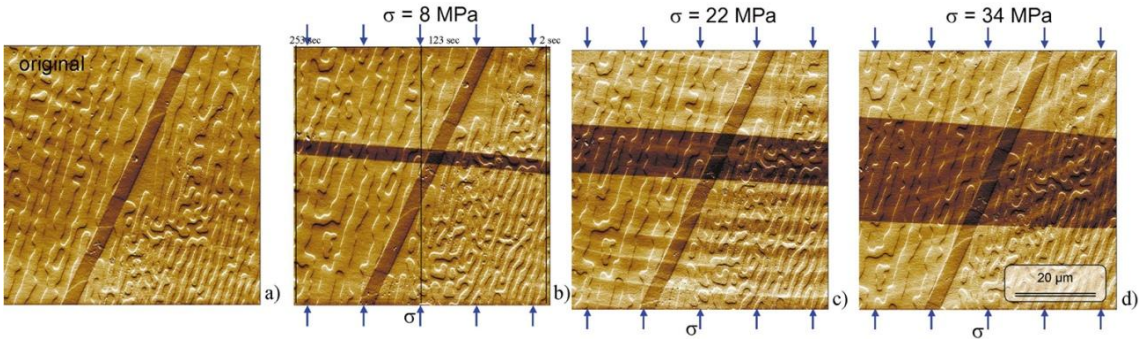

Figure 5.1: SFM topographs at various compressive stress levels showing nucleation and growth of a new domain. Note: the inclined dark band in each topograph crossing from top to bottom is reported as an artefact. (after Munoz Saldana *et al*.,[153]).

Ferroelastic switching in polycrystalline Lead Zirconate Titantate (PZT) under applied electric field was measured in-situ using a stroboscopic neutron diffraction techniques [168]. The change in relative intensity of the reflections indicated the domain switching due to electrical poling. Though the technique is promising, large collection times were required. Harrison *et al*. [169] investigated the dynamic response of single crystal $LaAlO_3$ in three point bending geometry using a stroboscopic X-ray diffractometer and combined dynamical mechanical analyser.

5.2. Experimental details

Domain evolution observations were made on two different BT specimens. In one of the specimens, the surface microstructure shows a single *a*2-oriented large domain with needle type *a*1 domains interspersed. Two different domain configurations were observed namely (i) a few widely spread needles with average spacing of 200-500 µm and (ii) a comb of fine needle domains with an average spacing of 10-15 µm. Hereafter, this specimen containing needle type domains is referred to as the "needle specimen". Domain evolution in various regions of interest on the surface of the needle specimen was studied using optical and synchrotron techniques. Domain evolution in another specimen, referred to as "specimen BT1", with a fine microstructure comprising *a* and *c* domains

was observed using synchrotron X-ray light. This specimen was primarily used to fine-tune the test procedure for X-ray observations; however, the results are also discussed in this chapter.

5.2.1. Specimen characterisation

Needle specimen: This was characterized to identify the domain types by synchrotron X-ray diffraction in section 4.6 of Chapter 4. In this specimen (Length: 10mm, Width: 4mm, thickness: 0.55mm), two regions of interest named, ROI-1, containing coarsely spaced needle domains in a matrix consisting of a large single domain, and ROI-2, comprising of many closely spaced fine needles, were identified for mechanical testing (figure 5.2(a) and (b)). Monochromatic X-ray light of energy 18.6 keV was used to study 2^{nd} order reflections of the {402} type. In the case of ROI-1, the needle domains were seen in the topographs and could be clearly identified as *a1* domains in a matrix comprising a single large *a2* domain, whereas in the comb region (ROI-2) both *a*1 and *a*2 reflections were observed confirming the presence of a comb of *a*1 needles surrounded by an *a*2 domain.

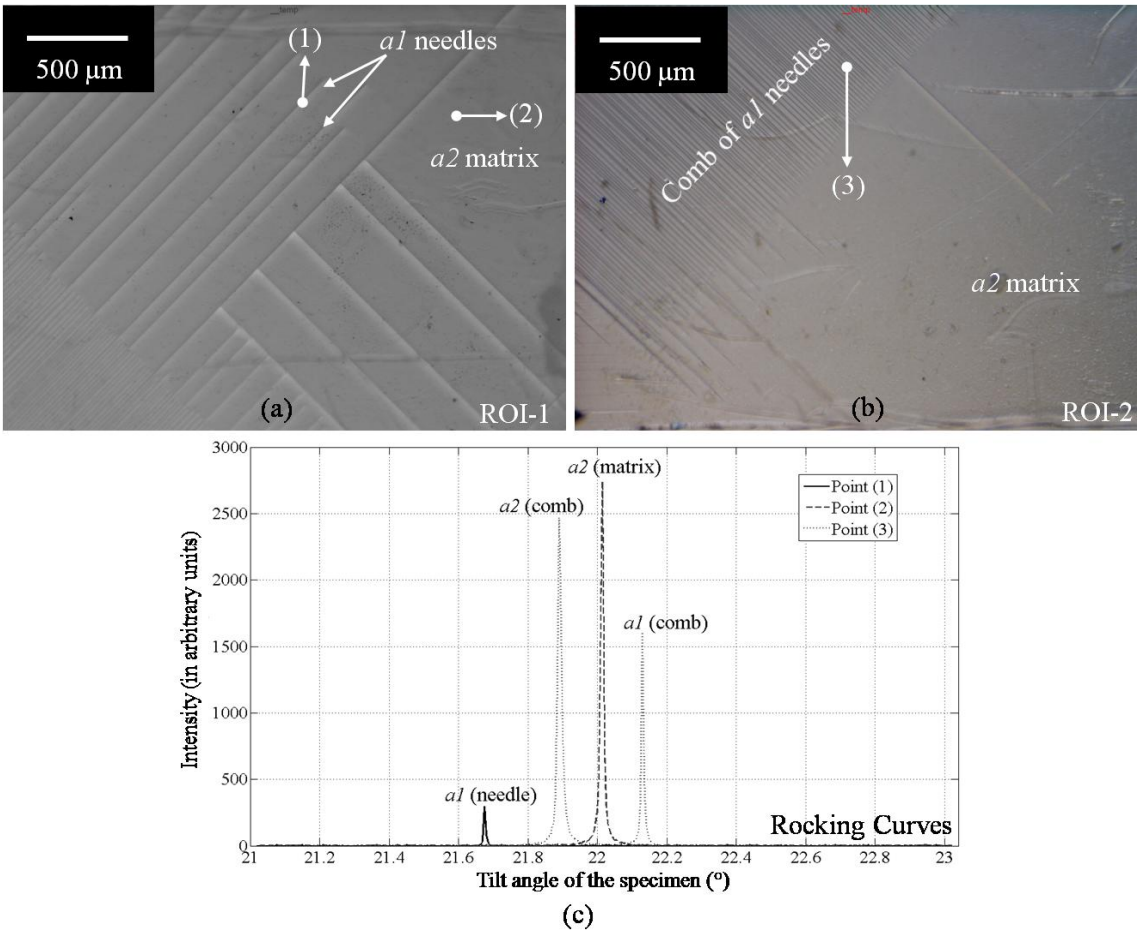

Figure 5.2: (a) In ROI-1, fine *a*1 needles are interspersed in a large *a*2 domain. Points (1) and (2) lie on needle and matrix respectively. (b) Near the left hand top of ROI-2, a comb of fine *a*1 needles is surrounded by an *a*2 domain. Point (3) overlaps on both *a*1 and *a*2 domains. (c) Rocking curves showing reflections at points (1) – (3) allowing unambiguous interpretation of distinct domain types.

This can be illustrated by rocking curves at points (1), (2) and (3) that lie in ROI-1 and ROI-2 (figure 5.2(c)). In ROI-1, Point (1) lies completely on the needle and gives a weak *a*1 domain reflection. A strong reflection can be seen for point (2) lying in the matrix comprising a single large *a*2 domain. The comb contains very fine needles of *a*1 type surrounded by an *a*2 domain and the rocking curve shows peaks for *a*1(comb) and *a*2(comb) for point (3).

Specimen BT1: Specimen BT1 (Length: 10mm, Width: 5.6mm and thickness: 0.55mm) was etched using 10% aqueous solution of HF for 20 seconds. Figure 5.3 shows an

optical micrograph of the entire specimen surface, where the dashed region marked "Synchrotron Observations" was observed in-situ using X-ray light. Figure 5.4 shows optical and AFM micrographs in the regions marked (1) and (2), showing an arrangement of *a* and *c* domain bands with fine domain spacing (~5-10 μm).

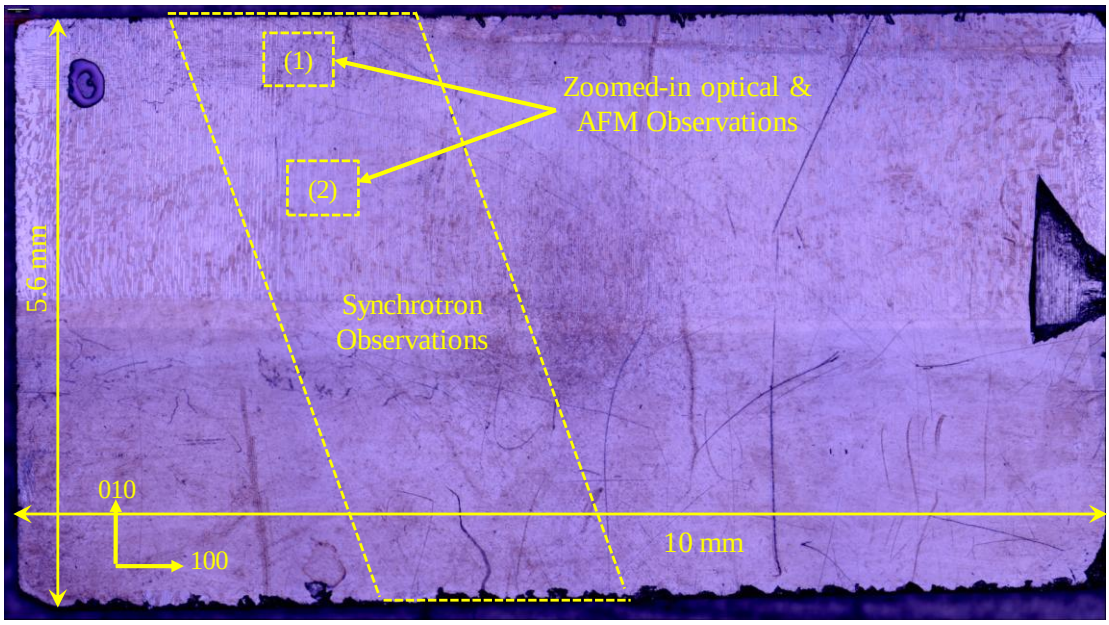

Figure 5.3: Optical micrograph of specimen BT1. A region observed during in-situ mechanical testing using X-ray light is marked "Synchrotron Observations".

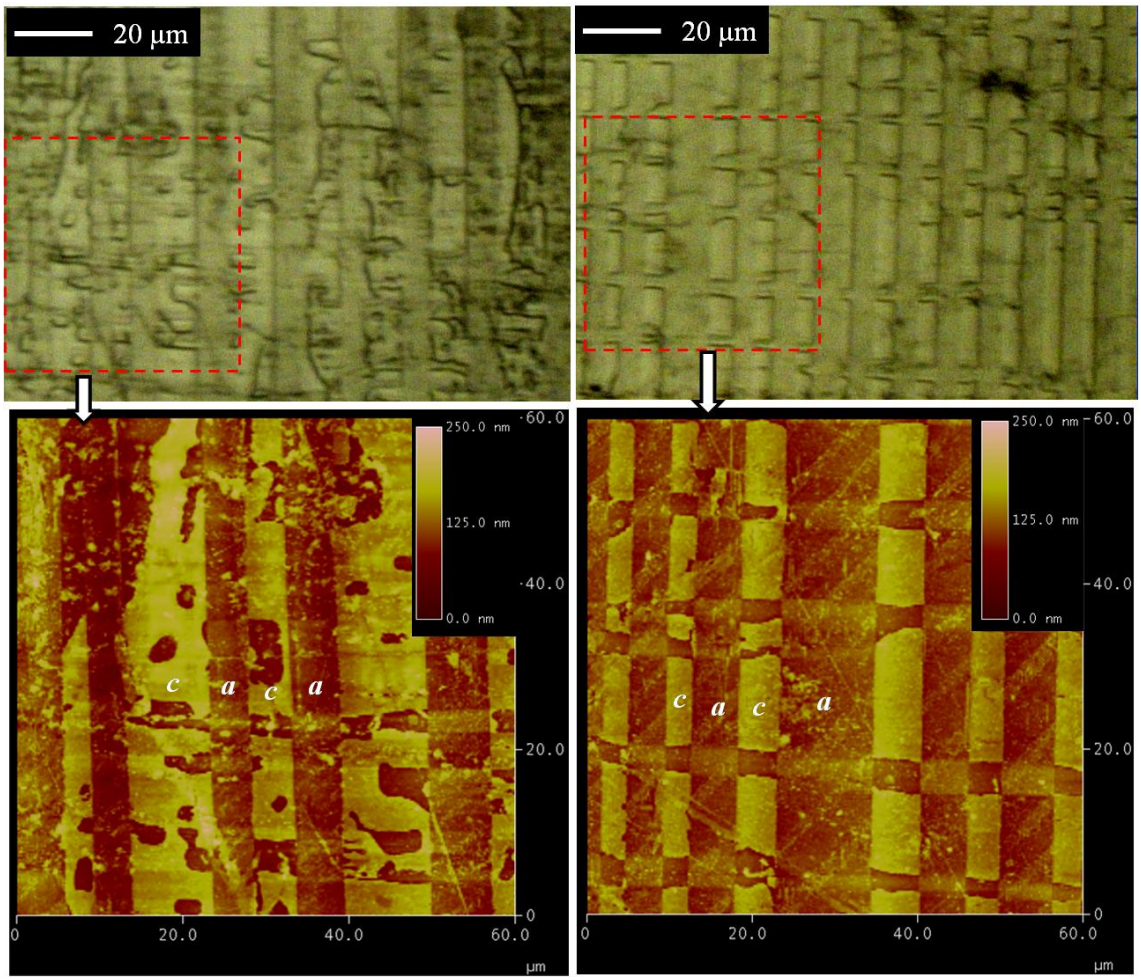

Figure 5.4: Optical micrographs and atomic force micrographs in regions (1) and (2) marked in figure 5.3. Alternate bands of a and c domains were observed with fine domain spacing.

5.2.2. Test set-up

A micromechanical test rig from Deben Ltd., UK fitted with a 200 N load cell was used to apply in-plane compressive load on the [001] oriented specimens. The specimen was clamped between the high carbon steel jaws of the test rig and mounted such that domain evolution could be observed. Separate measurements were done using Alicona's InfiniteFocus optical microscope and using synchrotron X-ray diffraction. Domain evolution observations for ROI-1 and ROI-2, schematically represented in figure 5.5, were made in separate loading cycles for optical and X-ray studies.

Test procedure for optical observations: Figure 5.5 shows an experimental set up for mechanical loading of the specimen under optical microscope. The specimen was mechanically loaded with compressive stress parallel to its longest side, in steps of about 0.45 MPa up to a maximum mean stress of 4.5 MPa.

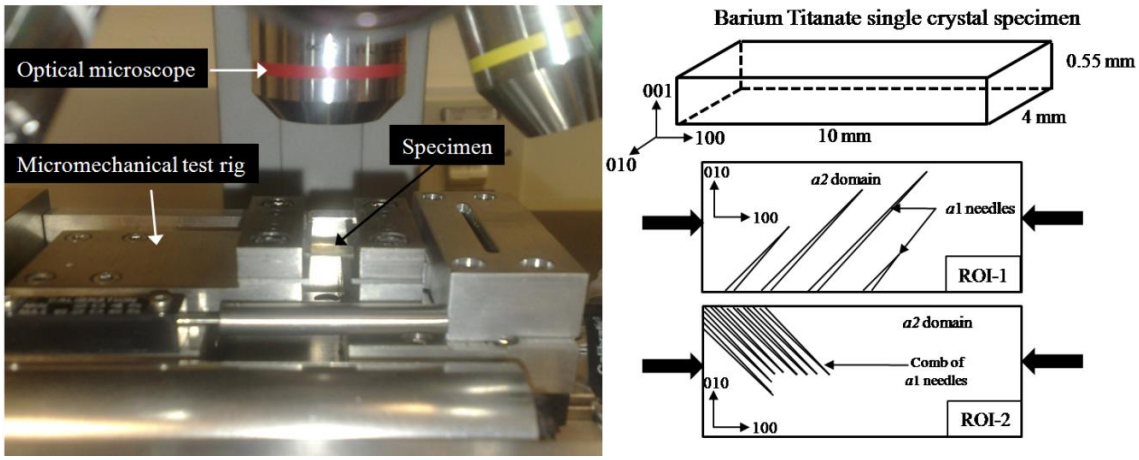

Figure 5.5: Experimental set up for in-situ mechanical testing of single crystal Barium Titanate specimen under optical microscope.

At each stress level, an optical micrograph of ROI-1 was captured. The load was held constant while capturing each optical micrograph. The specimen was fully unloaded in steps of 0.9 MPa with micrographs at each unloading step. This produced a set of micrographs corresponding to each load level showing domain evolution under mechanical loading. Another loading cycle, capturing optical micrographs of ROI-2 at No load (0 MPa), peak load (4 MPa) and at 2.7 MPa while unloading (Unload-2.7 MPa), was recorded.

Test procedure for synchrotron observations: Figure 5.6 shows an experimental set up for in-situ observations using synchrotron X-ray light. Specimen BT1 was mounted in the Deben test rig, fixed and centered on the diffractometer at Beamline B16. The 5.6 x 10 mm surface of the sample was used to produce reflection topographs. The MiniFDI X-ray eye camera was mounted on the diffractometer arm at a distance of 517 mm from the

sample. The specimen was exposed to a 2 x 2mm beam of 18.6 keV light and the 3rd order reflections of type {603} were used to distinguish between different domain types. This allowed distinguishing *c* domains from *a1* and *a2* domains.

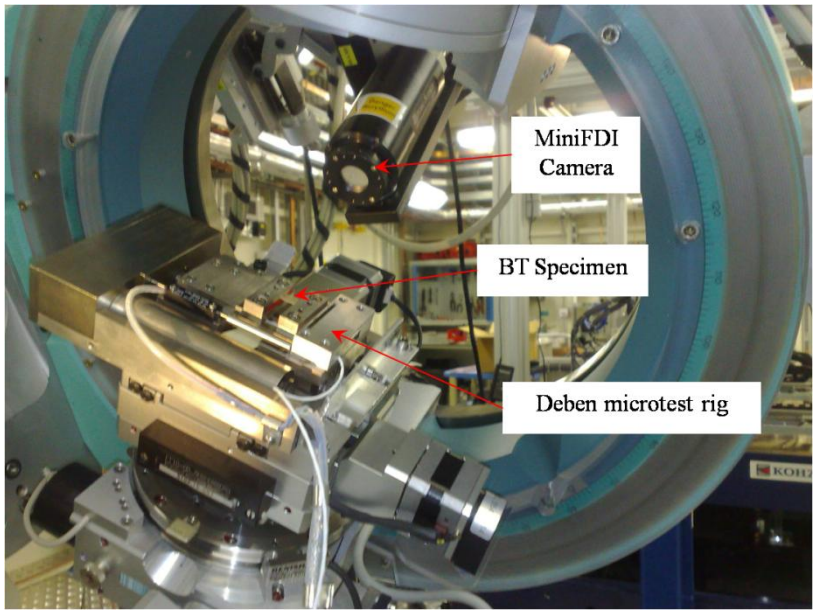

Figure 5.6: Specimen of BT single crystal mounted on a Deben microtest rig centered on the diffractometer.

Table 5.1 lists the reflections and corresponding angles.

Table 5.1: Asymmetric reflections and corresponding angles.

	c-reflection [306]	*a*1-reflection [603]	*a*2-reflection [360]
χ (°)	27.16	27.287	27.072
δ (°)	67.72	68.225	68.330
ω (°)	33.813	34.069	33.91

The sample was mechanically loaded with compressive stress parallel to its longest side, in steps of about 0.25 MPa up to a maximum mean stress of 1.7 MPa. At each stress level, reflection topographs were recorded by rocking the specimen through the full range of ω axis values at which reflections were observed. Topographs were collected at two δ values, one for *a*1 and *a*2 reflections and the other for *c* reflections, at a range of tilts in the ω axis defined by 33.55º to 34.25º in steps of 0.001º, with 1s integration time for each

image. This produced a set of topographs corresponding to each load level showing domain evolution under mechanical loading. The specimen was then fully unloaded and topographs were collected at 0.8 MPa and 0.03 MPa during unloading.

Next, the needle specimen was mounted in the Deben test rig. The specimen was loaded in a similar manner with the 4 x 10 mm surface exposed to a 2 x 2 mm beam of X-ray light of 18.6 keV energy. The MiniFDI X-ray eye camera was used at a working distance of 115 mm to produce reflection topographs using the 2^{nd} order reflections of {402} type at 18.6 keV (this is the same specimen as that described in section 4.7 of Chapter 4). Two regions of interest, ROI-1 and ROI-2, similar to the optical observations were observed one after the other under incremental mechanical loading. The needle specimen was loaded to a maximum mean stress of 2.6 MPa in steps of 0.5 MPa while recording topographs in ROI-1. Topographs were collected at a range of tilts in the ω axis defined by 21.02º to 23.02º in steps of 0.0025º with 1s integration time for each image. The specimen was then fully unloaded in steps of 1 MPa with topographs at each unloading step. In the case of ROI-2, observations were made up to a higher mean stress level of 4.5MPa using the same load step size and ω axis tilt range, but in steps of 0.005º. During unloading, topographs were collected in steps of 1.4 MPa. Table 5.2 summarizes the loading for each specimen.

Table 5.2: Maximum mean stress applied during each test using optical and X-ray techniques.

	Optical measurements – Peak stress	X-ray measurements- Peak stress
Specimen BT1	-	1.7MPa
Needle specimen (ROI-1)	4.5MPa	2.6MPa
Needle specimen (ROI-2)	4MPa	4.5MPa

5.3. Results: Mechanical testing of specimen BT1

The topographs collected at each load level were further processed by summing intensity over the full range of ω values. The resulting topographs for *a* domains and *c* domains at

each load step are shown in figure 5.7 and 5.8 respectively. The total diffracted intensity (camera count rate, no units) against the rocking angle (ω), gives a rocking curve, as shown for 0 MPa, 1.7 MPa and unload – 0.8 MPa.

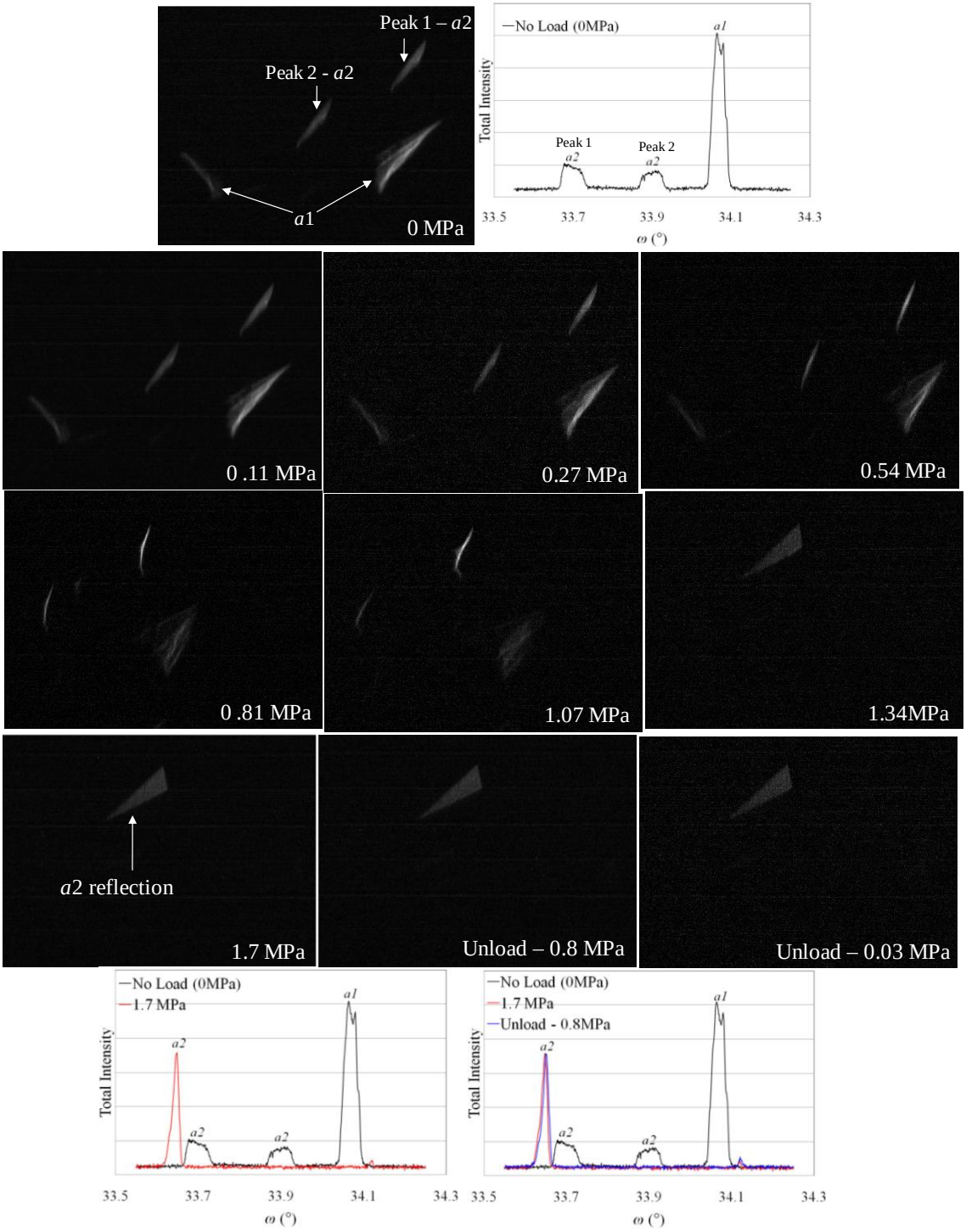

Figure 5.7: Topographs showing evolution of *a* domains in specimen BT1 at the various levels of compressive stress. Rocking curves enable identification of different domain types.

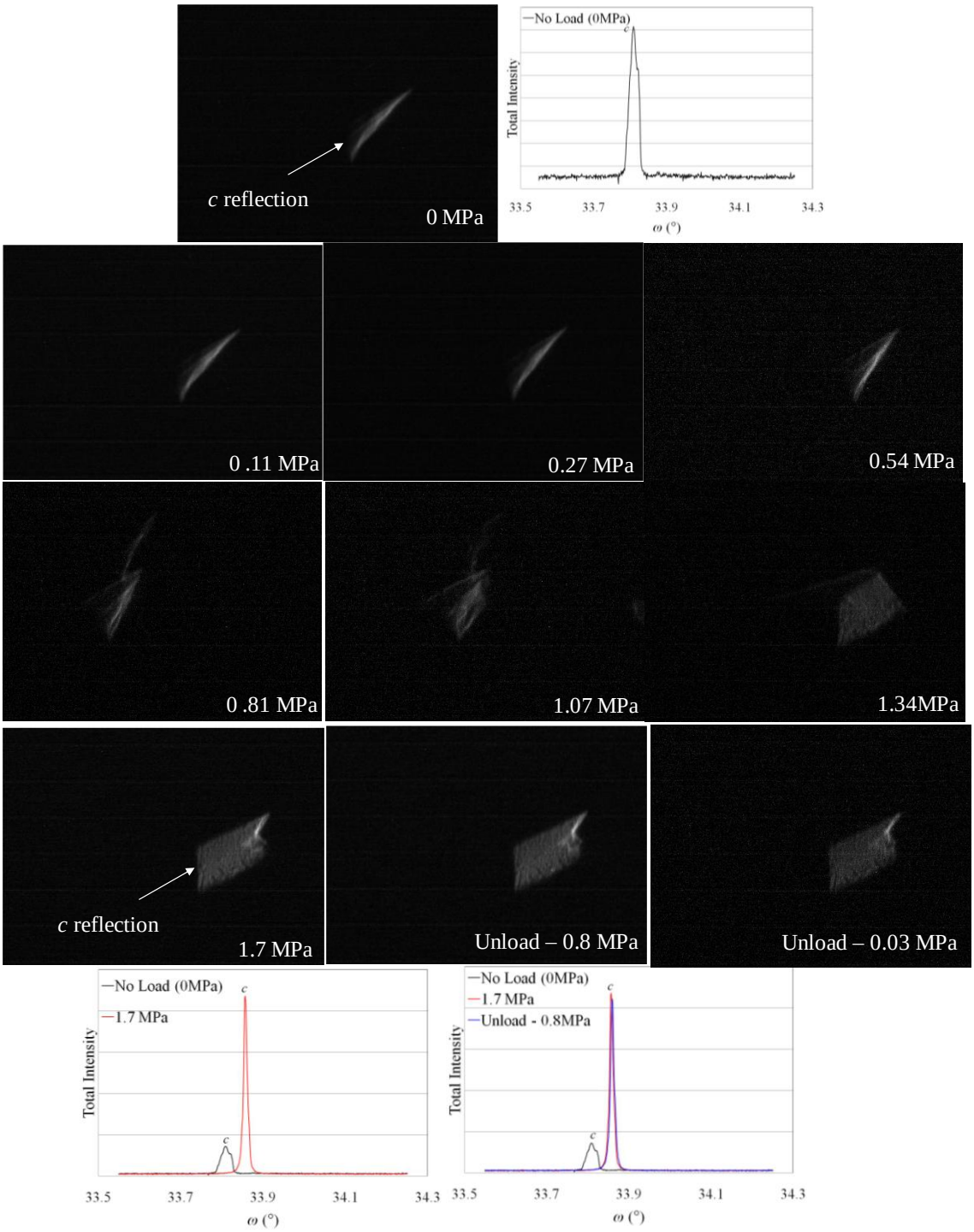

Figure 5.8: Topographs showing evolution of *c* domains in specimen BT1 at the various levels of compressive stress. Rocking curves enable identification of different domain types.

At 0 MPa, *a* and *c* domains are present on the specimen surface as the peaks corresponding to *a*2, *a*1 and *c* domains could be identified from the rocking curves (shown adjacent to the respective integrated topograph). The topographs at successive

load steps show clear transitions during loading, indicating that ferroelastic switching has occurred. In this process, *a1* domains, with their c-axis aligned to the uniaxial loading direction, switch to become *a2* domains and *c* domains. The switched domains have their *a*-axes aligned with the loading direction and since $a < c$ the switching process reduces the sample length, consistent with the compressive loading. The results confirm that relatively low stresses can reorganize the domain structure in BT, as suggested by the bulk measurements of Burcsu *et al*. [20]. It can be seen from figure 5.7 and 5.8 that the main ferroelastic switching ($a1 \rightarrow a2$ and $a1 \rightarrow c$ domains (90° switching)) transition occurred at a compressive stress level of about 1.07 MPa to 1.3 MPa. The switching criterion proposed in the micromechanical model developed by Hwang *et al*. [88] predicts that switching from $a1 \rightarrow a2$ and $a1 \rightarrow c$ would occur at the same threshold level (coercive stress) in this experiment once the external work done exceeds the energy required for switching. The evidence provided here shows that both the 90° switching events ($a1 \rightarrow a2$ and $a1 \rightarrow c$) occur at same stress level which is consistent with the switching criterion proposed in Hwang's model.

Figure 5.9 shows the rocking curves for *a* and *c* domains at all load levels. From the rocking curves, it can be seen that the intensity of *a1* domains is reducing while peaks for the *a2* and *c* domains grow as the applied compressive stress increases. The curves also provide evidence of small relative rotations of the domains (relative shift in ω values with increasing stress).

Finally, it can be seen from the rocking curves and topographs corresponding to unload – 0.8 MPa that removal of the stress does not affect the domain structure and the original structure at the beginning of loading was not restored. This suggests an almost irreversible ferroelastic switching process.

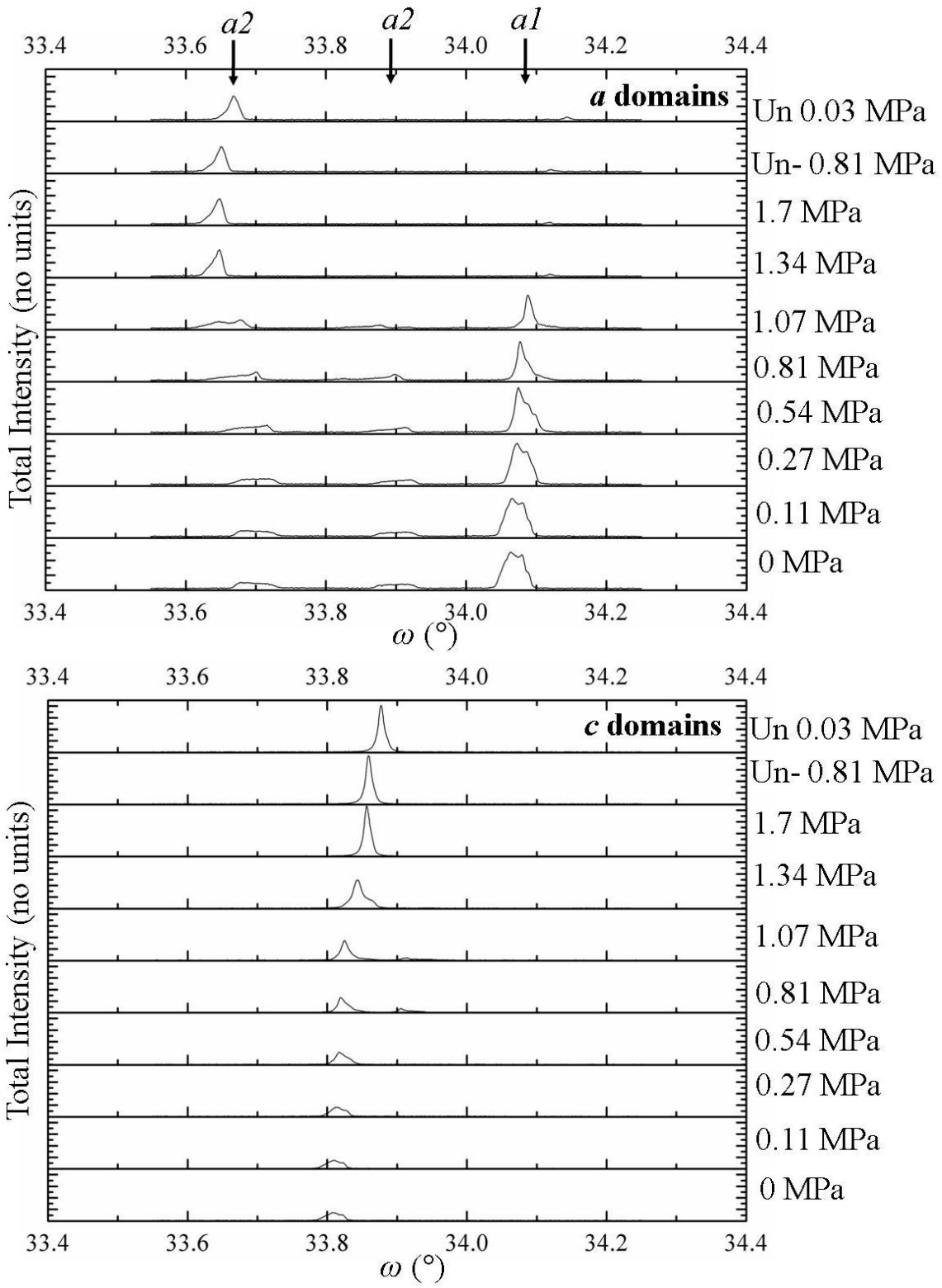

Figure 5.9: Rocking curves showing the *a* and *c* domain relative intensities evolving under mechanical load due to ferroelastic switching.

The microstructure in specimen BT1 was too fine to resolve individual domains using the MiniFDI camera (pixel size of 6.5μm). However, this experiment successfully establishes

the usefulness of the technique to study domain evolution using synchrotron X-ray diffraction and presents a qualitative representation of the ferroelastic domain evolution in a domain configuration containing finely interspersed *a* and *c* type of domains. The observations are consistent with the switching criterion used in several micromechanical switching models.

5.4. Results: Mechanical testing of needle specimen

In the case of the needle specimen, observations were made separately for ROI-1 and ROI-2. Next, the results of optical and X-ray measurements for these regions of interest are discussed separately.

5.4.1. Optical observations - ROI-1

Figure 5.10 shows optical micrographs in ROI-1 at selected load levels during loading and unloading. The direction of applied load is parallel to the c-axis of the *a1* domains. As the applied load is increased, needles of *a*1 domains were found to shorten in length. This behavior may be interpreted as a mechanism of ferroelastic switching in which the shortening of *a1* domain needles leaves behind a region of *a2* domain. However, it is not possible to identify the domain type in the switched region by optical observations alone. Upon unloading, the process partially reverses, and a few of the needles grow, but none return fully to their original length. This is consistent with irreversible ferroelastic (stress-induced) switching processes. The nucleation and growth of needle domains is widely recognized as a mechanism of domain switching when electric fields are applied to ferroelectric crystals [16,163]. Here, we confirm that ferroelastic switching can also proceed by a similar mechanism. Also, it can be seen that the broadly spaced domain needles are mobile at low stress levels (around 1-2 MPa), while the fine comb of needles marked “A” in figure 5.10 does not appear to move.

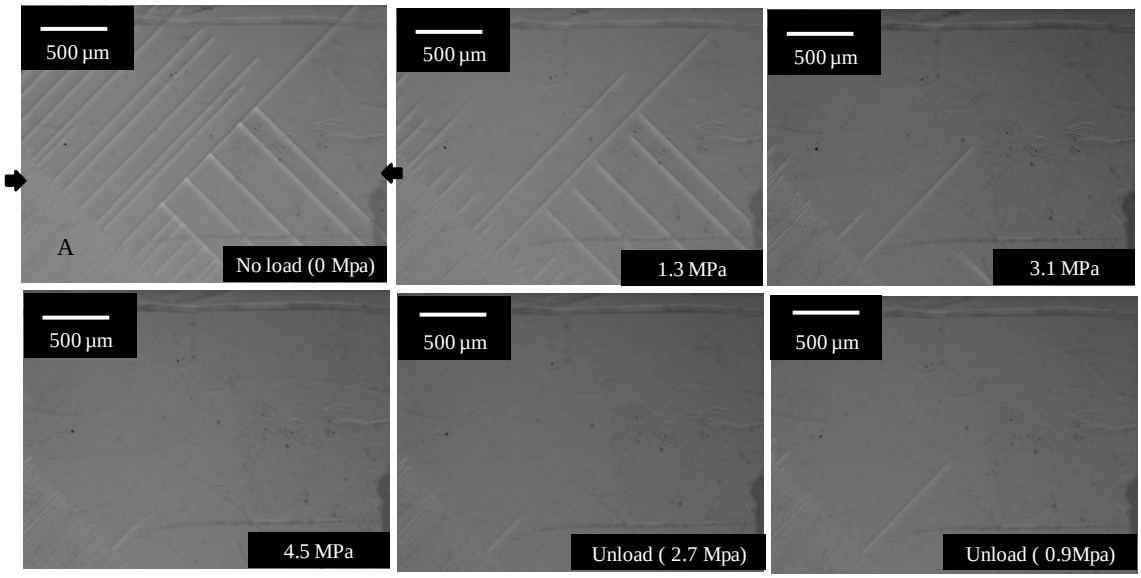

Figure 5.10: Optical micrographs showing the retardation of *a1* domains at various compressive load levels during loading and unloading.

5.4.2. Synchrotron observations - ROI-1

Figure 5.11(a) and (b) shows a topograph and rocking curve in ROI-1 at no-load (0 MPa) condition. A very small peak corresponding to *a*1 needle domains, a strong peak from the surrounding *a*2 domain and two peaks for *c* domains are seen in the rocking curve. The *c* domains appear to be closure domains near the specimen edges as discussed in section 4.8. A topograph obtained by summing the reflected intensity over the full range of ω values shows a strong reflection from the *a2* domain. Due to the close working distance, the reflections overlay on each other and *a*1 type needle domains are not seen due to their low intensity compared to the *a*2 domain.

The feature of interest is the group of *a1* needle domains that give rise to a weak peak around ω = 21.64° to 21.69°. By summing topographs taken over the range ω = 21.64° to 21.69° in 0.0025° steps, images of the *a1* domain needles were produced. Figure 5.12 shows the topograph of needle domains at 0 MPa.

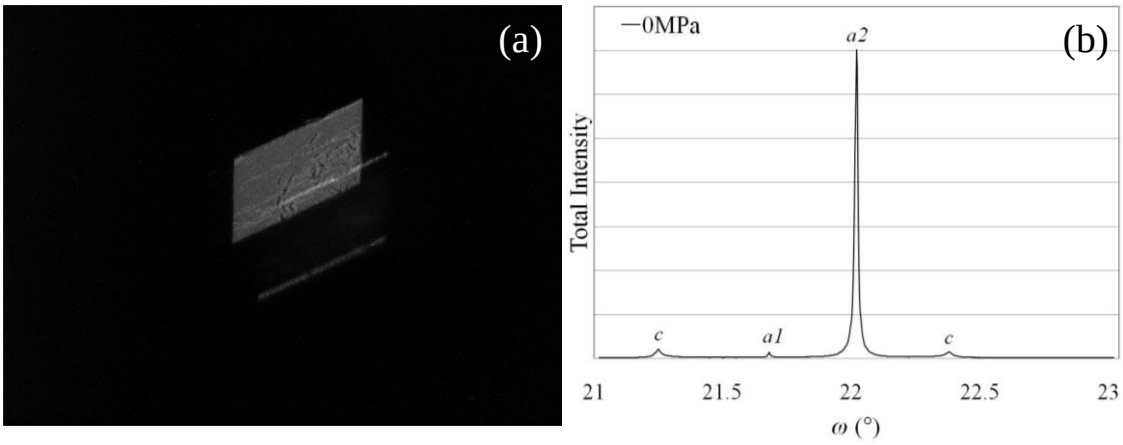

Figure 5.11: (a) Topograph at 0 MPa obtained by summing intensity over the full range of ω values. A strong *a*2 domain reflection could be seen along with two *c* domain reflections. (b) Rocking curve showing a peak at ω = 22.02° corresponding to the *a2* domain. The feature of interest is the *a1* domain peak occuring between ω = 21.64° to 21.69°.

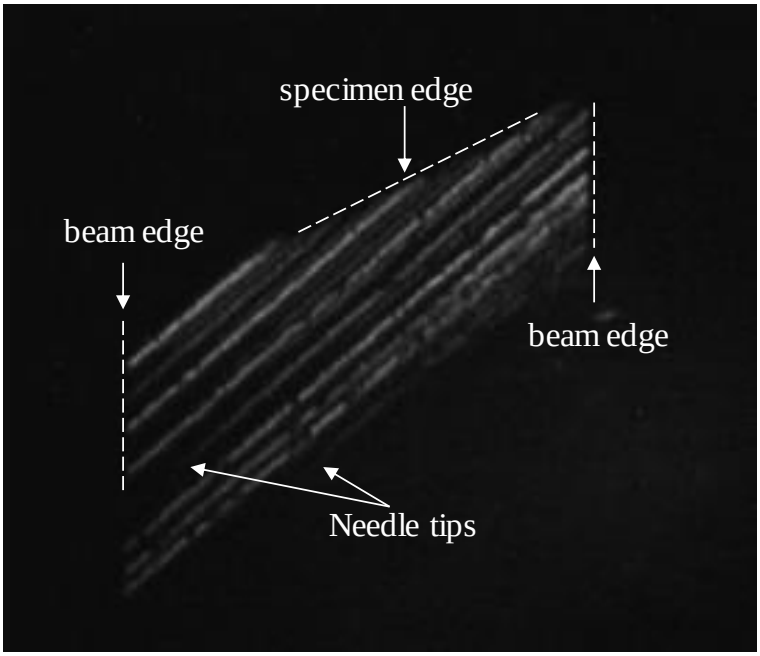

Figure 5.12: A topograph showing *a*1 needle domain reflection at 0 MPa.

It is important to identify the edges of the reflections in figure 5.12. The limit imposed by the 2 mm beam width gives a vertical cut-off producing edges seen at the left and right extremes of the reflection (labelled as beam edge). The 2 mm beam height was sufficient to cover the entire (foreshortened) sample width. The angled reflection edge, sloping from the top right, downwards and to the left in figure 5.12 corresponds to the specimen

edge. Some needle tips can be seen in the image. Other needles pass through the region and their tips cannot be seen. At various compressive stress levels, topographs similar to figure 5.12 were obtained to observe the behaviour of the needle domains under the compressive stress (figure 5.13).

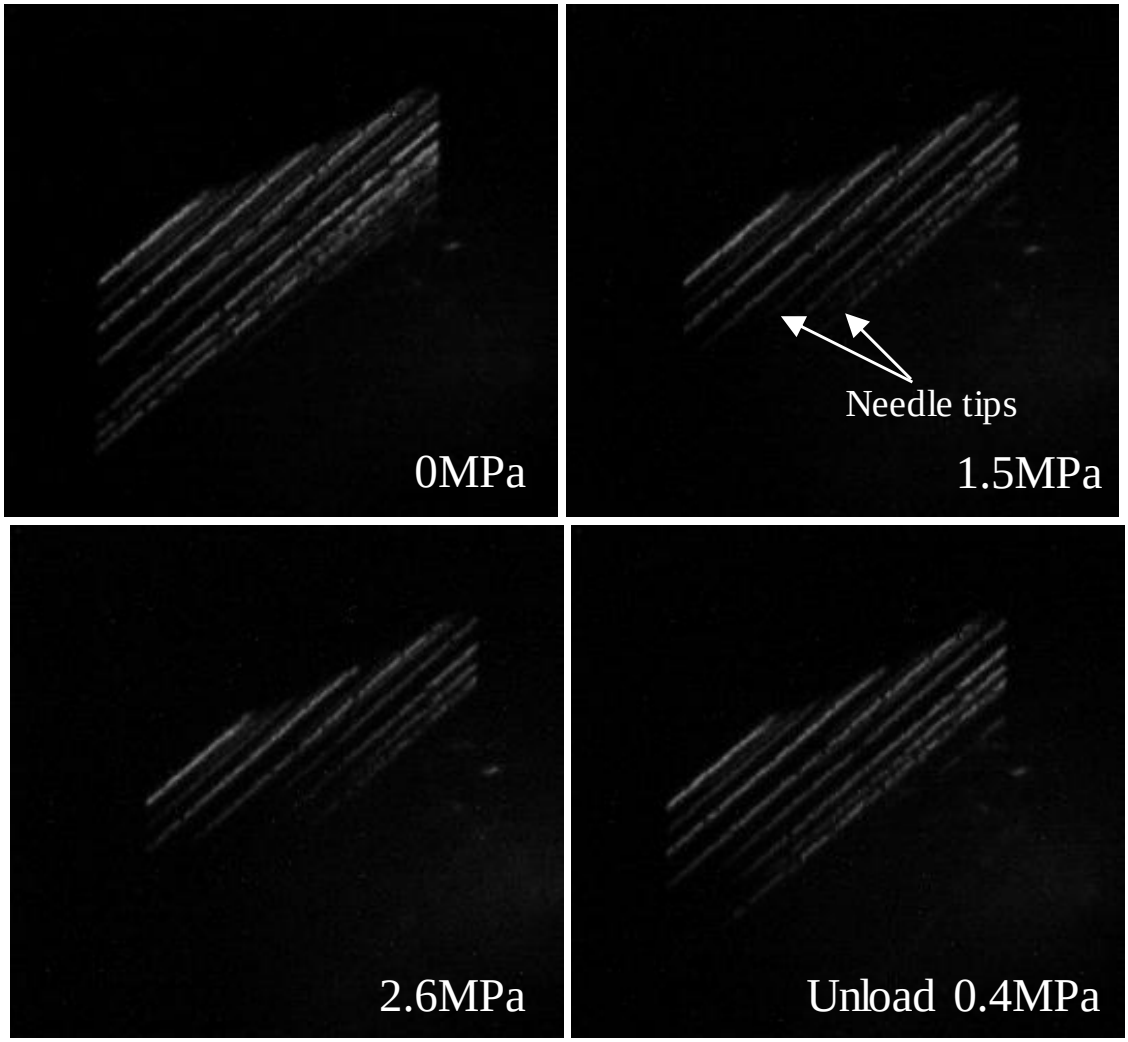

Figure 5.13: Topographs showing the *a1* domain reflections at various compressive load levels. Shortening of the needles with increasing stress could be seen from the retreat of the needle tips.

The specimen edge remains unchanged in all the topographs in figure 5.13. However, the lower edge of the reflection, corresponding to the extent of the needle domains, gradually retreats upwards as loading is increased. Thus the *a1* domain needles shorten under load, in agreement with the optical observations. The advantage of observing this with synchrotron diffraction is that the we can state with certainity which domain types are

present. Figure 5.14 shows the rocking curves at various stress levels. Comparing the curves for no-load (0 MPa) and peak stress (2.6 MPa) (figure 5.14(a),(c)), it can be seen that no additional *c* domain reflections appear at peak stress. Hence, this is a mechanism of ferroelastic switching in which the *a1* domain needle switches to *a2* domain only, with increasing stress. Upon unloading, the process partially reverses, and the needles grow, but do not return fully to their original length (Figure 5.13 – Unload 0.4MPa and Figure 5.14(b),(d)). Rocking curves in a range of ω values corresponding to the *a*1 domains indicate the change in domain volume fraction. The experiment also confirms that the needle domains are present at or extend to near the sample surface (penetration depth ≈ 36 μm at 18.6 keV).

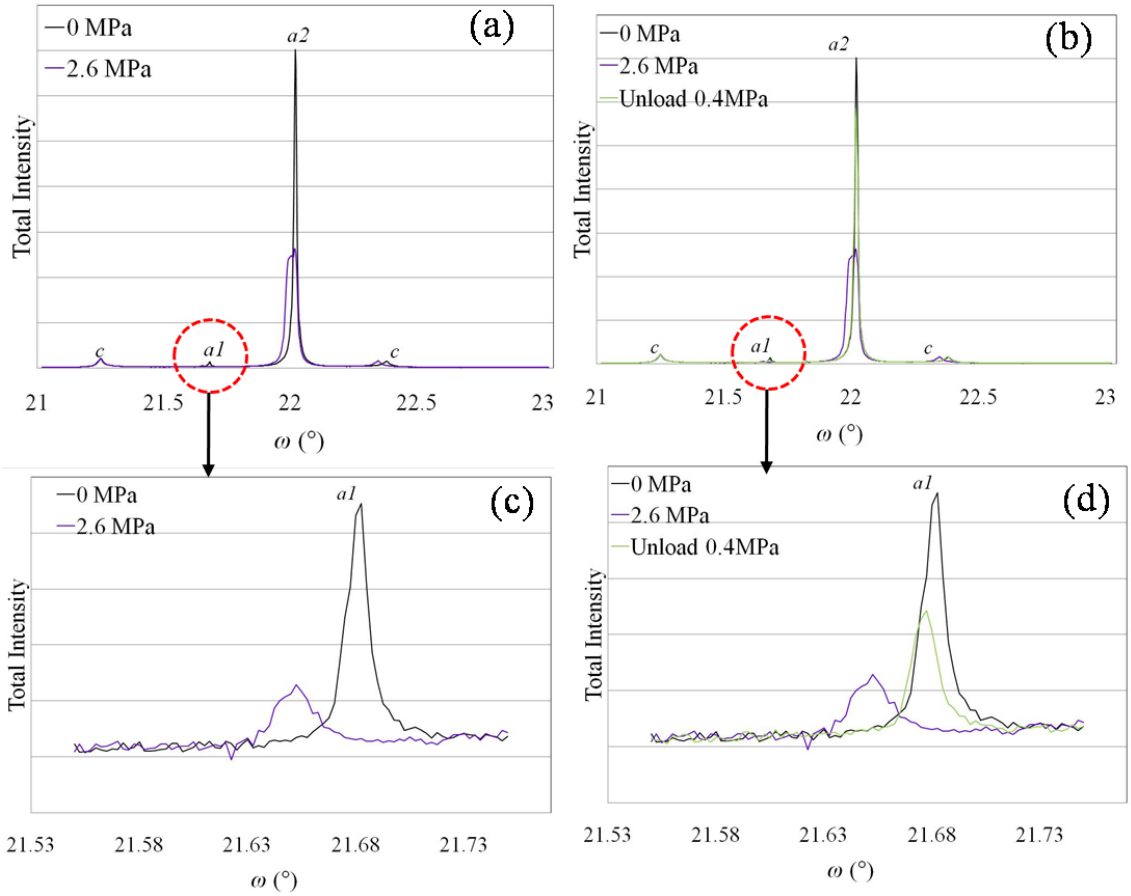

Figure 5.14: Rocking curve comparisons at no-load (0 MPa), peak stress (2.6 MPa) and Unload – 0.4 MPa.

5.4.3. Optical observations - ROI-2

Figure 5.15 shows the micrographs at various stress levels in ROI-2 containing a comb of needles. Fixed surface features allow a measurement of the movement of the tips of needles in a comb.

Careful examination shows that the comb of needles retracts by Δx_1 = 80 µm ± 5 µm under 4 MPa load. Upon unloading to 2.7 MPa, the retardation (Δx_2) was around 50 µm. Thus, a fine comb of needles is found to be more stable than coarsely spaced needles under applied stress. Micrographs for ROI-1 and ROI-2 at "Unload 2.7MPa" show that the removal of stress causes a significant reversal of switching for the comb of needles compared to coarsely spread needles. This was not the case for specimen BT1 where the switching is almost irreversible. This evidence suggests that the domain configuration strongly influences the switching behaviour. Models of ferroelastic/ferroelectric switching often assume a single threshold load level (coercive field/stress) at which switching occurs and the domain configurations are not taken into consideration. Futhermore, Hwang's model [88] would suggest simultaneous switching of $a1 \rightarrow a2$ and $a1 \rightarrow c$ in this experiment. However, no $a1 \rightarrow c$ switching is observed here, although it did occur in specimen BT1.

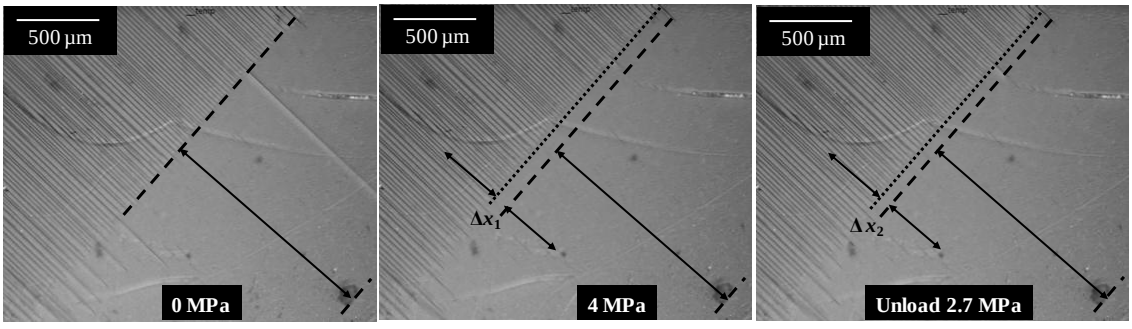

Figure 5.15: Top row – Optical micrographs showing the retardation of a comb of *a1* domain at various compressive load levels during loading and unloading. Bottom row – Zoomed-in micrographs of an area marked with black coloured dotted rectangle.

This experiment highlights the need for considering the domain patterns during model development. It is clear from the present experiment that broadly spaced domain needles are mobile at very low stresses (around 1-2 MPa) while fine combs of needles remain stable even at higher stress levels. It is also evident that the switching process depends on the pre-existing domain structure. The stress was not taken beyond 4 MPa because of the risk of breaking the sample. In preliminary tests, samples failed by fracture at mean stress values of 5-5.5 MPa.

5.4.4. Synchrotron observations - ROI-2

Figure 5.16(a) and (b) show a topograph and rocking curve in ROI-2 at the no-load (0 MPa) condition. The rocking curve at unloaded state shows a strong peak of *a*2 domains surrounded by separate peaks from *a*1 and *a*2 domains within the comb region and a closure *c* domain peak.

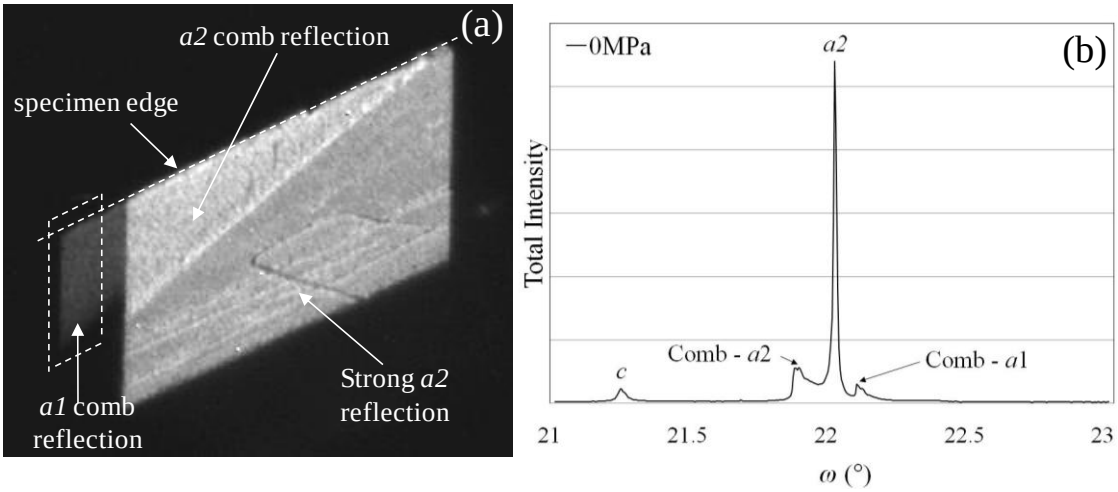

Figure 5.16: (a) Topograph at 0 MPa obtained by summing intensity over the full range of ω values. (b) Corresponding rocking curve.

The topograph (figure 5.16(a)) shows a strong reflection from *a2* domains over the whole region, and a weak reflection from the *a*1 comb which is overlaid by the *a*2 comb reflection. It is difficult to completely separate the two *a*1 and *a*2 reflections as the peaks are close; spatially the reflections also overlay due to the close working distance. Also, at

higher stress values, the peak positions shift such that the *a*1 comb peak merges with the strong *a*2 peak.

Figure 5.17(a) and (b) show the rocking curve comparison at no-load (0 MPa), peak stress (4.5 MPa) and at unload-0.3 MPa. Figure 5.17(c) and (d) show the same rocking curves with a narrow ω range (ω = 21.65 to 22.25). Upon loading to 4.5MPa, the *a2* peak broadens and reduces in height along with a tilt by a few hundredths of a degree in ω.

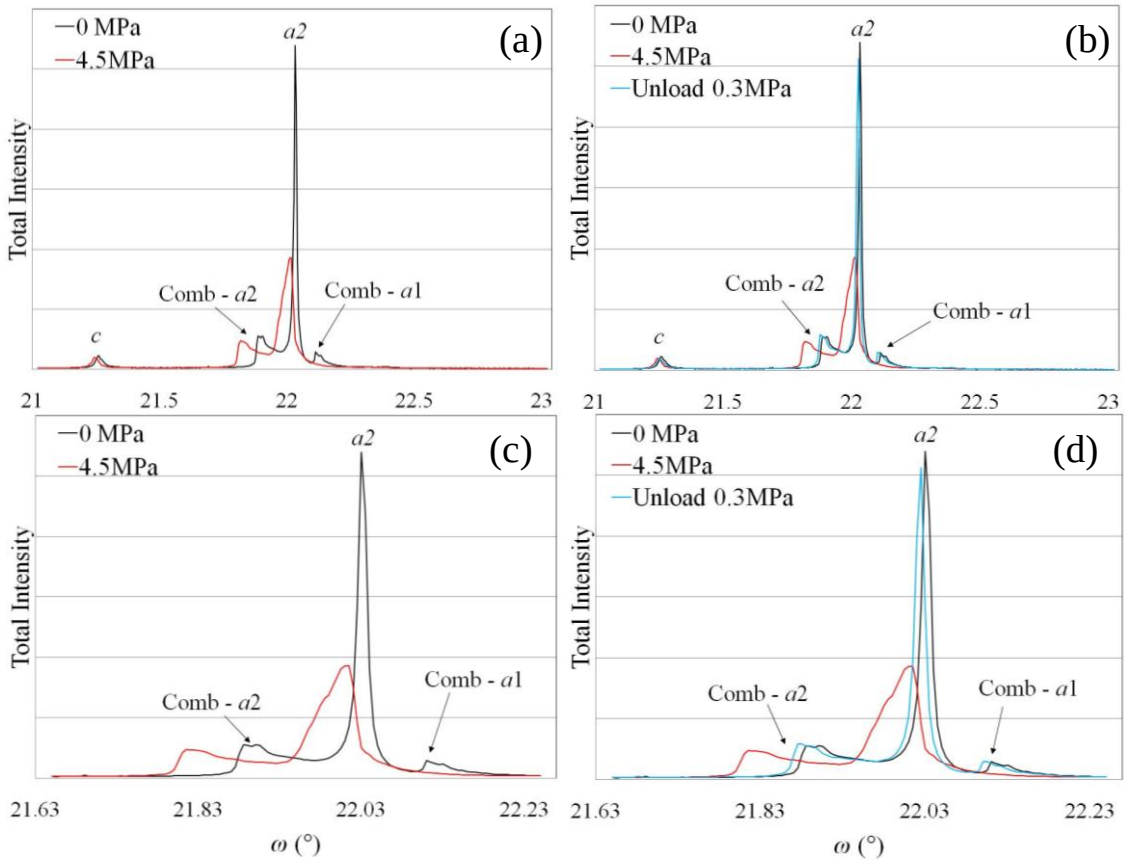

Figure 5.17: Rocking curve comparisons at no-load (0 MPa), peak stress (4.5 MPa) and Unload – 0.3 MPa.

Also, from figure 5.17 (a) and (c) , it can be seen that the comb - *a*1 peak disappears, or becomes indistinct, at 4.5MPa. Superficially, this suggests that the *a*1 needles in the comb may have shortened and thereby undergone ferroelastic switching to *a2* domains. However, this was investigated further by examining the topographs at various stress

levels, as explained in the next paragraph. Upon unloading, the peak corresponding to comb-*a*1 reappears suggesting that the original domain structure has been restored. This is in good agreement with the optical observations where a partial reversal of switching during unloading was observed for comb needles. Small relative rotations of the reflecting lattice planes are also evident from the rocking curves.

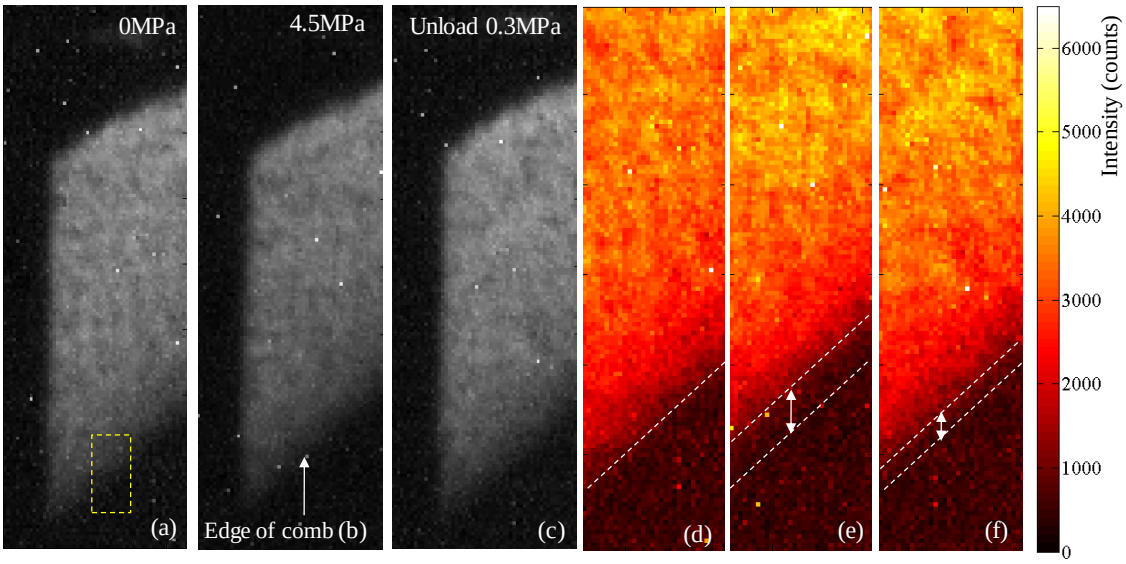

Figure 5.18: (a) to (c): Topographs of a protruding *a*1 comb reflection confirming the presence of *a*1 comb domains at peak stress level. (d) to (f): Close examination of the edge of the *a*1 comb.

As it is difficult to separate the *a*1 and *a*2 reflections, an attempt is made to estimate the retraction of the *a*1 comb by cutting out a small section of the *a*1 comb reflection that protrudes out of the overlapping reflections. This section was carefully identified in each topograph. Due to straining of the crystal, a spatial shift of the reflections was observed in the topographs. The specimen edge was used as a reference for locating the protruding *a*1 comb reflection as outlined by dotted white lines in figure 5.16. The topographs (a) to (c) in figure 5.18 were obtained by summing intensities in the prodruding section of *a*1 comb reflection over the full range of ω values. Examination of this region shows that the comb of *a*1 needles remains present throughout, and its range of ω angles overlaps with that of the surrounding *a2* matrix. Further investigation of the topographs reveals that the comb

of needles is rather stable to load, showing little or no change in size. The edge of the *a*1 comb, in the region defined by a yellow coloured rectangle marked in figure 5.18(a), was examined closely (see figure 5.18(d)-(f)). At 4.5 MPa, the edge has retreated by about 10 pixels or 172 µm accounting for foreshorting. The edge moves back towards its original position upon unloading and the retardation is about 5 pixels or 86 µm. However, due to the pixellation in the topographs, it is difficult to estimate the retardation of the comb edge accurately. Instead, it is possible to estimate the change in area fraction of the *a*1 comb by using the total intensities of the *a*1 and *a*2 comb reflections.

5.5. Change in area fraction: ROI-2

A small square area, see "1" and "2" in figure 5.19(a), was identified near the specimen edge such that it could be readily located in both the *a*1 and *a*2 reflections at all load levels. The aim is to use this area, away from the comb edge, to study any changes in the *a*1:*a*2 domain area ratio during loading.

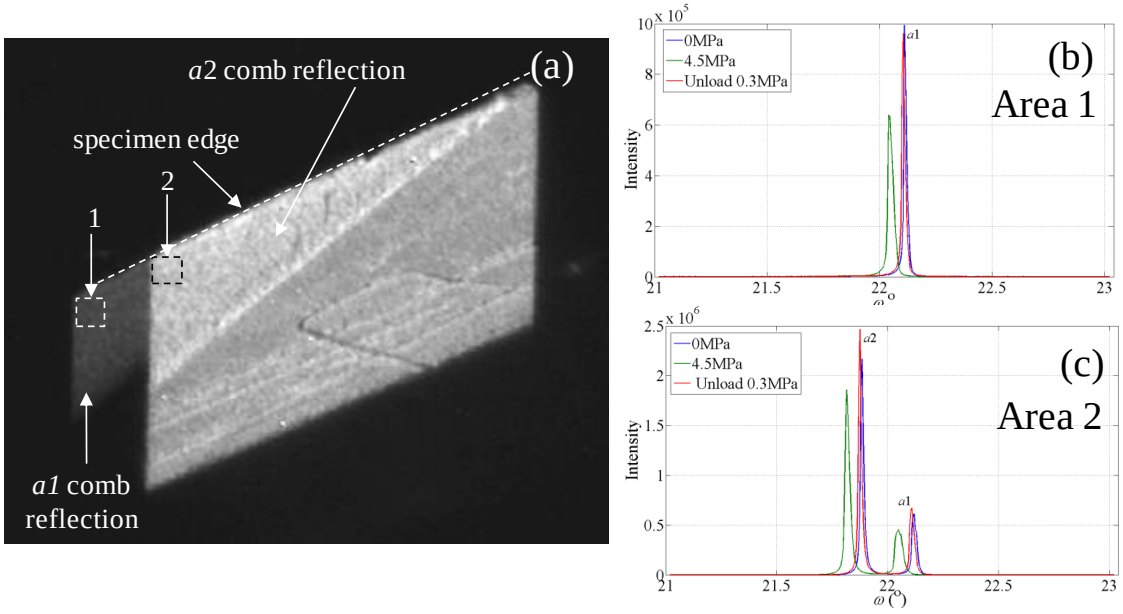

Figure 5.19: (a) Integrated topograph at 0 MPa. A 34 x 34 pixel area, marked "1" and "2" within *a*1 and *a*2 comb regions. (b) and (c) rocking curves for area "1" and "2" respectively.

The needles in the comb region are too fine to be resolved individually by the miniFDI camera. The *a*1 and *a*2 comb reflections are of similar shape and are shifted horizontally and vertically in the topographs due to the different χ and δ values of the reflections respectively. As area "1" and "2" lie at a fixed and small distance from the specimen edge, the reflections can be expected to be due to the *a*1 and *a*2 comb at the same spatial position on the specimen surface. Note that there is relatively little distortion of the images due to straining.

The intensity was summed over these 34 x 34 pixel square areas in each topograph, to give a rocking curve for areas "1" and "2", as shown in figure 5.19(b) and (c). It can be seen from figure 5.19(b) that the rocking curve of area "1" shows a single peak corresponding to the *a*1 comb. The rocking curve of area "2" shows two peaks corresponding to the overlapping reflections from *a*1 and *a*2 comb regions, but the peaks are well separated. Note that the *a*1 peak in figure 5.19(c) is from a different spatial position on the specimen surface than the *a*2 peak. Meanwhile the *a*2 peak in figure 5.19(c) arises from the same place on the specimen surface as the *a*1 peak in figure 5.19(b). At 4.5MPa, the *a*1 peak in figure 5.19(b) and *a*2 peak in figure 5.19(c) decrease in height and broaden. Upon unloading, both the peaks return to match closely with the no-load (0 MPa) condition.

Next, the ω value corresponding to maximum intensity (ω_{max}) in the *a*1 peak in figure 5.19(b) and *a*2 peak in figure 5.19(c) was found. Area fractions of *a*1 and *a*2 domains at each load step in a chosen 34 x 34 pixel square area "1" and "2" were found as follows: (i) First the total intensity in each peak I_{a1} and I_{a2} were found by summing intensities over a range of ω, given by $\delta\omega = 0.135°$ on either side of ω_{max}. (ii) Then, the ratio $I_{a1}/(I_{a1}+I_{a2})$ was used to estimate the area fraction of the *a*1 comb. Similary, $I_{a2}/(I_{a1}+I_{a2})$ gave the area

fraction of the *a*2 comb. Figure 5.20(a) shows the area fraction of *a*1 domains plotted at various stress values. The area fraction of *a*1 domains has reduced by about 1% from no-load to peak load suggesting that a small amount of domain switching has taken place in the comb region. Also, upon unloading, almost all the area fraction is restored, which is consistent with the observations made using optical micrographs and X-ray topographs.

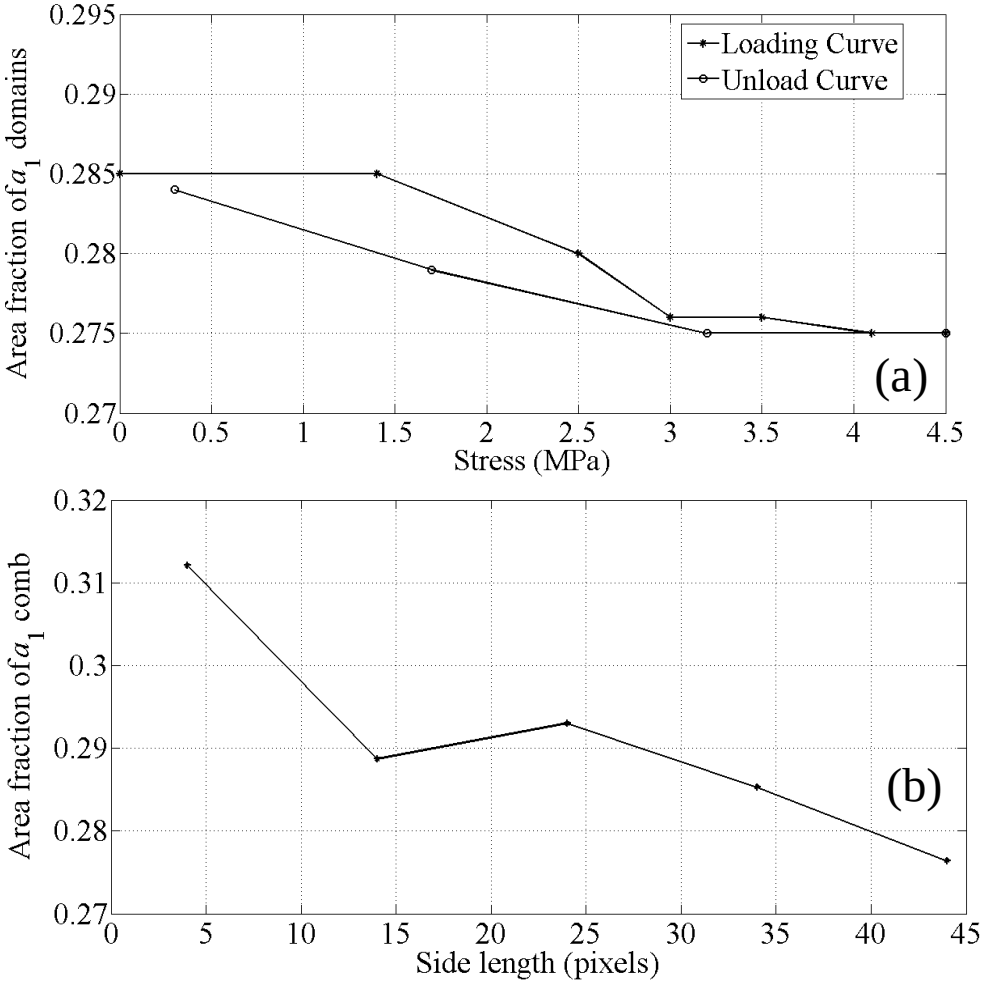

Figure 5.20: (a) Area fraction of *a*1 domains during loading and unloading (b) Effect of changing the size of square area on volume fraction at no-load condition (0 MPa).

The size of square areas "1" and "2" was varied to check the sensitivity of these measurements. The maximum size of square that could be selected so that area "1" lies in the region of *a*1 comb that does not overlap the *a*2 reflections is 45 pixels square. Figure 5.20(b) shows area fraction of *a*1 comb for various sizes of square. For square sizes

below 14 and above 34 pixels, area fraction seems to be very sensitive to the size of the square. A reasonably stable value was obtained for sizes from 14 to 44.

5.6. Change in area fraction: ROI-1

In the optical observations of ROI-1, close examination of the domain configuration at no load revealed that a number of long needles extend beyond the comb of closely spaced needles (see area "A" in figure 5.10). Using image processing, a threshold contrast between needle domains and surround matrix was identified, and the area fraction of *a*1 needles at each load level was found. Note that the optical microscopy data includes the contributions from sub-surface domains and so may overestimate the area fraction (see figure 5.21).

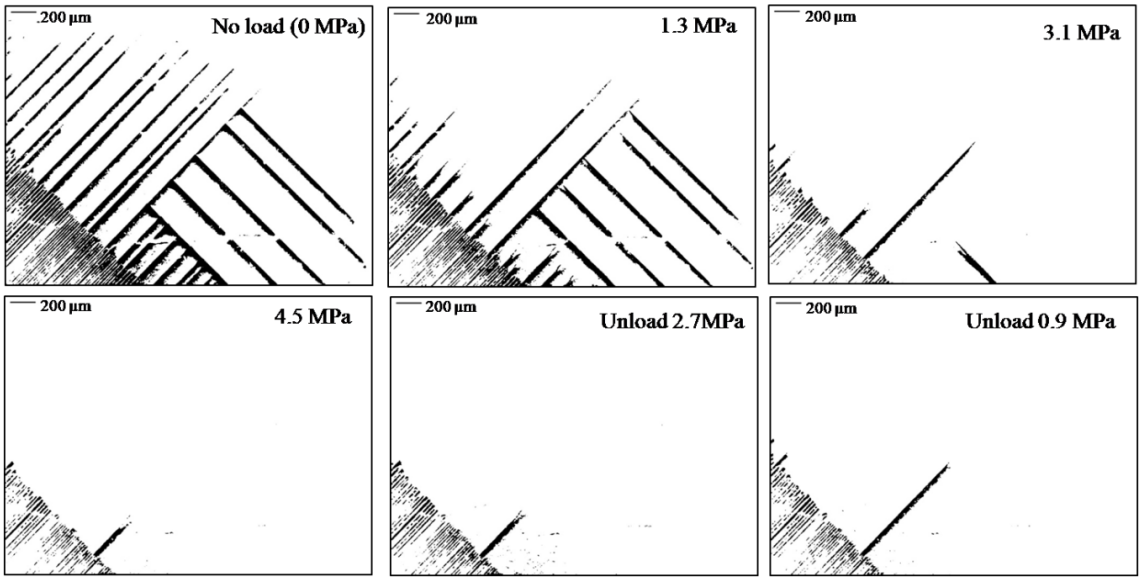

Figure 5.21: Area fraction of *a*1 domains is obtained at each stress level.

The area fraction of *a*1 needles is plotted against the nominal applied compressive stress in figure 5.22(a). It can be seen that at peak stress the area fraction of *a*1 needles drops to about $1/8^{th}$ of its initial value. Also, upon unloading the specimen, very little reversal of switching takes place.

The change in area fraction is also obtained from synchrotron measurements. Note that this curve is not directly comparable with the optical measurements as the regions observed were different in the two experiments. Fewer needles were present in the region observed by the X-ray light. Also, the synchrotron observations are limited to surface only whereas sub-surface domains may contribute in the optical observations.

It can be seen from the rocking curve comparison (figure 5.14) that the peaks corresponding to $a1$ needles and $a2$ domains could be separated easily. At each load step, by summing intensity over the range of ω values for $a1$ needles and $a2$ domains, total intensity, I_{a1} and I_{a2}, could be obtained. The ω range, used in the case of the $a1$ peak is 21.53° to 21.73° and that for the $a2$ peak is 21.8° to 22.2°; these ranges were chosen such that the peaks always lie within the range. Figure 5.22(b) shows the $a1$ domain fraction ($I_{a1}/(I_{a1}+I_{a2})$) at various stress levels. The change in fraction of $a1$ needles is much smaller than that measured by optical microscopy as may be expected for the reasons outlined above.

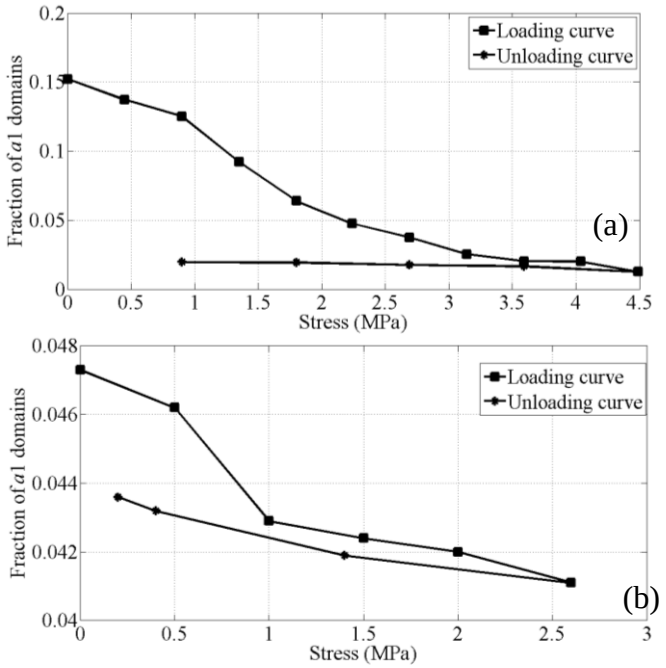

Figure 5.22: Area fraction of $a1$ type needle domains decreases with the applied compressive stress obtained by (a) optical measurements (b) synchrotron measurements.

5.7. Needle geometry during comb retardation

Two distinct measurements of the comb retardation have been made: (i) retardation Δx of the needle tips in the comb using optical microscopy and (ii) change in area fraction of the needles using synchrotron X-ray diffraction. Using these measurements, the retardation of needles in the comb is analysed further. Here, the aim is to understand the needle geometry during the comb retardation. Consider an evenly spaced set of *a*1 type needles in a large *a*2 domain as shown in figure 5.23(i).

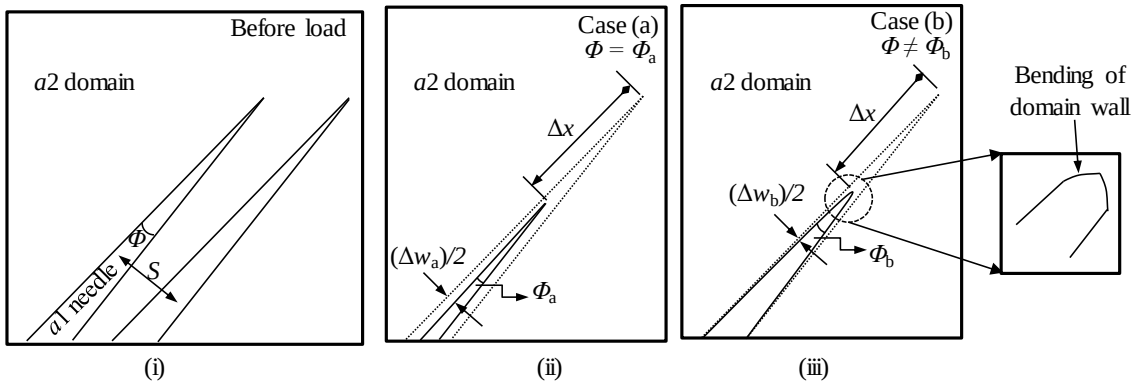

Figure 5.23: (i) Schematic of spaced *a*1 type needles in a matrix of single *a*2 domain. Two possible mechanisms of needle retardation are shown in (ii) and (iii).

Let ϕ be the mean needle angle and S be the average needle spacing in a comb of needles at no-load condition. Under compressive stress, the needle could shorten by a distance, Δx. This would result in a change in area fraction of *a*1 needles (Δf) is given as $\Delta f = \Delta w/S = \phi\Delta x/S$ where Δw is a change in the width of the needles.

Two possible mechanisms of needle shortening are outlined in figure 5.23(ii) and (iii). A needle can retreat without a change in the shape i.e. maintaining the same mean needle angle so that $\phi = \phi_a$ (figure 5.23(ii)). This will be referred to as case (a). In the other mechanism, the needle could shorten by changing the mean needle angle i.e. $\phi \neq \phi_b$. This will be referred to as case (b), where the domain walls may bend near the tip as

shown in figure 5.23(iii). Both retardation mechanisms give a change in width Δw_a and Δw_b respectively. In both cases, the same retardation (Δx) could be obtained.

Now, from the optical measurements in the comb of needles, the mean needle angle and needle spacing was measured to be 0.8° and 12.5 μm respectively. The retardation of the comb at a stress of 4 MPa was measured to be around 80 μm (figure 5.15) giving the change in volume fraction, Δf, to be around 0.09 or 9%. However, X-ray measurements for ROI-2 give the change in area fraction at peak stress to be around 1%, which is very small compared to the estimation from optical measurements.

Now, though both the retardation mechanisms involve a change in width as well as tip distance, the change in width Δw_b, is smaller than Δw_a as the needle width does not reduce greatly at a far distance from the tip in case (b). Due to lesser change in width, the change in the intensity of the reflected light would be smaller in case (b) compared to case (a). This will give smaller change in area fraction. As the change in area fraction estimated from the synchrotron measurements is smaller compared to the optical observations, needles geometry seems to follow the mechanism as in case(b) during comb retardation.

5.8. Conclusions

Microstructure evolution in single crystal Barium Titanate was observed in-situ under mechanical loading using optical microscopy and X-ray reflection topography. In the case of a specimen containing *a* and *c* type domains, ferroelastic switching is observed in which *a1* domains switch to become *a2* and *c* domains (90° switching). As the switching events occurred at the same stress level, the observations are consistent with the switching criterion proposed in Hwang's micromechanical model. Topographs at incremental loading states show the transitions that occur at each loading step. In another

specimen, containing mainly in-plane *a*1-*a*2 needle domains, compressive mechanical loading caused shortening of the needles. Optical measurements showed ferroelastic switching of *a*1 needles leaving behind a region of *a*2 domains. A comb of closely spaced needles was also imaged under compressive loading and it is found that the comb was stable to a load level that would produce shortening of widely spaced needle domains. This suggests that the domain configurations affect the switching, contrary to the assumptions of several models. Constitutive models that can account for such effects should be developed. The evidence is also contrary to the assumption that switching happens at a single critical value of coercive field/stress as is assumed in some micromechanical models. Quantitative measurements gave useful insights into the possible mechanisms of needle retardation. The use of optical and X-ray techniques complemented each other, providing both qualitative and quantitative data for comparison.

6. Conclusion and Future Work

To fully realize the potential in single crystals, an improved understanding of the microstructure and the evolution of the microstructure under electromechanical loading is necessary. In this work, macroscopic measurements and microstructural observations were performed on Lead Magnesium Niobate – Lead Titanate (PMN-PT) and Barium Titanate (BT) single crystal ferroelectrics respectively. In this chapter, key results are summarized along with a discussion of the future work.

6.1. Macroscopic measurements

6.1.1. Results

In the polarization rotation test developed by Huber and Fleck [67], a poled specimen is subjected to an electric field at an angle in the range of 0° to 180° to the initial direction of polarization. First, the polarization rotation tests were carried out on a polycrystalline Lead Zirconate Titanate (PZT) specimen. The results were in good agreement with the published data. Lesser values of remnant polarization around 90° raised questions about the boundary conditions at the free surfaces. To test the boundary conditions, the polarization rotation test was extended to two new specimen geometries such that the thickness to width ratio (aspect ratio) is varied by 2 orders of magnitude (shape dependency tests). The result of shape dependency tests suggested that the charged side faces may impose a constraint on switching and varying specimen geometry does affect this test.

Next, the polarization rotation tests were conducted on PMN-PT single crystals with a specimen geometry close to cubic. The results showed a gradual increase in the change in electric displacement due to the ferroelectric switching. For loading angles near to 90°,

higher values of remnant polarization were observed which suggests that PMN-PT is more polarizable in certain directions. Also, the dielectric permittivity showed a noticeable variation as the electric loading direction is altered, in contrast to polycrystalline PZT. This suggests an anisotropic behaviour which can be expected for single crystals.

Strains in two directions, parallel to the electric field and perpendicular to the electric field, were measured on two opposite faces of the specimen. The butterfly hysteresis loop showed a noticeable variation in the magnitudes of strains measured on the opposite faces. This suggests that local variations in the composition or domain structure have an effect on the strain measurements. In the polarization rotation test, the 90° specimen showed a large change in strain which needed further understanding with respect to switching systems and hence, the polarization rotation tests were simulated using a micromechanical model presented in Chapter 3.

6.1.2. Future work

The polarization rotation tests gave a set of multi-axial measurements which are useful for validating constitutive models describing ferroelectric switching. The tests could be readily extended for other single crystal ferroelectric materials. In the present work, strain gauges were used to measure the strain response. Due to the small area sampled, measurements were susceptible to local effects. For accurate quantitative measurements, other techniques such as laser interferometry, optical birefringence and X-ray diffraction may prove useful.

Macroscopic tests with simultaneous application of electric field and mechanical stress could be helpful in understanding the non-linear behaviour of ferroelectrics. Figure 6.1 shows a schematic for possible testing configurations.

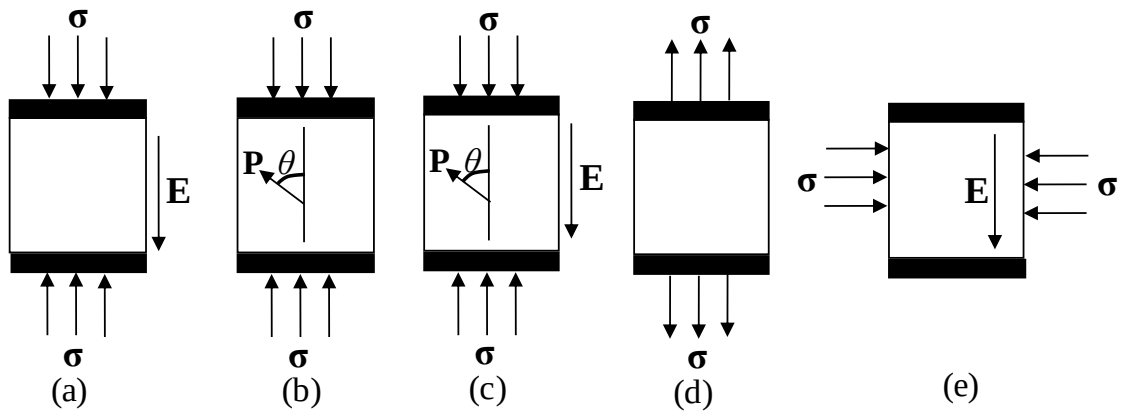

Figure 6.1: Possible configurations for macroscopic testing.

An arrangement similar to figure 6.1(a) where uniaxial compressive stress (**σ**) and electric field (**E**) is applied simultaneously has been used by Burcsu *et al*. [20] for BT single crystals and Shieh *et al*. [68] for polycrystalline BT and PZT. Figure 6.1 (a) describes what is already done while Figures 6.1 (b), (c), (d) and (e) present possible configurations which could be tested. A specimen could be poled initially and uniaxial compressive stress could be applied at an angle θ to the initial direction of polarization (see figure 6.1(b)). This is similar to the polarization rotation test except for the mechanical stress in second step. As mechanical stress could only give 90° switching, it would be of interest to compare the switching behaviour with the results of polarization rotation tests given in chapter 2. Figure 6.1(c) is basically an extension of the testing configuration in figure 6.1(b) where an electric field and the mechanical stress could also be applied simultaneously at an angle to the initial polarization direction. The test configurations represented in figure 6.1(b) and (c) would be useful in understanding the behaviour of single crystals where multiaxial loading states occur, such as in interdigital arrangement of electrodes in stack actuators or near crack tips. Applying uniaxial tension to the specimen is another option as shown in figure 6.1(d), however it could be very difficult to carry out due to the low fracture strength of the crystals. This test could be useful for

understanding the material behaviour in the tension side of bending bimorphs under electrical loading. Finally, electric loading and uniaxial compression could be applied perpendicular to each other which would help to understand the situation arising in compression side of bending bimorphs under electrical loading.

6.2. Modelling

6.2.1. Results

The aim of the modelling was to assist the interpretation of the macroscopic experiments described in chapter 2. A rate dependent micromechanical model based on a switching criterion proposed by Hwang *et al*. [88] was developed to simulate the polarization rotation test results on PMN-PT.

The model was separately implemented for the tetragonal and rhombohedral crystal systems. For each system, domains were represented by a set of crystal variants. Each variant corresponds to a distinctive polarization vector direction and can be assigned a certain volume fraction. When the work done by external loading exceeded the energy required for switching (Hwang's switching criterion), domain switching was realised by a transfer of volume fraction from the switching variant to the switched variant. To stabilise the volume fraction transformations, rate dependency was introduced.

First, the model was calibrated against the experimental dielectric hysteresis and butterfly hysteresis loops and a satisfactory agreement between the simulations and the experimental results were obtained by choosing appropriate model parameters. Next, the polarization rotation tests were simulated and results for both the crystal systems qualitatively agree with the experimental data. Further comparison was done using the total change in the remnant polarization at each loading angle. While the tetragonal model gave qualitatively similar behaviour to that of the experimental data, the magnitude of the

remnant polarization attained was typically less than that in the experiments. Availability of fewer switching systems is a reason for the low remnant polarization values. Contrary to this, the rhombohedral model, gave higher values of remnant polarization for almost all the angles except for when $\theta \approx 90°$. The model's response was explained by examining the volume fraction transfers at each loading angle. An average response, obtained by assuming equal fractions of tetragonal and rhombohedral phases, matches closely with the experimental data for almost all the angles except for when $\theta \approx 90°$.

The strain response of the model was then compared with the experiments and it was found that the model massively overestimates the strain response for certain cases such as when $\theta = 90°$ in the tetragonal system and $\theta = 45°$ or $135°$ in the rhombohedral system. As 180° switching does not produce any strain, the overestimates were believed to be due to the operation of 90°, 71° and 109° switching systems in the model. The model was further adjusted to allow only 180° switching so that only piezoelectric strain contributes to the strain response. A better agreement was then found between the simulated strain response and experimental measurements.

Due to the intrinsic coupling between polarization and strain in the micromechanical model, it was difficult to simulate both the responses with high accuracy. Also, the model does not take into account the detail of domain configurations that may have an effect on polarization switching.

6.2.2. Future work

In the present work, polarization switching between the crystal variants of the same crystal system was allowed. It would be of interest to explore the switching between a crystal variant of the tetragonal system and a crystal variant in the rhombohedral system. This would require a modified switching criterion where the energy required for

switching within the phase is different than that required across the phase. Further, the domain to domain interactions could be incorporated in the model. Finally, it would be of value to develop the model in a way that the local domain configurations could be considered in the model. One way could be to use different rate parameters for switching between certain crystal variants. Such crystal variants could be chosen depending on the local domain patterns. However, this would require extensive experimental evidence for model validation.

The shape dependency tests on polycrystalline PZT suggest that the boundary conditions have an effect on the switching. It would be of interest to simulate the different boundary conditions in polarization rotation tests by finite element methods.

6.3. Mapping of domain structure in BT single crystal

Various techniques such as surface treatment, optical and electron microscopy, X-ray and neutron diffraction and scanning probe methods are available for mapping the domain structure in ferroelectrics. A literature review of commonly used imaging methods suggested that using multiple techniques would be advantageous due to the following reasons: (a) the different capabilities of each technique may complement each other giving distinct information and (b) there is lack of a common method that can reveal all the domain information at varying length scales.

6.3.1. Results

In this work, the aim was to identify and map different domain types in single crystal BT. In an [001] oriented sheet of BT single crystal, typically *a* domains and *c* domains are observed: In *a* domains, the polarization is parallel to the crystal surface while *c* domains have polarization perpendicular to the crystal surface. Multiple techniques were used for mapping the domain structure starting with optical microscopy of the surface of a BT

specimen. Though, suitably oriented domain walls could be seen, it was not possible to identify the domain types.

Next, successive experiments were carried out by reflection topography using unfocussed monochromatic synchrotron X-ray light. In all the experiments, domains were mapped by rocking the specimen through a range of tilts and recording topographs at each tilt position. In the 1st experiment, symmetric reflections differentiating between the *a* and *c* domains were recorded over a 10 x 10 mm specimen surface. Reflection topographs were then processed to obtain orientation maps for the entire specimen surface showing relative tilt between the adjacent domains. The majority of the crystal surface contained finely interspersed *a* and *c* domains and intensity maps gave an indication of their relative proportions.

To confirm the synchrotron results, the crystal used in synchrotron experiment was etched and observed using optical microscopy, scanning electron microscopy (SEM) and atomic force microscopy (AFM). Several regions of the specimen were mapped using atomic force microscopy utilizing the topographic unevenness due to etching to reveal the local domain patterns. The optical and scanning electron microscopy enabled imaging over larger specimen areas and gave an estimate of the typical domain spacing. The domain fraction estimated using the intensity maps in the synchrotron experiment were in good agreement with those computed using the optical and scanning electron microscopy observations. Typical domain spacing was found to be less than 10 μm and could not be resolved in the 1st synchrotron experiment due to the limitations of the detector pixel size.

The synchrotron experimentation was further developed to map the fine domain structure using a high resolution camera with a capability of zooming-in on regions of interest on the specimen surface (2nd experiment). Asymmetric reflections were used in this

experiment to differentiate between in-plane *a* domains (*a*1 and *a*2) and *c* domains. Though the experiment was successful in identifying *a*1, *a*2 and c domains, clear domain patterns could not be seen due to the fuzziness in the topographs. The fuzziness could be minimised using a smaller specimen to detector distance, but it was challenging in this experiment due to the space constraints.

In the 3rd synchrotron experiment, a specimen containing coarsely spaced in-plane domains was mapped using asymmetric reflections. Use of small specimen to detector distance greatly improved the clarity of the topographs allowing mapping of fine needles having width of about 10 μm. A composite image was produced using multiple scans over the entire specimen surface (10 x 4 mm). The composite image showed a good agreement with optical micrographs and also revealed the presence of closure domains which were not seen in the optical micrographs of the specimen. The method was also successful in revealing small relative tilts between the domains at each point on the specimen surface.

Next, Piezoresponse force microscopy (PFM) was used to map the domain structure. The vertical and lateral PFM resolved out-of-plane (*c*+ and *c*-) and in-plane (*a*1+, *a*1-, *a*2+ and *a*2-) domains respectively. Finally, observed domain configurations were correlated with theoretically predicted rank-2 laminated domain patterns.

The distinct capabilities of the various techniques used were necessary in order to gain a consistent interpretation of the microstructure. The present study shows that different visualization techniques such as X-ray diffraction, etching followed by AFM, SEM and optical microscopy, PFM, when used in combination, allow mapping of the surface domain structure in BT with specific domain orientation information.

6.3.2. Future work

It would be of interest to explore the possibility of reducing the specimen to detector distance to about 200 mm while using the high resolution camera. Also, observations of the domain structure were restricted to the surface of the specimen in this work. It is of value to map the structure inside the crystal generating a full 3-dimensional picture of the domains present. Such sub-surface and 3-dimensional microstructure maps would rely on higher energy light available at, for example, the I12 (JEEP) beamline. The techniques developed in this study could be a starting point towards such 3-dimensional mapping.

Use of multiple techniques seems to be important for revealing distinctive domain information. One of the main issues while observing the microstructure in the same specimen using several techniques is locating the same region of the specimen surface. Development of a specimen stage that could be used across various instruments without a need of specimen removal would be very useful. While such a common specimen stage exists for optical and SEM observations, it would be helpful to have a stage that can be used across more instruments such as AFM, synchrotron diffractometer.

6.4. In-situ observations of domain evolution

6.4.1. Results

Under externally applied electrical or mechanical loads, a complete or partial reorientation of the domain structure takes place due to the movement of domain walls. The aim was to observe the microstructure evolution in single crystal BT in-situ under mechanical loading. Optical microscopy and X-ray reflection topography was used to observe the domain evolution.

First, a specimen containing a fine microstructure of *a* and *c* type of domains was loaded in compression and topographs were captured at each load level using synchrotron X-ray

reflection topography. Successive topographs at incremental loading showed the transitions that occur at each loading step. A ferroelastic switching in which *a*1 domains switch to become *a*2 and *c* domains (90° switching) was observed. Both of these switching events occurred at same stress level. This is consistent with the switching criterion proposed in Hwang's micromechanical model [88] which assumes that a switching would occur at single threshold level (coercive field/stress) once the external work done exceeds the energy required for switching.

A specimen containing mainly in-plane *a*1 needle domains interspersed in a large *a*2 domain was observed using optical microscopy where micrographs were captured at each load level. The compressive mechanical loading caused shortening of the needles providing evidence of a ferroelastic switching of *a*1 needles leaving behind a region of *a*2 domains. A comb of closely spaced needles was also imaged under compressive loading using optical microscope and it is found that the comb was stable to a load level that would produce shortening of widely spaced needle domains. Thus, this evidence suggests that domain configurations influence the switching behaviour and constitutive models that can account for such effects should be developed. Quantitative measurements gave useful insights into the possible mechanisms of needle retardation. The qualitative and quantitative data could be used for validating models describing the switching in ferroelectrics.

6.4.2. Future work

A technique for in-situ observation of domain evolution was further developed to apply electric fields and mechanical loads simultaneously as shown in figure 6.2 (a). The compressive mechanical loading is applied using the Deben rig and electric field is

applied perpendicular to the mechanical loading. A zoomed-in view of the specimen is shown in figure 6.2(b).

Domain evolution was observed using this technique; however, the domain wall movements were rapid when electric field and mechanical stress were applied simultaneously. Further development is needed to capture such ballistic domain wall motion, using stroboscopic or high speed photography methods.

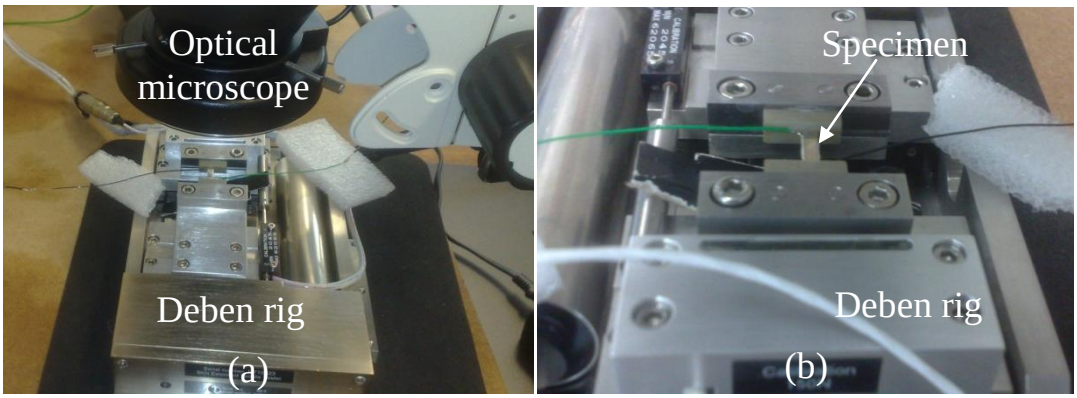

Figure 6.2: In-situ electromechanical testing using optical microscopy.

Finally, as PFM proved capable of distinguishing between all the domain types in tetragonal BT, in-situ domain evolution studies with PFM and applying compressive stress could yield valuable data. However, space constraints in scanning probe systems pose challenging limits on the experimentation.

Appendix 1

List of publications, conference proceedings and talks

Journal papers – published/accepted

- Tsou N.-T., Potnis P. R., and Huber J. E., 2011, "Classification of laminate domain patterns in ferroelectrics," *Physical Review B*, 83,184120, pp. 1-6.
- Potnis P. R., Tsou N.T., and Huber J. E., 2011, "A Review of Domain Modelling and Domain Imaging Techniques in Ferroelectric Crystals," *Materials*, 4(2), pp. 417-447.
- Potnis P. R., Huber J. E., and Sutter J. P., 2011, "Synchrotron mapping of laminate microstructures in barium titanate single crystals," *Ferroelectrics*, 422(1), pp 33-39.

Conference Proceedings

- Potnis P. R., Huber J. E., Sutter J. P., Hofmann F., Abbey B., and Korsunsky A. M., 2010, "Mapping of domain structure in Barium Titanate single crystals by synchrotron x-ray topography," *Proceedings of SPIE*, 7644, pp. 1-10.

Conference presentations/seminars:

- Mapping of domain structure in Barium Titanate single crystals by synchrotron x-ray topography, Behaviour and Mechanics of Multifunctional Materials and Composites, SPIE, San Diego, USA, March 2010.
- Synchrotron mapping of laminate microstructures in barium titanate single crystals, ISAF-ECAPD, Edinburgh, UK, August 2010.
- Mapping of domain structure in single crystal ferroelectrics, Microscience, Royal Microscopy Society, London, UK, July 2010 (Poster).
- XRD, SEM and AFM study of ferroelectric microstructure, Solid Mechanics and Materials group seminar series, Oxford, UK, November 2009.
- Poster presentations in Diamond User Meeting, Diamond Light Source, UK (September 2010) and Workshop on X-ray & Neutron Scattering in Multiferroic and Ferroelectric Materials Research, NPL, UK, September 2011.

References

[1] Haertling G. H., 1999, “Ferroelectric ceramics: history and technology,” Journal of the American Ceramic Society, 82(4), pp. 797–818.

[2] Jaffe H., 1958, “Piezoelectric ceramics,” Journal of American Ceramic Society, 41, pp. 494-498.

[3] Lines M. E., and Glass A. M., 1977, Principles and Applications of Ferroelectrics and Related Materials, Clarendon press, Oxford.

[4] Park S. E., and Shrout T. R., 1997, “Ultrahigh strain and piezoelectric behaviour in relaxor based ferroelectric single crystals,” Journal of Applied Physics, 82(4), pp. 1804-1811.

[5] Fousek J., 1991, “Ferroelectricity: Remarks on historical aspects and present trends,” Ferroelectrics, 113(1), pp. 3–20.

[6] Ye Z.-G., 2008, Handbook of advance dielectric, piezoelectric and ferroelectric materials, Woodhead publishing limited, Cambridge.

[7] Tagantsev A. K., Cross L. E., and Fousek J., 2010, Domains in Ferroic Crystals and Thin Films, Springer New York, New York, NY.

[8] Damjanovic D., 1998, “Ferroelectric, dielectric and piezoelectric properties of ferroelectric thin films and ceramics,” Reports on Progress in Physics, pp. 1267-1324.

[9] Nye J. F., 1985, Physical Properties of Crystals: Their Representation by Tensors and Matrices, Clarendon press, Oxford.

[10] Moulson A. J., and Herbert J. M., 2003, Electroceramics: Materials, Properties, Applications, Wiley, London.

[11] Kungl H., and Hoffmann M. J., 2010, “Effects of sintering temperature on microstructure and high field strain of niobium-strontium doped morphotropic lead zirconate titanate,” Journal of Applied Physics, 107(5), p. 054111.

[12] Oakley C. G., and Zipparo M. J., 2000, “Single crystal piezoelectrics: a revolutionary development for transducers,” Ultrasonics Symposium, 2000 IEEE, IEEE, pp. 1157–1167.

[13] Kuwata J., Uchino K., and Nomura S., 1982, “Dielectric and piezoelectric properties of $0.91PB(Zn_{1/3}Nb_{2/3})O_3$-$0.09PbTiO_3$ single crystals.,” Japanese Journal of Applied Physics, 21, pp. 1298-1302.

[14] Cross L. E., 1987, “Relaxor ferroelectrics,” Ferroelectrics, 76(1), pp. 241-267.

[15] Merz W. J., 1954, “Domain Formation and Domain Wall Motions in Ferroelectric $BaTiO_3$ Single Crystals,” Physical Review, 95(3), pp. 690–698.

[16] Little E. A., 1955, “Dynamic behaviour of domain walls in barium titanate,” Physical Review, 98(4), pp. 978–984.

[17] Forsbergh P., 1949, “Domain structures and phase transitions in barium titanate,” Physical Review, 76(8), pp. 1187–1201.

[18] Burcsu E., Ravichandran G., and Bhattacharya K., 2000, “Large strain electrostrictive actuation in barium titanate,” Applied Physics Letters, 77(11), p. 1698.

[19] Burcsu E. N., 2001, “Electromechanical behavior of 90° domain motion in barium titanate single crystals,” Proceedings of SPIE, pp. 121-130.

[20] Burcsu E., Ravichandran G., and Bhattacharya K., 2004, “Large electrostrictive actuation of barium titanate single crystals,” Journal of the Mechanics and Physics of Solids, 52(4), pp. 823–846.

[21] Wada S., Suzuki S., Noma T., Suzuki T., Osada M., Akihana M., Park S. E., Cross L. E., and Shrout T. R., 1999, “Enhanced piezoelectricity of barium titanate single crystals with engineered domain configuration,” Japanese journal of applied physics, 38, pp. 5505-5511.

[22] Wada S., Muraishi T., Yokoh K., Yako K., Kamemoto H., and Tsurumi T., 2007, “Domain Wall Engineering in Lead-Free Piezoelectric Crystals,” Ferroelectrics, 355(773573599), pp. 37-49.

[23] Setter N., Damjanovic D., Eng L., Fox G., Gevorgian S., Hong S., Kingon a, Kohlstedt H., Park N. Y., Stephenson G. B., Stolitchnov I., Taganstev a K., Taylor D. V., Yamada T., and Streiffer S., 2006, “Ferroelectric thin films: Review of materials, properties, and applications,” Journal of Applied Physics, 100(5), p. 051606.

[24] Damjanovic D., Muralt P., and Setter N., 2001, “Ferroelectric sensors,” IEEE Sensors Journal, 1(3), pp. 191-206.

[25] Cross L. E., 1995, “Ferroelectric materials for electromechanical transducer applications,” Japanese journal of applied physics, 34, pp. 2525-2532.

[26 Land C. E., and Thacher P. D., 1969, “Ferroelectric ceramic electrooptic materials and devices,” Proceedings of the IEEE, 57(5), pp. 751-768.

[27] Park S. E., and Shrout T. R., 1997, “Characteristics of relaxor-based piezoelectric single crystals for ultrasonic transducers,” IEEE Transactions on Ultrasonics, Ferroelectrics and Frequency Control, 44(5), pp. 1140-1147.

[28] Ritter T., Geng X., Kirk Shung K., Lopath P. D., Park S. E., and Shrout T. R., 2000, “Single crystal PZN/PT-polymer composites for ultrasound transducer applications.,” IEEE transactions on ultrasonics, ferroelectrics, and frequency control, 47(4), pp. 792-800.

[29] Gururaja T. R., Panda R. K., Chen J., and Beck H., 1999, "Single crystal transducers for medical imaging applications," 1999 IEEE Ultrasonics Symposium. Proceedings. International Symposium (Cat. No.99CH37027), 2, pp. 969-972.

[30] Saitoh S., Kobayashi T., Harada K., Shimanuki S., and Yamashita Y., 1998, "A 20 MHz single-element ultrasonic probe using 0.91Pb($Zn_{1/3}Nb_{2/3}O_3$-0.09$PbTiO_3$ single crystal.," IEEE transactions on ultrasonics, ferroelectrics, and frequency control, 45(4), pp. 1071-6.

[31] Wlodkowski P., 2001, "The development of high-sensitivity, low-noise accelerometers utilizing single crystal piezoelectric materials," Sensors and Actuators A: Physical, 90(1-2), pp. 125-131.

[32] Jiang X. N., Rehrig P. W., Hackenberger W. S., Moore J., Chodimella S., and Patrick B., 2004, "Single Crystal Piezoelectric Actuators for Advanced Deformable Mirrors," ASME Conference Proceedings, ASME, pp. 37-42.

[33] Jiang X., Rehrig P. W., Hackenberger W. S., Smith E., Dong S., Viehland D., Moore J. J., and Patrick B., 2005, "Advanced piezoelectric single crystal based actuators," Proceedings of SPIE, SPIE, pp. 253-262.

[34] Aksel E., and Jones J. L., 2010, "Advances in Lead-Free Piezoelectric Materials for Sensors and Actuators," Sensors, 10(3), pp. 1935-1954.

[35] Fan H., Zhao L., Tang B., Tian C., and Kim H., 2003, "Growth and characterization of PMNT relaxor-based ferroelectric single crystals by flux method," Materials Science and Engineering B, 99(1-3), pp. 183-186.

[36] Fang B., Xu H., He T., and Luo H., 2002, "Growth mechanism and electrical properties of PbO_3 single crystals by a modified Bridgman method," Journal of crystal growth, 244, pp. 318-326.

[37] Chen W., and Ye Z., 2001, "Top seeded solution growth and characterization of piezo-/ferroelectric (1-*x*)Pb($Zn_{1/3}Nb_{2/3}$)O_3-*x*$PbTiO_3$ single crystals," Journal of Crystal Growth, 233, pp. 503-511.

[38] Kitamura K., Yamamoto J., Iyi N., Kirnura S., and Hayashi T., 1992, "Stoichiometric $LiNbO_3$ single crystal growth by double crucible Czochralski method using automatic powder supply system," Journal of Crystal Growth, 116(3-4), pp. 327-332.

[39] Rehrig P. W., Trolier-McKinstry S., Park S. E., and Messing G. L., 2000, "Dielectric and electromechanical properties of barium titanate single crystals grown by templated grain growth.," IEEE transactions on ultrasonics, ferroelectrics, and frequency control, 47(4), pp. 895-902.

[40] Remeika J., and Jackson W. M., 1954, "A method for growing barium titanate single crystals," Journal of the American Chemical Society, 76(3), pp. 940–941.

[41] Matthias B., 1948, "The growth of barium titanate crystals," Physical Review, 73(7), pp. 808–809.

[42] Berlincourt D., and Jaffe H., 1958, “Elastic and piezoelectric coefficients of single-crystal barium titanate,” Physical Review, 111(1).

[43] Belruss V., Kalnajs J., Linz A., and Folweiler R., 1971, “Top-seeded solution growth of oxide crystals from non-stoichiometric melts,” Materials Research Bulletin, 6(10), pp. 899–905.

[44] Kurosaka A., Ajimura S., Nakao O., Tomomatsu K., and Tominaga H., 1995, “Process for preparing barium titanate single crystals,” EP Patent.

[45] Rytz D., Wechsler B., Nelson C., and Kirby K., 1990, “Top-seeded solution growth of $BaTiO_3$, $KNbO_3$, $SrTiO_3$, $Bi_{12}TiO_{20}$ and $La_{2-x}Ba_xCuO_4$,” Journal of Crystal Growth, 99(1-4), pp. 864–868.

[46] Noheda B., Cox D., Shirane G., Gao J., and Ye Z.-G., 2002, “Phase diagram of the ferroelectric relaxor (1-x)$PbMg_{1/3}Nb_{2/3}O_3$-x$PbTiO_3$,” Physical Review B, 66(5), pp. 1-10.

[47] Guo Y., Luo H., Ling D., Xu H., He T., and Yin Z., 2003, “The phase transition sequence and the location of the morphotropic phase boundary region in (1-x)[$Pb(Mg_{1/3}Nb_{2/3}O_3$]-x$PbTiO_3$ single crystal,” Journal of Physics: Condensed Matter, 15(2), p. L77-L82.

[48] Xu G., Luo H., Xu H., and Yin Z., 2001, “Third ferroelectric phase in PMNT single crystals near the morphotropic phase boundary composition,” Physical Review B, 64(2), pp. 1-3.

[49] The Audi Magazine.

[50] Mullerfiedler R., and Knoblauch V., 2003, “Reliability aspects of microsensors and micromechatronic actuators for automotive applications,” Microelectronics Reliability, 43(7), pp. 1085-1097.

[51] Pritchard J., Bowen C. R., and Lowrie F., 2001, “Multilayer actuators: review,” British Ceramic Transactions, 100(6), pp. 265-273.

[52] Furuta A., and Uchino K., 1993, “Dynamic Observation of Crack Propagation in Piezoelectric Multilayer Actuators,” Journal of the American Ceramic Society, 76(6), pp. 1615-1617.

[53] Schneider G. A., 2007, “Influence of electric field and mechanical stresses on the fracture of ferroelectrics,” Annual Review of Materials Research, 37, pp. 491-538.

[54] Häusler C., Jelitto H., Neumeister P., Balke H., and Schneider G. a, 2009, “Interfacial fracture of piezoelectric multilayer actuators under mechanical and electrical loading,” International Journal of Fracture, 160(1), pp. 43-54.

[55] Busche M., 2001, “Fracture and domain switching by indentation in barium titanate single crystals,” Scripta Materialia, 44(2), pp. 207-212.

[56] Cross L. E., 2004, “Lead free at last,” Nature, 432, pp. 24-25.

[57] Maeder M. D., Damjanovic D., and Setter N., 2004, "Lead Free Piezoelectric Materials," Journal of Electroceramics, 13(1-3), pp. 385-392.

[58] Saito Y., Takao H., Tani T., Nonoyama T., Takatori K., Homma T., Nagaya T., and Nakamura M., 2004, "Lead-free piezoceramics," Nature, 432(7013), pp. 84–87.

[59] Li X., and Luo H., 2010, "The Growth and Properties of Relaxor-Based Ferroelectric Single Crystals," Journal of the American Ceramic Society, 93(10), pp. 2915-2928.

[60] Feng Z., 2003, "Dependence of high electric-field-induced strain on the composition and orientation of $Pb(Mg_{1/3}Nb_{2/3})O_3$–$PbTiO_3$ crystals," Solid State Communications, 126(6), pp. 347-351.

[61] Viehland D., Ewart L., Powers J., and Li J. F., 2001, "Stress dependence of the electromechanical properties of ⟨001⟩-oriented $Pb(Mg_{1/3}Nb_{2/3})O_3$]–$PbTiO_3$ crystals: Performance advantages and limitations," Journal of Applied Physics, 90(5), p. 2479.

[62] Viehland D., 2006, "Effect of Uniaxial Stress Upon the Electromechanical Properties of Various Piezoelectric Ceramics and Single Crystals," Journal of the American Ceramic Society, 89(3), pp. 775-785.

[63] McLaughlin E. a, Liu T., and Lynch C. S., 2004, "Relaxor ferroelectric PMN-32%PT crystals under stress and electric field loading: I-32 mode measurements," Acta Materialia, 52(13), pp. 3849-3857.

[64] Mclaughlin E., Liu T., and Lynch C., 2005, "Relaxor ferroelectric PMN-32%PT crystals under stress, electric field and temperature loading: II-33-mode measurements," Acta Materialia, 53(14), pp. 4001-4008.

[65] Shanthi M., and Lim L. C., 2009, "Combined electric field and stress-induced R-O phase transformation in [011]-poled $Pb(Mg_{1/3}Nb_{2/3})O_3$–(28–32)%$PbTiO_3$ single crystals of [011]-length cut," Applied Physics Letters, 95(10), p. 102901.

[66] Li F., Li S., and Fang D., 2005, "Domain switching in ferroelectric single crystal/ceramics under electromechanical loading," Materials Science and Engineering B, 120(1-3), pp. 119-124.

[67] Huber J., and Fleck N., 2001, "Multi-axial electrical switching of a ferroelectric: theory versus experiment," Journal of the Mechanics and Physics of Solids, 49(4), pp. 785–811.

[68] Shieh J., Huber J. E., and Fleck N. A., 2003, "An evaluation of switching criteria for ferroelectrics under stress and electric field," Acta Materialia, 51(20), pp. 6123-6137.

[69] Zhou D., Kamlah M., and Laskewitz B., 2006, "Multi-axial non-proportional polarization rotation tests of soft PZT piezoceramics under electric field loading," Proceeding of SPIE, 6170, pp. 617009-1-617009-9.

[70] Kamlah M., 2001, "Ferroelectric and ferroelastic piezoceramics–modeling of electromechanical hysteresis phenomena," Continuum Mechanics and Thermodynamics, 13(4), pp. 219–268.

[71] Pathak A., and McMeeking R., 2008, "Three-dimensional finite element simulations of ferroelectric polycrystals under electrical and mechanical loading," Journal of the Mechanics and Physics of Solids, 56(2), pp. 663-683.

[72] Landis C., 2002, "Fully coupled, multi-axial, symmetric constitutive laws for polycrystalline ferroelectric ceramics," Journal of the Mechanics and Physics of Solids, 50(1), pp. 127-152.

[73] Sawyer C. B., and Tower C., 1930, "Rochelle salt as a dielectric," Physical Review, 35(3), p. 269.

[74] Wan Q., Chen C., and Shen Y. P., 2005, "Effects of stress and electric field on the electromechanical properties of $Pb(Mg_{1/3}Nb_{2/3})O_3$–$0.32PbTiO_3$ single crystals," Journal of Applied Physics, 98(2), p. 024103.

[75] Park S., and Hackenberger W., 2002, "High performance single crystal piezoelectrics: applications and issues," Current Opinion in Solid State and Materials Science, 6(1), pp. 11-18.

[76] Hall D., 2001, "Nonlinearity in piezoelectric ceramics," Journal of materials science, 36(19), pp. 4575–4601.

[77] Bhattacharya K., and Ravichandran G., 2003, "Ferroelectric perovskites for electromechanical actuation," Acta Materialia, 51(19), pp. 5941-5960.

[78] Bassiouny E., Ghaleb A., and Maugin G., 1988, "Thermodynamical formulation for coupled electromechanical hysteresis effects–I. Basic equations," International journal of engineering science, 26(12), pp. 1279–1295.

[79] Bassiouny E., Ghaleb A., and Maugin G., 1988, "Thermodynamical formulation for coupled electromechanical hysteresis effects–II. Poling of ceramics," International journal of engineering science, 26(12), pp. 1297–1306.

[80] Bassiouny E., 1989, "Thermodynamical formulation for coupled electromechanical hysteresis effects—III. Parameter identification," International Journal of Engineering Science, 27(8), pp. 975-987.

[81] Bassiouny E., and Maugin G., 1989, "Thermodynamical formulation for coupled electromechanical hysteresis effects–IV. Combined electromechanical loading," International Journal of engineering science, 27(8), pp. 989–1000.

[82] Cocks A., and Mcmeeking R., 1999, "A phenomenological constitutive law for the behaviour of ferroelectric ceramics," Ferroelectrics, 228(1), pp. 219-228.

[83] Damjanovic D., 1997, "Stress and frequency dependence of the direct piezoelectric effect in ferroelectric ceramics," Journal of Applied Physics, 82(4), p. 1788.

[84] Ricinschi D., Harnagea C., Papusoi C., Mitoseriu L., Tura V., and Okuyama M., 1998, "Analysis of ferroelectric switching in finite media as a Landau-type phase transition," Journal of Physics: Condensed Matter, 10(2), pp. 477-492.

[85] McMeeking R. M., and Landis C. M., 2002, “A phenomenological multi-axial constitutive law for switching in polycrystalline ferroelectric ceramics,” International Journal of Engineering Science, 40(14), pp. 1553–1577.

[86] Lynch C., 1996, “The effect of uniaxial stress on the electro-mechanical response of 8/65/35 PLZT,” Acta Materialia, 44(10), pp. 4137-4148.

[87] Landis C., 2004, “Non-linear constitutive modeling of ferroelectrics,” Current Opinion in Solid State and Materials Science, 8(1), pp. 59-69.

[88] Hwang S., Lynch C., and Mcmeeking R., 1995, “Ferroelectric/ferroelastic interactions and a polarization switching model,” Acta Metallurgica et Materialia, 43(5), pp. 2073-2084.

[89] Huber J., 2005, “Micromechanical modelling of ferroelectrics,” Current Opinion in Solid State and Materials Science, 9(3), pp. 100-106.

[90] Cao H., and Evans A. G., 1993, “Nonlinear Deformation of Ferroelectric Ceramics,” Journal of the American Ceramic Society, 76(4), pp. 890-896.

[91] Zhou D., Wang Z., and Kamlah M., 2005, “Experimental investigation of domain switching criterion for soft lead zirconate titanate piezoceramics under coaxial proportional electromechanical loading,” Journal of Applied Physics, 97(8), p. 084105.

[92] Hall D. a, Steuwer a, Cherdhirunkorn B., Mori T., and Withers P. J., 2004, “A high energy synchrotron X-ray study of crystallographic texture and lattice strain in soft lead zirconate titanate ceramics,” Journal of Applied Physics, 96(8), p. 4245.

[93] Hall D., Steuwer A, Cherdhirunkorn B., Withers P., and Mori T., 2005, “Micromechanics of residual stress and texture development due to poling in polycrystalline ferroelectric ceramics,” Journal of the Mechanics and Physics of Solids, 53(2), pp. 249-260.

[94] Hall D., Steuwer A, Cherdhirunkorn B., Mori T., and Withers P., 2006, “Analysis of elastic strain and crystallographic texture in poled rhombohedral PZT ceramics,” Acta Materialia, 54(11), pp. 3075-3083.

[95] Rogan R. C., Üstündag E., Clausen B., and Daymond M. R., 2003, “Texture and strain analysis of the ferroelastic behavior of $Pb(Zr,Ti)O_3$ by in situ neutron diffraction,” Journal of Applied Physics, 93(7), p. 4104.

[96] Jones J. L., Slamovich E. B., and Bowman K. J., 2005, “Domain texture distributions in tetragonal lead zirconate titanate by x-ray and neutron diffraction,” Journal of Applied Physics, 97(3), p. 034113.

[97] Fernandes R. P., Herber R.-P., Kunz L., Mgbemere H. E., and Schneider G. a, 2010, “Area fraction quantification of ferroelectric domain orientations in $BaTiO_3$ using piezoresponse force microscopy,” Journal of Applied Physics, 108(4), p. 044103.

[98] Noheda B., 2002, “Structure and high-piezoelectricity in lead oxide solid solutions,” Current Opinion in Solid State and Materials Science, 6(1), pp. 27-34.

[99] Ye Z., 2002, “Crystal chemistry and domain structure of relaxor piezocrystals,” Current Opinion in Solid State and Materials Science, 6(1), pp. 35-44.

[100] Liu Q., and Huber J., 2006, “Creep in ferroelectrics due to unipolar electrical loading,” Journal of the European Ceramic Society, 26(13), pp. 2799-2806.

[101] Huber J., Fleck N. A., Landis C. M., and Mcmeeking R. M., 1999, “A constitutive model for ferroelectric polycrystals,” Journal of the Mechanics and Physics of Solids, 47(8), pp. 1663-1697.

[102] Belov a. Y., and Kreher W. S., 2007, “Micromechanics of Ferroelectrics: From Domain Walls to Piezoceramic Devices,” Ferroelectrics, 351, pp. 79-87.

[103] Haug A., Huber J. E., Onck P. R., and Giessen E. Van der, 2007, “Multi-grain analysis versus self-consistent estimates of ferroelectric polycrystals,” Journal of the Mechanics and Physics of Solids, 55(3), pp. 648-665.

[104] Arlt G., 1996, “Switching and dielectric nonlinearity of ferroelectric ceramics,” Ferroelectrics, 189(1), pp. 91-101.

[105] Arlt G., 1997, “A model for switching and hysteresis in ferroelectric ceramics,” Integrated Ferroelectrics, 16(1), pp. 229-236.

[106] Hooton J. A., and Merz W. J., 1955, “Etch Patterns and Ferroelectric Domains in $BaTiO_3$ Single Crystals,” Physical Review, 98(2), pp. 409–413.

[107] Li J. Y., and Liu D., 2004, “On ferroelectric crystals with engineered domain configurations,” Journal of the Mechanics and Physics of Solids, 52(8), pp. 1719–1742.

[108] Liang Y., Kato H., Taya M., and Mori T., 2000, “Infinitesimal approach to the crystallography of martensitic transformation: application to Ni-Ti,” Scripta Materialia, 43(6), pp. 535-540.

[109] DeVries R. C., and Burke J. E., 1957, “Microstructure of Barium Titanate ceramics,” Journal of the American Ceramic Society, 40(6), pp. 200-206.

[110] Tsai F., Khiznichenko V., and Cowley J., 1992, “High-resolution electron microscopy of 90° ferroelectric domain boundaries in $BaTiO_3$ and $Pb(Zr_{0.52}Ti_{0.48})O_3$,” Ultramicroscopy, 45(1), pp. 55-63.

[111] Soergel E., 2005, “Visualization of ferroelectric domains in bulk single crystals,” Applied Physics B, 81(6), pp. 729-751.

[112] Potnis P. R., Tsou N.-T., and Huber J. E., 2011, “A Review of Domain Modelling and Domain Imaging Techniques in Ferroelectric Crystals,” Materials, 4(2), pp. 417-447.

[113] Hatano J., Suda F., and Futama H., 1973, “Improved powder-pattern technique for delineating ferroelectric domains,” Japanese Journal of Applied, 12(10), pp. 1644-1645.

[114] Robinson G., and White R., 1967, “Scanning electron microscopy of ferroelectric domains in barium titanate,” Applied Physics Letters, 10(11), pp. 320–323.

[115] Potnis P. R., Huber J. E., Sutter J. P., Hofmann F., Abbey B., and Korsunsky A. M., 2010, "Mapping of domain structure in Barium Titanate single crystals by synchrotron x-ray topography," Proceeding of SPIE, pp. 1-10.

[116] Matthias B., and Hippel A. Von, 1948, "Domain structure and dielectric response of barium titanate single crystals," Physical Review, 73(11), pp. 1378–1384.

[117] Merz W. J., 1952, "Domain properties of $BaTiO_3$," Physical Review, 7, pp. 421-422.

[118] Mulvmill M., Uchino K., Li Z., and Cao W., 1996, "In-situ observation of the domain configurations during the phase transitions in barium titanate," Philosophical Magazine Part B, 74(1), pp. 25-36.

[119] Grubsky V., MacCormack S., and Feinberg J., 1996, "All-optical three-dimensional mapping of 180° domains hidden in a $BaTiO_3$ crystal," Optics letters, 21(1), pp. 6–8.

[120] Glazer A. M., Lewis J. G., and Kaminsky W., 1996, "An Automatic Optical Imaging System for Birefringent Media," Proceedings of the Royal Society A: Mathematical, Physical and Engineering Sciences, 452(1955), pp. 2751-2765.

[121] MacCormack S., and Feinberg J., 1996, "Revealing 180° domains in ferroelectric crystals by photorefractive beam coupling," Applied Optics, 35(30), pp. 5961–5963.

[122] Uesu Y., Kurimura S., and Yamamoto Y., 1995, "Optical second harmonic images of 90° domain structure in BaTiO3 and periodically inverted antiparallel domains in $LiTaO_3$," Applied Physics Letters, 66(17), p. 2165.

[123] Niizeki N., and Hasegawa M., 1964, "Direct Observation of Antiparallel 180° Domains in $BaTiO_3$ by X-Ray Anomalous Dispersion Method," Journal of the Physical Society of Japan, 19(4), pp. 550-554.

[124] Park B. M., Chung S. J., Kim H. S., Si W., and Dudley M., 1997, "Synchrotron white-beam X-ray topography of ferroelectric domains in a $BaTiO_3$ single crystal," Philosophical Magazine A, 75(3), pp. 611-620.

[125] Fogarty G., Steiner B., Cronin-Golomb M., Laor U., Garrett M. H., Martin J., and Uhrin R., 1996, "Antiparallel ferroelectric domains in photorefractive barium titanate and strontium barium niobate observed by high-resolution x-ray diffraction imaging," Journal of the Optical Society of America B, 13(11), p. 2636.

[126] Čáslavsk`y J., and Polcarová M., 1964, "Observation of ferroelectric domains on barium titanate by X-ray diffraction microscopy," Czechoslovak Journal of Physics, 14(6), pp. 454–458.

[127] Roshchupkin D. V., Irzhak D. V., and Antipov V. V., 2009, "Study of $LiNbO_3$ and $LiTaO_3$ ferroelectric domain structures using high-resolution x-ray diffraction under application of external electric field," Journal of Applied Physics, 105(2), p. 024112.

[128] Daniels J. E., Finlayson T. R., Davis M., Damjanovic D., Studer A. J., Hoffman M., and Jones J. L., 2007, "Neutron diffraction study of the polarization reversal

mechanism in $[111]_c$-oriented $Pb(Zn_{1/3}Nb_{2/3})O_3$–$xPbTiO_3$," Journal of Applied Physics, 101, p. 104108.

[129] Hall D. a, Evans J. D. S., Oliver E. C., Withers P. J., and Mori T., 2007, "In-situ neutron diffraction study of the rhombohedral to orthorhombic phase transformation in lead zirconate titanate ceramics produced by uniaxial compression," Philosophical Magazine Letters, 87(1), pp. 41-52.

[130] Jones J. L., 2007, "The use of diffraction in the characterization of piezoelectric materials," Journal of Electroceramics, 19(1), pp. 69-81.

[131] Aristov V. V., Kokhanchik L. S., Meyer K.-P., and Blumtritt H., 1983, "Scanning electron microscopic investigations of peculiarities of the $BaTiO_3$ ferroelectric domain contrast," Physica Status Solidi (a), 78(1), pp. 229-236.

[132] Bihan R., 1989, "Study of ferroelectric and ferroelastic domain structures by scanning electron microscopy," Ferroelectrics, 97, pp. 19-46.

[133] Gruner D., and Shen Z., 2010, "Direct Scanning Electron Microscopy Imaging of Ferroelectric Domains After Ion Milling," Journal of the American Ceramic Society, 93(1), pp. 48-50.

[134] Hu Y. H., Chan H. M., Wen Z. X., and Harmer M. P., 1986, "Scanning Electron Microscopy and Transmission Electron Microscopy Study of Ferroelectric Domains in Doped $BaTiO_3$," Journal of the American Ceramic Society, 69(8), pp. 594-602.

[135] Blank H., and Amenlinckx S., 1963, "Microscopy, Direct Observation of Ferroelectric Domains In Barium Titanate By Means Of Electron microscopy," Applied Physics Letters, 2(7), pp. 140-142.

[136] Malis T., and Gleiter H., 1976, "Investigation of the structure of ferroelectric domain boundaries by transmission electron microscopy," Journal of Applied Physics, 47(12), p. 5195.

[137] Bursill L., and Lin P. J., 1984, "Microdomains observed at the ferroelectric/paraelectric phase transition of barium titanate," Nature, 311, pp. 550-552.

[138] Floquet N., Valot C., Mesnier M., and JC, 1997, "Ferroelectric domain walls in $BaTiO_3$: Fingerprints in XRPD diagrams and quantitative HRTEM image analysis," J ournal of Physics III France, 7, pp. 1105-1128.

[139] Park B. M., and Chung S. J., 1994, "Optical, Electron Microscopic, and X-ray Topographic Studies of Ferroic Domains in Barium Titanate Crystals Grown from High-Temperature Solution," Journal of the American Ceramic Society, 77(12), pp. 3193-3201.

[140] Zhang B. Y., Jiang F. M., Yang Y., Yin Q. R., and Kojima S., 1996, "Electron acoustic imaging of $BaTiO_3$ single crystals," Journal of Applied Physics, 80(3), pp. 1916-1918.

[141] Burnett T. L., Comyn T. P., Merson E., Bell a J., Mingard K., Hegarty T., and Cain M., 2008, "Electron backscatter diffraction as a domain analysis technique in

$BiFeO_3$-$PbTiO_3$ single crystals.," IEEE transactions on ultrasonics, ferroelectrics, and frequency control, 55(5), pp. 957-62.

[142] Farooq M. U., Villaurrutia R., MacLaren I., Burnett T. L., Comyn T. P., Bell a J., Kungl H., and Hoffmann M. J., 2008, "Electron backscatter diffraction mapping of herringbone domain structures in tetragonal piezoelectrics," Journal of Applied Physics, 104(2), p. 024111.

[143] Cheng S.-Y., Ho N.-J., and Lu H.-Y., 2008, "Micro-Indentation-Induced Domain Switching in Tetragonal Barium Titanate," Journal of the American Ceramic Society, 91(11), pp. 3721-3727.

[144] Burnett T. L., Weaver P. M., Blackburn J. F., Stewart M., and Cain M. G., 2010, "Correlation of electron backscatter diffraction and piezoresponse force microscopy for the nanoscale characterization of ferroelectric domains in polycrystalline lead zirconate titanate," Journal of Applied Physics, 108(4), p. 042001.

[145] Bonnell D. A., 2001, Scanning probe microscopy and Spectroscopy: Theory, Techniques and Applications, John Wiley & Sons: Hoboken, NJ, USA.

[146] Kalinin S. V., Rodriguez B. J., Jesse S., Karapetian E., Mirman B., Eliseev E. A., and Morozovska A. N., 2007, "Nanoscale Electromechanics of Ferroelectric and Biological Systems: A New Dimension in Scanning Probe Microscopy," Annual Review of Materials Research, 37, pp. 189-238.

[147] Kalinin S. V., Morozovska A. N., Chen L. Q., and Rodriguez B. J., 2010, "Local polarization dynamics in ferroelectric materials," Reports on Progress in Physics, 73(5), p. 056502.

[148] Gruverman a, and Kholkin a, 2006, "Nanoscale ferroelectrics: processing, characterization and future trends," Reports on Progress in Physics, 69(8), pp. 2443-2474.

[149] Eng L., Friedrich M., Fousek J., and Günter P., 1996, "Deconvolution of topographic and ferroelectric contrast by noncontact and friction force microscopy," Journal of Vacuum Science Technology B, 14(2), pp. 1191-1196.

[150] Eng L. M., Friedrich M., Fousek J., and Gunter P., 1996, "Scanning force microscopy of ferroelectric crystals," Ferroelectrics, 186(1), pp. 49-52.

[151] Nakatani N., 1979, "Microscopic Structure of Cleavage Surface of Ferroelectric Tri-Glycine Sulfate," Japanese Journal of Applied Physics, 18(3), pp. 491-500.

[152] Luthi R., Haefke H., Meyer K., Meyer E., Howald L., and Gijntherodt H., 1993, "Surface and domain structures scanning force microscopy of ferroelectric crystals studied with scanning force microscopy," Journal of Applied Physics, 74(12), pp. 7461-7471.

[153] Munoz-Saldana J., Schneider G., and Eng L., 2001, "Stress induced movement of ferroelastic domain walls in $BaTiO_3$ single crystals evaluated by scanning force microscopy," Surface Science, 480(1-2), p. L402–L410.

[154] Jungk T., and Soergel E., 2006, "Contrast Mechanism for Visualization of Ferroelectric Domains with Scanning Force Microscopy," Ferroelectrics, 334(1), pp. 29-34.

[155] Kalinin S., and Bonnell D., 2001, "Local potential and polarization screening on ferroelectric surfaces," Physical Review B, 63(12), pp. 1-13.

[156] Proksch R., and Kalinin S., 2009, "Piezoresponse Force Microscopy," Microscopy Today, 17(06), p. 10.

[157] Pang G., and Baba-Kishi K., 1998, "Characterization of butterfly single crystals of $BaTiO_3$ by atomic force, optical and scanning," Journal of Physics D: Applied Physics, 2846, pp. 2846-2853.

[158] Tsou N., Potnis P., and Huber J., 2011, "Classification of laminate domain patterns in ferroelectrics," Physical Review B, 83(18), pp. 1-6.

[159] Shu Y. C., Yen J. H., Chen H. Z., Li J. Y., and Li L. J., 2008, "Constrained modeling of domain patterns in rhombohedral ferroelectrics," Applied Physics Letters, 92(5), p. 052909.

[160] Shu Y. C., and Bhattacharya K., 2001, "Domain patterns and macroscopic behaviour of ferroelectric materials," Philosophical magazine b-physics of condensed matter statistical mechanics electronic optical and magnetic properties, 81(12), pp. 2021-2054.

[161] Tsou N. T., and Huber J. E., 2010, "Compatible domain structures and the poling of single crystal ferroelectrics," Mechanics of Materials, 42(7), pp. 740-753.

[162] Fousek J., and Brezina B., 1960, "The movement of single 90° domain walls of $BaTiO_3$ in an alternating electric field.," Czechoslovak Journal of Physics B, 10, pp. 511-550.

[163] Fousek J., and Brezina B., 1961, "The motion of 90° wedge domains in $BaTiO_3$ in an alternating electric field," Czechoslovak Journal of Physics, 11, pp. 344-384.

[164] Miller R. C., and Savage A., 1960, "Motion of 180° domain walls in metal electroded barium titanate crystals as a function of electric field and sample thickness," Journal of Applied Physics, 31, p. 662.

[165] Kim S., Chung T., and Kim D., 1993, "Effect of external compressive stress on the domain configuration of barium titanate ceramics," Journal of the European Ceramic Society, 12(2), pp. 147-151.

[166] Shieh J., Yeh J. H., Shu Y. C., and Yen J. H., 2009, "Hysteresis behaviours of barium titanate single crystals based on the operation of multiple 90° switching systems," Materials Science and Engineering: B, 161(1-3), pp. 50-54.

[167] Bordas J., Glazer a M., and Hauser H., 1975, "The use of synchrotron radiation for X-ray topography of phase transitions," Philosophical Magazine, 32(2), pp. 471-489.

[168] Jones J., Hoffman M., Daniels J., and Studer a, 2006, “Ferroelastic contribution to the piezoelectric response in lead zirconate titanate by in situ stroboscopic neutron diffraction,” Physica B: Condensed Matter, 385-386, pp. 100-102.

[169] Harrison R. J., Redfern S., Buckley A., and Salje E. K. H., 2004, “Application of real-time, stroboscopic x-ray diffraction with dynamical mechanical analysis to characterize the motion of ferroelastic domain walls,” Journal of Applied Physics, 95(4), p. 1706.